Thermosensitive Injectable Pluronic Hydrogels for Controlled Drug Release

B.SHRIKY

PHD

2018

Thermosensitive Injectable Pluronic Hydrogels for Controlled Drug Release

Characterisation of thermal, rheological and structural properties of injectable pharmaceutical formulations.

Banah SHRIKY

Submitted for the Degree of

Doctor of Philosophy

Faculty of Engineering and Informatics

University of Bradford

2018

Thermosensitive Injectable Pluronic Hydrogels for Controlled Drug Release

Characterisation of thermal, rheological and structural properties of injectable pharmaceutical formulations.

Banah Shriky

Abstract

This study seeks to develop smart hydrogel formulations for injectable controlled drug delivery from Pluronics to enhance patients compliance, decrease side effects, reduce dose and frequency.

A biocompatible copolymer, Pluronic F127 was probed as the main ingredient for the injectable systems owing its low gelation concentration and ease of modification the system properties through excipients addition. The matrix properties were studied through a series of thermal, rheological and structural (SAXS/SANS) experiments as a function of concentration and shear rate, covering both static and dynamic environments. It has shown that gelled viscosity (and structure) can be critically controlled by shear rate and the structures recorded do not match those predicted for sheared colloids. Two further Pluronics F68 and F108, were studied showing similar but shifted gelation properties to F127.

Effects of additives were studied by introducing different Mw PEGs and a model hydrophobic drug 'ibuprofen' to a F127 20% formulation. PEGs addition effects on the system properties and gelation transition were largely dependent on the Mw used in the blend, which became more prominent with increasing chain length.

Ibuprofen's addition has resulted in reduced gelation temperature and smaller hard spheres without having a great effect on the system rheological properties compared to neat gels.

Blends containing both additives PEG and ibuprofen exhibited a synergistic effect, where comparisons show that Ibuprofen had the largest effect on the blends lowering gelation boundaries and slightly increasing the size of the hard spheres indicating the necessity of full characterisation of the formulation with any API.

Keywords: Thermosensitive, Gel, Thermal properties, Rheological properties, SAXS, SANS, Drug Release, Pluronic, Colloidal Crystals, Delivery Systems.

Acknowledgements

First and foremost, I want to thank my supervisors Prof Tim Gough, Prof Adrian Kelly and Dr Mohammad Isreb for their valuable advice, support and guidance throughout my PhD.

My most sincere gratitude goes to my principal supervisor Tim for being the exceptional mentor he is. I'm thankful for his patience, profound insight and arguably - good sense of humour… Go Petawatt!

I'm grateful for our fantastic technical staff; Glen Thompson and Dave Barker for helping with my continuous sample environment problems and machining the scattering experiment rigs out of scribbles.

Thanks are also due to IRC staff members Ben, Elaine and John for all the interesting discussions during breaks and showing me the good side of academia.

I would like to thank 'team cool' past (Max), present (Millan) and honorary members (Vasiliki and Ramisha).. and Micky L for the never-ending supply of intriguing conversations and laughter.

Huge thanks to my local and overseas family and friends for their constant motivation during this journey. In particular, my cheering squad, Lubaba, Ruba and May for their understanding and always willingness to listen.

Lastly, deep gratitude is owed to my family for their unconditional love and encouragement. For my hard-working parents and my siblings 'the three musketeers' whom always believed in me and provided endless support.

I wouldn't have gotten this far without you.

This is dedicated to everyone who wanted to learn a little bit more.

List of publications:

Shriky, B., Kelly, A., Isreb, M. and Gough, T. (2017). Injectable hydrogels for controlled release drug delivery. In: Europe Africa Conference Polymer Processing Society (PPS), Dresden, Germany: PPS32, pp.S13-262.

Shriky, B., Kelly, A., Isreb, M. and Gough, T. (2017). Injectable hydrogels for controlled release drug delivery. Oral presentation in: Polymer Processing Engineering (PPE), Bradford, United Kingdom.

Masato, D., Babenko, M., Shriky, B., Gough, T., Lucchetta, G., & Whiteside, B. (2018). Comparison of crystallization characteristics and mechanical properties of polypropylene processed by ultrasound and conventional micro-injection molding. The International Journal Of Advanced Manufacturing Technology, 99(1-4), 113-125. doi: 10.1007/s00170-018-2493-9.

Shriky, B., Kelly, A., Isreb, M. and Gough, T. (2018). Hydrogels for controlled drug delivery. 3rd Edwards Symposium - New Horizons in Soft Matter, Cambridge, United Kingdom.

Shriky, B., Kelly, A., Isreb, M. and Gough, T. (2018). P70 - Polymer Engineering International/ UK-China AMRI, Bradford, United Kingdom.

Shriky, B., Kelly, A., Isreb, M. and Gough, T. (2018). Hydrogels for controlled drug delivery. Annual Innovative Engineering Research Conference (AIERC 2018), Bradford, United Kingdom.

Work from this thesis has been featured in: Rogers, S. and Mahmoudi, N. Sans2d, Wide Q-range Time of Flight SANS. Presented at large structure user meeting (2018).

Three publications are currently in the late stages of preparation from work presented in this thesis.

Table of contents

List of Figures:

List of Tables:

Nomenclature:

Abbreviations

ALG	Alginate
API	Active Pharmaceutical Ingredient
BA	Bioavailability
BCC	Body Cubic Centred
BSA	Bovine Serum Albumin
CD	Cyclodextrin
CGC	Critical Gelation Concentration
CGT	Critical Gel Tempreature
CMC	Carboxymethyl Cellulose
CMC	Critical Micelle Concentration
CMT	Critical Micelle Concentration
DDS	Drug Delivery Systems
DLS	Dynamic Light Scattering
DSC	Differential Scanning Calorimetry
ECMs	Cell Extracellular Matrices
ELPs	Elastin-Like Polymers
FCC	Face Cubic Centred
FWHM	Full Width Half Maximum
FDA	Food And Drug Administration (USA)
GPC	Gel Permeation Chromatography
GRAS	Generally Recognized As Safe
GRR	Galactose Removal Ratio
HA	Hyaluronic Acid
HCP	Hexagonal Close Packed
HPC	Hydroxypropyl Cellulose
HPMC	Hydroxypropyl Methylcellulose
IBU	Ibuprofen
IPNs	Interpenetrating Polymer Networks
LAOS	Large Amplitude Oscillaty Shear
LCST	Lower Critical Solution Temperature
LLC	Lyotropic Liquid Crystalline
LVE	Linear Viscoelastic
MC	Methyl Cellulose
MDSC	Modulated Differential Scanning Calorimetry
MEMS	Mechanical Micro-Devices
Mw	Molecular Weight

NIPAAm	N-Isopropylacrylamide
NMR	Nuclear Magnetic Resonance
ODT	Order-Disorder Transition
OOT	Order-Order Transition
PBO	Polybutylene Oxide
PCL	Polyε-Caprolactone
PEB	Polyethylene Butyl
PEG	Polyethylene Glycol
PEO	Polyethylene Oxide
PI	Polyisoprene
PLA	Polylactic Acid
PLGA	Poly(Lactide-Co-Glycolide)
PMBs	Pullulan Microbeads
PNP	Polymer-Nanoparticle
PPO	Poly Propylene Oxide
PS	Polystyrene
PVP	Poly(vinylpyrrolidone)
RCP	Random Close Packed
ROA	Route Of Administration
rPBPs	Recombinant Protein-Based Polymers
SANS	Small Angle Neutron Scattering
SAXS	Small Angle X-Ray Scattering
SDD	Sample-To-Detector Distance
SIS	Shear Induced Structures
SLD	Scattering Length Density
TGA	Thermogravimetric Analysis
UCST	Upper Critical Solution Temperature
UV	Ultra-Violet
VE	Viscoelastic

Symbols:

G^0	Free energy
S	Entropy
H^0	Enthalpy
R	Ideal gas constant
A	Unimer number / Surface area
N_{agg}	Micellar aggregation number
p	Micelles number
T	Temperature
R_{HS}	Hard sphere radius
R_m	Micelle raduis
R_h	Hydrodynamic radius
R_g	Radius of gyration
ϱ	Density
φ	Volume fraction
τ	Shear stress
τ_y	Yield stress
$\tau(\lambda)$	Relaxation time
F	Force
$\dot{\gamma}$	Shear rate
v	Velocity
h	Shear gap
γ	Strain
η	Viscosity
$G(t)$	Relaxation modulus
G	Shear modulus
E	Young's modulus
δ	Shift angle
G^*	Complex shear modulus
G'	Stage modulus
G''	Loss modulus
$tan\ \delta$	Damping factor
ω	Angular frequency
k_B	The Boltzmann constant
Pe	Peclet number
q	Scattering vector
d_{Bragg}	Distance between Particles
λ	Wavelength

Chapter 1 Introduction, Objectives and Thesis outline:

1.1. Introduction

Advances in biomedical and material sciences have led to a flourish in developing and exploring the use of selective Drug Delivery Systems (DDSs) that offer unprecedented control of the administered drug release rate over a desired period of time, protection of the delivered therapeutic agent against degradation and safety from accidental release, therefore reducing the side effects and enhancing efficacy compared to conventional dosage forms. Global revenue for DDSs is estimated to be £139.6 billion in 2013 and is expected to grow at a compound annual growth rate (CAGR) of around 3.2 % to reach £163.32 billion by 2018 (Barichello et al., 1999, Dewan, 2014).

These DDSs are manufactured in the form of emulsions, liposomes microspheres and gels. They are self-sustainable systems that work as drug reservoirs or carriers that can be optimised depending on the application requirements and release the bioactive molecules when triggered by specific stimuli, offering spatial and temporal control over the release process. This reactive function to an endogenous or exogenous stimulus has earned them a place among the “smart” materials. Examples include; Doxil, ThermoDox and Nanotherm which have entered their clinical phases (Hatefi and Amsden, 2002, Alvarez-Lorenzo and Concheiro, 2014).

Gels have been a prominent research topic for on-demand delivery systems in the past few decades, about 3000 papers on gel DDSs have been published in PubMed database in the past 5 years. Gels can be incorporated in different formulations using a wide variety of substrates, that can be tailored to be minimally invasive and biocompatible polymers that are manufactured based on the targeted tissue and therapeutic agent properties.

Smart gel systems have tunable porosity allowing controlled loading and release from the gel network; they work as depots that are injected into the body as solutions before they undergo a first order transition producing flexible soft hydrogel matrices in situ at the physiological temperature. They have good

adhesion and low interfacial tension resembling living cell extracellular matrices (ECMs) and body tissues, which reduces the possibility of auto immune responses.

From an economic perspective, these DDSs are easy to handle with minimum training. They can be designed to adjust the release, degradation and clearance rates, which will reduce dosing frequency, hence improving patients compliance and potentially reducing health care expenses (Bhattarai et al., 2010, Ebara et al., 2014).

1.2. Aim:

The scope of this dissertation is to provide a comprehensive study of a smart injectable polymeric delivery system. By evaluating the gelation, microscopic and macroscopic structural changes of a readily available polymer (Pluronic F127) as a model base formulation.

Pluronic F127 polymeric solutions can undergo a phase change at the biological temperature (37°C) when used in relatively low concentrations. The transition can be tuned using different excipients or other Pluronics, allowing property adjustment without disturbing the system dynamics.

A simple injectable formulation containing a thermosensitive polymer (F127) and a model drug would be loaded into a syringe in solution state. Upon injection, the temperature change transforms the polymeric solution into a gel. The gel matrix

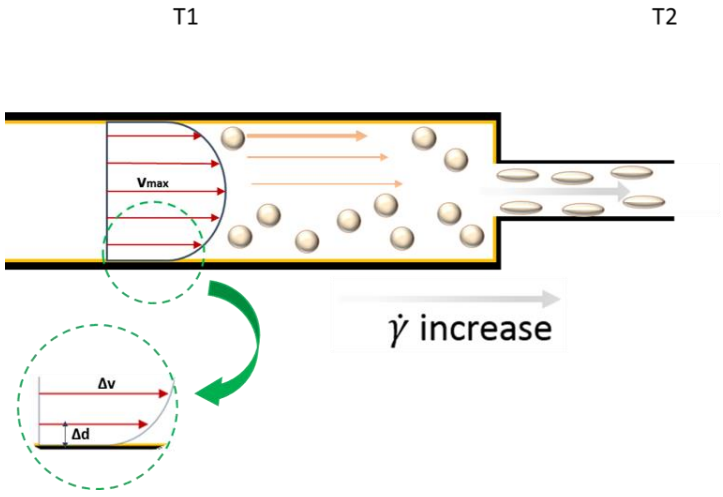

Figure 1-1 Schematic of the syringe during the injection process.

works as a depot entrapping the drug and releases it slowly over a desired time. Figure (1-1) offers an overview of the injection process.

The injectable system behaviour is governed by the coupled fluid dynamics and thermal processes and understanding these inseparable rheological and thermal interactions is critical for the development of a successful product.

These systems are relatively well characterised in the literature due to their widespread usage across many fields (e.g. cosmetics, pharmaceuticals, cell culture and biological additive manufacturing). However less attention has been paid to the intricate strongly coupled influences arising during application and their implications on performance. Further complications manifest when compositional alterations are made to the gel systems, whether by changing the polymer, additives and drug types or their concentrations.

1.3. Thesis outline:

Following this brief introduction, Chapter 2 will be dedicated to the literature review: discussing the different gel types, ongoing research on these materials and applications for DDSs. These are followed by sections on the key aspects of micellisation / gelation thermodynamics. Then finally connect the macro- and micro-properties through the correlation of gels rheological behaviour to their internal structure.

Chapter 3 looks at the materials used to prepare the formulations investigated in this study, along with overviews of the experimental techniques, instrumental setups and test variables utilised. The last section in this Chapter was designated for methodological development, which provides insights to pure materials characterisation and test optimisation processes.

Chapter 4 aims to provide in-depth investigation of the neat Pluronics structural properties that were studied during and after the completion of the transitional ordering. Compositional and the environmental changes were examined by a variety of experimental measurements under both static and dynamic conditions that were discussed earlier in Chapter 3.

Chapter 5's main focus is to study polymeric gel blends. A group of varied molecular weight homopolymers (PEG) was utilised to probe the effects of introducing a common pharmaceutical ingredient with a range of different hydrophilicities to aqueous systems of F127 to control the physical properties of the formulations. The blends thermal, rheological and structural properties were elevated and compared to the neat systems as a function of PEG's concentration and Mw.

Chapter 6 takes the research a step closer toward developing a drug delivery system. To develop a model DDS an API; Ibuprofen (IBU) was introduced to neat systems of F127 and PEG-blends with different Mw. The IBU-blends were studied and compared to the neat and PEG-blends to explore the resultant aspects of the addition on the formulation's structure. The DDS properties were evaluated in comparison to results from Chapter 5.

Chapter 7 concludes the study with a general discussion based on results from the previous Chapters and suggestions for future work.

Efforts were made to tackle the transitional aspects of these key systems from a multidisciplinary point of view, aiming to provide a true understanding of the complex behaviour of these functional materials with wide application fields including drug delivery. Efforts were made to cover a broad sample pool; including concentrations and molecular weights to provide a better insight of the compositional attributes on the product structure. Which were evaluated by diverse environmental setups and measuring systems to offer a meaningful comparisons and reduced error. The data acquired in this study will help to predict the structural trends in similar smart materials allowing their optimal exploitation in many industries.

Chapter 2 Literature review

Dosage forms is an umbrella term used to describe the physical state or the route of administration (ROA) used to deliver an active pharmaceutical ingredient (API) into the body, which depends on the API's properties and the patient. The oral route is the most popular for its convenience and least adverse effects compared to the parenteral route. However, the slow onset of action, short circulation times and the reduced bioavailability (BA) due to incomplete absorption and hepatic metabolism necessitates for multiple dosing or the use of higher doses. This limits this route and makes it unsuitable for the delivery of bio-sensitive agents.

A drug delivery system (DDS) refers to any device or formulation that enables the introduction of the therapeutic agent into a living body to generally improve its safety and efficacy. The advantages of any DDS can be discussed from three perspectives:

a) Therapeutically they help to boost the pharmacokinetics/ pharmacodynamics maintaining constant drug levels and reducing adverse effects by either controlling the site of release, optimising the duration of action or both.

b) Patient compliance by simplifying administration courses and reducing dosing frequency.

c) Economically DDS can decrease the cost of overall health care as a result of dose reduction and patient care resources (Allen and Ansel, 2013). Moreover, developing a new controlled release DDS with enhanced features is very rewarding for manufacturers and their supply chains. The US abbreviated new drug application (ANDA) allows manufacturers to apply for ANDA-exclusivity (which originated under the orphan drug act) to protect newly developed DDS containing drugs that have already been approved making it challenging for generic manufactures to reproduce even after the original drug patents expire (Ranade and Cannon, 2011).

The first generation of controlled release systems relied on regulating the release mechanisms including dissolution, diffusion and erosion. Continuous efforts have been made to produce small-scale DDS to introduce them in to the body in easily implantable/injectable formats for both intermittent and continuous delivery. Micro-fabricated devices are often implanted and examples of used implants

include; a variety of types Mechanical Micro-Devices (MEMS) including microchips (Sharma et al., 2006), Bimatoprost sustained-release implants (Lewis et al., 2017) and various commercial subdermal contraceptive implants (e.g. Implanon® and Jadelle®) (Ali et al., 2016).

The second generation aimed to control API distribution through activation modulation. The formulation can contain stimuli responsive excipients that protect the API until the desired site of release is reached (Yoshida et al., 2013).The third generation, often regarded as carriers, have the stimuli responsive properties of the second generation with integrated feedback functionality, making them more suitable for physiological uses. Stimuli responsive or smart DDS are often used interchangeably in most cases referring to formulations containing materials of varied complexity that experience conformational transitions (e.g. solubility, aggregation, shape, etc.) corresponding to a specific signal: either internal (pH change, temperature change or hormone levels) or external (ultrasound, light or radiation) to regulate the drug release. Prepared as liposomes, micelles or antibodies to occupy nano- and microscales, these DDSs offer ease of parenteral administration (local or systematic) as solutions, emulsions or nanogels with targeted specific release profiles. Nonetheless, the use of the term “smart” has sparked a lot of debates and some references strictly use it when the changes are reversible and proportional to the strength of the signal (LaVan et al., 2003).

2.1. Gels in drug delivery:

Gel based dosage forms are most commonly known for topical applications, however gelling agents have been introduced to drug delivery systems in various formats to enhance manufacturing, properties and control drug release (Troy et al., 2006). Hydrogels can be incorporated in drug eluting DDSs, either by incorporating the gel into the bulk of the device or by coating it with gelling agent. For the first type, the gel is the main carrier matrix releasing a templated API to target tissues as in injectable gels and soft contact lenses prepared by molecularly imprinted hydrogels (MIPS). Alternatively, the device surface is coated by layers of gelling agent or grafted to inhibit biofilm formation (Alvarez-Lorenzo and Concheiro, 2014). Other examples include integrating hydrogels into tablets of compressed dispersions containing API and gelling agents have been

used as release modifiers in monolithic matrix tablets (Colombo et al., 2000). Where they have been introduced to oral DDSs to protect the API, hinder its dissolution, moderate release from the tablet and therefore and improving BA. Examples include matrix based tablets, where the drug is dispersed in a hydrophilic matrices as in polyamide rate-modulated DDS (Hauptmeier and Becker, 2007) and cross-linked monoolefinic matrices (Mueller and Heiber, 1985).

2.2. Injectable gels for DDS:

Injectable hydrogels are gels that can be formed in situ after being injected into the body and activated to deliver a huge variety of active biomolecules that include: drugs, growth factors, chemokines and therapeutic cells to aid with different tissue regeneration e.g. bone and cardiac tissues.

The precursor 'solution' can be introduced in a minimally invasive manner directly to the area of interest allowing it to reach even hard-to-access areas, where it gels forming a depot before releasing the cargo over a designed period of time. The choice of the gelling agents and dependently the underlying performance is determined by: the material crosslinking, biodegradability and the biochemical stability. These factors inevitably reflect on the multitude of physical, structural and mechanical behaviours of the gel matrix during and after injection.

The gel design should focus on the salient features desired for the application. Key considerations when designing/formulating an injectable gel usually correlate to the properties discussed above. The therapeutic agents' transport is essentially a property of the hydrogel's internal structure and the encapsulated active agent. The two structures' affinity governs the release from the gel matrix, accomplished by mechanisms such as swelling, diffusion or erosion or a combination of these. The degradation of the gel structure depends on the material utilised but usually occurs either by surface or bulk erosion. The former occurs when the water uptake or enzyme transport is slower than the polymer chain scission while the majority of biodegradable hydrogels are reported to degrade by the latter mechanism due to high water content and permeability (Bae

et al., 2013). Ideally the hydrogel degradation can be controlled by modifying the gelling polymer backbone.

The mechanical behaviour reflects the hydrogel's structure-property relationship and conveys the structural transitions the hydrogel DDS undergoes during administration by passing through different environments (temperature and shear), which can affect its stability, the loaded material deposition and release (Aguado et al., 2012, Amer et al., 2017).

Physiochemical compatibility relate to both the tissue adhesiveness and bioactivity. Which as the rest of the features can be controlled by adding linker molecules that mediate binding to tissues and stabilise the DDS in the site of action without attenuating pharmacokinetics (Seliktar, 2012).

2.3. Gels - an overview:

Gels are a collection of soft matter classes that include disparate varieties of complex polymeric materials with one common feature among them regardless of their origin; the ability to imbibe large amounts of water or biological fluids without being dissolved after they undergo a phase transition from the disordered sol state to an intermediately ordered gel state. A gel has the soft mechanical properties of a solid yet lacks the solid's atomic order (quasi-solid). The gel is formed by the association of colloid particles by the increase of inter-particulate interactions connecting the sub-units together, leading to the formation of a three-dimensional network which acts as a self-sustainable container immobilising the solvent within the network by the forces of surface tension (Araki et al., 1998, Lee, 2008).

Generally, gels can be classified based on the solvent entrapped within the network, the building block types or forces bringing them together. When the continuous phase is an organic solvent the gel is referred to as organogel while hydrogels are the product of hydrogelator bonding in aqueous solutions (Murdan et al., 2005, Vintiloiu and Leroux, 2008). While the cross-linking mechanisms in both types are quite similar, in this study we will be referring only to hydrogels. In this study we will focus on hydrogels that are formed by two different linking mechanisms; chemical and physical hydrogels - with an emphasis on the latter type for drug delivery applications. Figure (2-1) show different gel types classified according to their cellular interaction.

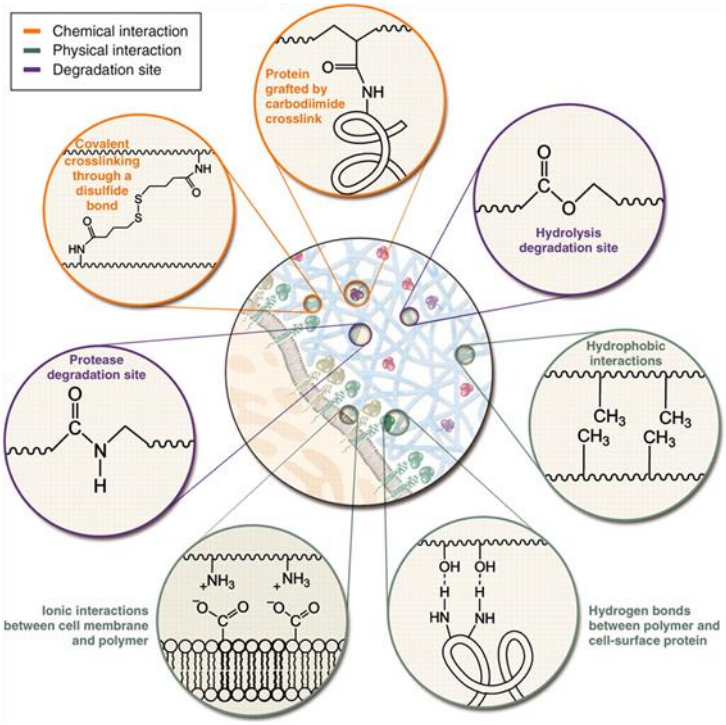

Figure 2-1 different gel types based in their interactions with cellular interface (Seliktar, 2012).

2.4. Chemical hydrogels:

Chemically cross-linked gels display covalent bonding connecting the polymer chains by adding a cross-linker to activate the polymer or conjugating the chains directly; the linker can be a group or a small molecule. Chemical cross-linking complexity ranges from adding simple compounds such as genipin and dextran–tyramine conjugates – both sourced from natural resources (Chen et al., 2004, Jin et al., 2007), different types of radical polymerisations (Durand and Hourdet, 1999, Sun et al., 2008, Bearat et al., 2012, Škvarla et al., 2014, Alexander et al.,

2014), ring opening reactions (Jeong et al., 1999a, Fujimoto et al., 2009, Lin et al., 2012, Ayano et al., 2012, Soledad Lencina et al., 2014). And the widely preferred click reactions Michael addition and Schiff base formation due to their efficiency to form gels in situ at physiological conditions (Yu et al., 2011) (Martínez-Sanz et al., 2011) (Peng et al., 2013), (Patenaude et al., 2014).

The main property of these gels is their irreversibility, once the adjacent units are linked they cannot go back to the original state - as in thermosetting materials, a preferable function for some applications. The hydrogel characteristics can be controlled by adjusting the cross-linking agent concentration or via adding stimuli sensitive physically gelling agents to the matrix such as methacrylic acid (pH-sensitive) or N-isopropylacrylamide (temperature-sensitive) (Hennink and van Nostrum, 2002). A schmatic of in situ cross-linked gels is displayed in Figure (2-2).

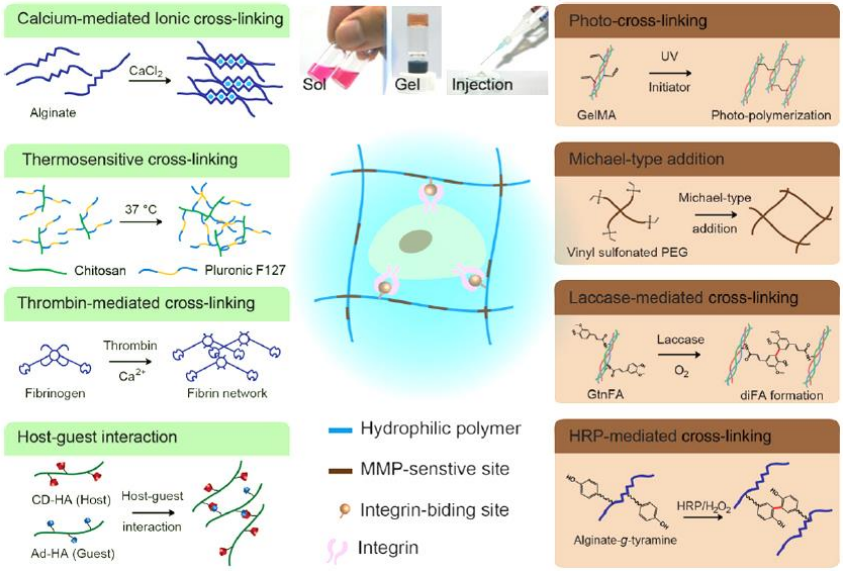

Figure 2-2 Schematic representation of the fabrication of in situ cross-linkable hydrogels(Park and Park, 2017)

2.5. Physical gels

The gel structure in this type is acquired by joining the units by physical bonds either by controlling the intramolecular forces balance within the polymer chains or the environment to form a network without any addition of initiators.

For a physical hydrogel formation, the polymer-polymer interactions must be strong enough to form semi-permanent junctions. The network should be able to absorb and retain water inside the polymer network.

“Smart” hydrogels spontaneously form a network as a response to specific stimuli, these hydrogels are classified according to their particular triggers e.g. pH, UV photopolymerization, stereocomplexation, charge interaction, ultrasound, electromagnetic radiation and temperature (Peppas et al., 2000), (Peppas et al., 2000, Ruel-Gariépy and Leroux, 2004, Hoare and Kohane, 2008, Domb, 2011, Matanović et al., 2014, Priya James et al., 2014).

2.6. Thermosensitive hydrogels:

The self-assembly in these stimuli responsive polymeric hydrogels is thermodynamically driven, using materials that exhibit a phase separation due to change in the system’s solubility upon increasing the temperature to reach a lower critical solution temperature (LCST). Below this LCST the polymeric chains are completely in the soluble state, taking a random coil conformation. As the temperature increases, dehydration takes place due to hydrophobic interactions leading to aggregation. For polymers with a LCST an increase in temperature results in negative free energy (ΔG) of the system, leading to increased entropy (ΔS) (Ward and Georgiou, 2011). Polymers with upper critical solution temperature (UCST) are less favoured since they require high temperatures which can be unsuitable and even destructive for drugs and biomaterials (Priya James et al., 2014).

Based on the system temperature response, thermosensitive hydrogels can be subdivided into negatively and positively thermosensitive. Negatively thermosensitive hydrogels contract upon heating above their LCST while the positively thermosensitive hydrogels exhibit contraction above UCST. For drug release applications, negatively thermosensitive systems are more relevant. Where they control the active ingredient’s release through pulsation mechanism, with “on” at low temperature and “off” at high temperature (Hoffman, 1995). Examples of negatively thermosensitive systems include: P(NIPAAm) co-polymers and Interpenetrating Polymer Networks (IPNs). Sometimes these

systems are referred to as ‘squeezing hydrogels’ due to their swelling-shrinking behaviour. Successful on–off release profiles have been utlised in delivering Bovine Serum Albumin (BSA) (Dinarvand and D'Emanuele, 1995), Indomethacin and Ketoprofen (Mukae et al., 1990, Katono et al., 1991).

Positively thermosensitive hydrogels work by the same pulsatile squeeze effect but with an opposite temperature response, these gels trap the drug at low temperatures and release it at high temperatures. Examples include formulations of microcapsules with a membrane of nano-sized P(NIPAAm) and IPNs of poly N-isopropylacrylamide (PNIPAAm) as well as tailored nano-porous silica (Ichikawa and Fukumori, 2000, Shin et al., 2001). Even though the thermoreversiblity in these hydrogels can only be accomplished by physical cross-linking, chemical bonding can take place in the early stages of polymerisation, which can improve the hydrogels longevity inside the body and improve their mechanical properties (Qiu and Park, 2012).

2.7. Gelling agents for thermosensitive hydrogels:

In this section, thermally responsive hydrogels will be discussed in terms of their gelling agent’s origin, classified into two main categories natural and synthetic gelators. Providing examples for both types, their gelation limits (concentration, temperature) and recent applications in the field.

2.7.1. Natural and modified natural polymers

2.7.1.1. Polysaccharide and cellulose derivatives:

Compared to the majority of natural polymers that form gels at low temperatures, poorly soluble cellulose shows a reverse thermo-gelation property at elevated temperatures, which can be explained by its water interaction at high temperatures. Introducing hydrophobic groups to cellulose can increase the solubility and the temperature response by controlling the Degree of Substitution (DS) of the cellulose hydroxyl- group.

a) Methyl cellulose (MC):

Methyl cellulose is the simplest cellulose derivative and has been used for decades (Heymann, 1935) – see Figure (2-3). At low concentrations (1–10 wt. %) MC solutions are known to be liquid at low temperature but able to gel when heated. Some groups have reported gelation temperatures of 40-50°C (Kobayashi et al., 1999, Li et al., 2001, Mayol et al., 2014) while others 60-80°C (Liu et al., 2004, Bain et al., 2012). The degree of substitution has a great effect on MC's LCST which may explain the wide range recorded. MC gelation can be modified to occur at the physiological temperature using mono and divalent salts or by blending it with other synthetic or natural polymers such as; poly (acrylic acid), carboxymethyl cellulose (CMC), polyethylene glycol (PEG), hyaluronic acid (HA) and chitosan. MC has been used to control the release of BSA from low molecular weight HA hydrogel blends (Mayol et al., 2014) and low viscosity MC formulations were tested as an injectable scaffold for traumatic brain injury, the formulation was reported to gel in situ without any toxicity issues (Tate et al., 2001).

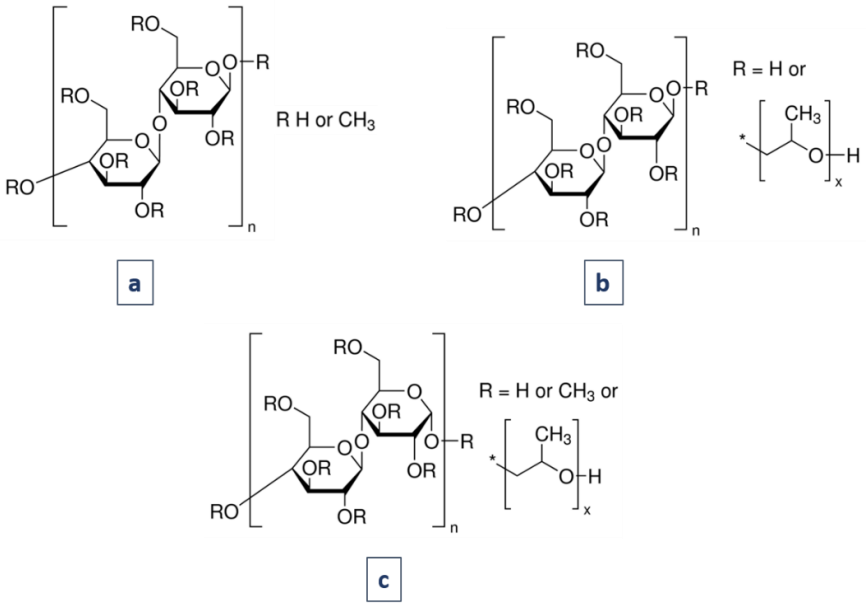

Figure 2-3 Structure of (a) MC, (b) HPC and (c) HPMC (Sigma-Aldrich, 2018).

b) Hydroxypropyl cellulose (HPC):

HPC is a water–soluble cellulose derivative, prepared by reacting alkali cellulose which with propylene oxide at elevated temperature and pressure to substitute the hydroxyl group on the anhydroglucose units of cellulose (Furia, 1973).

HPC structure is shown in Figure (2-3). The concentrated solutions (40 – 90 %) form an iridescent cholesteric liquid crystalline phase due to the ordering or worm-like micelles when heated to approximately 40°C, HPC phase diagram is displayed in Figure (2-4) (Werbowyj and Gray, 1980). Similar to MC, the gelation temperature depends on the degree of molar substitution of propylene oxide and the polymer molecular mass. Wach et al. reported the reduction of the critical gelation concentration to moderate values (20 - 40%) through irradiating the solutions with gamma rays (Wach et al., 2002). HPC-L with residual lignin exhibited gelation at body temperature, where the drug release is regulated by differences in osmotic pressure rather than gel swelling-shrinkage as for the original HPC (Uraki et al., 2004, Uraki et al., 2006).

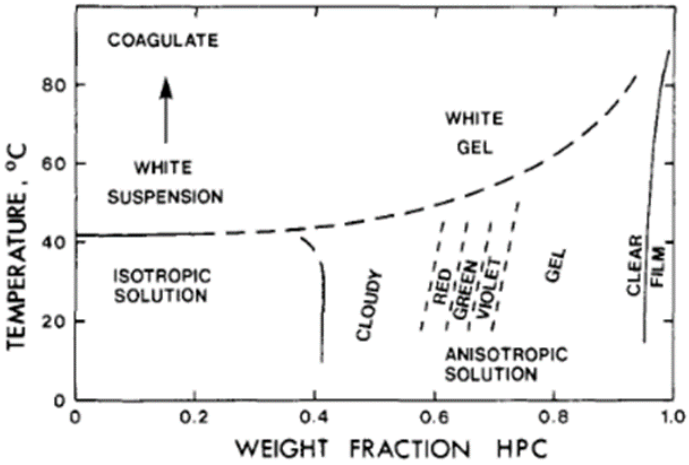

Figure 2-4 Phase diagram of HPC-water system (Werbowyj and Gray, 1980).

c) Hydroxypropyl methylcellulose (HPMC):

HPMC is widely used in oral controlled release drugs with some applications in creating tissue scaffolds – see Figure (2-3). The thermal phase transition occurs between 75 and 90°C but can be lowered to 40°C by reducing the hydroxypropyl molar substitution (Ruel-Gariépy and Leroux, 2004). Analogous to the other cellulose derivatives, HPMC solution gelation is driven by hydrophobic interactions that result in methoxy- substitution (Joshi, 2011). It is mainly integrated in injectable delivery systems as a micro/nanoparticle carrier. Asius et al. used HPMC 1 wt. % as an subcutaneous gel carrier of microspheres (Asius et

al., 2004), formulations of two polymer-nanoparticle (PNP) containing HPMC hydrogels that gels at 25°C successfully delivered BSA with no signs side-effects (Appel et al., 2015). Sustained release of two growth factors (TGF-β1 and GDF-5) was maintained up to 28 days utilising biphasic systems of pullulan microbeads (PMBs) added to silanized HPMC (Henry et al., 2017).

d) Xyloglucan:

Xyloglucan is a plant polysaccharide existing in seeds that works as a crosslinking agent of cellulose micro fibrils in the primary cell wall – see Figure (2-5). The most extensively researched type is extracted from the tamarind seed and has a backbone consisting of glucose residues, with side groups of xylose attached through glyosidic linkage. It exhibits thermoreversible behaviour when partially degraded by β-galactosidase to remove galactose residues. Thermosensitive gels can be obtained after accomplishing a minimum galactose removal ratio (GRR) of 35 %. Xyloglucan solutions of 1-3 wt. % exhibit both LCST and UCST (Shirakawa et al., 1998, Zhou et al., 2007, Almeida et al., 2014). Gels containing a low percentage of 3 wt. % exhibited the highest elastic modulus values ever recorded for any biological or synthetic physical hydrogel - approximately 100,000 Pa at 20 °C (Nisbet et al., 2006, Brun-Graeppi et al., 2010).

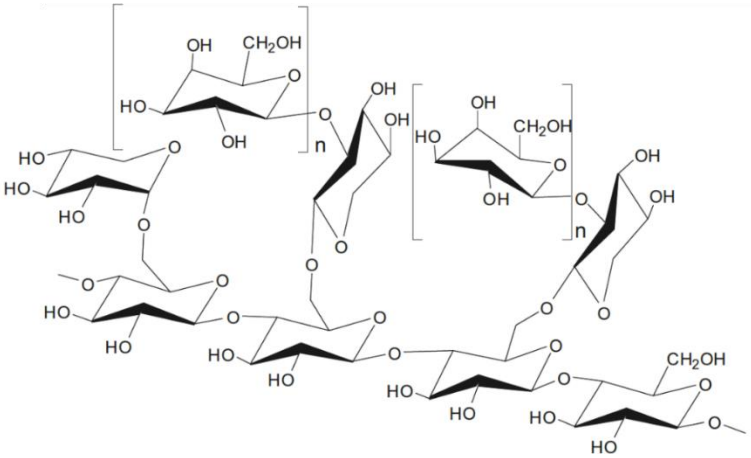

Figure 2-5 the structure of the repeating units of xyloglucan (Brun-Graeppi et al., 2010).

e) Alginate (ALG):

Alginates are polyanionic polysaccharides derived from brown sea algae, composed of 1-4-linked β-D-mannuronic acid (M-blocks) and α-L-guluronic acid (G-blocks) – see Figure (2-6) (Padoł, 2016). They are widely used in food,

pharmaceutical and medical regeneration fields (Lee and Mooney, 2012, Aguado et al., 2012). Alginates have the ability to form hydrogels easily in the presence of multivalent ions (e.g. Ca^{+2}) creating ionic cross-linking which results in gelation of alginate aqueous solutions (Rowley et al., 1999). Alginate hydrogels alone exhibit no thermal sensitivity and have poor mechanical strength, but can be added to other polymeric hydrogels to aid their biocompatibility, biodegradability and immunogenicity. Physical or chemical modification as in ALG-g-PNIPAAm co-polymerisation (Tan et al., 2012), ALG-g-P(NIPAM-co-NtBAM) N-isopropylacrylamide (NIPAM) and N-tert-butylacrylamide (Matanović et al., 2014), formulations containing poly(ethylene glycol)-co-poly(ε-caprolactone) (PEG-co-PCL) are prepared in situ, obtaining injectable thermosensitive reversible hydrogels (Lee and Mooney, 2012). Alginate containing hydrogels have been reported to locally sustain the delivery of vascular endothelial growth factor (VEGF) for 15 days compared to 72 hours after a bolus injection of ischaemic mouse (Lee and Mooney, 2012) and 10 hours in the case of ophthalmic drug delivery of pilocarpine (Park and Park, 2017). A myriad of responsive interpenetrating polymer networks (IPN) and alginate composite gels have been formulated to provide controlled drug delivery (Dragan, 2014).

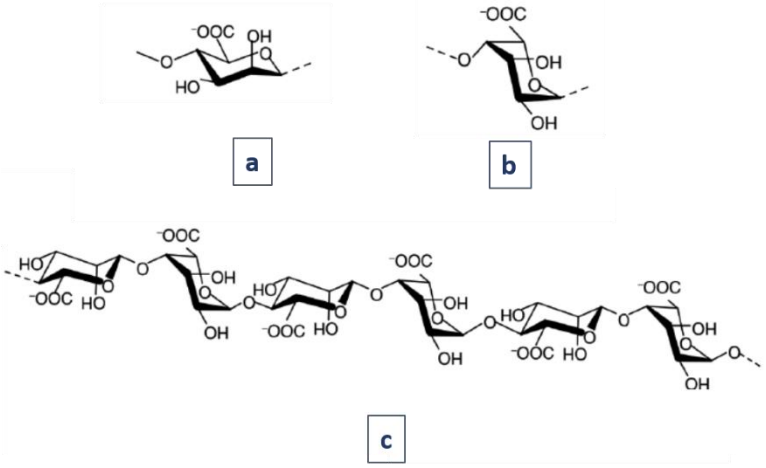

Figure 2-6 structure of alginate. (a) β-D-mannuronic acid (M), (b) α-L-mannuronic acid and (c) MG-block (Padol, 2016)

f) Chitosan:

Chitosan is a linear amino-polysaccharide composed of β-(1, 4)-linked D-glucosamine and N-acetyl-D-glucosamine obtained by alkaline deacetylation of chitin - a predominate component of crustacean and insect shells. Chitosan

structure is shown in Figure (2-7). Known for its biocompatibility, biodegradability and low immunogenicity, chitosan is a hydrophilic, pH-dependent polymer that forms thermo-sensitive hydrogels when neutralised due to reduced electro-static repulsion and the domination of hydrophobic forces. Hydrogels can be obtained using small concentrations up to 2 wt. % of chitosan (Ruel-Gariépy and Leroux, 2004, Liu et al., 2004, Matanović et al., 2014, Ruel-Gariépy et al., 2004). Chitosan hydrogels have been obtained by the addition of polyol salts such as dibase β-glycerophosphate (GP) to chitosan solutions, successfully controlling the release of Paclitaxel for over a month. This formulation was later commercialised under the name BST-CarGel® (Ruel-Gariépy et al., 2000, Ruel-Gariépy et al., 2004).Similar chitosan based formulations were used in the delivery of Camptothecin (Berrada et al., 2005), Doxoubicin (Bhattarai et al., 2010) and Dipyridamole for 30 days from injection (Liu et al., 2011).

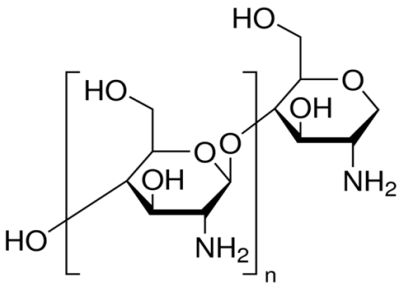

Figure 2-7 structure of chitosan (Sigma-Aldrich, 2018).

g) Cyclodextrin complexes (CDs):

Cyclodextrins are natural cyclic polysaccharides composed of 6-8 d (+)-glucose units linked by 1, 4-linkages and have 3 types α-, β- and γ-CD respectively. They have a unique hollow torus-like shape and hydrophobic cavity that gives them the ability to bind with any suitable hydrophilic polymer through non-covalent interactions to form a physically cross-linked hydrogel that exhibit a necklace-like supramolecular structure, schematic is shown in Figure (2-8) (Li et al., 2003). The inclusion complexation has also been used to form a thermo-reversible hydrogel with β-CD by physical crosslinking induced between PPO segments and β-CD. α-CD has proven to aid Pluronic F127 gelation at lower concentrations while maintaining hydrogel stability and controlling drug release for days – see Figure (2-8) (Simões et al., 2012, Simões et al., 2014). Formulations of various derivatives β-CD with Pluronic F127 have been investigated as drug carriers

(Dreiss et al., 2009, Valero et al., 2016). A hydrogel synthesised from PEG grafted dextran and α-CD showed promising results for injectable delivery systems (Huh et al., 2001).

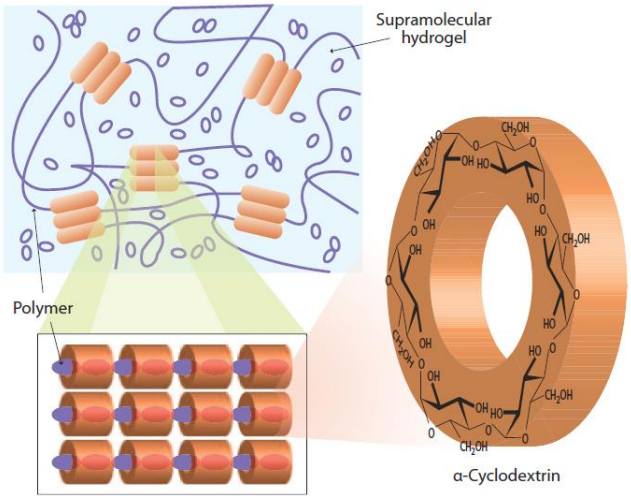

Figure 2-8 Formation of a supramolecular hydrogel of α-CD and high molecular weight PEO (Li et al., 2010)

2.7.1.2. Protein-based polymers (PBPs):

Recombinant Protein-based polymers (rPBPs) are high molecular weight repetitive units of amino acid sequences encoding different polymer arrangements prepared by recombinant DNA technology. The production process allows total control over the sequence, molecular weight and stereochemistry, which reflects the desired product physiochemical properties including; temperature response and ability to retain water – see Figure (2-9). (Jeong et al., 2002, Kabasci, 2013). Elastin-Like Polymers (ELPs) contain two blocks of alternating hydrophobic and charged amino acids exhibit a reversible thermo-gelling ability. Reportedly, ELPs release drugs by diffusion (Herrero-Vanrell et al., 2005, Massodi et al., 2009) - but proteolytic release has been recorded as well in formulations containing Glucagon-like peptides and Curcumin (Price et al., 2014). Other commonly used PBPs include β-hairpin peptides known as the MAX peptide family, which include a variety of stimuli responsive proteins (Yan et al., 2012), including thermosensitive MAX3 which has been designed to encapsulate varied macromolecules and cells (Pochan et al., 2003).

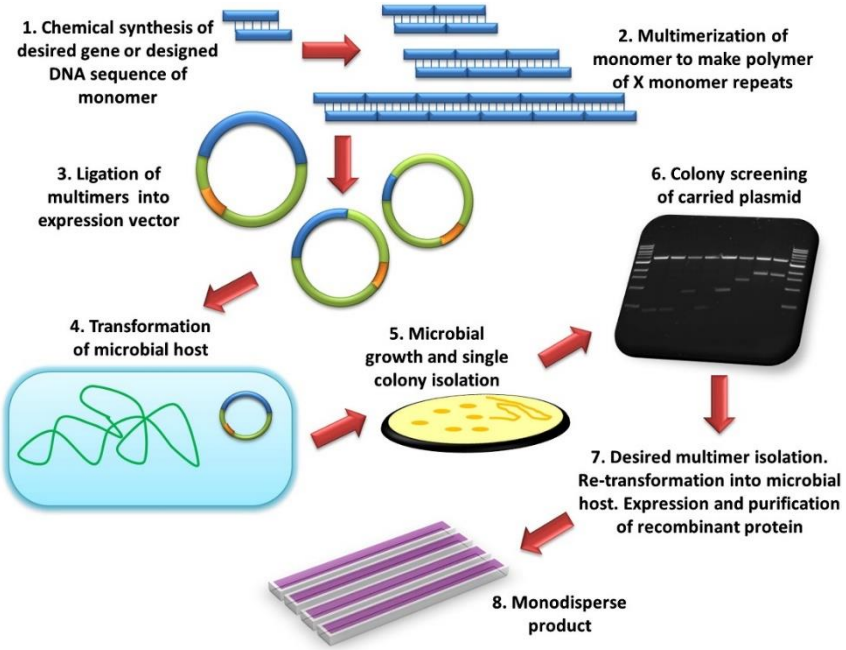

Figure 2-9 Generalized schematic of recombinant polymer synthesis (Price et al., 2014).

2.7.2. Synthetic polymers:

2.7.2.1. Poly N-Isopropylacrylamide (NIPAAm or NIPAm):

NIPAAm and its derivatives are the most extensively investigated thermosensitive reversible systems – see Figure (2-10). NIPAAm is a synthetic non-biodegradable polymer with a sharp sol-gel transition temperature at 32 °C that is not affected by polymer concentration but strongly dependent upon additives, which allows the LCST to be easily increased by incorporation of hydrophobic copolymers or salts making it promising for biomedical applications (Klouda and Mikos, 2008). Positive results were acquired after introducing biocompatible and biodegradable linkers into its backbone. Matrices prepared with PLA-PEG-PLA blocks showed promising results for controlled short term release of Ofloxacin mediated by diffusion at 37°C (Chen et al., 2012). A formulation of grafted poly (N-Isopropylacrylamide) with chitosan had an LCST of 38°C, the curcumin loaded hydrogels were effective against prostate cancer cell line (PC-3) (Sanoj Rejinold et al., 2011). Microgels consisting of PNIPAAm and poly(ethylene glycol) diacrylate (PEG-DA) were investigated for improved porosity and thermal sensitivity (Zhang and Chu, 2005). A novel chemically cross-

linked hydrogel was synthesised using dextrin and pNIPAm in the presence of N,N′-methylene bis(acrylamide) (MBA) as a linker, to form (c-Dxt/PNIPAm), the new matrix was tested in a tablet format to administer Ornidazole and Ciprofloxacin but according to the published rheological data can also be promising as an injectable system (Das et al., 2015).

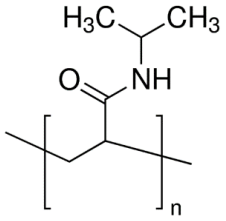

Figure 2-10 Chemical structure of N-Isopropylacrylamide (Sigma-Aldrich, 2018).

2.7.2.2. Amphiphilic block copolymers

Amphiphilic block copolymers are made of two or more covalently bonded polymers with varied hydrophilicity. The blocks' chain architecture can be engineered to take any form, from simple linear AB diblocks to complex star shaped polymers (Zeng et al., 2005, Wei et al., 2007).

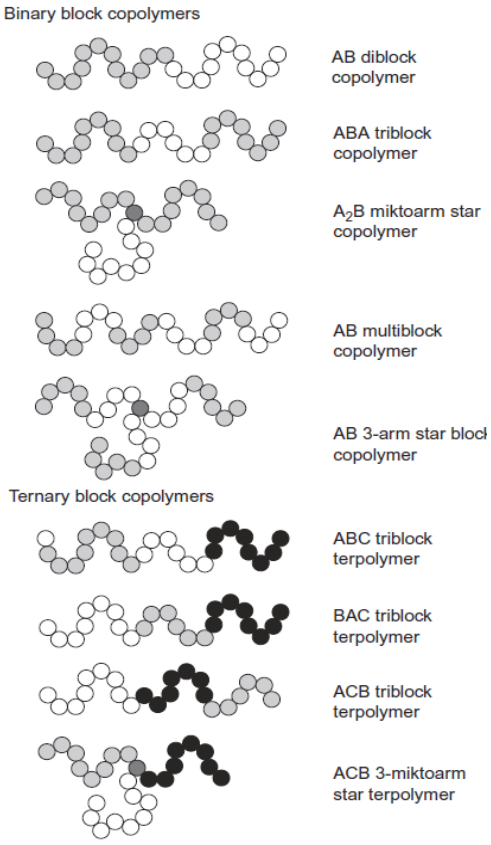

Figure 2-11 examples of block copolymer architectures (Sadeghi and Sayaf, 2014)

For a specific copolymer, the degree of polymerisation for the whole copolymer (N) and the polymerisation degree for one of the blocks (Ni) can be controlled to give practically endless block copolymer types (Larson, 1999), see Figure (2-11).

When in solution, the block copolymer chains, containing both hydrophilic and hydrophobic moieties exist in a single polymer chain state (unimers). Unimers associate into spherical micelles in a selective solvent (Ɵ-solvent) upon reaching a specific concentration (critical micelle concentration or CMC). The micelle structure depends on the building blocks. Traditionally the core of the micelles is made up of the hydrophobic block and the corona contains the more soluble hydrophilic blocks, however reversed micelles with a reverse structure can be formed. Under specific conditions, an increase in concentration (critical gel concentration CGT) micelles ordering lead to the formation of a gel lattice (Hamley, 1998). Figure (2-12) shows a simplistic schematic of amphiphiles micellisation and gelation – that which does not take into consideration the interactions occurring during these process.

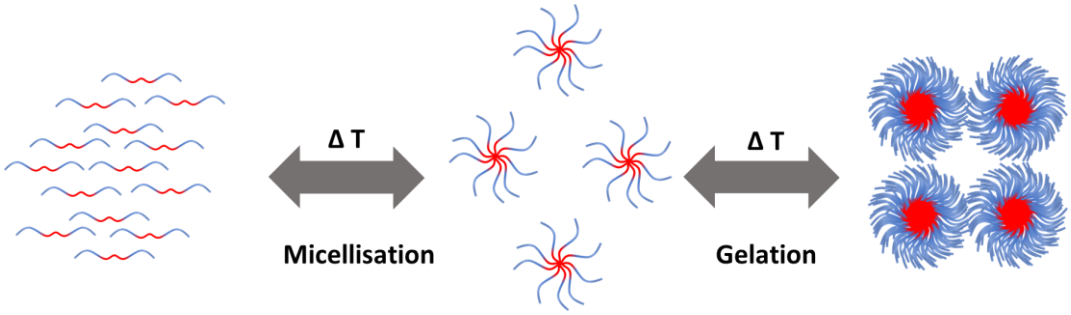

Figure 2-12 Schematic showing amphiphiles during the micellisation and gelation.

Most of the amphiphilic copolymers used in drug delivery systems are PEO-based copolymers (PEO-b-polyesters or PEO-b-poly(L-amino acid)s and they have been used as emulsifiers, dispersants and anti-hemolytic agents before more recent applications as hydrogel matrices, owing to their low cost and toxicity, enhanced thermodynamic stability compared to liposomes, increase passive accumulation in tumours through good permeability and retention (Hamley, 2005). Depending on the therapeutic agent moiety size and solubility, the courier micelles can either entrap the agent inside the core or attach it to the corona.

a) PEG/PLGA or PLLA blocks:

Poly (ethylene glycol-b- L-lactic acid-co-glycolide b-ethylene glycol) (PEG–PLGA–PEG) and Poly (ethylene glycol-b-L-lactic acid-b-ethylene glycol) (PEG–PLLA–PEG) blocks exhibit a reversible phase change. PEG–PLGA–PEG sol-to-gel transition is believed to be through micellar growth with an increase in aggregation number N_{agg} (N_{agg} is the number of polymer molecules within one micelle) driven by hydrophobic forces. The transition temperature is controlled by changing the Molecular weight (Mw) of the block, especially the middle hydrophobic block. The system has proven to be a good controlled release reservoir for Ketoprofen and Spironolactone for two months. Figure (2-13) shows the phase diagram and Spironolactone release profile from PEG–PLGA–PEG gel matrix (Jeong et al., 1999b, Jeong et al., 2012). PLGA-PEG-PLGA blocks are commercially available by the name ReGel®, where the PEG has an Mw of 1000 g/mol and the DL-lactide/glycolide molar ratio is 3. The triblock was reported to encapsulate both drugs and proteins for periods ranging from 1 to 6 weeks (Qiao et al., 2005).

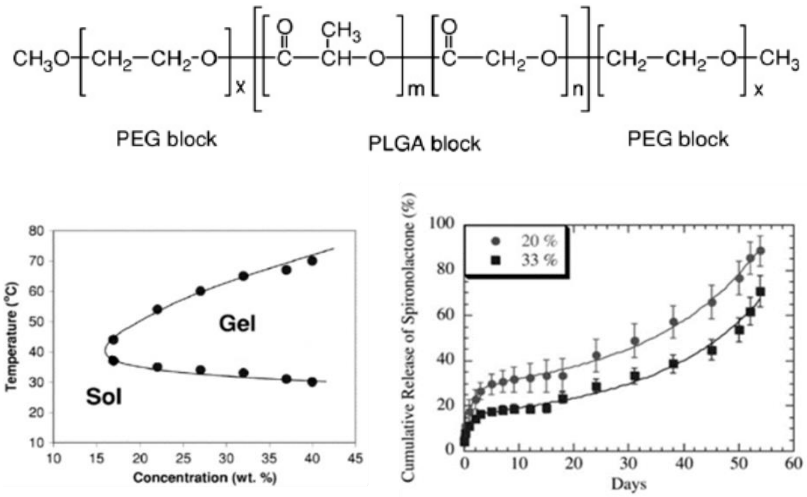

Figure 2-13 (Top) Chemical structure of a PEG–PLGA–PEG triblock copolymer. (Bottom-left) phase diagram of PEG–PLGA–PEG (550–2810–550) in aqueous solution indicating gelation temperatures for each concentration. (Bottom-right): Spironolactone release in PBS buffer at a load of 0.25% (Jeong et al., 2012)

b) PEG/PCL:

Poly (ethylene glycol)-poly (ε-caprolactone)-poly (ethylene glycol) or PEG-PCL-PEG a biodegradable biocompatible polymer - see Figure (2-14). The

micellisation is driven by the hydrophobic interactions of PCL blocks to reduce exposure to water when solubility is reduced. Similar to the previously discussed copolymers, the gelation transition shows dependence on molecular weight and concentration (Hwang et al., 2005). PEG-PCL-PEG hydrogels have been studied after loading of hydrophilic (vitamin B12 and BSA) and hydrophobic (Honokiol) drugs, the triblock performance and gelation being dependent on the block's chain length and the copolymer concentration in the formulation. The effect of the structural topology was investigated by the same group, where the inner and outer blocks were inverted to formulate PCL-PEG-PCL. The two copolymers gelled at the same concentration, although this inverted triblock had a lower gelation temperature than PEG-PCL-PEG (Gong et al., 2009). Gou et al. encapsulated Honokiol into PCL-PEG-PCL nanoparticles which were added into a Pluronic F127 matrix at concentration of 20 wt.% that controlled drug release for more than six days after injection (Gou et al., 2008).

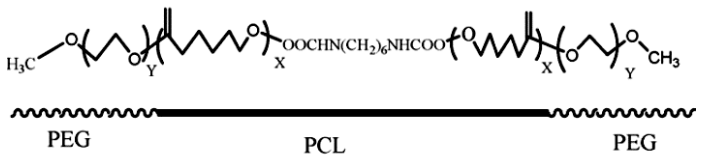

Figure 2-14 The chemical structure of a PEG-PCL-PEG triblock (Gong et al., 2009).

c) PEO/PPO:

Poly (ethylene oxide)-poly(propylene oxide)-poly(ethylene oxide) (PEO-PPO-PEO) are often known by the commercial names Poloxamer® or Pluronic® surfactants and are a family of non-ionic amphiphilic triblock copolymers first synthesised in 1970's. Pluronics are composed of two units; hydrophilic ethylene oxide (EO) and hydrophobic propylene oxide (PO) as shown in Figure (2-15). The physical structure and hydrogen bonding formation ability depends on the number of repeat units of each block, where longer PEO chains result in smaller cores and larger shells.

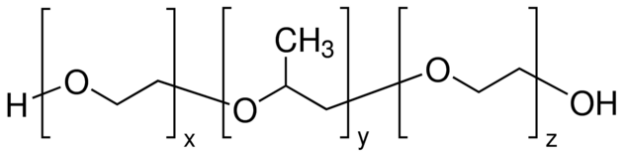

Figure 2-15 The chemical structure of a PEO-PPOL-PEO triblock copolymer. Where x=z (Sigma).

The Pluronics family contains more than 30 different registered triblocks commonly used in many industries - table (2-1) shows Pluronic block copolymer specifications from the Official Monograph NF 19 provided by the BASF corporation and European Pharmacopoeia (BASF, 2004, Europe and Commission, 2004). The different mesophases appearing in the phase diagrams depend on the PEO/PPO ratio in the triblocks (i.e. the m/n ratio) with larger ratios correlating to larger numbers of possible mesophases formed. It has been suggested that the copolymer CMT can be determined by the PPO concentration and that the gelling temperature depends on the total copolymer concentration, where micellisation is facilitated by larger PPO blocks and the overall percentage of PEO in the polymer (Wanka et al., 1994).

Table 2-1 Properties of commonly used Pluronics (BASF, 2004).

Commercial (Pluronic ® name)	124 L44NF	188 F68NF	237 F87NF	338 F108NF	407 F127NF
Physical Form	Liquid	Solid	Solid	Solid	Solid
pH, 2.5% aqueous	5.0 – 7.5	5.0 – 7.5	5.0 – 7.5	5.0 – 7.5	5.0 – 7.5
Cloud point, 10%	71–75 °C	>100 °C	>100 °C	>100 °C	>100 °C
Butylated Hydroxytoluene (BHT), ppm	_	50 – 125	50 – 125	50 – 125	50 – 125
Molecular Weight	2090 to 2360	7680 to 9510	6840 to 8830	12700 to 17400	9840 to 14600
Weight % PEO	46.7 ± 1.9	81.8 ± 1.9	72.4 ± 1.9	83.1 ± 1.7	73.2 ± 1.7
Number of EO units	10-15	75-85	60-68	137-146	95-105
Number of PO units	18-23	25-30	35-40	42-47	54-60
Heavy Metals	0.002% max.	0.002% max.	0.002% max.	0.002% max.	0.002% max.
HLB	12–18	>24	>24	>24	18–23

2.8. Aspects of self-assembly in PEO block copolymers:

2.8.1. Micellisation:

As briefly mentioned, dilute block copolymers can associate to form micelles in good solvents. The micelles have a relatively compact core and a heavily solvated corona. Micellisation can be defined as the concentration at which a sufficient number of micelles are formed as detected by a specific method at the state of equilibrium. As in surfactants, micellisation in block copolymers obeys the closed association model. Where unimers A exist in equilibrium with micelles that contain p molecules. The related equations are given by:

$$A \rightleftharpoons \left(\frac{1}{p}\right) A_p \qquad \textit{Equation 2-1}$$

Where the association constant K:

$$K = \left[A_p\right]^{1/p}[A]$$

Equation 2-2

For the micelles to form at a fractional extent α, K is given by:

$$K = [\frac{\beta}{1-\alpha}](\frac{\alpha}{p\beta})^{1/p}[A]^{(-1+\frac{1}{p})}$$

Equation 2-3

Where, β=(1- α)+ α/p, for large association numbers larger than 50 (1/p →0) with no temperature dependency give a $K \approx [A]^{-1}$ and a free energy of:

$$\Delta_{mic}G^0 = -RT \ln K \approx RT \ln[A]$$

Equation 2-4

For solutions above CMC (Attwood and Florence, 1983)

$$\Delta_{mic}G^0 \approx RT \ln[cmc]$$

Equation 2-5

This gives an enthalpy of:

$$\Delta_{mic}H^0 = R\frac{d\,ln(cmc)}{d(\frac{1}{T})}$$

Equation 2-6

A further analysis model has been suggested by Goldstein for blocks forming spherical micelles that takes in consideration the lengths of the different blocks and their effect on the core-shell micellar structure (Thompson and Love, 2017). At isothermal conditions, the micellisation is believed to be due to the dehydration of the PEO and CMT decreases with increasing polymer concentration (Alexandridis and Hatton, 1994, Wanka et al., 1994).

Micellisation enthalpy values for Pluronic copolymers are around 170-340 kJ/mol, considerably larger than their analogue poly(ethylene oxide)-poly(butylene oxide)- poly(ethylene oxide) (PEO-b-PBO-b-PEO), these endothermic values being responsible for the negative CMC dependence explained by the hydrophobic effect. By binding to water molecules the unimers enforce an entropically unfavoured more ordered structure than water's ice-like structure. This disruption is reduced upon the formation of the stable micelles, therefore they are entropically more favoured compared to the unimers. The solubility of both PPO and PEO segments decrease with temperature, leading to increased packing of PPO segments in the core, expulsion of water from the micellar core, and shrinking of the PEO.

As suggested by Elias, CMC is not a colligative property and the value obtained is expected to depend on the measurement method and batch variation, resulting in different levels of polydispersity and impurities remaining from the polymerisation reaction (Hamley, 2005). Consequently, this reflects on the final gel structure in some cases (Ricardo et al., 2012) and the obtained association parameters, which themselves are model dependent. Thus, this has led to somewhat inconclusive CMC values in the literature, as in the case of Pluronic L64. This phenomenon has been referred to as Anomalous Micellisation (Zhou and Chu, 1988).

2.8.2. Gelation

A further increase in the micellar volume fraction results in chains overlapping, leading to further association and when a certain value, the critical gelation concentration (CGC), is reached the micellar solution is ordered into a lyotropic liquid crystalline (LLC) phase, a complex liquid phase that exhibits characteristics of both an anisotropic crystalline solid and an isotropic liquid analogous to those formed by low molecular weight surfactant solutions.

Pluronics have been shown to have varied mesophasic structures, cubic phase can be formed from spherical micelles and a hexagonal phase of rod-like micelles. The micellar association to form ordered mesophases is referred to by order-disorder transition (ODT). LLCs are highly dependent on the molecular properties of the polymeric species and their interaction in the system: differences in the hydrocarbon chain's weight, temperature and the existence of additives in the system whether that is a co-solvent or co-solute. It is predicted that Pluronic mesophases are more diverse than those presented in the literature; the existence of nematic and bicontinuous phases is speculated but deeper investigations are required for their proof (Wanka et al., 1990).

The block copolymers can undergo further ordering into different mesophases with different properties than the first formed phase, following an order-order transition (OOT). These phases have been induced by controlling the gelation parameters or by the application of external stimulus – see Figure (2-16) (Wanka et al., 1994, Mortensen and Pedersen, 1993).

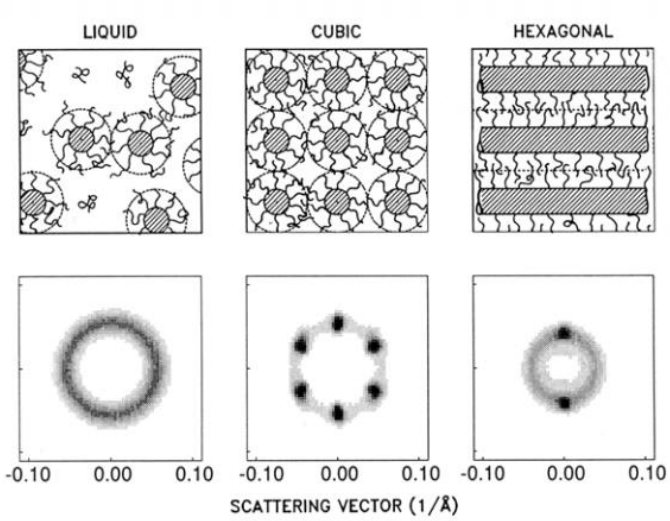

Figure 2-16 Top row: Schematic illustration of interacting micelles, spherical at low temperature. Bottom row: Two-dimensional scattering functions as obtained perpendicular to the shear plane of 25% solution $EO_{2s}PO_{40}EO_{2s}$. The three columns represent P85 at T = 25°C, T = 27°C, and T = 68°C (Mortensen and Pedersen, 1993).

Mortensen was the first to describe the liquid crystal aggregates formed in Pluronics as hard spheres that usually exist in polymeric suspensions and the packed micelle state causing the gelation as hard-sphere crystallisation (Mortensen and Talmon, 1995). In some cases the hard sphere radius (R_{HS}) is used as a structural micellar parameter at the gel state since the micellar radius (R_h) can be difficult to determine accurately due to the micelles overlapping/interacting after gelation. R_{HS} is not regarded as an absolute physical value but as an effective interaction parameter to measure the minimum intermicellar distance in the gel network (Pozzo and Walker, 2007b).

For the ordering transition to initiate, the micellar volume fraction, φ, needs to reach $\varphi_c = 0.74$ for face cubic centred (FCC) or hexagonal close packed (HCP) structures, $\varphi_c = 0.68$ for a body cubic centred (BCC) structure or $\varphi_c = 0.494$ for primitive cubic. The CGC [g/dm^{-3}] for a polymer can be predicted using:

$$cgc = \frac{10^3 \phi_c \varrho_a}{\delta}$$

Equation 2-7

Where ϱ_a is the density of the dry polymer and the expansion factor δ, is given by:

$$\delta = v_s / v_a$$

Equation 2-8

Where v_s is the hard sphere volume and v_a is the dry volume. At the hard sphere thermodynamic volume vt , δ= δt which in turn is largely determined by the solvation factor of the coronal block. This depends on the micellar structure and the solvent's selectivity. δt is less dependent on the polymer's actual composition and more on the solvent quality. This δt value can be reduced by increasing the temperature, using a poor solvent or by adding salt.

From equation (2.7), the critical gelation concentration is controlled by the opposing effects caused by reduced solubility of both PEO and PPO blocks. Elevated temperatures imbalance the equilibrium between unimers and micelles causing micellar volume fraction reduction due to contraction of the PEO blocks which is opposed by PPO blocks /water hydrophobic interactions that lead to an increase in the micellar volume fraction (Hamley, 2005).

Above CMT the volume fraction of micelles increases linearly with temperature until a plateau value φ=0.53 is reached, where micelles crystallise onto a cubic lattice. Thermodynamically, this process is similar to the micellisation. The gelation free energy and enthalpy can be acquired from:

$$K_{gel} = \frac{[B_M]_{eq}^{\frac{1}{M}}}{[B]_{eq}} \approx \frac{1}{[B]} \ (for\ large\ M)$$

Equation 2-9

$$[B]_{eq} = [A]_{eq}/p$$

Equation 2-10

$$\Delta_{gel} G^0 = -RT \ln K \approx RT \ln([A]_{eq}/p)$$

Equation 2-11

$$\Delta_{gel} H^0 = R \frac{d \ln [A]_{eq}}{d\left(\frac{1}{T}\right)} = R \frac{d \ln c_{eq}}{d\left(\frac{1}{T}\right)}$$

Equation 2-12

Where the subtext eq refers to equilibrium state (Hamley, 2005).

2.8.3. Effects of additives:

The addition of another species to a neat system will introduce new forces. The interaction of the triblock with the added materials will depend strongly on the additive's concentration and structural properties including; chain architecture, charge and molecular weight. The additives can be the loaded API or excipients (or both) to improve the formulation properties that can be co-solvents or co-solutes including: salts, homopolymers and surfactants. The addition can lead to either synergistic or antagonistic effects, retarding or enhancing attraction forces in the matrix, thus reflecting on the thermal sensitivity, rheological/mechanical properties and the formation of different mesophases through the changing entropy. This gives the advantage of controlling the system functionality through changing additives types and concentrations. However, this is still a complex field requiring further research when the excipients involved are surfactants themselves, whether the resultant micelles and therefore the LLC networks are structurally formed by mixed micelles or just a blend of the two different types (Lee, 2008).

The added materials molecular weight and chain configuration are important factors controlling its interaction with the micelles. For instance PEO homopolymer, when added in low molecular weights did not cause any changes in the gel structure or the gelation onset, while higher concentrations of low molecular weight or low concentrations of high molecular weight PEO was capable of disturbing the gel dynamics (Malmsten and Lindman, 1993). Similar molecular weight dependency was observed for systems containing poly(vinylpyrrolidone) PVP (Ricardo et al., 2012). Homopolymer impurities may naturally exist as a polymerisation by-product and, depending on their concentration or type, different mesophases can be formed leading to discrepancies in the published values, e.g. the different cubic phases reported for Pluronic F127 in the literature before and post purification (Mortensen et al., 2008). The addition of a hydrophobic low molecular weight PPO400 homopolymer to F127 systems promoted earlier micellisation by expelling the remnant water from the micellar core. The resultant gels were reported to show BCC with smaller radii than the neat FCC systems (de Lima et al., 2015).

The addition of hydrocarbons is expected to affect hydrophilic-hydrophobic balance, where attraction between the PO segments dominate over the repulsions between the PEO segments, leading to reduce micellisation boundaries, as recorded in results for oils (p-xylene and tert-butylbenzene) and several drugs (Aspirin, Erythromycin and Ibuprofen) (Malmsten and Lindman, 1993, Basak and Bandyopadhyay, 2013)

According to their effects on gelation, salt can be divided into two groups based on their interaction with water, salting-in and salting-out effect. The first group include salts such as NaCl / KCl/ $CdCl_2$/KF which promote water self-hydration through hydrogen bonding and compete with the polymer to bind with the free water molecules leading to reduced solubility of polymer and shifting the CMT to lower temperatures, leading to earlier gelation (Hamley, 2005). While the second salts such as NaSCN and KI have the opposite effect by reducing self-hydration, increasing polymer hydration and therefore delaying micellisation onset (Linse and Malmsten, 1992, Jørgensen et al., 1997)

2.9. An overview of viscosity and flow properties:

Rheology is the study of material deformation under flow. Usually the rheological properties of materials are explored and measured as a function of deformation rate or frequency. The rheological behaviour of the material can be explained by using the two-plates model - see schematic in Figure (2-17). The material is sandwiched between two parallel plates; a moving upper plate and stationary bottom one. A moving upper plate will generate a shear stress (τ = F/A) and shear rate ($\dot{\gamma}$ = v/h). The shear rate will depend on the upper plate's velocity and the dimensions of the measuring system used. The force exerted on the measuring system is parallel to the flow direction. Combining these two terms will give the shear viscosity, ɳ:

$$\eta = \tau/\dot{\gamma}$$

Equation 2-13

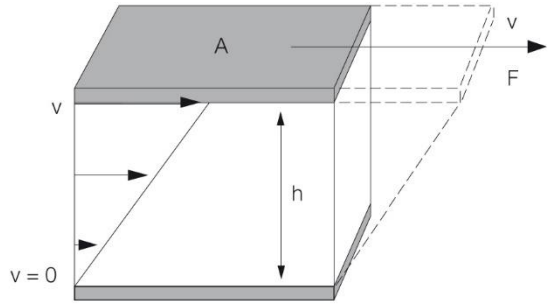

Figure 2-17 Calculation of shear stress and shear rate using the two-plates model with shear area A, gap width h, shear force F, and velocity v (Mezger, 2015).

Based on their behaviour, materials are classified into: (1) elastic (ideal solids with Hookean behaviour), (2) viscous (ideal liquids exhibiting Newtonian behaviour) and (3) viscoelastic materials possessing both liquid and solid characteristics that under applied shear rates may appear as either shear thinning or shear thickening - see Figure (2-18) (Mezger, 2011).

Newton defined the viscosity of ideally viscous liquids using eq (2-13) as the resistance to flow, which is proportional to the applied flow velocity. This behaviour is illustrated by the dashpot model – see Figure (2-19). As long as the load is applied, the dashpot fluid will move at a constant velocity, at the final position the fluid will experience the deformation to the full extent. When the movement is ceased the fluid remains permanently in the same deformed condition. Examples of Newtonian fluids include water and pure oils.

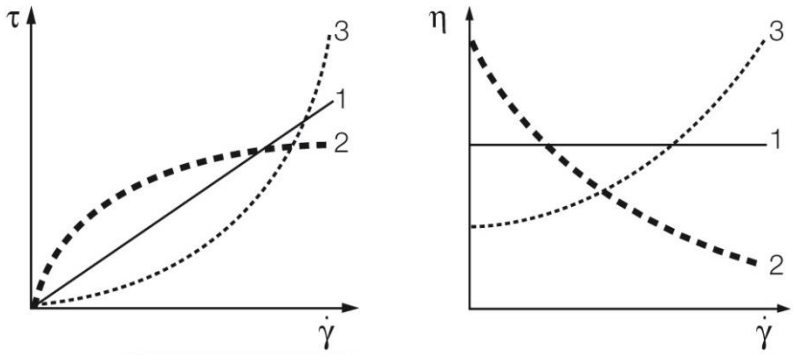

Figure 2-18 Flow curves (left) and viscosity curves (right) for (1) ideally viscous, (2) shear-thinning, and (3) shear-thickening flow behaviour (Mezger, 2011).

Ideally elastic behaviour is described by Hooke's law and can be illustrated by the behaviour of a spring – see Figure (2-19). The spring shows an immediate deflection (or the elastic material deformation) upon the application of force which is proportional to the applied force. When the load is removed, the spring reverts back instantly and completely to its original state. Ideally elastic solids are dominated by strong molecular/ atomic interactions giving them stiffness and rigidity, e.g. steel, aluminium.

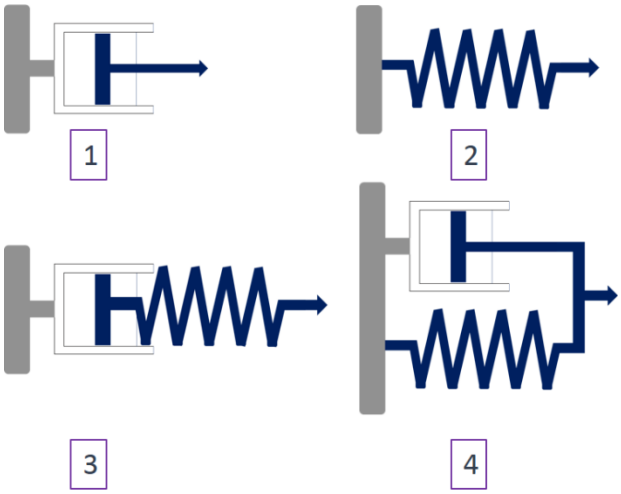

Figure 2-19 Illustrations of models describing rheological behaviours using springs and dashpots: (1) Newtonian liquids. (2) Hookean solids. (3) Maxwell's VE liquids (4) Kelvin/Voigt VE solids.

In ideally elastic solids, the ratio of shear stress to shear strain at a constant temperature applied is referred to as shear modulus, G modulus:

$$G = \tau/\gamma$$

Equation 2-14

G modulus values remain constant within the linear-elastic range and are material dependent and due to the material intermolecular structure. Shear modulus values can be converted to Young's modulus E values and vice versa from;

$$E = 2G(1 + \mu)$$

Equation 2-15

Where μ is the Poisson's ratio, the ratio between the lateral and the corresponding axial deformation. 0 ≤ μ ≤ 0.5. When μ = 0, as in the case of ductile

materials, E is given by:$E = 2G$. Whereas μ = 0.5 for incompressible and isotropic materials $E = 3G$.

Viscoelastic (VE) materials simultaneously show both viscous and elastic behaviours. The dual properties are best described using a combination of a spring and a dashpot connected together, representing the elastic and viscous components, respectively. Dependent on the physical state of the material the VE behaviour can be expressed using either the Maxwell or Kelvin/Voigt laws.

Maxwell's model for VE liquids adapts a spring and a dashpot coupled in a series. After a load cycle, the material experiences two contrasting reactions from its different parts. An immediate elastic response shown by the recoiling spring and an unchanged state of the dashpot, that remains fixed with no re-formation that represents the viscous counterpart. This is an irreversible deformation and fails to completely return to its pre-load state.

The Kelvin/Voigt model can be illustrated using a spring and dashpot paired in parallel to a rigid frame. Consequently, the two objects can only be deformed together and they are limited by each other boundaries. This results in a time-dependent deformation. After removing the load the material shows a complete but delayed reformation. This class of materials display a reversible deformation and are therefore referred to as VE solids.

Yield stress is an important characteristic of VE materials. It is defined as the lowest shear-stress value above which a material will behave like a fluid, and below which the material will act like a solid (according to EN ISO 3219-1). Yield stress depends on the test and analysis method thus it is an indication of the material performance and a vital parameter during processing and application.

2.9.1. Dynamic mechanical properties:

The viscoelastic behaviour can be examined by dynamic mechanical tests known as oscillatory tests. Oscillatory motion can be explained through the two-plates model in which the upper plate moves back and forth and the bottom plate is stationary. The application of constant speed corresponds to a constant oscillation frequency (ω) with this frequency being the reciprocal of the period in

the resultant sinusoidal strain signal and the curve's amplitude equals the maximum deflection. For VE materials the recorded signal (with time-dependent deflection/reformation as established from the spring-dashpot model) experiences a time lag, known as phase shift angle δ, or less widely known as the loss angle with values always between 0° and 90°. Values of δ = 0° and 90° hold for ideally elastic and viscous materials, whereas the value for VEs can be anything in between these two limits.

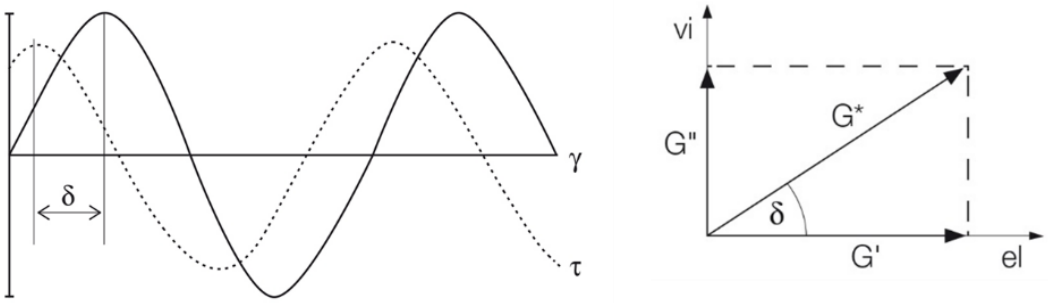

Figure 2-20 (left) VE behaviour as a sinusoidal function versus time. (right) relationship between complex shear modulus G, storage modulus G' and loss modulus G'' using the phase-shift angle δ (Mezger, 2015).*

Under oscillatory conditions Hooke's law from eq (2-17) applies in the complex form, with the sinusoidal functions of shear stress and strain to give the complex shear modulus G*:

$$G^* = \tau(t)/\gamma(t)$$

Equation 2-16

From trigonometry, adding together the concepts of phase angle, the elastic response represented by the storage modulus (G') and viscous response indicated by the loss modulus (G") gives:

$$|G^*| = \sqrt{(G')^2 + (G")^2}$$

Equation 2-17

And the ratio between the dynamic moduli G' and G" in terms of the phase shift is referred to as the loss factor or damping factor:

$$tan\ \delta = G"/G'$$

Equation 2-18

Damping factor is considered a vital parameter to determine important transitional events within the studied material where:

At sol state	$tan\ \delta > 1$, ($G" > G'$)
At gel or solid state	$tan\ \delta < 1$, ($G' > G"$)
At the sol-gel transition crossover	$tan\ \delta = 1$, ($G" = G'$)

Alternatively, the results can be presented as a complex viscosity (η*), not measured directly but analysed mathematically from the sinusoidal functions of the time dependent τ and $\dot{\gamma}$ values, η* is given by:

$$\eta_* = \tau\ (t)/\dot{\gamma}\ (t)$$

Equation 2-19

2.9.2. Nonlinear rheology:

The complex fluid's rheological properties are usually investigated by two classes of flow; either within the linear viscoelastic (LVE) or the non-linear deformation regions. The former has been discussed earlier in the text and covers most common oscillation techniques used, and is useful to understand the microstructure and the VE rheological behaviour under small strain. However, in most processing operations the LVE is exceeded thus characterising the only the linear viscoelastic properties is not sufficient for a full understanding.

In order to probe non-linear response, large amplitude oscillatory shear (LAOS) is applied to force the material out of the LVE region where microstructural anisotropy is more pronounced. A schematic showing the limits of the two ranges is displayed in Figure (2-21).

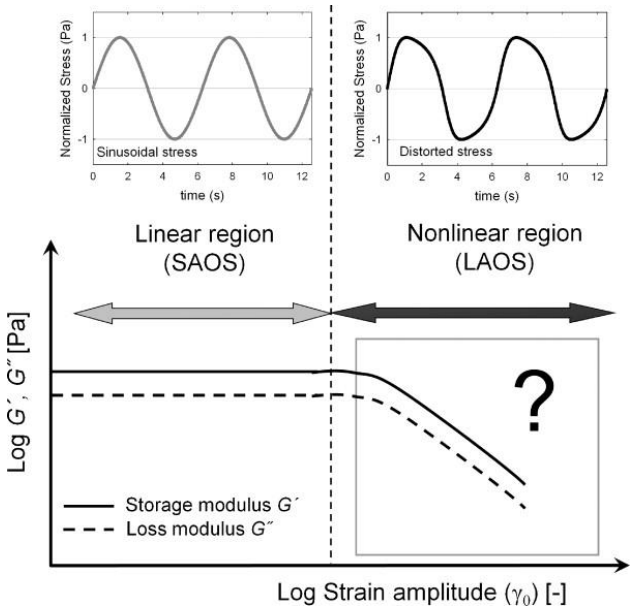

Figure 2-21 An Illustration of the strain sweep showing linear and nonlinear viscoelastic region (Hyun et al., 2011).

Recently research performed in the nonlinear regimen has been proven a powerful tool to study shear induced structures, their origin and relationship to the diverse interactions within the material. However, care must be taken in analysing data generated under large strain oscillations since stress is no longer sinusoidal due to the presence of higher harmonics. Network theory simulations predict the existence of four behavioural classes of complex fluid LAOS responses. Experimental research suggests that in addition to the primary classes, combinations of several types can be formed (Sim et al., 2003, Hyun et al., 2011).

2.9.3. Shear Heterogeneity:

A polymeric solution is considered a VE liquid if at low frequencies G” > G’ acts as an ideal liquid and at high ω forms a temporary network that exhibiting G’ > G”. However, the structure is named a VE gel if G’ > G” is maintained throughout the whole sweep. Micellar systems have been reported to exhibit a more complex rheological behaviour than normal polymeric solutions, showing both features of fluids and solid gels. The complexity arises due to micellar polydispersity and their shear induced structures (SIS). These structures, as mentioned earlier in this Chapter, can be either short or long term structures depending of the system and the environmental conditions. The system homogeneity can be changed with shear application, inducing local phase separation in the flow direction. This either

creates flowing layers with different concentration, and thus varied rheological properties or areas with varied orders of self-assembled structures. Either of these disturb the shear gradient.

Several localised shear instabilities can be present in the shear gap owing to the material properties, the measuring system flow or a combination of both. Some of these irregularities identified by Mezger are illustrated in Figure (2-22).

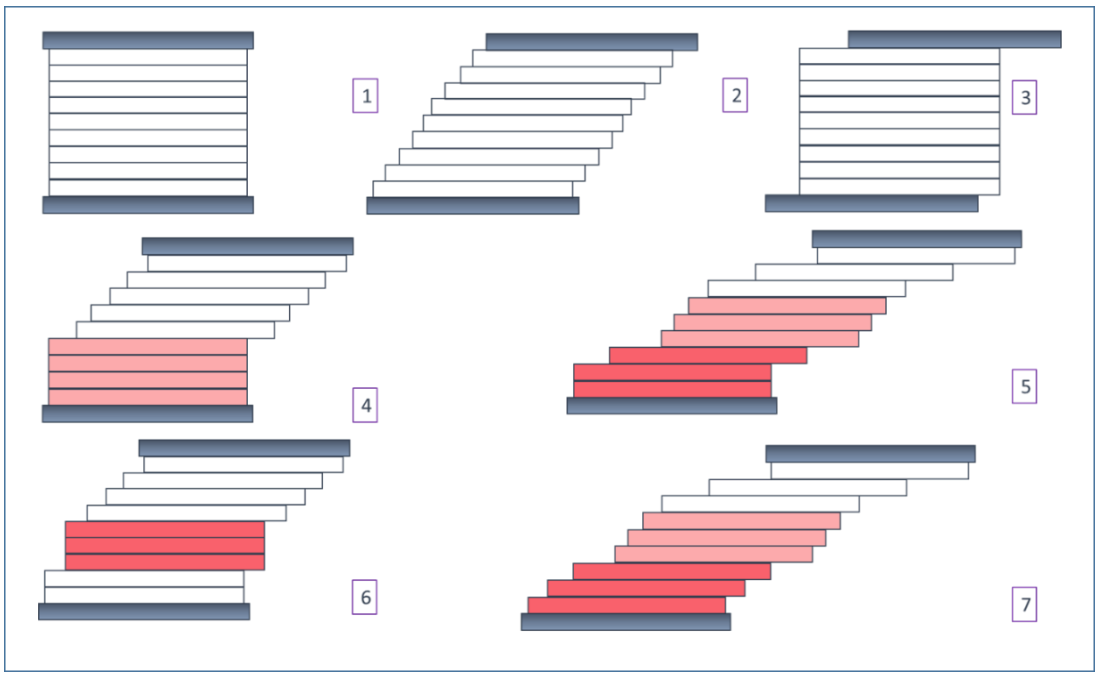

Figure 2-22 Shear flow in the gap according to the two-plates model; (1) rest state(no shear); (2) homogenous flow under steady shear; (3) wall-slip as a result of material internal cohesion and lack of wall surface adhesion; (4) plastic adhesion where only a portion of the sample undergoes homogenous flow;(5) transient behaviour with a start-up effect (time dependent); (6) shear banding with a medium band showing different viscosity; (7) shear banding with three different viscosities. Reproduced from Mezger (2011).

2.9.3.1. Wall-slip or wall depletion:

Slip can be attributed to the measuring system wall roughness/curvature and the material properties including; viscoelasticity and solid particle interactions with the wall. At low stress values a discontinuity in the shear rate is generated at the material-wall interface, with a layer experiencing higher shear rate (usually low-viscosity) than the bulk and the particles migrate toward the outer cylinder where the shear rates are less intense, creating a lubrication effect.

Common features of wall-slip can manifest as unexpected lower Newtonian plateaus, low yield stress values and low curve breakage. This slippage effect is the greatest at low shear rate and in most cases at higher shear rates, its effects become negligible (Barnes, 1995). The effect of slippage is more pronounced in high concentrations, where almost all measuring system geometries show wall-slip but is also prevalent in geometries with narrow gaps and smooth surfaces. It can be assessed using the Mooney method and reduced by using serrated geometries (Ahuja and Singh, 2009).

2.9.3.2. Shear banding:

Shear banding, referred to in soft matter as gradient banding, is a product of the formation of layers or bands with different viscosities after start-up shear en route to steady state, resulting in non-monotonic flow curves. It can be either a transient or an ultimate steady state response but can be challenging when dealing with ergodic materials (Fielding, 2016).

Banding is still controversial in complex fluids, and there is not yet a universal model to fully understand or predict it. In its most simple from, the imposed shear during banding is demonstrated by the classical Lever rule: $\dot{\gamma} = (1 - \alpha_h)\dot{\gamma}_l + \alpha_h\dot{\gamma}_h$, where α_h is the proportion of the high shear band. Deviances are often recorded, especially at the low shear rates when the shear banding is in competition with wall slip, until critical $\dot{\gamma}$ values are reached and wall slip is concomitantly reduced (Divoux et al., 2016).

So far, microscopic models based on tube theory have been able to predict banding in entangled polymeric fluids and worm-like micelles (WLM) (Cates and Fielding, 2006), but they are not widely used. Phenomenological diffusion based models as Johnson-Segalman and Giesekus are too coarse to differentiate micelles from other polymeric forms (Divoux et al., 2016). Extensive work has been done on WLM, which are used in much lower concentrations than copolymers and surfactants, raising the complexity factor when considering these models for copolymer solutions due to flow-concentration coupling (Fielding and Olmsted, 2003).

Banding can viewed as a shear induced phase transition, the shear bands are aligned to form more ordered structures or a nematic material. Although the semidilute regimen's shear induced state (SIS) does not exhibit the same magnitude of order observed at higher concentrations, the state of symmetry is still evidently present. The macrostructures can be monitored using Rheo-optical observations (LaFollette and Walker, 2011), and flow-visualisation methods that use reflecting tracers. Along with the well-established scattering techniques that can be used for to investigate both micro and macrostructural studies simultaneously (Manneville et al., 2007, Manneville, 2008).

2.10. Gels in rheology:

Rheologically a gel is a liquid suspension of colloidal particles capable of ordering into a quasi-solid state which will not flow under its own weight. Spherical molecules have positional order but no orientational order, order is being usually lost upon reversing the parameters (melting) in one step back to the formation of an isotropic liquid. Rod like molecules have both orientational and positional orders, even though the latter might only exist partially. This allows the molecules to align in a common direction while the centres of molecules might take random positions. Disordered solutions of spherical micelles are not viscoelastic unless a threshold of volume fraction is reached - similar to suspensions of hard spheres (Larson, 1999). Similarly, the cylindrical micelles need to exceed their persistence length to exhibit viscoelastic properties (Cates and Fielding, 2006).

2.10.1. The rheology of blocks:

Rheologically the term gel is used to refer to a substance with a finite yield stress without any indication of the substance's physical structure, and classically has been determined using the simple tube inversion method within a specific time scale. As mentioned earlier, polymeric triblock gels are formed due to the micellar association into cubic phases, transforming from Newtonian liquids in the micellar phase to shear thinning fluids with a crystalline mesophase (Mortensen and Talmon, 1995). The descriptive terms 'hard' and 'soft' gels have been introduced by Hvidt et al. (1994) after experiments on Pluronic P94 solutions. Kelarakis et al. quantified the hard gel yield stress in diblock polymers (τ_y = 40 Pa) by

combining rheology and the Tube Inversion Method (TIM) (Hamley, 2005). However, according to Eiser, studies on micellar cubic systems show that the yield stress is specific to FCC gels and no measured values have been recorded for BCC phases. Thus defining a gel based on the existence or absence of a yield stress alone might be sufficient (Eiser et al., 2000b).

It is widely believed that the dynamic shear moduli values after gelation are frequency independent, where the storage modulus always dominates over the loss modulus but expanding the previously experimental range has proven otherwise to reveal that that only applies on the storage modulus and while the loss modulus passes through a frequency dependent minimum ($G'' \sim \omega^2$). Some reports use the gel storage modulus as an arbitrary classification parameter to differentiate the soft and hard gels, where $G' \gtrsim 10^3$ Pa for soft gels and $G' \gtrsim 10^4$ Pa for hard gels (Habas et al., 2004).

The flow behaviour of the semidilute and concentrated block copolymer solutions that forms gels is often mapped onto copolymer melts, where the compositional (chain structure and concentration) and environmental (e.g. temperature and shear) fluctuations have pronounced effects on the rheological response. The intimate connection between gels and melts is reflected by the usage of the same terms for both systems even though the events they correspond to may not be closely related.

The rheological response is a macroscopic manifestation of the internal structural changes from micellar disorder to ordered gel state driven by temperature and/or under the applied shear field (Higgins et al., 1988) that appears as an abrupt increase in viscosity or shear moduli. This close relationship will be highlighted in the text with a focus on polymeric blocks forming cubic phases.

Thermal gelation of Pluronic L64 was observed to follow that of the gelation percolation transition, which when applied to complex fluids predicts a universal scaling for structural and rheological parameters at the transition point. The predicted scaling of $G' \approx G'' \approx \Delta\omega$ was proven using neutron scattering data. The shape of PEO-PBO diblocks phase diagrams led to the suggestion that a similar

process led to the gelation, even though the dynamic shear moduli have not been examined (Hamley, 2005).

Under shear application, the colloidal paracrystal lattice layers to minimise the flow resistance undergo a structural transition that results in the formation of aligned hexagonal packed layers parallel to the flow direction. Loose and Ackerson (1994), in their layers stacking model predicted that under lower shear rates a zig-zag ordering is expected, which with increasing shear rate, degenerates to a straight line of sliding layers, with both mechanisms exhibiting distinctive scattering patterns evident by x-ray or neutron scattering, as shown in Figure (2-23).

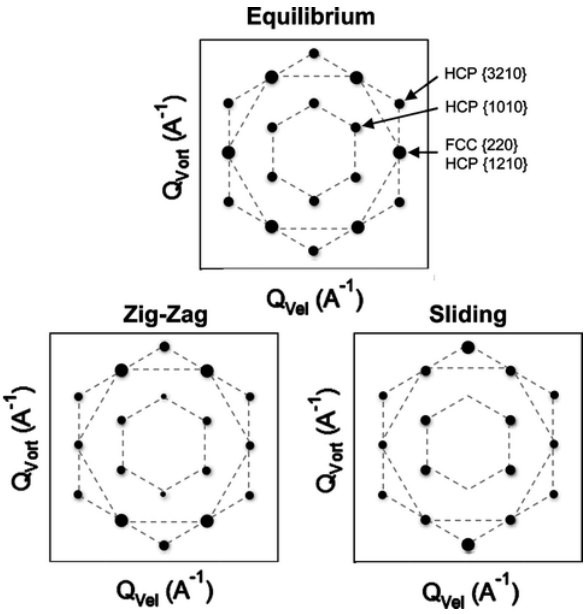

Figure 2-23 A schematic of scattering predicted in the radial geometry based on the sliding layers model (Pozzo and Walker, 2007a).

LaFollette and Walker have compared the static phase diagrams of Pluronic F123 reported to pack into different crystal lattices dependent on temperature and concentration (FCC and HCP) to the shear induced changes using a couette geometry. The OOT to mixed random phase of hexagonal and cubic crystals was probed by Rheo-SANS – a combination of rheological and small angle neutron scattering (LaFollette and Walker, 2011).

Scattering experiments performed on two different concentrations Pluronic P85, which exhibit BCC structure, confirmed the shear induced hexagonal crystals

formation rather than simple alignment in flow direction. The authors reported that the application of steady and oscillatory shear resulted in different structures, stabilities and relaxations but no rheological data was published (Slawecki et al., 1998). Higher levels of structural organisation were accomplished after oscillatory shear on Pluronic F127 gels and the final gel structure was retained throughout the test period of one month after shear (Pozzo and Walker, 2007a).

The rheological block copolymer behaviour is hugely dependent on the block's structure and the test conditions applied. Solutions of Pluronic P84 of 4% at 42°C experienced shear melting at 136 s^{-1} under capillary flow as demonstrated by isotropic scattering in simultaneous SAXS measurements (Castelletto et al., 2007) while Rheo-SANS show that $PEO_{86}PBO_{10}$ in 0.2M K_2SO_4 gel retained its shear induced structures even after high shear values of 250,000 s^{-1} without any melting (Hamley et al., 1998a).

Dao et al. used two Pluronics, P123 and P103 that approximately share the same structure, dimensions, ODT around room temperature and OOT around 30°C. Both form the cubic phase at ODT albeit with unexpectedly different paracrystals, FCC was indexed in P123 and BCC in P103, and the two triblocks have an HCP structure at OOT. The difference between the two triblocks was amplified after the OOT with the addition of BSA to the gel matrices, resulting in a Random close packed (RCP) structure after alignment of P123 while changes were observed in P103 (Dao et al., 2017).

Chapter 3 Materials and methods

3.1. Materials and preparation:

3.1.1 Materials:

Three types of Pluronics were investigated in the study; Pluronic® F127, F68 and F108. The respective commercial names being Kolliphor® 407, Kolliphor® P-188 and 338. Technical information about these Pluronics were provided in the introduction, and a summary of their properties are provided in table (3-1) below. For the gel blends Polyethylene glycol (PEG) with different Mw = 1,000, 2,000, 20,000, 200,000 and 2,000,000 g/mol were added. Ibuprofen was used for the drug loaded systems (Mw = 206.29 g/mol). Deionized water was used in all cases as a solvent except for SANS and when it was replaced by deuterium oxide. All the materials used were purchased from Sigma-Aldrich (St. Louis, MO) and used as received without further purification. The MSDS for all the materials are readily available on the manufacturer's (Sigma-Aldrich) website.

Table 3-1 Properties of commonly used Pluronics (BASF, 2004). CMC data obtained from references a: (Sigma-Aldrich, 2018): and b (Alexandridis and Hatton, 1994).

Commercial (Pluronic ® name)	188 F68NF	338 F108NF	407 F127NF
Physical Form	Solid	Solid	Solid
pH, 2.5% aqueous	5.0 – 7.5	5.0 – 7.5	5.0 – 7.5
Cloud point, 10%	>100 °C	>100 °C	>100 °C
Butylated Hydroxytoluene (BHT), ppm	50 – 125	50 – 125	50 – 125
Molecular Weight	7680 to 9510	12700 to 17400	9840 to 14600
Weight % PEO	81.8 ± 1.9	83.1 ± 1.7	73.2 ± 1.7
Number of EO units	75-85	137-146	95-105
Number of PO units	25-30	42-47	54-60
Heavy Metals	0.002% max.	0.002% max.	0.002% max.
HLB	>24	>24	18–23
CMC at 25°C (w/v %)	0.033[a]	4.5[b]	0.7[a] - 0.1[b]

3.1.2 Neat gels preparation:

The samples were prepared by the cold method described by Schmolka (1972). Water was chilled to 4°C and the Pluronic was slowly added with light stirring until complete dissolution was achieved. For high concentrations, the preparation temperature was lowered down to zero °C if required during the preparation. The final clear solutions were refrigerated overnight allowing the solutions to rest. After 24 hours clear Pluronic solutions were kept chilled under 4°C in labelled containers.

3.1.3 Gel blends preparation:

The same protocol from 3.1.2 was adopted. After the Pluronics dissolution, excipients were added to the clear solutions, except for those with high molecular weights of 200,000 and 2,000,000 g/mol which were dissolved in water first prior to Pluronics addition. For Ibuprofen blends, the API was added to the formulation in the last step after complete dissolution of polymers. Table (3-2) show all the formulations prepared in the study.

Table 3-2 Formulation combinations prepared in the study.

NO.	F127	F68	F108	PEG Mw g/mol (1%)	IBU (1%)
1	0.10%	-	-	-	-
2	1%	-	-	-	-
3	5%	-	-	-	-
4	10%	-	-	-	-
5	15%	-	-	-	-
6	20%	-	-	-	-
7	22.50%	-	-	-	-
8	25%	-	-	-	-
9	30%	-	-	-	-
10	35%	-	-	-	-
11	-	20%	-	-	-
12	-	25%	-	-	-
13	-	30%	-	-	-
14	-	35%	-	-	-
15	-	40%	-	-	-
16	-	45%	-	-	-
17	-	-	20%	-	-
18	-	-	25%	-	-
19	-	-	30%	-	-
20	-	-	35%	-	-
21	-	-	40%	-	-
22	20%	-	-	1000	-
23	20%	-	-	2000	-
24	20%	-	-	20000	-
25	20%	-	-	200000	-
26	20%	-	-	2000000	-
27	20%	-	-	-	Y
28	20%	-	-	1000	Y
29	20%	-	-	2000	Y
30	20%	-	-	20000	Y
31	20%	-	-	200000	Y
32	20%	-	-	2000000	Y

3.2. Experimental methods:

3.2.1. Thermal analysis:

3.2.1.1. Thermogravimetric Analysis (TGA):

a) The method

Thermogravimetric Analysis is a thermal quantitative technique, where the substance mass is monitored continuously as a function of temperature or time in a controlled atmosphere - see Figure (3-1). TGA relies on a high degree of precision for three measurements: mass change, temperature and temperature change. The thermogravimetric curves provide information on: (1) decomposition temperatures, (2) thermal stability in inert and oxidising atmospheres and (3) compositional analysis of polymers and their purity. The mass change is usually associated with the evaporation of residual solvents when degradation takes place, or when thermal reactions occur (Crompton, 2010). TGA can be coupled with Fourier transform IR (FT-IR) and Mass spectrometry (MS) to offer more accurate compositional analysis (Barnett, 1997).

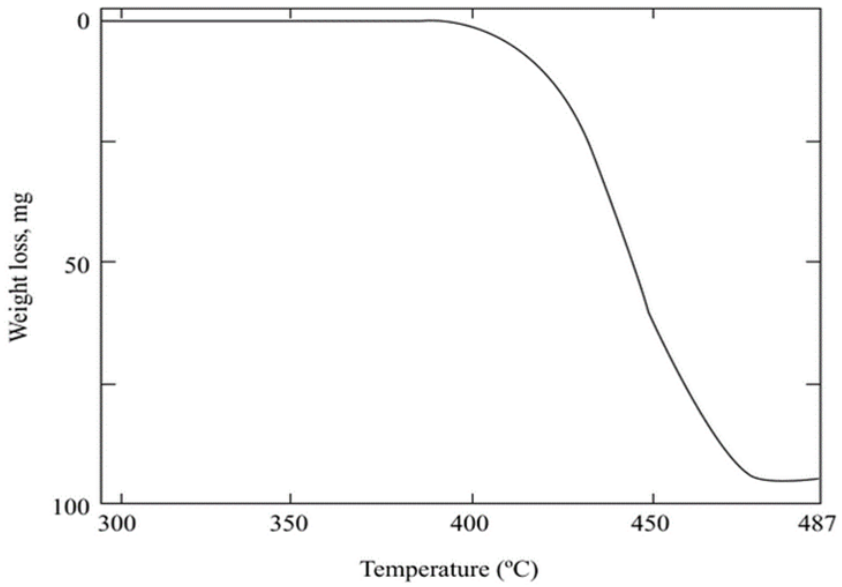

Figure 3-1 Thermogravimetric curve for the degradation of polyethylene (Crompton et al., 2005).

b) Experimental procedures:

TA Discovery TGA (New Castle, USA) was used for all the experiments. Platinum-HT pans were burned clean by butane torch, tared then loaded with

samples via calibrated pipette. The materials were subjected to a temperature ramp of 5° C/min applied from 25 to 400° C with nitrogen as a purge gas to determine the formulations' weight accuracy and compare their stability over the runtime.

Figure 3-2 (left) TA Discovery TGA and (right) TA Discovery DSC.

3.2.1.2. Differential scanning calorimetry (DSC)

a) The method

Calorimetry is a method investigating material structure changes associated with any thermal event during heating, cooling or with time at isothermal conditions, making it useful to investigate phase transitions such as micellisation and gelation. The technique measures the difference in heat flow rate (heat capacity) of a sample compared to a reference as a function of time and temperature. The sample and reference are subjected to controlled identical temperature conditions. DSC is the most widely used thermal analysis technique to provide qualitative and quantitative measurements for many physical transitions and chemical reactions associated with production or consumption of heat as indicated by sharp peaks (Gill et al., 1993, Höhne et al., 2003). The furnace contains a diffusion-bonded type E thermocouple made of chromel and constantan alloys that provides continuous heat transfer measurements for both sample and reference. Purge gas is used for heating/cooling the sample and the

reference and enters through an orifice in the heating block wall between the raised platforms.

Conventional DSC applies linear heating and/or cooling rates to both the sample and reference, which can be adjusted up to 200°C/min.

Modulated DSC (MDSC) applies different heating rates simultaneously and measures the effect on the heat flow. The underlying heating rate provides the Total Heat Flow (supplied by normal DSC), while the modulated heating rate measures the heating flow corresponding to heating rate (or Reversing Heat Flow) and the Non-Reversing Heat Flow that responds to absolute time / temperature - see Figure (3-3).

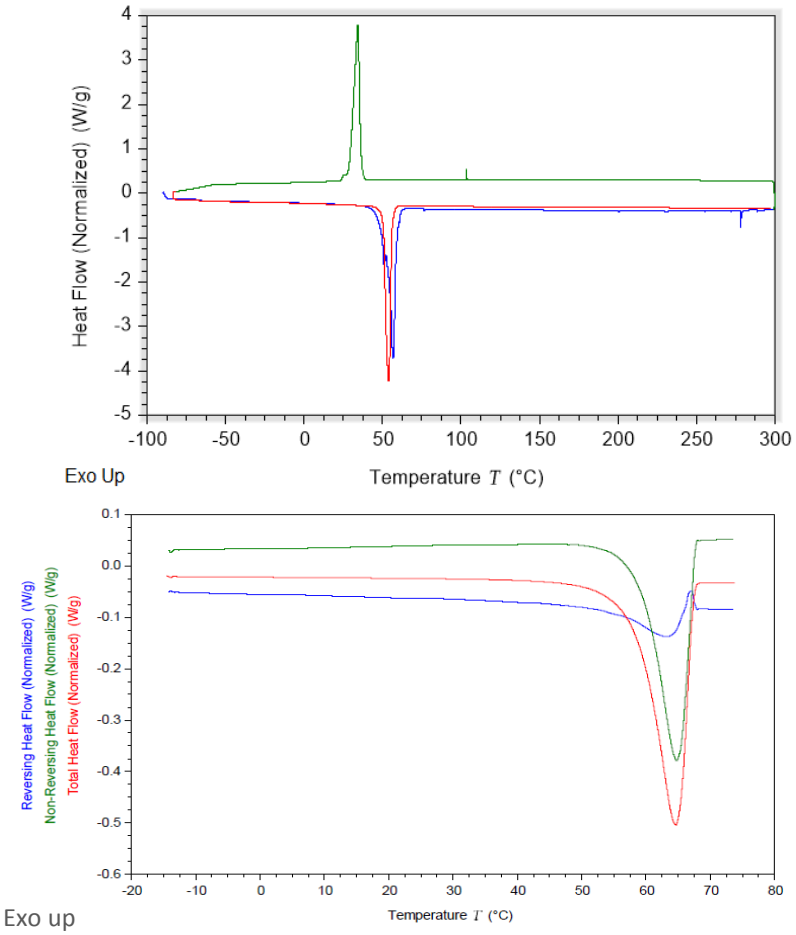

Figure 3-3 (right) A pure Pluronic F127 DSC thermogram using standard pans. (left) A typical MDSC run for PEO N10®.

MDSC doesn't measure the reversibility or the irreversibility of transitions. However the changes detected in Heat Capacity (C_p) can give an idea on the

transition's reversibility. Thermally driven events such as crystallisation, evaporation and molecular relaxations appear in the Non-Reversing signal while melting is shown in the Reversing signals (Thomas, 2005).

b) Experimental procedures:

TA Discovery DSC connected to a RCS-90 cooling system was used to carry out the DSC runs (New Castle, USA) - see Figure (3-2).The samples were loaded to pre-weighed pans that were crimped with their respective dies and finally loaded into the instrument. Standard aluminium pans were used for testing pure polymers and aluminium T-zero pans were used for the gel systems. According to the preliminary results, T-zero hermetic pans performed better than the conventional T-zero as larger gel volumes can be loaded and the hermetic seal prevents any evaporation, jeopardizing the runs integrity. Two ramping runs were performed. The run starting temperatures were aimed to be close to the solutions freezing temperatures between 0 and -20°C and heating tests run to 75°C. Heating rates ranging between 1 and 20 °C/min were used for test optimisation. For all runs nitrogen was used as a purge gas at 25 ml/min flow rate. The software TA TRIOS ver. 3.3.1 was used to compute the results. Runs were repeated a minimum of three times to ensure repeatability.

3.2.2. Rheometry:

a) The method

As mentioned in the introduction, flow properties of injectable systems are of great importance, relating to both processing and application. The rheological behaviour is measured in terms related to the material viscosity by controlling the parameters applied to the material, whether that be stress or strain. Rheometers are categorized according to the probed flow properties: simple shear and extensional flow. Dependent on the flow generated, shear rheometers are classified into rotational and capillary rheometers. Figure (3-4) shows the two types.

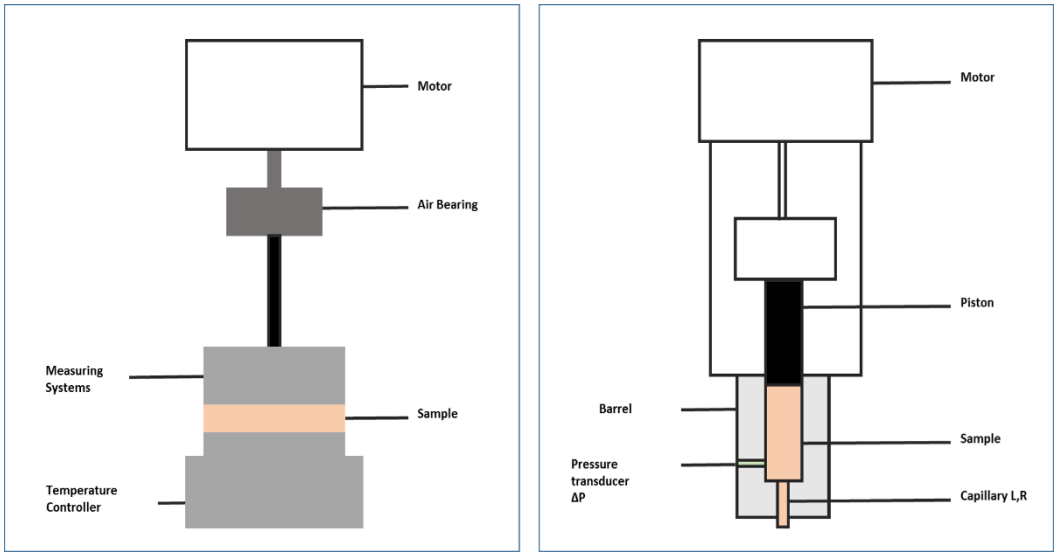

Figure 3-4 Schematic diagram of Rheometers: (Left) drag flow rheometer (Right) Capillary rheometer.

Most commercially available instruments are shear rheometers, in which are either based on drag flow or pressure. In the former, the material is sheared against a solid surface with basic design that combines a controller unit with position sensor (displacement transducer) and motor that can accommodate different flow geometries namely; parallel plate, cone and plate and concentric cylinders (Couette flow). Some different measuring systems are shown in Figure (3-5). The motor and transducer are usually integrated into single unit. Modern rheometers offer controlled stress and controlled strain within the same instrument. The data acquired from each measuring system may vary, due to the inherited geometric differences, the sample properties and the secondary flow effects rising during the measurement. For further information regarding the different flow geometries please refer to Chapter 5 of 'Macosko's : Rheology: Principles, Measurements, and Applications' and Chapter 10 of 'Mezger's: The Rheology Handbook'.

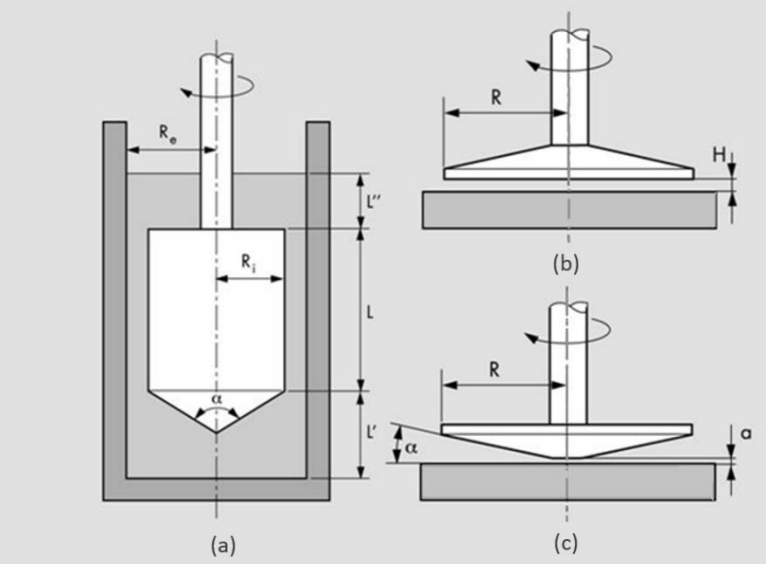

Figure 3-5 Measuring systems (MS) with different geometries: (a) concentric cylinder system MS CC (Searle type), (c) cone-plate system MS CP, (b) parallel plate system MS PP- edited from the original reference ((Mezger, 2011) .

Capillary rheometers are driven by pressure flow, where a piston drives the material flow at a constant flow rate through a die of known dimensions - see schematic in Figure (3-4). They are mainly used to monitor and control polymer melts during industrial processes, providing information about the viscosity over different processing conditions at relatively high shear rates. Capillary rheometry is an interest of this study since it mimics the injection process when a solution or a gel inside a syringe is displaced by a piston through a barrel. For an incompressible sample with Newtonian, laminar and steady flow with a parabolic velocity profile, when using a circular capillary with a radius r the flow will follow the Hagen-Poiseuille equation:

$$\Delta p = \frac{8\eta l Q}{\pi r^4}$$

Equation 3-1

Where,

Q: flow rate

l: length of the capillary die

r: radius of the capillary die

η: the viscosity at the shear rate applied

The wall shear stress τ_w and the apparent shear rate at the wall $\dot{\gamma}_{aw}$can be calculated according to:

$$\tau_w = \frac{r\Delta p}{2L}$$

Equation 3-2

$$\dot{\gamma}_{aw} = \frac{4Q}{\pi r^3}$$

Equation 3-3

For non-Newtonian fluids with non-parabolic velocity profile the Weissenberg-Rabinowitsch correction should be applied:

$$\dot{\gamma}_w = \frac{1}{4}\dot{\gamma}_{aw}[3 + \frac{1}{n}]$$

Equation 3-4

Where n is the exponent of power law constitutive equation. For a Newtonian fluid n=1 and $\dot{\gamma}_w = \dot{\gamma}_{aw}$ (Macosko, 1994).

For a syringe injection, the pressure drop is mainly generated by the needle, since the barrel has considerably larger radius and shorter length than of the needle its pressure drop is taken to be negligible. The viscous force applied on the plunger F_v (syringeability) can be estimated from:

$$F_v = 8\eta l_n Q\left(\frac{r_b^2}{r_n^4}\right)$$

Equation 3-5

Where subscripts n and b refer to the needle and barrel, respectively. The total injection force will combine F_v and the piston friction F_P between the stopper and the syringe barrel, which can vary between different manufacturers and materials used (Allmendinger et al., 2014).

$$Injection\ force = F_v + F_P$$

Equation 3-6

b) Experimental procedures:

Rheometry experiments were conducted on Anton-Paar Physica MCR 301 and 501 rheometers (Graz, Austria) - see Figure (3-6). A Peltier plate (P-PTD200) accompanied with A Peltier plate -controlled hood (H-PTD200) were used for preliminary studies with measuring systems CP and PP (R=12.5mm). A Peltier Couette cylinder C- PTD200 was used with a measuring system CC27 (R_i=26.66 mm, R_e=28.92 mm, V_{sample}=19.4 ml).

Figure 3-6 Anton-Paar Physica MCR 301 with CC27 and C- PTD200 in use the sample cover.

An overview of tests utilised in this study:

1-Rotational tests:

These are usually preformed under two regimens; either by pre-setting the velocity (by adjusting speed/shear rate) or the driving force (by adjusting torque or shear stress). The first simulates flow a dependent application, while the latter is useful for force-dependent application. Both are essential for our formulation's response when syringed and injected. Different tests were performed by fixing either the shear rate or temperature constant and ramping the other variable.

i. Constant shear rate tests: were performed to determine the temperature dependency, correlation with concentration and effect of additive.

ii. Shear rate ramps: to determine flow behaviour at ramping shear rate and constant temperatures 5 and 37°C. The results were analysed to determine the yield stress values.

iii. Stress relaxation tests: Sometimes referred to as step strain tests; there are used to analyse the viscoelastic through behaviour performing one deformation step (γ should be within the LVE range) followed by a relaxation phase. The relaxation extent depends largely on the material's viscous / elastic components and the wait period after the test. Additionally in the case of the gels under study temperature.

iv. Stain rate frequency sweep (SRFS): This test is used to measure the viscoelastic properties (relaxation behaviour) by keeping the strain rate constant. This gives access to long relaxation times that not accessible with regular frequency sweeps (Läuger, 2014).

2-Oscillatory tests:

Oscillatory tests help to examine the viscoelastic structural arrangements in material that allows to separate the material elastic (G') and viscous (G")

components. The setup parameters required for the tests include applied strain value γ and ω, is the oscillation frequency.

i. Amplitude sweeps:

Small amplitude oscillatory shear (SAOS): The first test to be performed to define the limits (γ_L) for linear the viscoelastic region (LVE), where the samples show no deformation or irreversible destruction, important for both frequency and temperature sweeps.

Large amplitude oscillatory shear (LAOS): With application of large strain values the LVE is exceeded and the sample is within the non-linear viscoelastic region (NL range) similar to the application of extensional load or compression. These tests are performed to study the complex rheological behaviour which occurs in multiple regions within one sweep. Both SAOS and LAOS were performed at constant temperatures and frequencies.

ii. Frequency sweeps: As the name implies the sample is subjected to variable frequencies while maintaining fixed amplitude and temperature. These tests provide information about the material stabilisation/ particle interactions, phase separation and additionally the material relaxation through determination of cross-over point(s) in G' and G". The subsequent frequency dependency confirms the material structure.

iii. Temperature sweeps: This test is similar to the constant shear temperature ramp but performed in oscillatory mode with fixed strain and frequency values, offering detailed information about the changes in the dynamic moduli values with temperature.

A schematic showing the MS movements for the rotational and oscillatory modes is displayed in Figure (3-7) and a summary of the tests performed is presented in table (3-3).

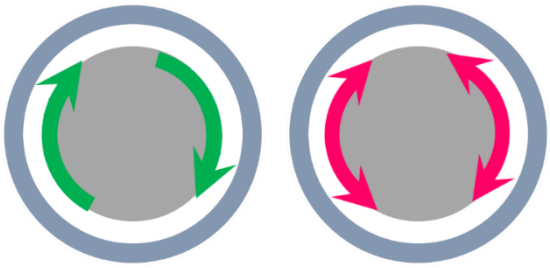

Figure 3-7 Measuring system movements corresponding to the test modes. Right showing oscillation and left rotational test modes.

Table 3-3 A summary of rheological tests and parameters used in the study.

Test type	Test	Temperature [°C]	Set variable(s)
Rotational	Const. shear rates	Ramp: 0 to 45	$\dot{\gamma}$ = 10 , 20 ,50 and 100 s^{-1}
	Shear rate ramp.	5 and 37	$\dot{\gamma}$ = 0.01 to 1500 s^{-1}
	Stain rate frequency sweep (SRFS)	37	$\dot{\gamma}$ =0.1,0.5,1,5,10 s^{-1}
	Stress relaxation	5 and 37	γ = 0.2%
Oscillation	Amplitude sweep	5 and 37	ω =10 rad/sec
	Frequency sweep	5 and 37	γ = 0.2%
	Temperature sweep	Ramp 0 to 100	ω =10 rad/sec

3.2.3. Small angle x-ray and neutron scattering:

a) The method

Small angle X-ray and neutron scattering are utilised regularly in condensed matter structural studies due to the similar magnitude of their electromagnetic wavelength (around 1 Å) to most interatomic distances of interest. These methods involve measuring the scattered beam intensity of the material as a function of the scattering vector or the angle of incidence (θ) which for small angle measurements is about 5°, making the techniques ideal for systems like Pluronics

with particle sizes in the order of 10-100 nm (10-1000 Å). The scattering vector (q) is the difference between the incident (k_i) and diffracted wave vectors (k_s), $q = k_s - k_i$. For elastic scattering $|k_s| = |k_i|$ and the wave vector magnitude is:

$$q = |q| = 4\frac{\pi \sin(\theta/2)}{\lambda}$$

Equation 3-7

where λ is the wave length of x-rays or neutrons.

Small angle neutron scattering (SANS) and Small angle x-ray scattering (SAXS) differ in the radiation nature of the electro-magnetic radiation (EMR) for x-rays compared to neutrons being a neutral atomic particle. These techniques have be used to determine micellar system dimensions and the collected data can be fitted to provide information about the inter-micellar / intra-micellar interactions. The analysed detractions data can used to determine the morphology or the orientation in the system before and after gelation. The in-phase detractions (peaks) q values correspond to the particles arrangement in the crystal lattice, commonly known in crystallography as Bragg peaks. The position of the maximum (first peak = q*) indicating the distance between the individual particles can be determined using Bragg's law:

$$d_{Bragg} = 2\pi/q_{peak}$$

Equation 3-8

In our experiments we are only going to focus on elastic-in phase scattering that changes direction but the magnitude of the wave vector-gives rise to small angle scattering (SAS) even though inelastic scattering is growing popular in similar systems to those under study.

X-ray and neutrons interact differently with matter because they interact with different parts of material but the results of these interactions can be viewed complementary with the same analysis applicable to both techniques. The strength of the x-ray interactions with matter depend on the material's electron count, namely the electron density which increases with increasing atomic

number. Neutrons, unlike x-ray photons are not charged and have higher penetration allowing them to interact with the atomic nuclei. The nuclei's ability to scatter neutrons is determined by its scattering length density (SLD), which is independent of atomic number, thus different isotopes of the same element can have different SLDs as in the case of Hydrogen (H^1) and Deuterium (H^2). For hydrogen rich organic materials, scattering results are optimised through adjusting SLD values by selective deuteration of one or several species in the medium. A technique known by contrast matching or Babinet's principle, a common practice in studying micellar systems to provide further morphological information of the core-shell structures. However due to time/resources limitations and backed by data from previous studies that have obtained good quality data by only substituting the solvent, we settled to use to deuterium oxide without deuterating the triblock two components (Hamley, 2000, Roe, 2000)

SANS is disadvantaged over SAXS by the intrinsically low flux of neutron sources (nuclear reactors or spallation sources using cold source moderators) compared to the order of magnitude higher fluxes for x-ray sources that allows real time measurements (rotating anode or synchrotrons).

Small angle scattering methods have been utilised to study the structure of the polymeric system phase transitions. SAXS offered higher flux and better resolution (higher number of measurement points), making it perfect for time resolved studies. SANS presented the possibility of distinguishing the system components due to the contrast differences between the two blocks and the deuterated solvent used which provides more information about the system, enhancing the quality of the data collected. The scattering length densities (SLD) were calculated to be ρ_{PEO} = 6.79x10^9 cm^{-2}, ρ_{PPO} = 3.43x10^9 cm^{-2} and ρ_{Ibu} = 9.23x10^9 cm^{-2} with contrast values of 3.21x10^{21}, 3.60 x10^{21} and 2.94x10^{21} cm^{-2} for each one respectively.

Both techniques were utilised to perform static and under shear scattering measurements.

b) Experimental procedures:

3.2.3.1. Small Angle X-Ray Scattering (SAXS):

SAXS measurements were carried out at two facilities, the University of Bradford IRC laboratories and STFC - Diamond synchrotron (Rutherford Appleton Facilities-Didcot, UK). The different experimental setups are shown in Figures (3-8, 9, 10).

The first set of static experiments were performed on all samples using Anton-Paar's SAXSpace (Graz, Austria) with λ = 0.154 Å generated using a Cu Kα source (Xenocs, France). A Peltier temperature control stage (TC150) and a sample-to-detector distance (SDD) of 308 mm were used for all runs. Samples where loaded to quartz 1 ml capillaries in the solution state and left to stabilise at temperatures lower than the transition temperature before the tests. Temperature ranges explored were dependent on the samples (-2 to 100 °C). Additional runs of background and dark current were performed under the same conditions. Reductions and background subtraction were completed using SAXSquant software (Graz, Austria).

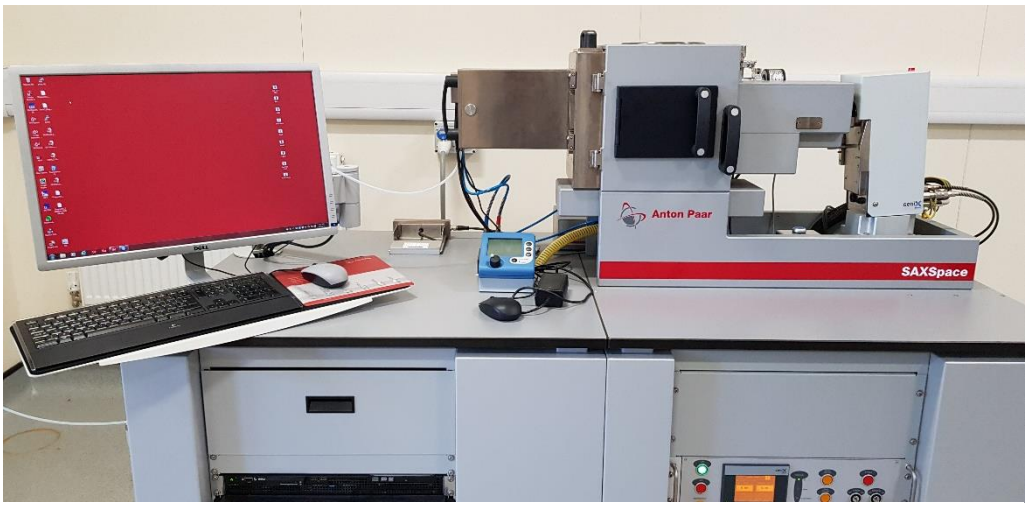

Figure 3-8 Anton Paar SAXSpace.

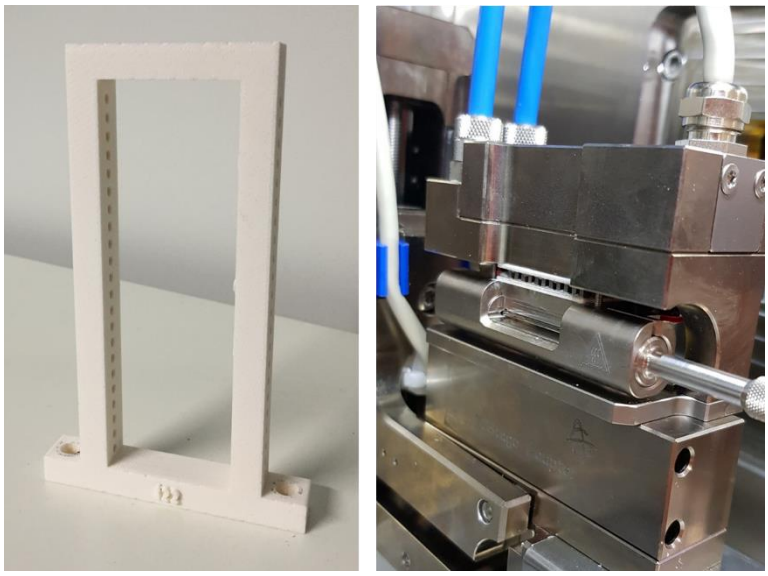

Figure 3-9 Right the capillary holder used for static SAXS measurements on I22. Left: TC 150 stage used for SAXSpace with quartz 1 ml capillaries.

The second set of static SAXS measurements was performed using beamline I22 at Diamond light source (Rutherford Appleton Facilities-Didcot, UK) equipped with x and y stages and a Pilatus P3-2M detector. Samples were loaded into Mark glass capillaries dimensions (L= 80mm, wall thickness = 0.01 mm, outer diameter = 1.5 mm) and mounted in front of the beam on a 3D printed ladder. Each sample was run twice; at room temperature and again after refrigeration overnight. Measurements were made in the range of $0.001 \leq q \leq 0.18$ [$Å^{-1}$].

Dynamic SAXS was performed using the same I22 beamline, with x-ray wavelength fixed 0.88 Å and SDD of 1.9 m permitting of measurements range $0.007 \leq q \leq 0.524$ [$Å^{-1}$]. Data was collected from two experimental setups; a) Constant shear with temperature ramps using Linkam optical Shearing System CSS450 (Tadworth, UK) with modified x-ray transparent Polyimide (Kapton) windows and a gap that was maintained at 500 µm for all runs. b) Injection of chilled formulations into in-house designed Polyimide reservoir mounted on an Aladdin remotely controlled syringe pump (World Precision Instruments, USA). During the experiments temperature control was maintained by a Lauda Eco-Re415 chiller. The Linkam's temperature distribution across the measurement window has been tested to ensure a homogenous cooling and heating profile with the shear application - see following Methodological Development.

Solidworks drawings for the Kapton Linkam windows and injection reservoir are provided in Figure (3-11).

I22 data reduction and processing was carried out using Diamond's in-house built software Dawn ver. 2.5.

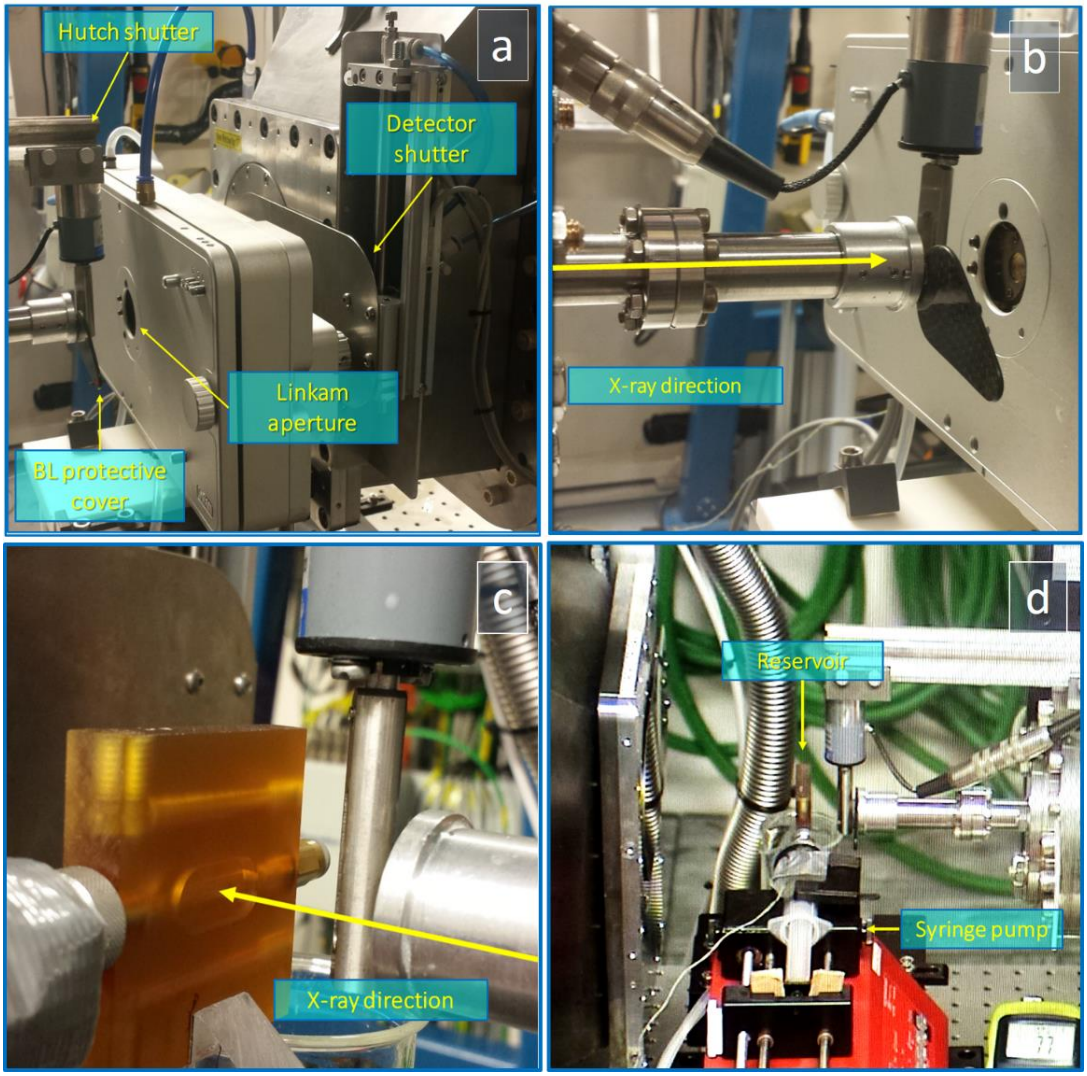

Figure 3-10 Experimental setups at beamline I22. Bottom (a+b) Linkam shear cell in front of the beam at 1-2 shear plane.(c+d) The mounted syringe and reservoir in front of the BL. (d) close-up to the Polyimide reservoir. Where 1-, 2-, and 3-directions are the coordinate indices representing the flow velocity (v), velocity gradient (Δv) and vorticity (ω) directions, respectively.

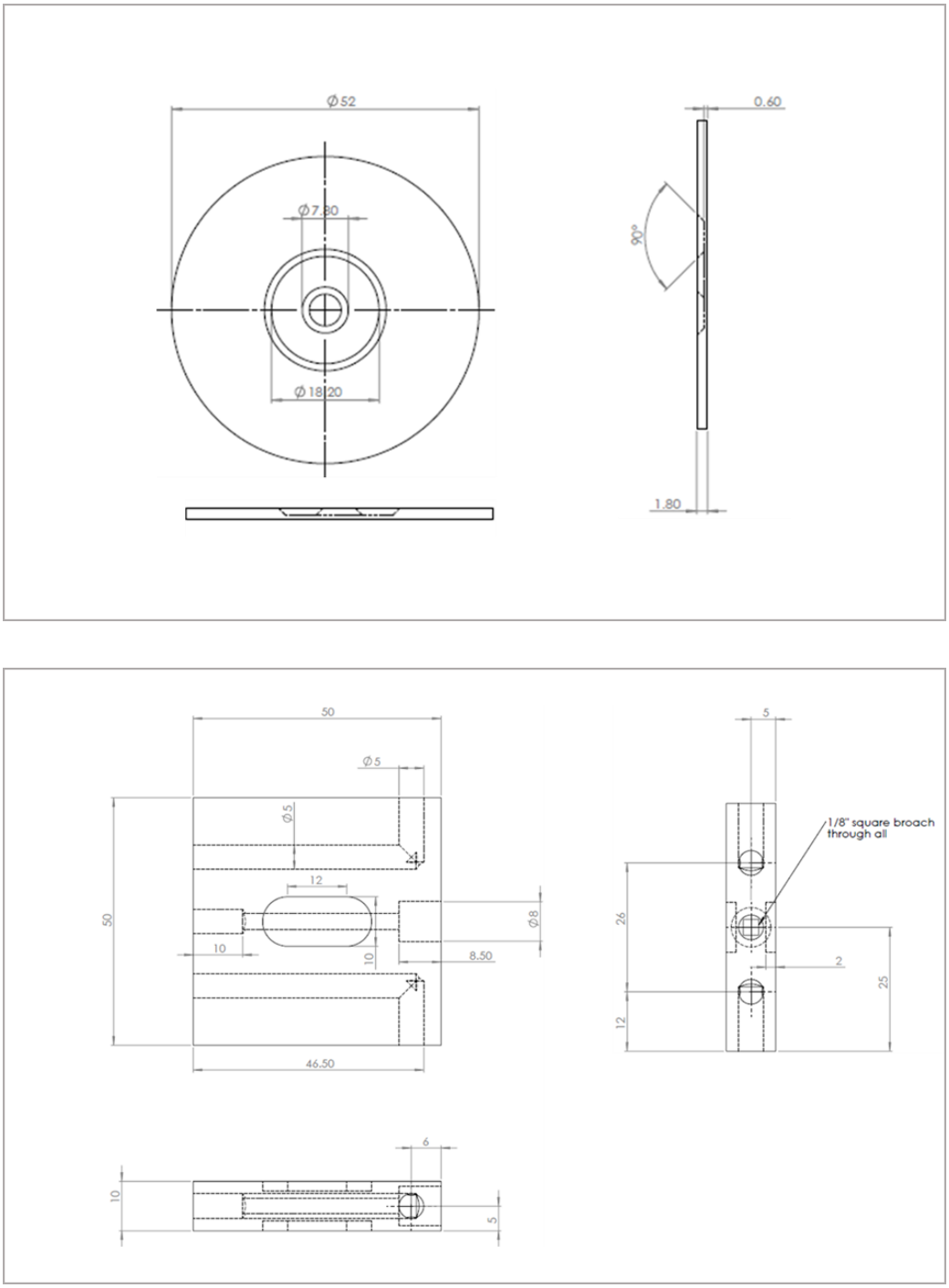

Figure 3-11 (Top) Kapton Linkam window and (Bottom) injection reservoir.

3.2.3.2. Small Angle Neutron Scattering (SANS):

SANS measurements were carried out using two large scale structure instruments at STFC -ISIS spallation neutron source (Rutherford Appleton Facilities-Didcot, UK).

a) Static measurements:

Static measurements were performed to observe the structural changes at two different temperatures; low temperature of 5°C (below CGT) and high temperature 37°C using the LOQ instrument at sample-to-detector distance of 4 m covering a range of $0.007 \leq q \leq 1.5$ [$Å^{-1}$]. Samples were loaded in the sol state into Hellma rectangular quartz cuvettes (110-QS) with path-lengths of 1 mm. Additionally two runs of pure deuterium oxide and the empty beam were conducted. Temperature was maintained throughout the tests by a circulating fluid. Figure (3-12) show the loaded samples in front of the neutron beam.

b) Rheo-SANS measurements:

Two sets of Rheo-SANS experiments were performed using a stress-controlled Anton Paar Physica MCR 501 rheometer (Graz, Austria) mounted in the SANS2D instrument: a) steady rheo-SANS and b) LAOS Rheo-SANS. The experiments used Anton Paar's SANS customised measuring cell CTD 200/GL connected to an Evaporation Unit (EVU-10), temperature controller (TC-30) and a quartz glass Couette measuring system (ME48) with an inner diameter of 50 mm and bob with outer diameter of 48 mm (Graz, Austria), where the neutron beam was directed in the radial direction perpendicular to the 1-3 flow direction. The sample-to-detector distance was fixed at 4 m covering a q range between $0.004 \leq q \leq 1.5$[$Å^{-1}$]. The sample size used was limited to 10 ml and between each run the samples were cooled below their respective gelation temperature. Figure (3-13) shows the experimental setup of Rheo-SANS experiments.

Softwares: SANS data reduction was performed using Mantid v.3.12.1 and Sasview v.4.1.2 was used for further analysis. Schematics of the two beamlines instruments are shown in Figure (3-14).

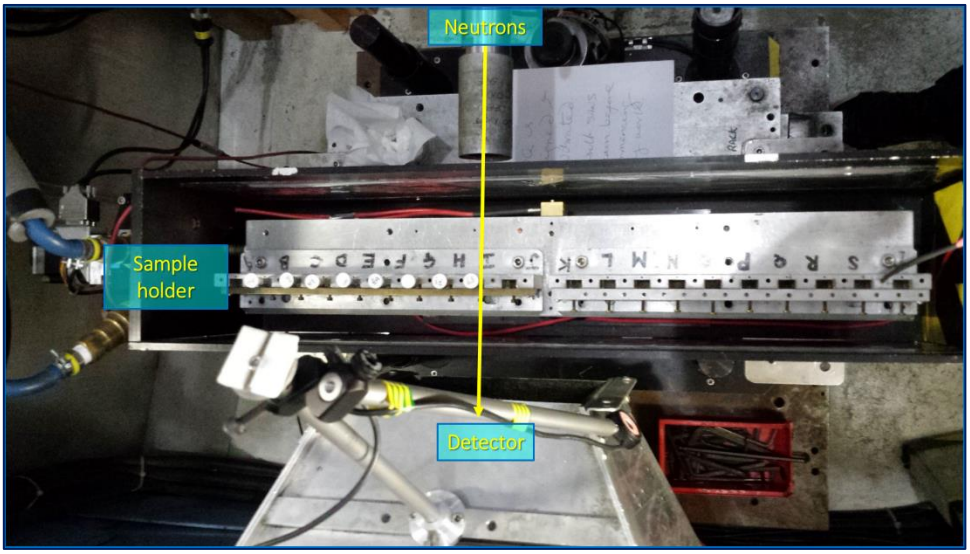

Figure 3-12 Static SANS performed using LOQ with samples loaded into the holder before measurements.

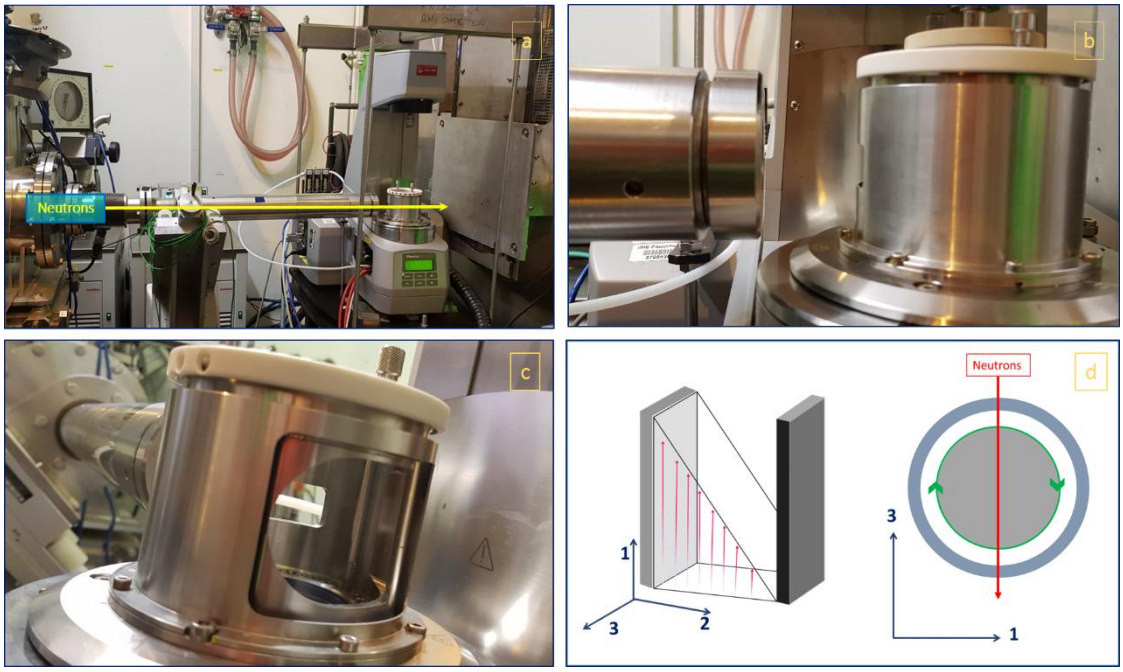

Figure 3-13 Rheo-SANS setup on beamline SANS2D. (a) MCR 501 rheometer mounted in front of SANS2D. (b) and (c) showing close ups of measuring cell. (d) A schematic scattering planes inside the Couette cell, where 1-, 2-, and 3-directions are the coordinate indices representing the flow velocity (v), velocity gradient (Δv) and vorticity (ω) directions, respectively.

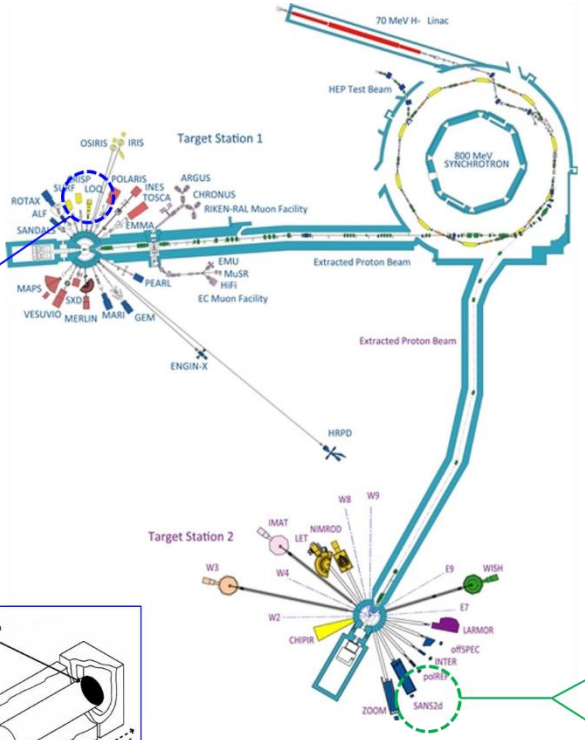

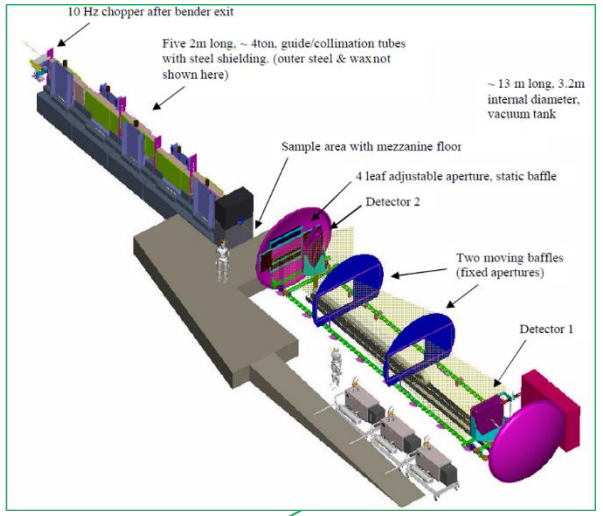

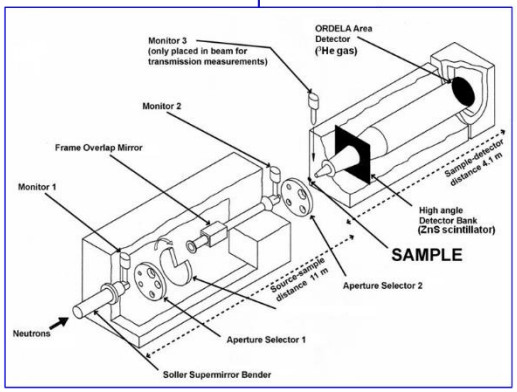

Figure 3-14 Schematics of the two beamlines instrument used in the study: LOQ and SANS2D at ISIS-RAL.

3.3. Methodological development:

3.3.1. Pure polymers thermal characterisation

The polymers were tested using aluminium standard pans from -90 to 100°C at a heating rate of 10°C/min.

a- Pluronics:

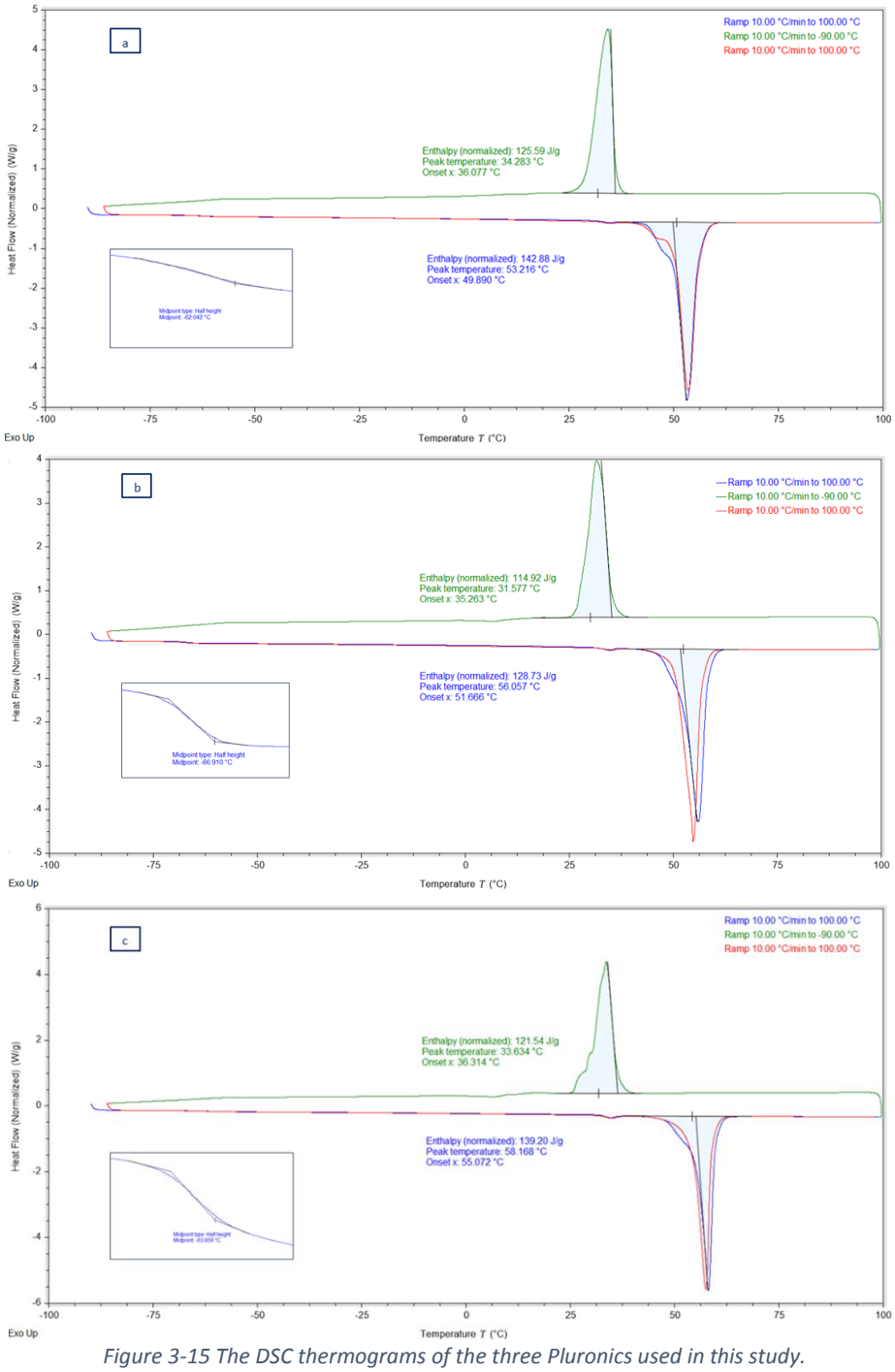

Figure 3-15 The DSC thermograms of the three Pluronics used in this study.

The triblock demonstrated a shift in melting temperature according to the polymer molecular weight where $T_{m\ (F108)} > T_{m\ (F127)} > T_{m\ (F68)}$ - as seen in Figure (3-15). However, neither the glass transition nor crystallisation temperatures displayed the same trend as can be seen in the thermograms. This discrepancy possibly occurred due to the copolymers polydispersity, which can be confirmed by gel permeation chromatography (GPC). Results summary are displayed in table (3-4):

Table 3-4 The T_g, T_m and T_c acquired from the Pluronics thermograms.

Pluronic ®	F68	F108	F127
Molecular Weight [g/mol]	7680 to 9510	12700 to 17400	9840 to 14600
Weight % PEO	81.8 ± 1.9	83.1 ± 1.7	73.2 ± 1.7
Number of EO units	75-85	137-146	95-105
Number of PO units	25-30	42-47	54-60
T_g [°C]	-63.66	-62.679	-66.91
T_m [°C]	53.216	58.168	56.057
T_c [°C]	34.283	33.634	31.577

b- PEGs:

Figure (3-16) shows an overlay of the pure PEGs in the range of -90 to 100°C. The homopolymers melting temperatures increased with increasing the molecular weight.

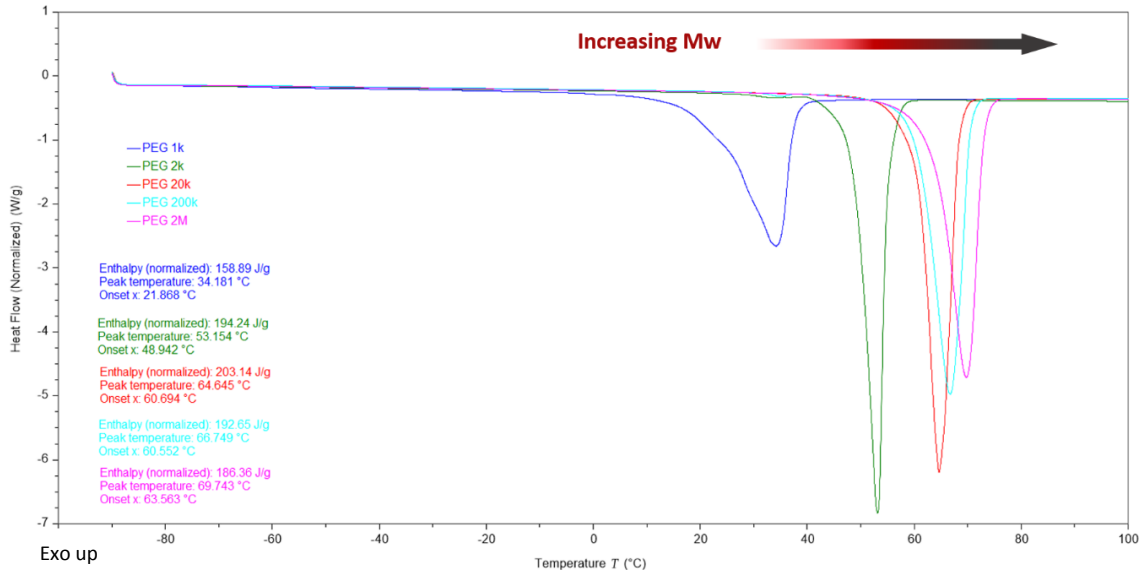

Figure 3-16 Pure PEGs thermograms with endothermic peaks corresponding enthalpy values, onset and peak temperatures.

3.3.2. Gel systems:

Choosing the pan type used for DSC runs is critical to ensure accurate and reproducible measurements. For our samples the intricate transitions sought justifies using Tzero pans, which to be more sensitive due to the pan flatness compared to a standard pan and the ability to accommodate liquid and gel samples easily with capacities ranging from 20 to 40 µl depending on the lid they are paired with (TRIOS manual).

Two combinations were compared; one of Tzero pans and lids and another with Tzero pans with Hermetic lids that allow an airtight seal. The latter were notably better to contain the samples with lower possibility of leakage and to minimise evaporation risk (which can alter the samples weigh thus results in affecting the runs accuracy). Additionally, Hermetic lids offered more freedom to control the sample size (up to 40 µl).

Thermograms of experiments with the two lid types are displayed in Figure (3-17, top). At low temperatures no difference was noticed between using the two lids in the transition region of interest but at higher temperatures the Hermetic lids show a more consistent and reproducible results owing to their sealing mechanism. Hermetic lids were opted for the due to the previously stated reasons concerning leakage and evaporation risks.

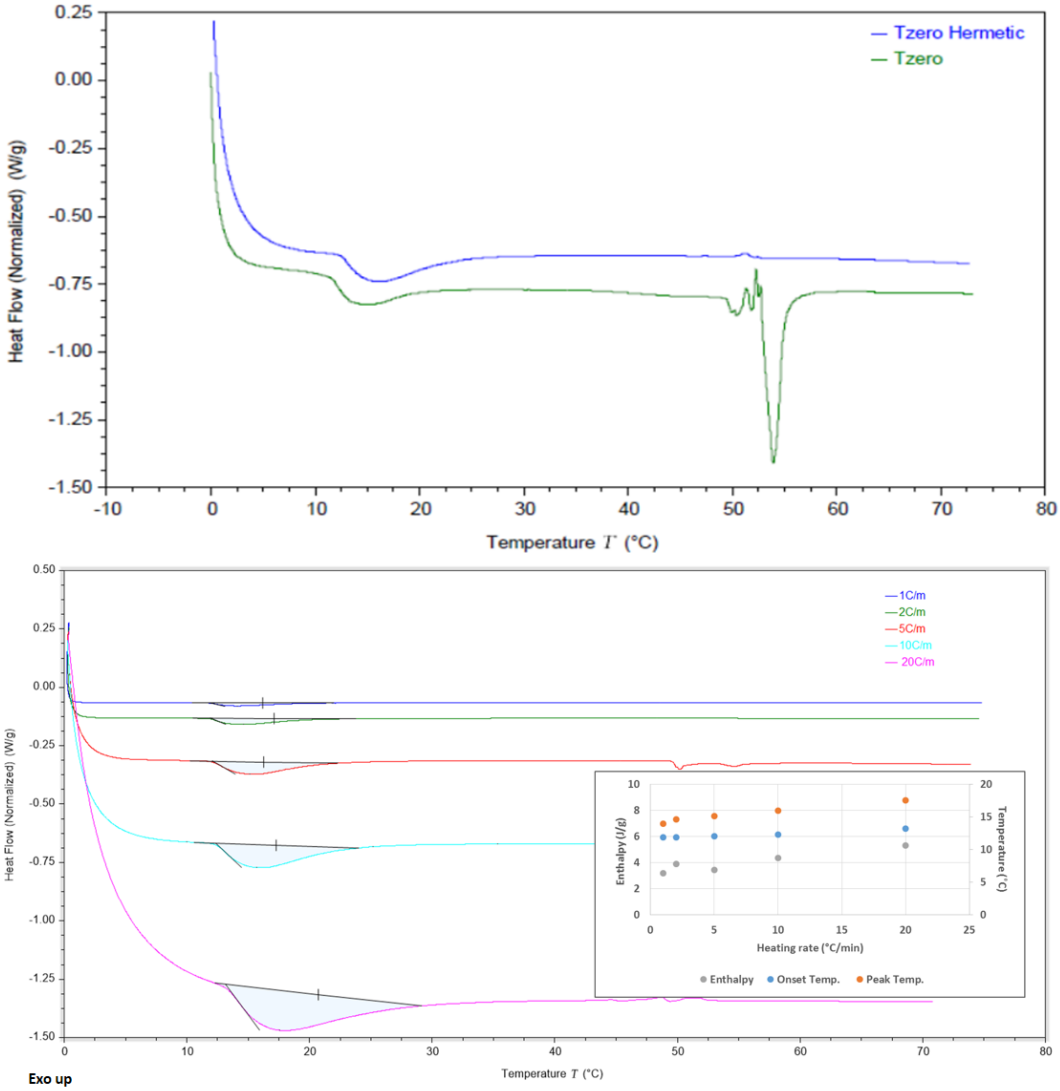

Figure 3-17 (Top) The effect of different pan lids on Pluronic F127 20% sample. (Bottom) an overlay of different heating rates on the same Pluronic F127 20% sample .

Heating rates have an important role in enhancing the signal's detection and using higher heating rates provide larger heat flow signals, however these should be appropriately modified according to the expected range of transition (Thomas, 2001). The results of five different heating rates for the material are shown in Figure (3-17, bottom). The thermograms show a heat flow increase and peaks shift to the right with increasing the applied heating rate. In this case it was found that the difference between the highest 20°C/min and the lowest heating rate 1 °C/min peak temperatures was about 4°C. Heating rates of 20°C/min were considered too large for the small range of interest and the difference between

rates 2-10 °C/min was less than 0.5°C. A heating rate of 10°C/min was chosen for this study due to the signal robustness and the moderate measuring time.

3.3.3. Rheological measurements:

A shear ramp test on F127 20% at 37°C from 0.001 to 1500 s^{-1} was used to explore the differences arising from using different measuring systems. Each test lasted for 17 minutes and a cover was used for all experiments to prevent evaporation. The three measuring systems (MS) depicted in Figure (3-5) were used: CC27, CP25 and PP25 with a gap of 0.102 mm. The recorded shear stress/ viscosity values were different according to the geometry used as demonstrated in Figure (3-18). The two plate based MS recorded higher values of stress and viscosity than the ones recorded for the Couette cylinder. This variation arises from the inherited difference in sample size (0.1 ml was used for plates to fill the gap plus trimming compared to 19.4 ml in CC27) and the exposure to the gel-air interface; which is larger for the former systems, causing quicker drying and thus increased viscosity. Unlike CP and CC, the shear rate values for PP and therefore the recorded viscosities, are highly dependent on the gap dimensions. However, the plate based MS showed higher stability than CC at shear rates up to 300 s^{-1} evident by the appearance of stress plateau. The multiple plateaus in stress plot obtained from CC confirms the MS ability to amplify shear inhomogeneities between the middle of the gap and the bob surface which according to Mezger, can create a shear rate difference of up to approximately 18%.

All the plots show the system's shear heterogeneity. CC was chosen as the MS to conduct the rest of the rheological measurements since it decreases the risk of sample evaporation by utilising larger sample volume (Mezger, 2014).

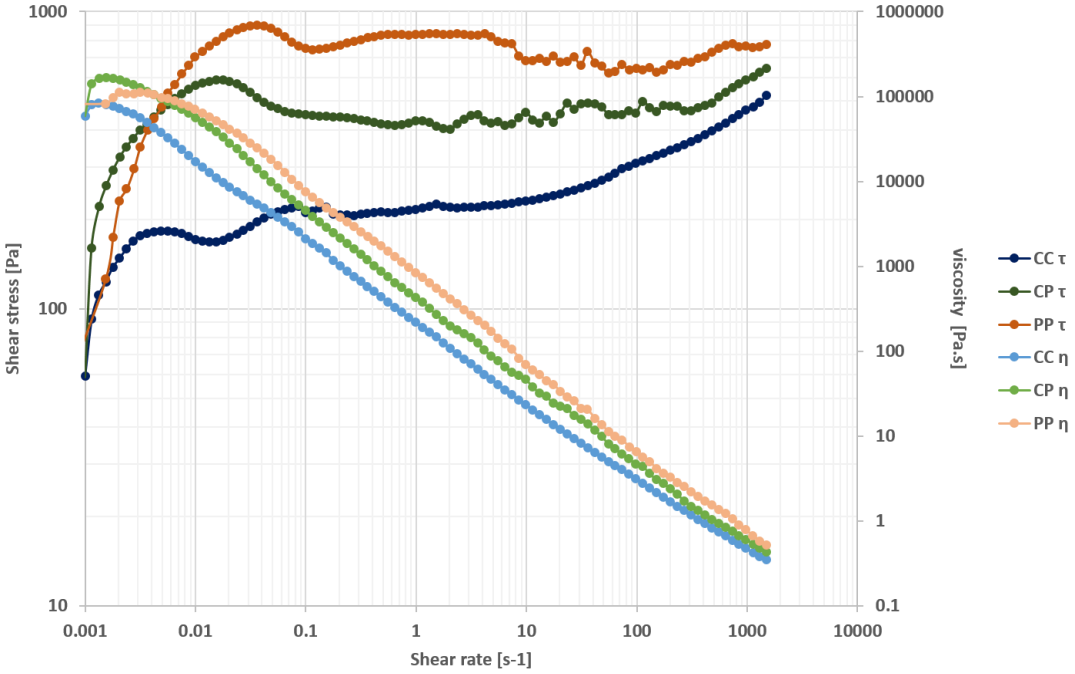

Figure 3-18 Shear ramps using the same samples and test parameters with different MS.

3.3.4. Scattering:

a- indexing

Table (3-5) was used in indexing peak positions from scattering experiments. Where the ratio is calculated based on peak n position to the first peak (q_n/q^*).

Table 3-5 The peak position ratios for BCC and FCC.

FCC Plane	Peak Position	Ratio	BCC Plane	Peak Position	Ratio
111	q*	1.00	110	q*	1.00
200	(√4/3)q*	1.15	200	(√2)q*	1.41
220	(√8/3)q*	1.63	211	(√3)q*	1.73
311	(√11/3)q*	1.91	220	(√4)q*	2.00
222	(√12/3)q*	2.00	310	(√5)q*	2.24
400	(√16/3)q*	2.31	222	(√6)*q	2.45
331	(√19/3)q*	2.52	321	(√7)q*	2.65
420	(√20/3)q*	2.58	400	(√8)q*	2.83
422	(√24/3)q*	2.83	411	(√9)*q	3.00
333	(√27/3)q*	3.00	420	(√10)*q	3.16

b- Linkam temperature distribution:

The Linkam was set up to perform a ramp at 2°C/min from 5°C to 50°C, followed by a hold time for 5 minutes. A modified black sapphire window with emissivity of 0.95 was used. FLIR X6540SC IR Thermal Camera (Wilsonville, USA) with integration of 1 frame/sec – see Figure (3-19). Two experiments were conducted on F127 20% sample while ramping temperature and recording the thermal profile: a static measurement and one under a constant shear rate of 20 s^{-1}.

The results demonstrated that although the two profiles were very similar, the shear enhanced the heat distribution within the measurement gap slightly. The thermal images for the first and last frames are shown in Figure (3-20), while the mapped profiles are plotted in Figure (3-21).

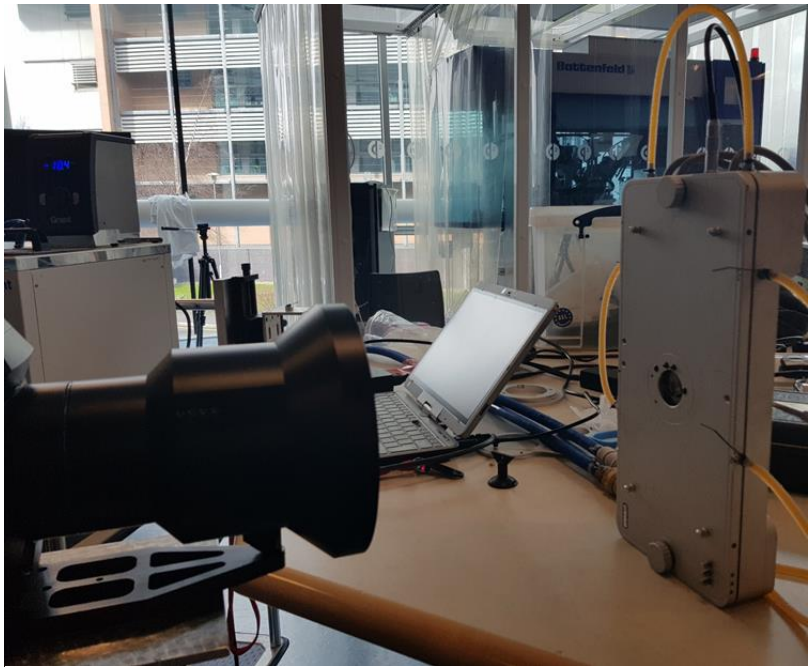

Figure 3-19 FLIR X6540SC IR Thermal Camera with the Linkam shear cell prior to measurement.

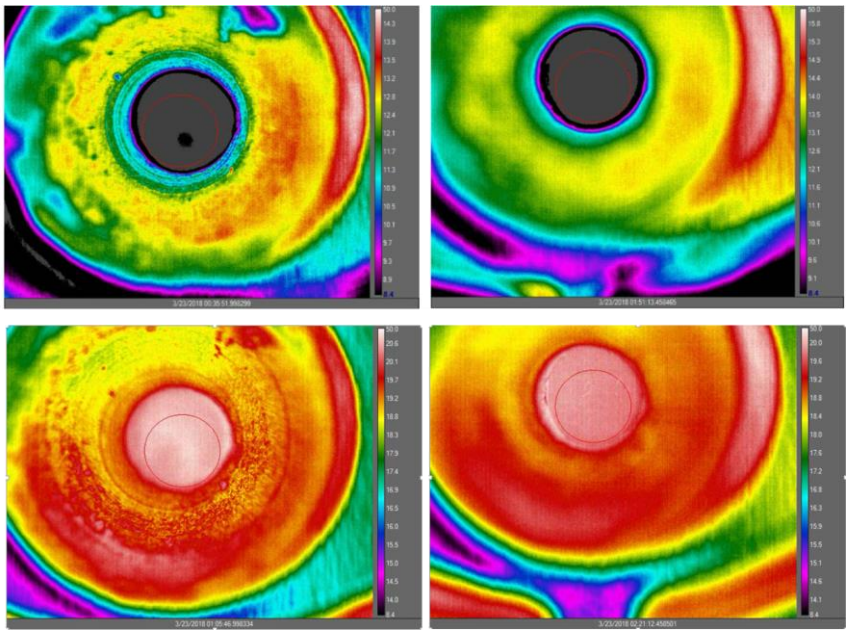

Figure 3-20 Thermal imaging profiles for top row for measurements at first frame (left) no shear (right) shear. Bottom row for measurements at last frame, where (left) no shear (right) shear.

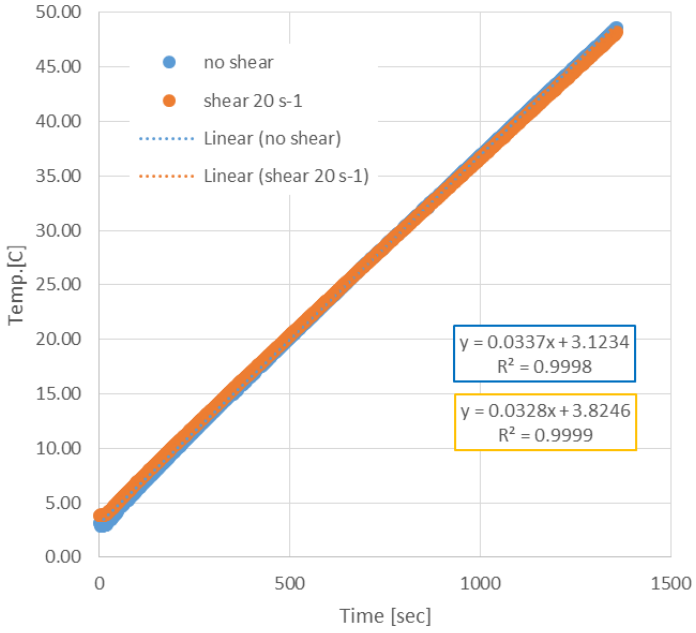

Figure 3-21Temperature distribution inside the Linkam window recorded by the thermal camera.

Chapter 4 Neat formulations

This Chapter aims to provide in-depth investigation of the neat Pluronic's structural properties studied during and after the completion of the transitional ordering. Compositional and environmental changes were examined by a variety of experimental measurements under both the static and dynamic conditions that were discussed earlier in Chapter 3.

4.1. Thermal Analysis of neat F127:

4.1.1 Thermogravimetric Analysis (TGA):

As mentioned before TGA is used to obtain information about the sample's stability and to determine the weight loss percentage with temperature. The results of 5°C/min ramp to 400°C are displayed in Figure (4-1). The weight loss appears to be a two-step transition in higher concentrations of which the first stage represents the weight loss% caused by losing water from the system and the second is due to Pluronic degradation.

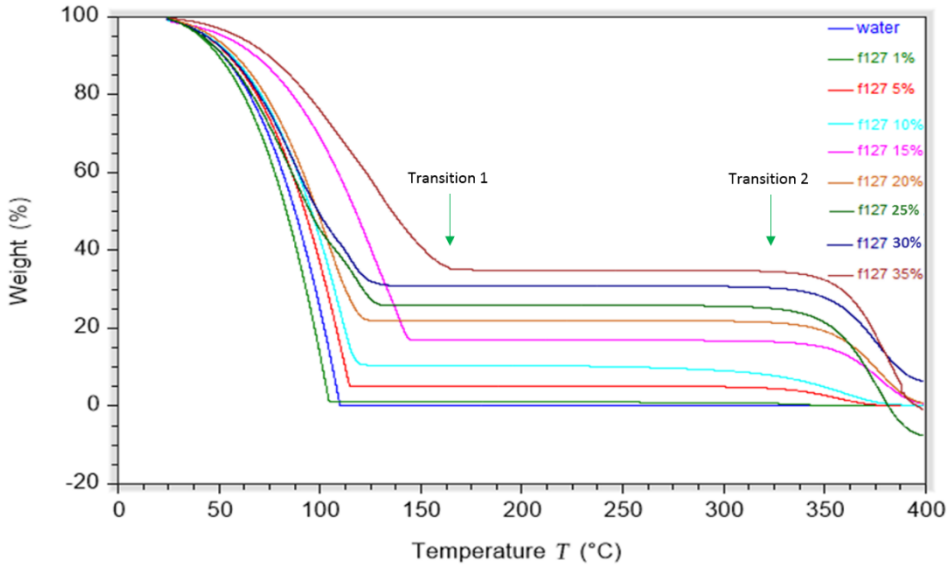

Figure 4-1 TGA heating ramp from room temperature to 400°C.

Most of the samples exhibited a monotonic first step of weight loss process as demonstrated in Figure (4-2). TGA transition (1) temperatures as function of F127 concentration.

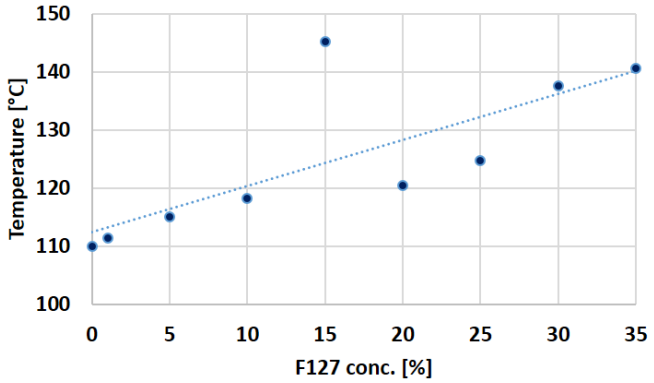

Figure 4-2 TGA transition (1) temperatures as function of F127 concentration.

From the previous results, the TGA data were normalised according to their respective transition temperature and time to reach the transition temperature in Figure (4-3), albeit marginal it was found that the mass loss gradient was negatively proportional to the copolymer concentration- where the its values increased slightly with increasing polymer percentage.

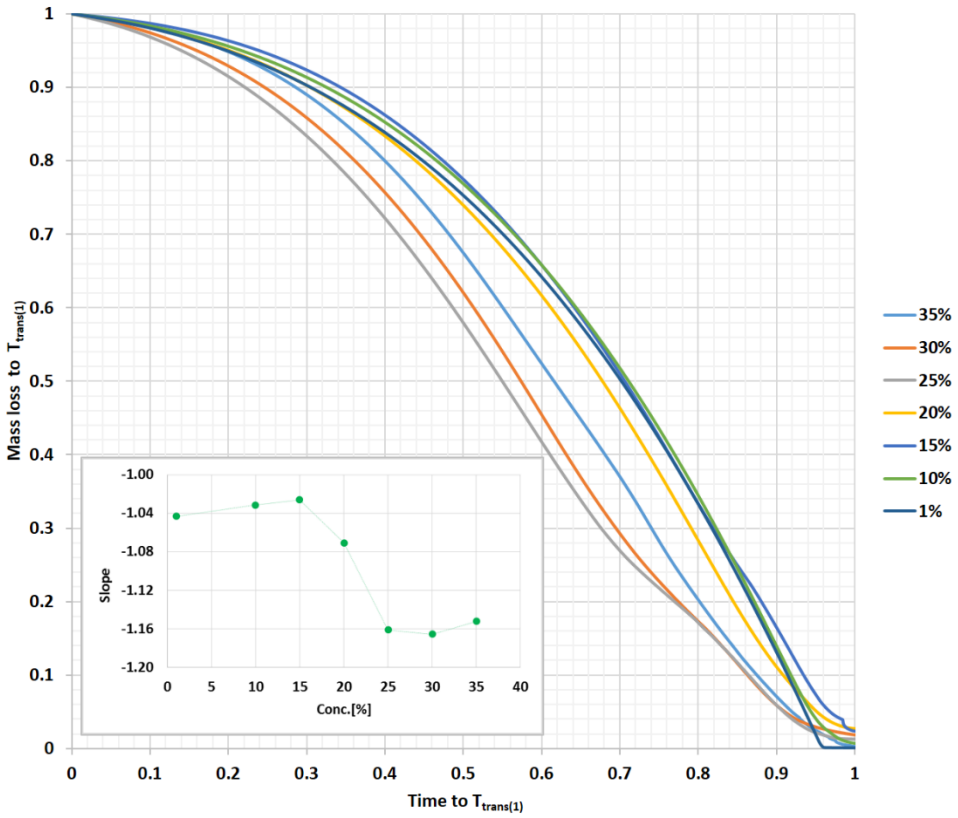

Figure 4-3 Normalised TGA data according to the formulations respective transition temperatures.

Figure (4-4) show the results of weight loss measurements for 300 min at isothermal conditions (25°C). Naturally, the higher concentration gels entrap water within their network for longer times due to their higher density of hydrogen bonding. Figure (a) embodies the weight-concentration relationship as a function of the total remaining weight and (b) the calculated remaining percentage of water (for each formulation). It can be observed that higher concentrations at the end of the test still contain a considerable amount of water. However, these assumptions were made without taking the experimental error that might have risen during the gel preparation process.

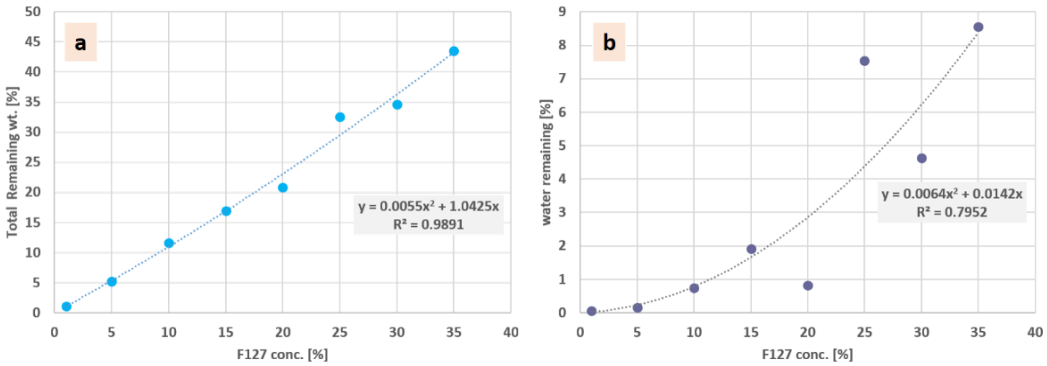

Figure 4-4 Percentage of water retained after TGA runs at isothermal conditions (25°C) for 300 minute.

4.1.2 Differential Scanning Calorimetry (DSC):

Calorimetry was used to detect the endothermic/exothermic transitions associated with the micellisation, gelation and structure melting by subjecting the prepared solution to continuous heating and cooling ramps. In DSC measurements the peaks correspond to the progressive formation or breakage of micelles/gel structure, where the onset temperatures correspond to initiation of micellisation or CMT and T_{endset} to the transition completion which in our case refers to gelation. Another critical point is the peak temperature, that should be proportional to number of the micelles formed in the solution (Pham Trong et al., 2008).

4.1.2.1 Static sample measurements:

At the beginning of the heating ramp, the thermograms start off flat until a decay appears that progresses into an endothermic peak signifying the micellisation /

crystallisation before the heat flow signal returns to its zero gradient. Mirrored heat signals are displayed in the opposite direction when the cooling ramp is performed, with only one distinctive exothermic peak disturbing the constant heat in almost the exact region of the endothermic peak in the heating ramp denoting the complete reversibility of the thermal transition and melting of the structure formed in the heating step. It can also be seen that conducting a second heat ramp which overlays the first ramp almost completely confirms this reversibility.

An example of a complete thermogram is displayed in Figure (4-5) and Figure (4-6) show a series of overlaid thermograms for samples from 15 to 35%.

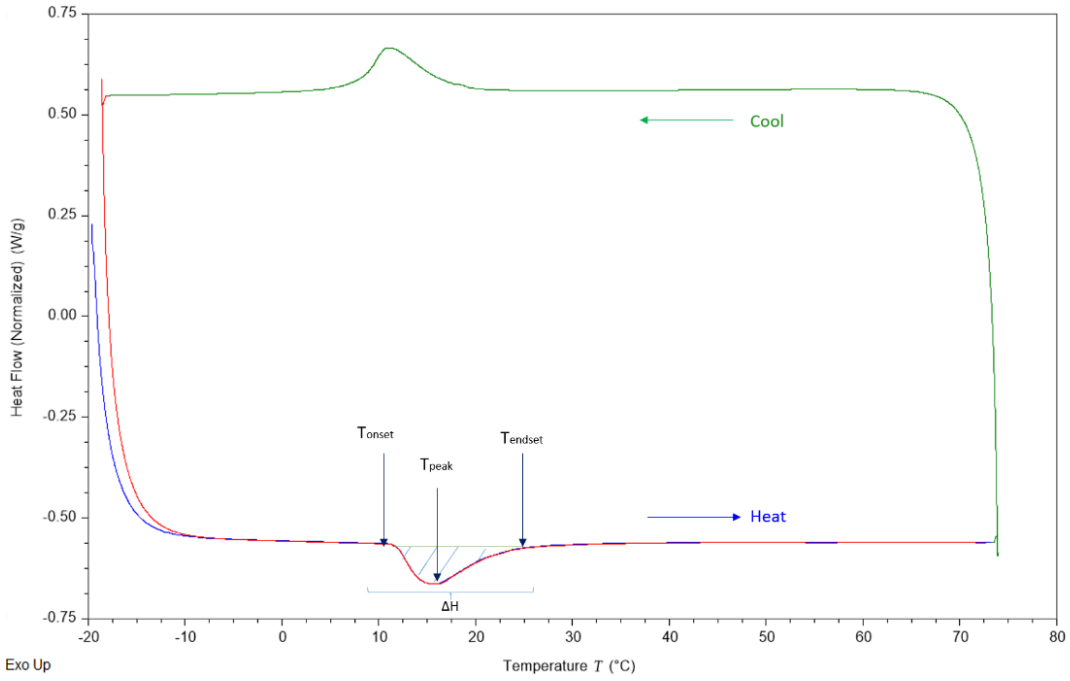

Figure 4-5 schematic of a thermogram showing Heat-Cool-Heat test on F127 20%.

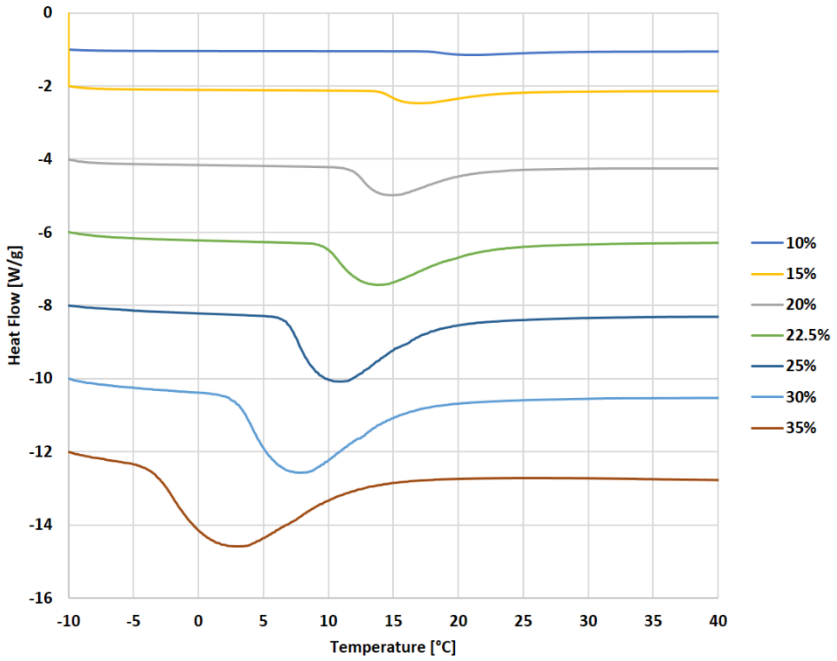

Figure 4-6 Normalised DSC thermograms for samples 15 to 35% separated vertically for clarity.

Based on the heating ramps results, four main parameters for sample concentrations of 1 to 35% are plotted in Figure (4-7). Onset and peak temperatures display linear trends, where both temperatures were reduced with the block copolymer concentration increase, as demonstrated by the 35% sample exhibiting the lowest onset compared to the highest recorded for 1%, highlighting the natural proportionally of concentration and micellisation. Similar behaviour was recorded in the cooling ramp. Upon repeating the tests, the recorded peaks standard deviation shared an average of ±0.27°C indicating excellent repeatability of experimental procedure.

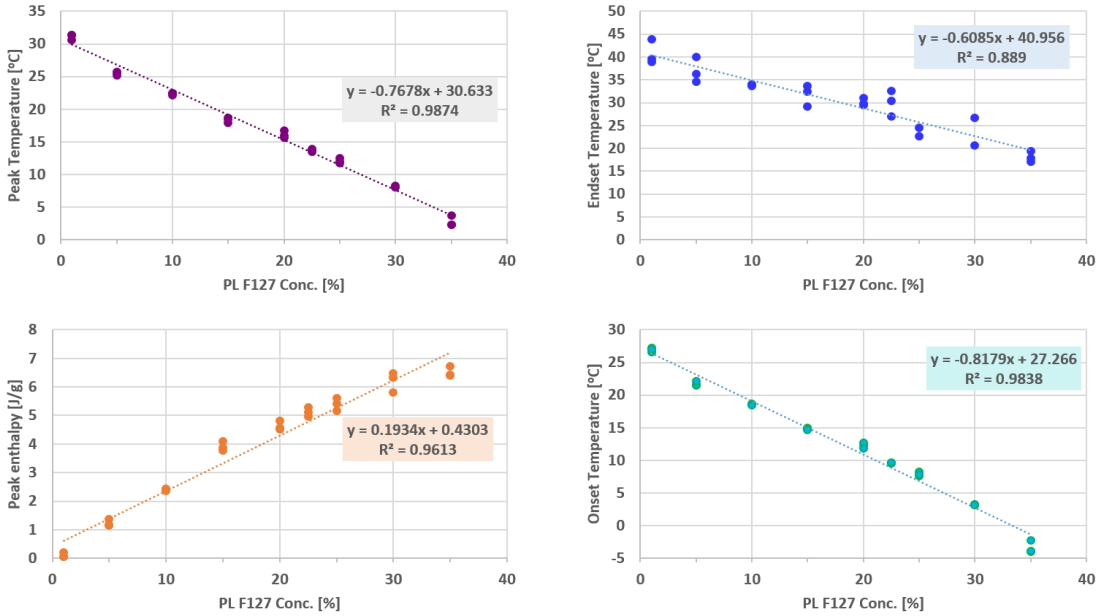

Figure 4-7 variables obtained from the different F127 concentrations thermograms, indicating onset, peak and endset temperatures. In addition to the endothermic peak enthalpies for each respective concentration.

A linear trend appears in the opposite direction for the enthalpy signal, the samples transition enthalpy increasing with the concentration in a similar trend to that observed by Pham Trong et al. (2008) and Zhang et al. (2013). Similar trends were registered for the calculated entropy values.

4.1.2.2 Modulated Differential Scanning Calorimetry (MDSC):

Standard conditions of 60 s modulation period, ±1.5°C modulation amplitude and a linear ramp of 1°C/min were used for the tests. No extra peaks other the specific micellisation peaks were detected in the MDSC thermograms - see Figure (4-8). The thermograms demonstrated that the transitional peak detected by the total signal (DSC standard) is composed of two underlying signals; Reversing and Non-Reversing heat flow. The reversing signifies changes in the system heat capacity due to the second signal of Non-Reversing heat flow symbolising the ordering (followed by crystallisation) event (Thomas, 2005).

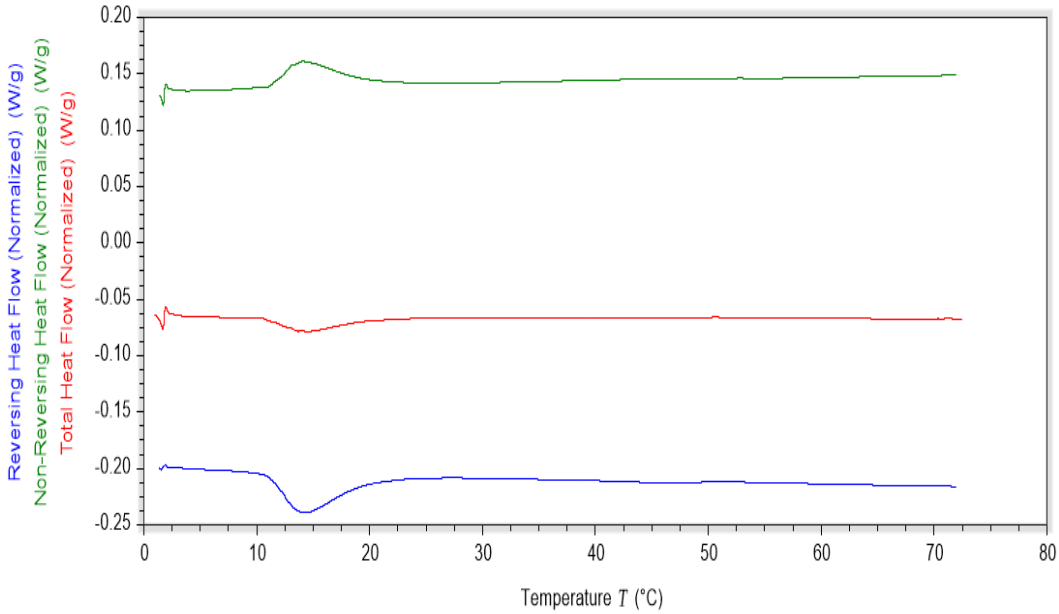

Figure 4-8 MDSC thermogram for F127 25% .

4.1.3 Thermomechanical measurements:

4.1.3.1 DSC-rheology correlation

To examine the correspondence of the data collected by dynamic rheological measurements to the static DSC ones, tests using each technique were performed using the same heating rate of 2°C/min with a shear rate of 10 s^{-1} for the rheology tests. The correlation is demonstrated in Figure (4-9) for both datasets. As per prediction, the shear viscosity experienced a reduction due to temperature response. The viscosity downward slope was getting predominate around 10°C which, parallel to the DSC detected peak's onset temperature. Both curves exhibit minimum values at 15°C before an abrupt increase in viscosity is matched by the endothermic peak T_{endset} , marking the end of transition at 25°C. This correlation held for the different concentrations tested, which validates the accurate equivalence of results acquired by two the different methods.

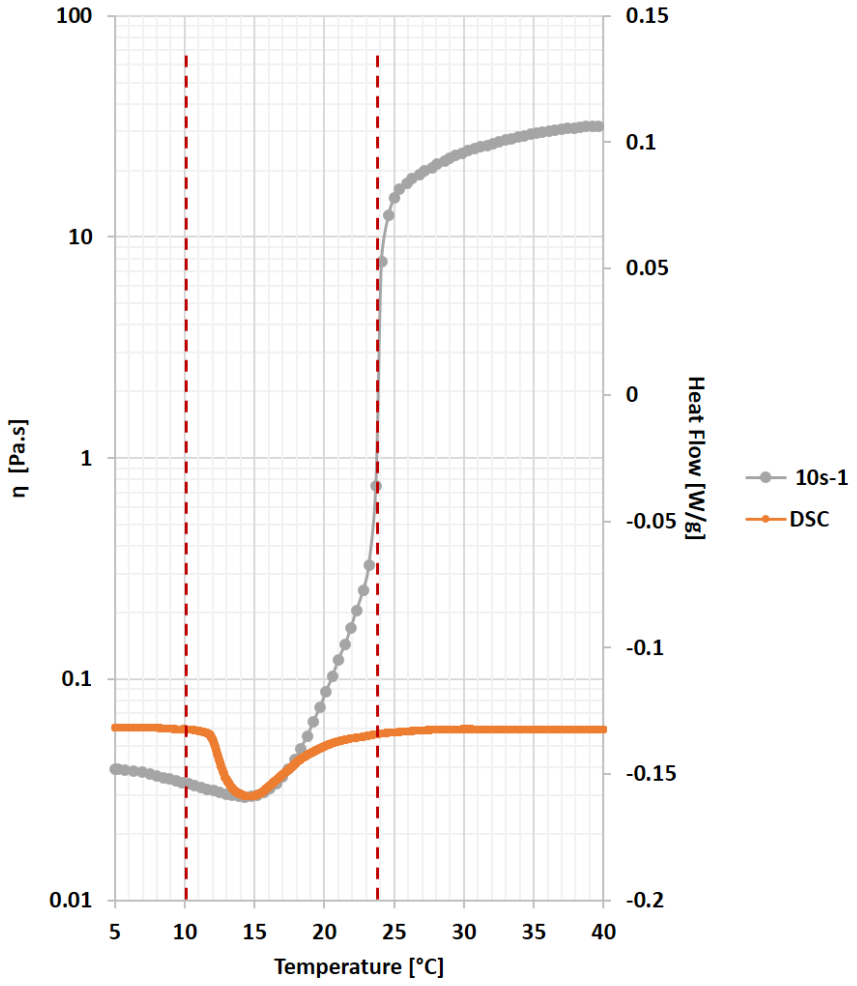

Figure 4-9 DSC and rheological tests correlation for F127 20% sample at the same heating rate of 2° C/min.

4.1.3.2 Sheared sample measurements:

To investigate the sheared structures stability after shear cessation, DSC runs of the sheared gels were conducted. The samples were sheared at constant rates and temperature ramping from 0 to 40°C. Following the rheological test termination the gels were held at 40°C allowing enough time to collect and run DSC tests on multiple specimens of the sample. For these measurements the temperature ramps were modified to start from 40 to -20°C before starting the heating and another cooling cycle. Only samples with defined structural transitions were tested for a minimum of three times, the range included 15-35% F127 concentrations. Figure (4-10) shows two DSC runs of two sheared and static samples of the same concentration.

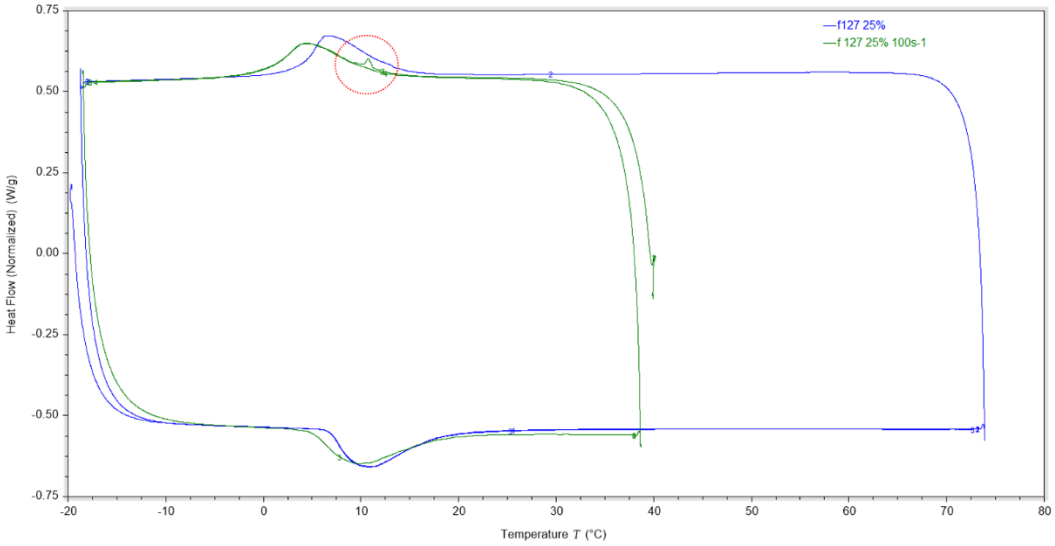

Figure 4-10 DSC thermograms for two different samples, blue static and green after the application of shear at 100 s^{-1}.

During the cooling step the sheared samples displayed an extra small peak contained within the usual exothermic peak which disappeared after heating the gel and didn't reappear in the second cooling step. This is marked with a red circle on the Figure. No correlation was found between the shear rate and the peak size or enthalpy - see Figure (4-11). However, multiple factors could have affected the results accuracy i.e. either during the specimens' collection from sampling site within the concentric cylinder, waiting/loading time and very low enthalpy values bordering the DSC limits of detection. Samples containing 15% were difficult to load since they revert back to the sol state rapidly at room

temperature and when the tests were conducted the characteristic peak detected in higher concentrations was absent.

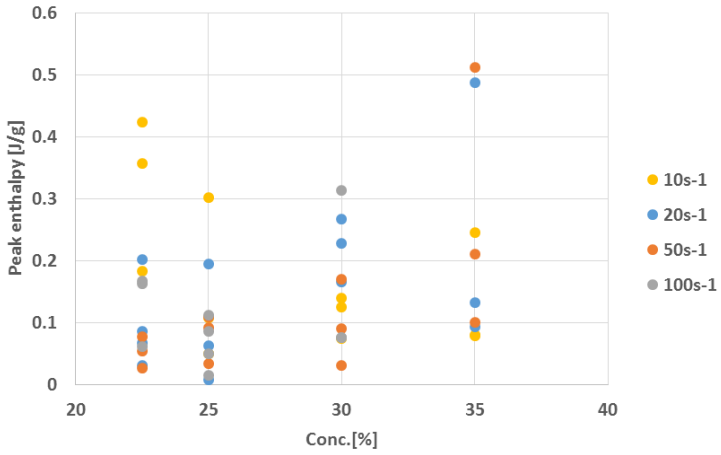

Figure 4-11 Enthalpy values of the shear exothermic peak recorded after applying different shear rates (10-100 s^{-1}), multiple points indicate the test repetitions.

The appearance of the peak implies that a structural change was introduced by the imposed shear – though small it may be enough to disturb the natural packing order of the micelles in the gel matrix as observed in non-sheared samples. The absence of the peak in the 15% concentration samples and its disappearance in higher concentrations in the second cycle confirms its temporal nature and the reversibility of the shear imposed change, therefore confirms the detectability of shear induced structures in F127 gels.

Complementary MDSC runs were performed but the signals recorded looked similar to the DSC thermograms and didn't unveil extra information as seen in Figure (4-12).

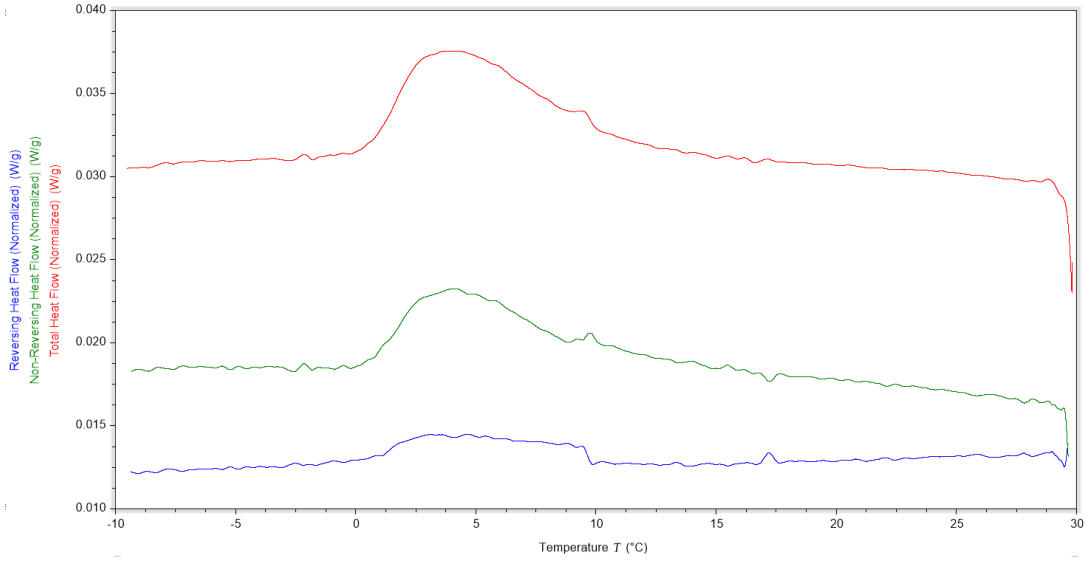

Figure 4-12 MDSC thermogram for F127 30% sheared at 100 s^{-1} prior to test. Test conditions: modulation amplitude 0.02, period of 40 seconds and heating ramp of 0.5°C.

4.2. Rheology Results of Neat F127:

4.2.1 Steady Shear

4.2.1.1 F127 Temperature ramps at constant shear:

Samples were subjected to four tests with constant shear rate values of 10, 20, 50 and 100s^{-1} while ramping the temperature from below the gelation transition range to 40°C. These results are plotted in Figures from (4-13) to (4-15) as functions of shear rate and the neat gel's concentration.

Figure (4-13) shows concentrations from 0 (pure water) up to 10% F127. The formulations tested are clearly in solution state, showing viscosities relatively comparable to water's viscosity with generally unchanging behaviour under different shear rates applied. The sample of 0.1 % concentration appeared to exhibit a lower viscosity than water indicating drag reducing properties of the polymeric solution, with a notable increase in viscosity with increasing the applied

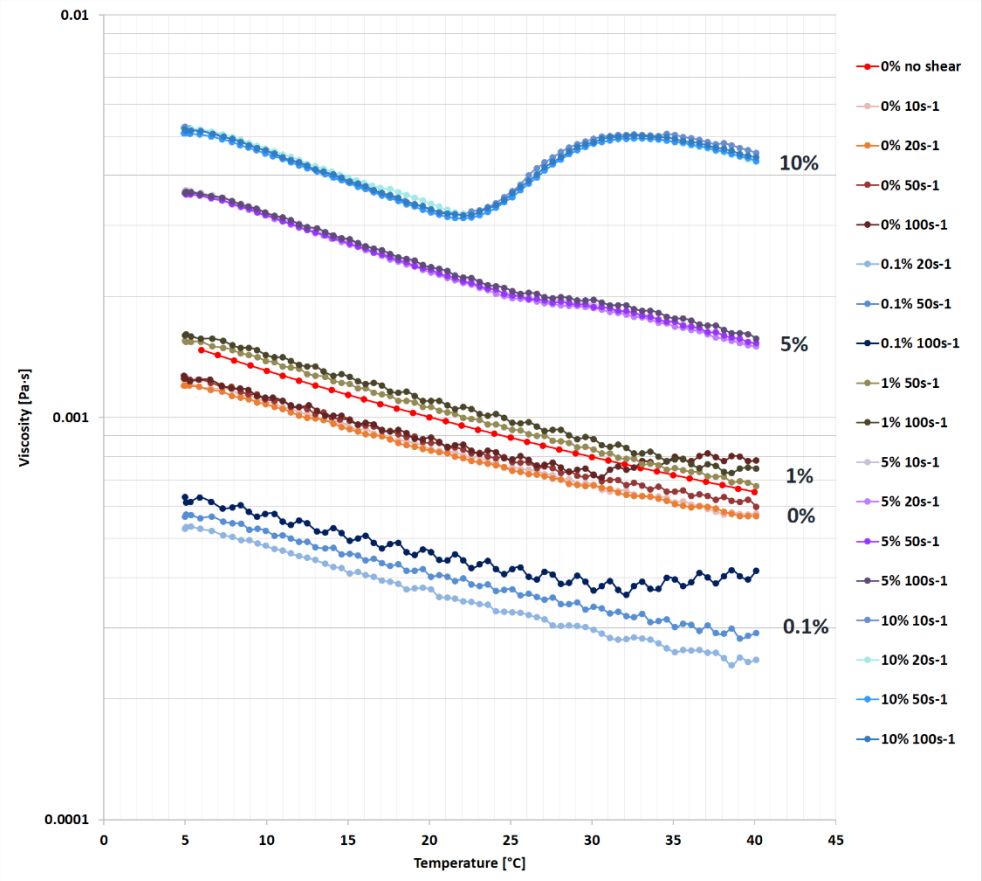

Figure 4-13 F127 Temperature ramps at constant shear rates on sample concentration 0 to 10%. Pure water's no shear viscosity values are the standard values recorded at different temperatures (Anton-Paar, 2018).

shear rate across the temperature range but this correlation was lost when the copolymer concentration was increased to 1%.

The viscosity of solutions containing 1 to 5% is reduced with temperature but lack any shear response, therefore can be considered Newtonian fluids. As F127 concentration was increased further to 10%, the standard viscosity reduced to a global minimum around 22°C, followed by a recovery to the initial viscosity range around 31°C.

As shown in Figure (4-14), with concentration increase the flow curves separate into three regions based on viscosity values; low, transitional and high. Sample 15% exhibits Newtonian behaviour at low temperatures, indifferent to the applied shear rate. Until a similar but sharper temperature response to the one observed in 10% at 20°C is then recorded demonstrated by viscosity reduction, followed by a tenfold viscosity increase. At 28°C the formulation undergoes an abrupt increase in viscosity followed by multiple bifurcation at 29°C indicating that a rheological transition is taking place correlating with the applied shear rate values.

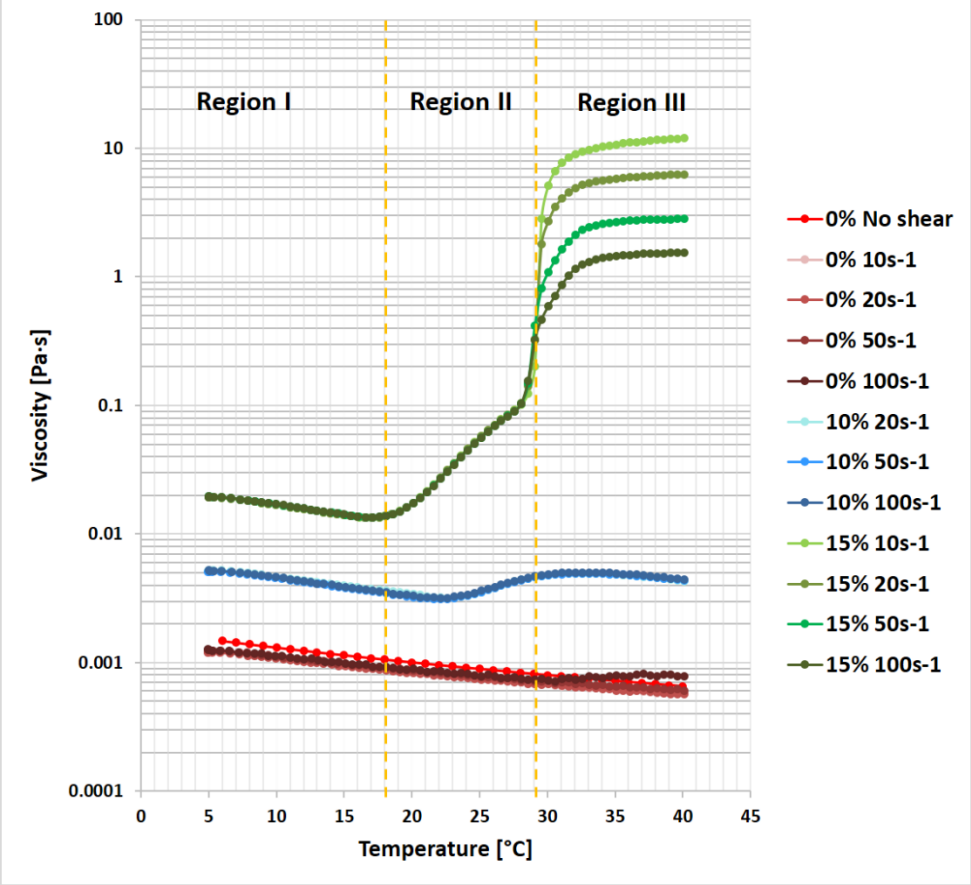

Figure 4-14 F127 Temperature ramps at constant shear rates on samples concentration 0, 10 and 15%.

Up to this concentration, all the different applied shear rates resulted in identical viscous responses.

However after 29°C, the sample exhibits a shear rate dependency that is maintained through the rest of the ramp, with lower viscosity values corresponding to higher shear rates.

The final viscosity differences between the highest and lowest shear rates are quantified by a whole decade, confirming the shear thinning behaviour of the system. From this stage the viscosity values remain constant within the same applied shear rate run until the end of the ramp, indicating that a final stable state has been reached, which is slightly temperature dependent as evidenced by a slight upward slope.

Figure (4-15) shows the viscosity measurements for concentrations from 15 to 35%. The same temperature and shear rate dependency for sample 15% persists across the rest of the formulations in respect to the concentration gradient, where

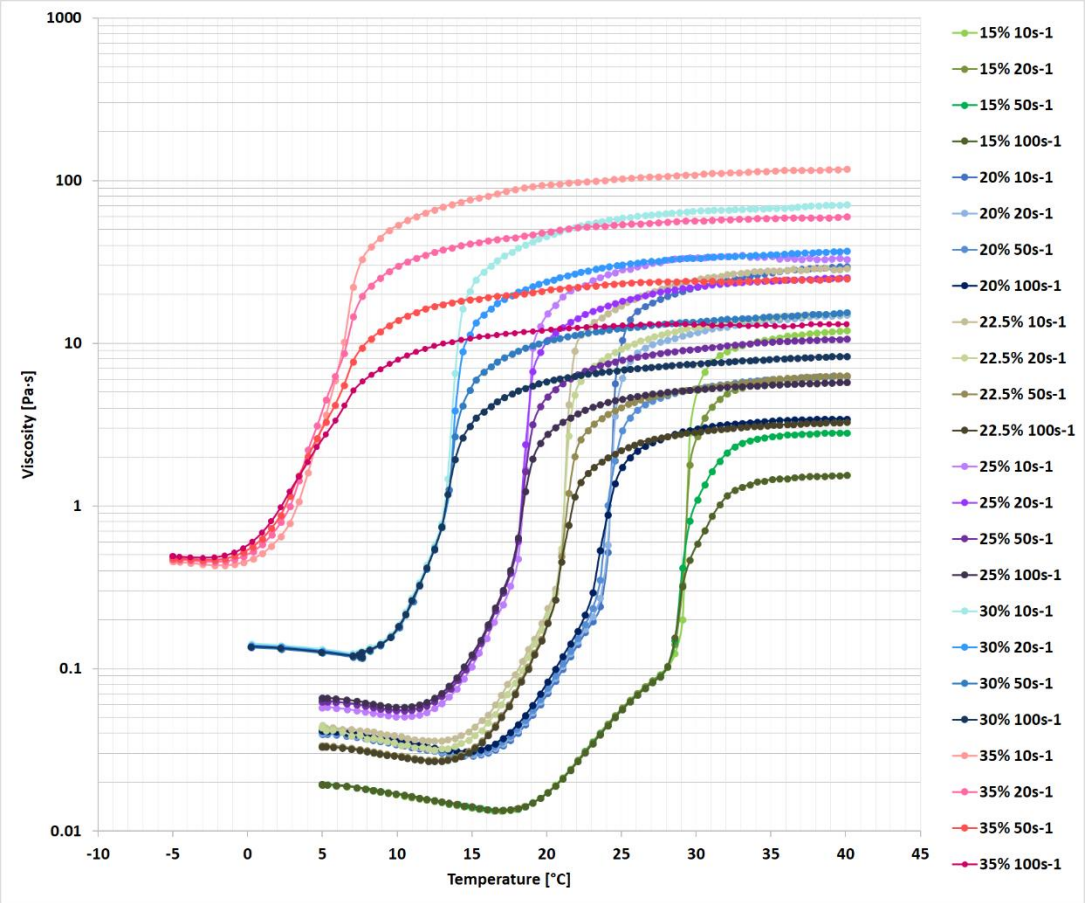

Figure 4-15 F127 Temperature ramps at constant shear rates on sample concentrations 15 to 35%.

the solutions undergo a minimum followed by an increase in viscosity as the ramps continue to reach a pivotal point where the system viscosity depends on the shear rate applied. The concentration was found to determine; a) the initial and final viscosity values, b) the shift in the transition 'onset' leading to the phase change in the polymeric matrices.

Naturally, the samples containing higher copolymer fractions have higher viscosities in both the low and high temperature regimes and experience earlier transitions than their lower counterparts. Additionally, the transition in the higher concentrations flow curves is smoother and occurs over two stages rather than three as noted for the 15% sample.

Two prominent thermal events can be elucidated from the flow diagrams of 15 to 35% concentration samples: those responses correspond to the micellar association taking place in the system, which is due to the increasing attraction forces bringing micelles together that grow promptly to form the new gel structure. The phase change is confirmed by the different rheological properties of the starting micellar fluid and the final matrix displaying higher viscosity values (three decades difference) and clear shear dependency demonstrated by the shear thinning behaviour with increasing the shear rate at identical thermal conditions, where $\eta_{10s^{-1}} > \eta_{20s^{-1}} > \eta_{50s^{-1}} > \eta_{100s^{-1}}$.

The critical points marking the transitions for each concentration are plotted in Figure (4-16), both plots quantifying the temperature and shear dependency of the systems and their proportionality to concentration.

For all the these tests, the samples were run in cycles of shear rates starting from the lowest shear values (10 s^{-1}), followed by cooling to erase the imposed shear history for 15 minutes allowing the formulation to revert back to the sol state and guaranteeing homogenised cooling inside the cylinder, before running the sample again at a higher shear rate and so forth.

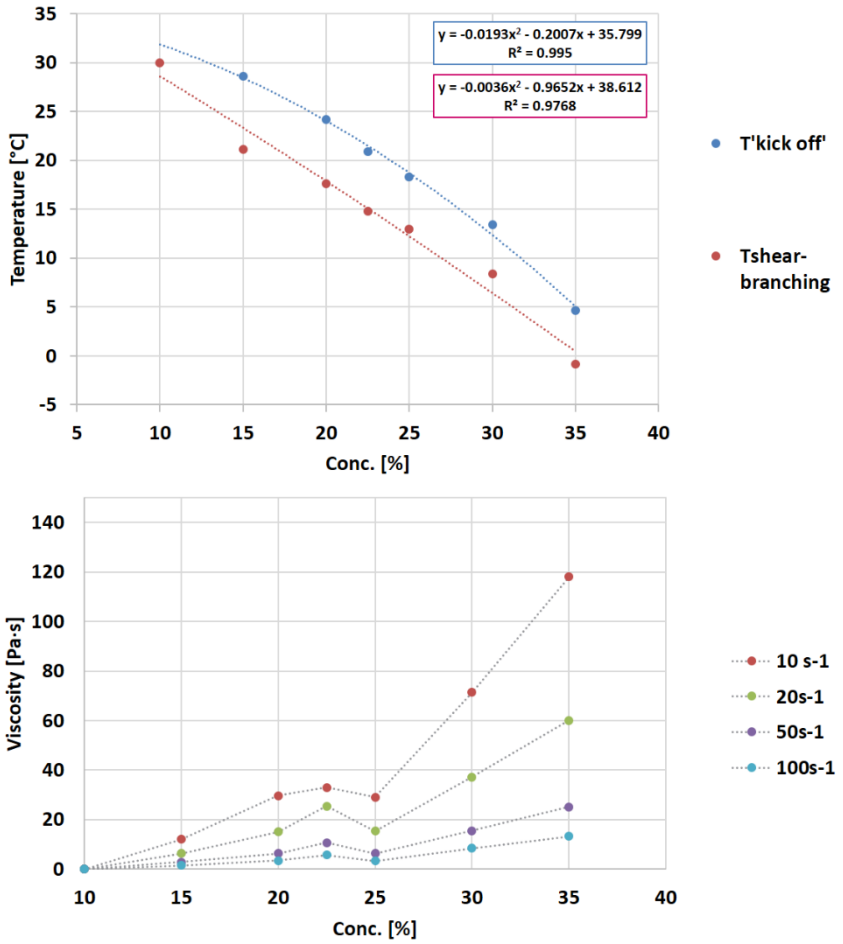

Figure 4-16 The critical points marking the transitions for temperature ramp results under constant shear plotted as function of temperature (top) and viscosity (bottom).

4.2.1.2 Shear rate ramps:

This is a complementary test to the one presented earlier to investigate the rheological behaviour at ramping shear rates and constant temperature. The formulations were tested at two temperatures; below gelation (0°C for high concentrations 30 and 35% and 5°C for rest of formulations) and above gelation (37°C) to study the material's responses at extreme conditions of sol and gel. Concentrations of interest were chosen based on the results from the previous tests, where the formulations chosen exhibited both shear and temperature responses with variable mechanical strength.

In Figure (4-17) samples were sheared at rates from 0.001 to 1500 s^{-1} at temperatures below their gelation onset - based on the data from Figure (4-15). All concentrations tested appear unstable in both plots of shear stress and

viscosity at shear rates below 1 s^{-1}. According to their response to shear rate, the formulations are divided into two groups; from 15 to 22.5% and 25 to 35%. Within the two groups we notice two distinctive behaviours; at low shear and high shear rates, from 0.00≤1 $\dot{\gamma} \lesssim$1 s^{-1} and 1$\lesssim \dot{\gamma} \leq$1500 s^{-1}, respectively.

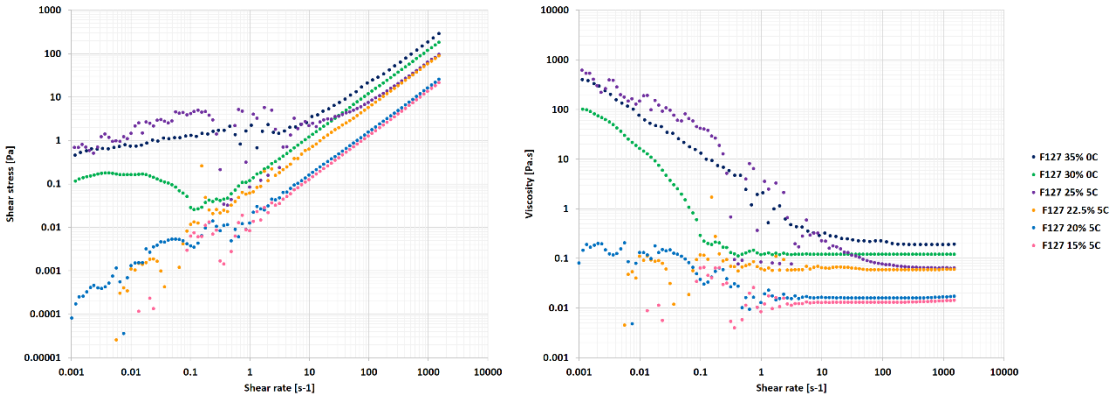

Figure 4-17 F127 shear ramps at 5°C on sample concentrations 15 to 35%.

Below 1 s^{-1} the results show clear instabilities that disappear above a critical shear; these shear instabilities observed can arise from multiple processes interplaying within the system's internal structure, applied shear and interactions at the measuring system interface.

At low shear rates, the lower concentrations experience breaks in flow curves and show contrasting flow behaviour to the higher concentration behaviour. Based on the complete curve recorded for sample 20%, the low concentration group exhibits low yield stresses at shear start-up, followed by shear thinning that stabilises above a critical value. The recorded data continued to fluctuate and break until the viscosity plateaued at around 1 s^{-1}. This confirms the appearance of localised shear heterogeneity in the gap. According to Barnes (1995) these concentrations are experiencing wall-slip before exceeding a critical shear rate and reaching steady state.

On the other hand, the high concentration group (25-35%) flow curves show higher stability and considerably enhanced yield stress values at low shear rates until the stress reaches a constant value and plateaus (25% is slightly off the trend at start-up but exhibits the same overall behaviour). After the critical shear rate, the three concentrations viscosities decrease with shear rate indicating

shear thinning in a similar fashion to lower concentrations, showing the behaviour of a yield stress fluid (Barnes, 1995).

When a complex fluid is sheared inside a smooth Couette cylinder, inhomogeneous flow at low shear rates will appear resulting in wall-slip. The slip layers are formed near the inside of the MS near the inner cylinder, where the shear rate is at its highest value and the shear gradient is moving toward the outer cylinder. In our case, for a yield stress fluid, as the shear rate increases the two regions of sheared (inner cylinder) and un-sheared bulk (outer cylinder) are homogenised and the observed viscosity decreases.

The second set of runs were carried out at 37°C. Figure (4-18) shows plotted results. The same concentration factor is evident as before. The viscosity graph shows clear shear thinning from the beginning until the end of the test. A further look at the stress strain graph confirms the thinning behaviour and reveals that the materials undergo several transitions during the ramp.

The shear stress values overshoot to reach an inflection point at shear stress τ_0, followed by a transient plateau around mid-range shear rates, before the recorded shear stress values start rising at higher shear values ending in upward slopes.

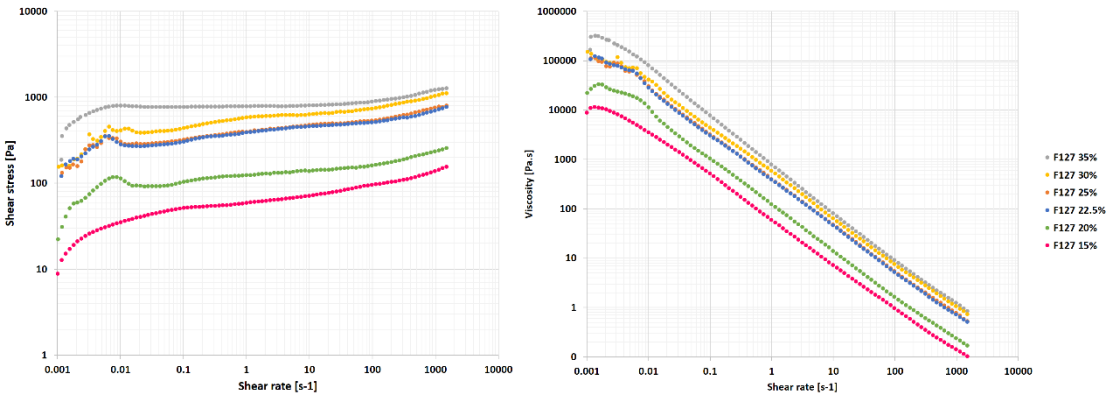

Figure 4-18 F127 shear ramps at 37°C on sample concentrations 15 to 35%.

All the samples can be described as yield stress-shear thinning materials and can be generally described in the terms of the Herschel-Bulkley model $\tau = K\dot{\gamma}^n + \tau_0$. However, in practice neither this model nor its extension with added infinite viscosity term η_∞ , $\tau = K\dot{\gamma}^n + \eta_\infty\dot{\gamma}^n + \tau_0$ provides a good fit to the non-monotonic curves for multiple reasons (Madlener et al., 2009). Herschel-Bulkley does not

take into consideration the shear heterogeneities causing behavioural changes due to shear banding with the characteristic two critical shear bands at low and high rates. Pictures after the test showed the formation of white rings around the rotating bob that remained stable until the sample was cooled again. These are macroscopic manifestations of shear bands migrating from high shear to low shear regions and can be observed in Figure (4-19). This transient behaviour has been recorded in many complex fluid systems of liquid crystals (Larson, 1998) and Pluronics (Manneville et al., 2007).

In Figure (4-20) a schematic shows the two types of shear heterogeneities the system undergoes.

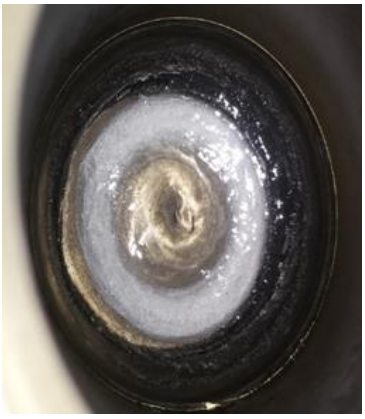

Figure 4-19 A photo of the Couette after the application of the shear ramps at 37°C on F127 20%.

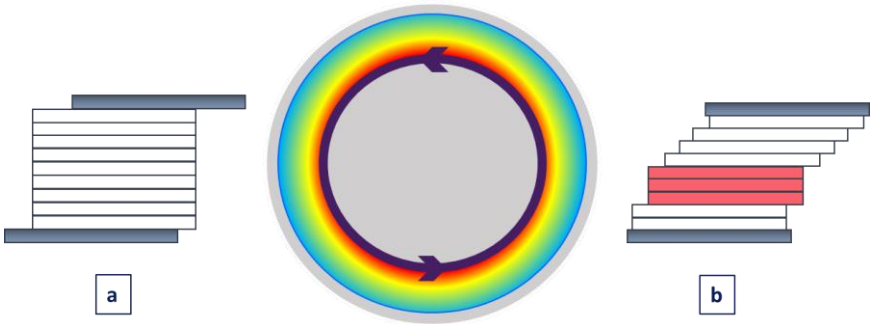

Figure 4-20 schematic showing two different shear heterogeneities rising inside a Couette cylinder with smooth walls during the application of shear rate; a) wall-slip and b) shear banding.

The data collected using the shear ramps is essential for both processing and formulation administration. The wall slip is strongly material dependent, it appears in both capillary and Couette geometries and correlates to the geometry's gap and roughness. More detailed information is required about the underlying origin of the slippage, which is usually performed using multiple cylinders following Mooney's method. In our case, slippage only appears in the sol state, but our description of the sol state is in truth very simplistic that does not take into consideration the micelle's state in the solution. However, in this study, higher shear rates will be applied than those expected for the appearance of slippage.

4.2.2 Oscillatory shear

4.2.2.1 Amplitude sweeps:

The first set of these tests was performed at 5 and 37°C to determine the LVE range limits to ensure that no irreversible destruction would be applied to the samples in the rest of the oscillation tests. The LVE limit was determined by the dynamic moduli from their LVE plateau values. Plots in Figures (1-21) show the same trends where the LVE is pushed to higher strains as Pluronic concentration and temperature increase.

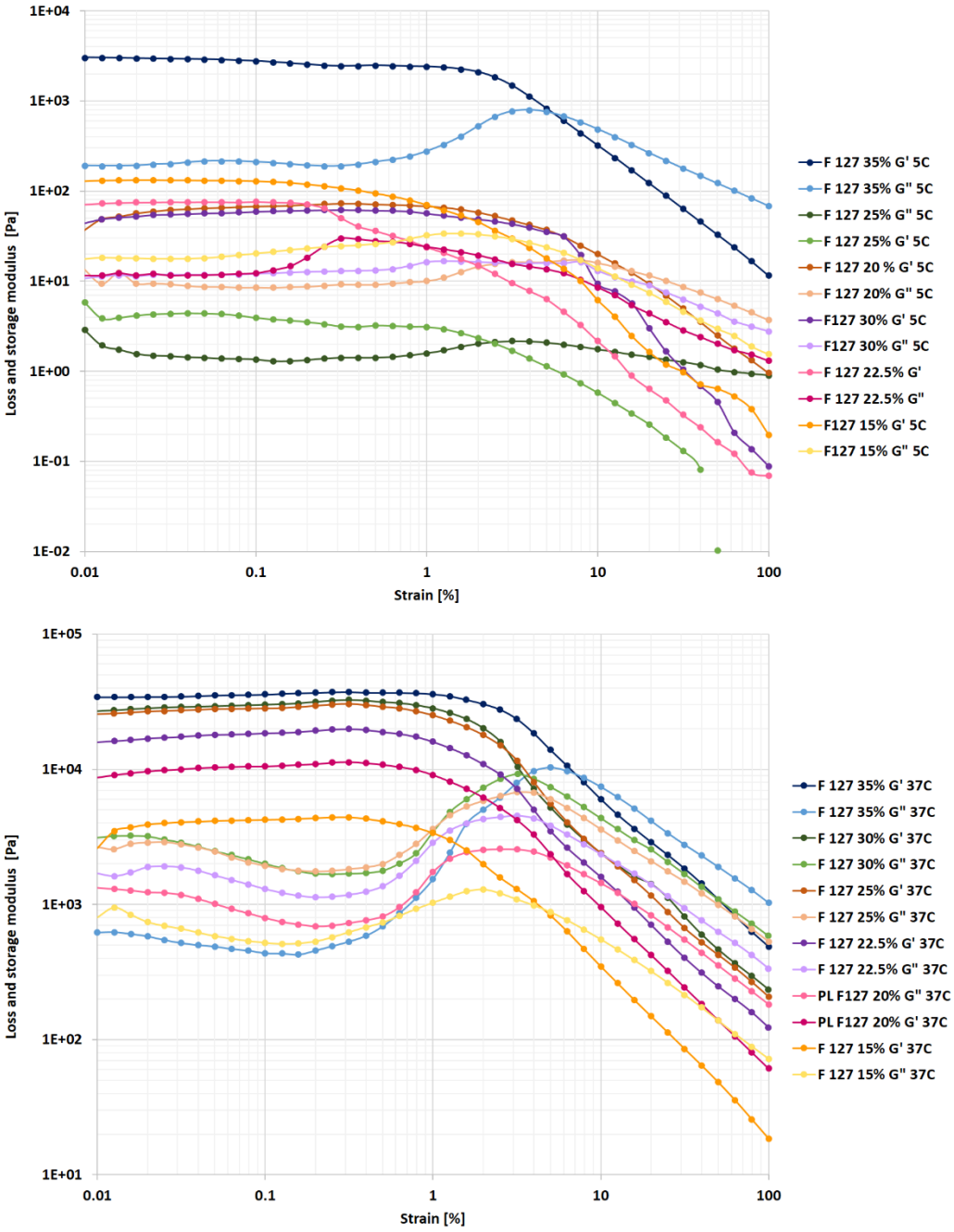

Figure 4-21 F127 amplitude sweeps result at: 5 (top) and 37°C (bottom).

The γ_L value was chosen to be 0.2% to allow extra freedom limits when temperature sweeps were performed.

4.2.2.2 Temperature Sweeps

Using the same heating rate as for the rotational mode temperature ramp tests the oscillation tests were conducted to further understand the material behaviour and to confirm the gelation transition point.

Two temperature ramps were performed at fixed strain and frequency (γ = 0.2%, ω = 10 rad/sec), one from 0 to 40°C and an extra set of tests with extended temperature range 0 to 100°C to determine the gel boundaries.

T- Sweep to 45°C

The dynamic shear moduli results for the first set are plotted in Figure (4-22) showing samples with concentrations from 10 to 35%. The results affirm the constant shear ramp results regarding the 10% sample's lack of phase change during the ramp as demonstrated by the moduli's parallel behaviour across the temperature range investigated. Interestingly throughout the whole ramp G' dominates albeit with a very small margin.

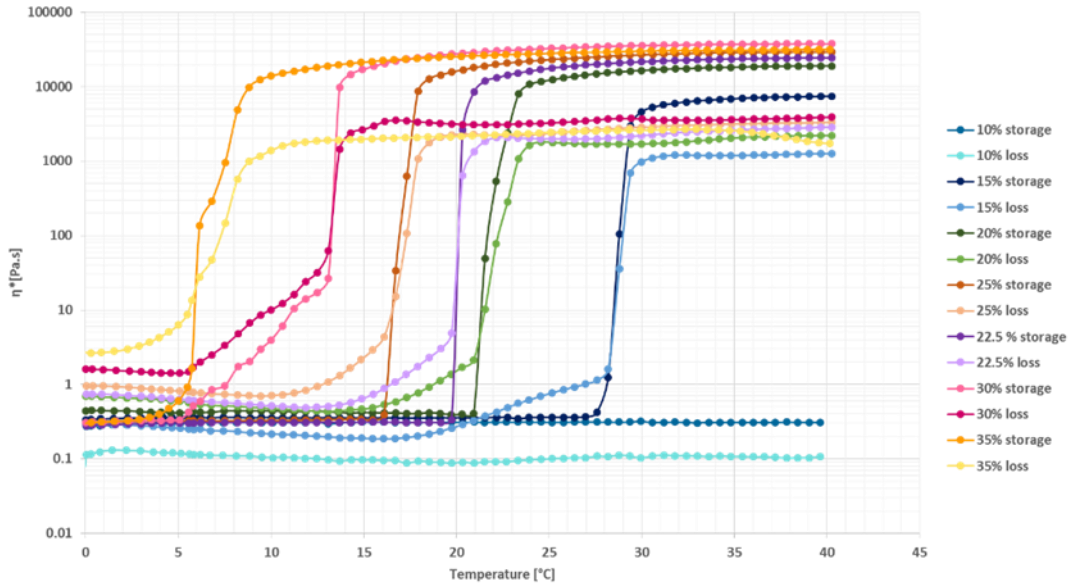

Figure 4-22 F127 temperature ramps under oscillatory shear from 0 to 45°C.

The early measuring points of dynamic moduli values from F127 25 to 35% show that G" have values higher than G', both moduli values increasing gradually until a critical temperature, where G' and G" cross. This is followed by a G' build-up

to exceed G" and stabilize in a plateau for the rest of the test. Plotting the results in damping factor, $tan\ \delta$ ($tan\ \delta$=G"/G') format allows the accurate determination of the crossover point where $tan\ \delta$ =1.

Values of $tan\ \delta$ are plotted as a function of F127 fraction in Figure (4-23). Initially, the gels damping factor exhibits a concentration dependent trend, until a maxima is reached that plummets to reach unity. A further drop follows to a concentration related low value that remains constant until the test is finished, indicating unchanging behaviour after gelation when the elastic modulus dominates. The critical temperatures where $tan\ \delta$ =1 were determined from the plots, except for 10% which did not show any signs of gelation and 35% where the transition was so abrupt (between 5.7 and 6.1°C) it wasn't possible to precisely determine the actual point under this experimental conditions.

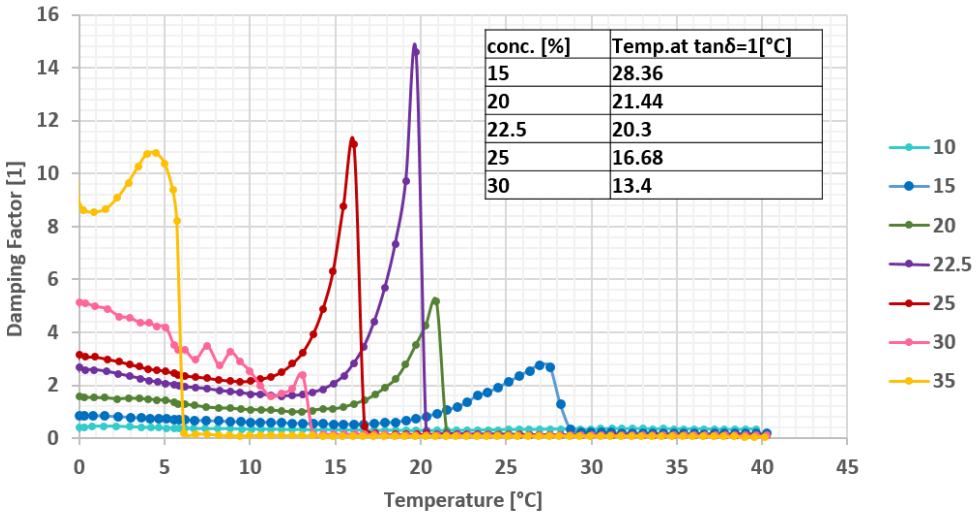

Figure 4-23 $tan\ \delta$ values during the temperature ramp under oscillatory shear.

Ramp to 100°C

The complex viscosity results of higher temperature runs (up to 10°C) are plotted in Figure (4-24). The first half of the ramp up to 50°C is similar to those what have been acquired for sweeps up to 45°C (η* data not shown) as expected. Further increases in temperature leads to complex viscosity reduction - indicating that a structural weakening. These results correlate to published data by the BASF technical paper on Pluronic F127 concentrations from 15-25% in Figure (4-25), which was performed in the rotational mode, though no recorded final viscosity data were published.

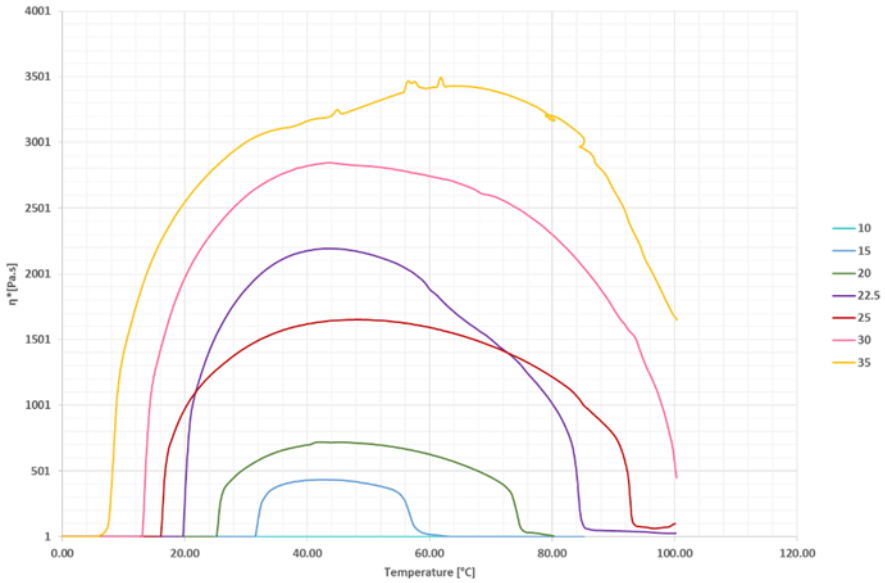

Figure 4-25 F127 complex viscosity values during the oscillatory shear ramps.

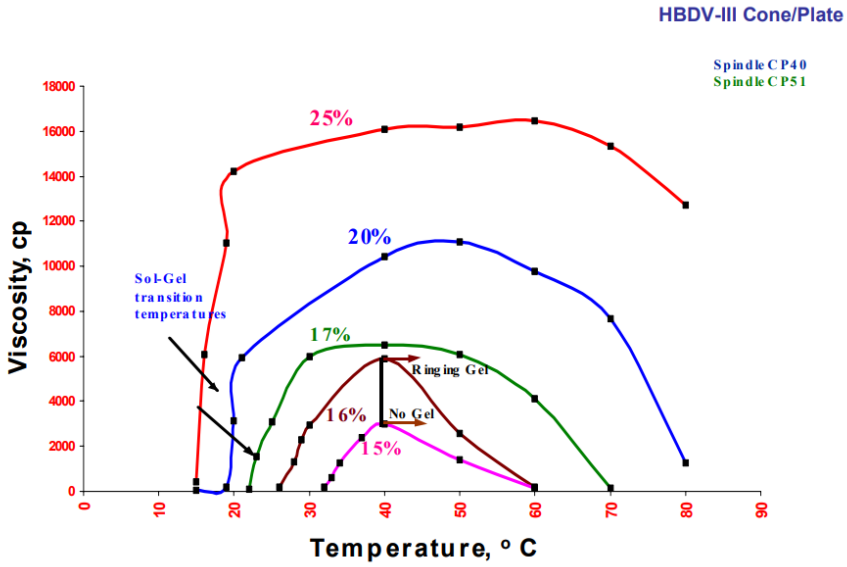

Figure 4-24 F127 viscosity as function of temperature and concentration (BASF, 2004).

The same trend can be seen in the dynamic moduli graphs in Figure (4-26). Here the storage modulus dominates over the loss modulus until 50°C, then both moduli drop approximately two decades. For 15% the dynamic moduli values fall to reach a small plateau (where G' still dominates) indicating structural softening and continue decrease to reach the same initial values recorded at the beginning of the test at 0°C, where G"> G' indicating that the formulation is regaining the solution state. However, this complete drop was not reciprocated by the rest of the gels.

The rest of the formulation's moduli decreased with increasing temperature to exhibit the same plateau stage 15% showed where G' is still higher than G", the samples moduli values showed a negative slope indicating a possible fall below the plateau values at higher temperatures. The width of plateau (representing the gel boundaries) was observed to depend on the F127 content, where higher concentrations had a broader range starting at the gelation transition as represented by the shear moduli surge and ending with their fall, demonstrating softening or melting.

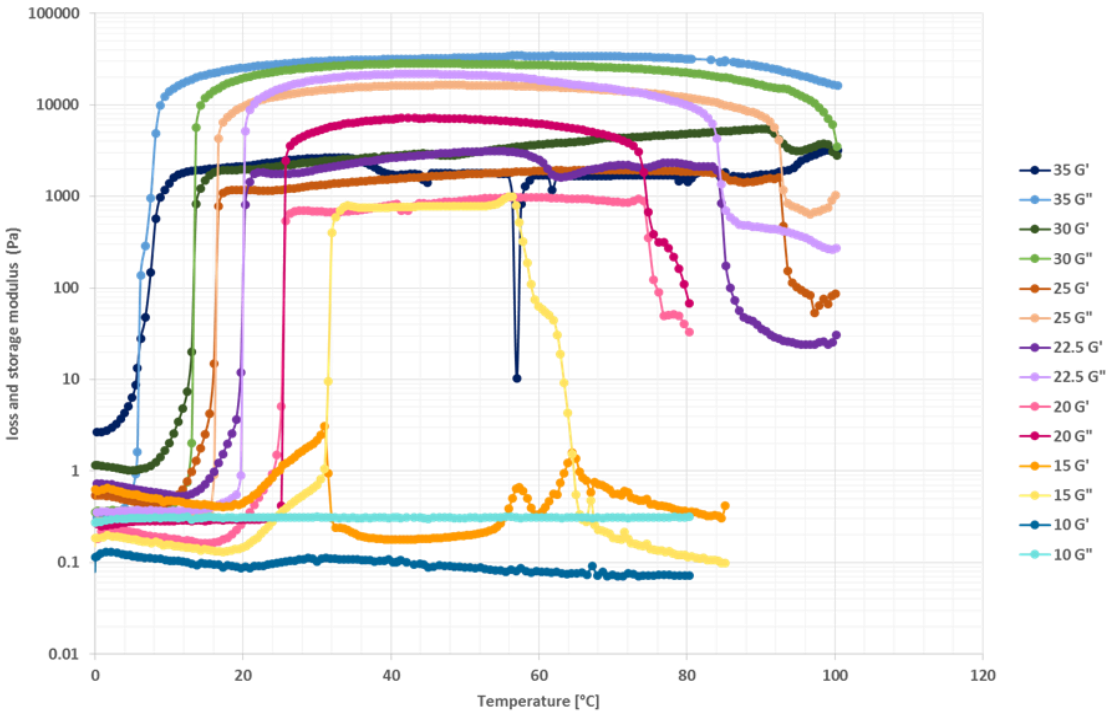

Figure 4-26 F127 10-35% dynamic moduli values during temperature ramp.

4.4.2.3 Frequency sweeps:

The sample frequency sweeps were run at 37 °C from 0.001 to 100 rad/sec. The gels showed overall dominance of G' across the tested frequency range as seen in Figure (4-27). The loss modulus for the sample increases toward the low frequencies, where the difference between the moduli is at its lowest. However, only the sample containing 15% showed a cross-over point at ω = 0.0056 rad/sec. It was clear that if the relaxation frequency existed it will appear in the lower spectrum than that accessible by standard tests, indicating a long relaxation time. As suggested in the literature the gels show weak frequency dependency if only the higher frequencies were inspected. Taking measurements has proven very difficult even with optimised tests and long measurement times at the lower end as instrumental noise continues to appear around the crossover's predicted range. The sample's complex viscosity showed power law shear thinning behaviour regardless of the running time across all concentrations. The elastic response of concentrations higher than 15% was found to follow $G' \sim \omega^{\beta}$, where the exponent β was 0.05 and G"/G'~ 0 (0.1), two predominate features common in soft glassy materials (SGM) (Chen et al, 2013).

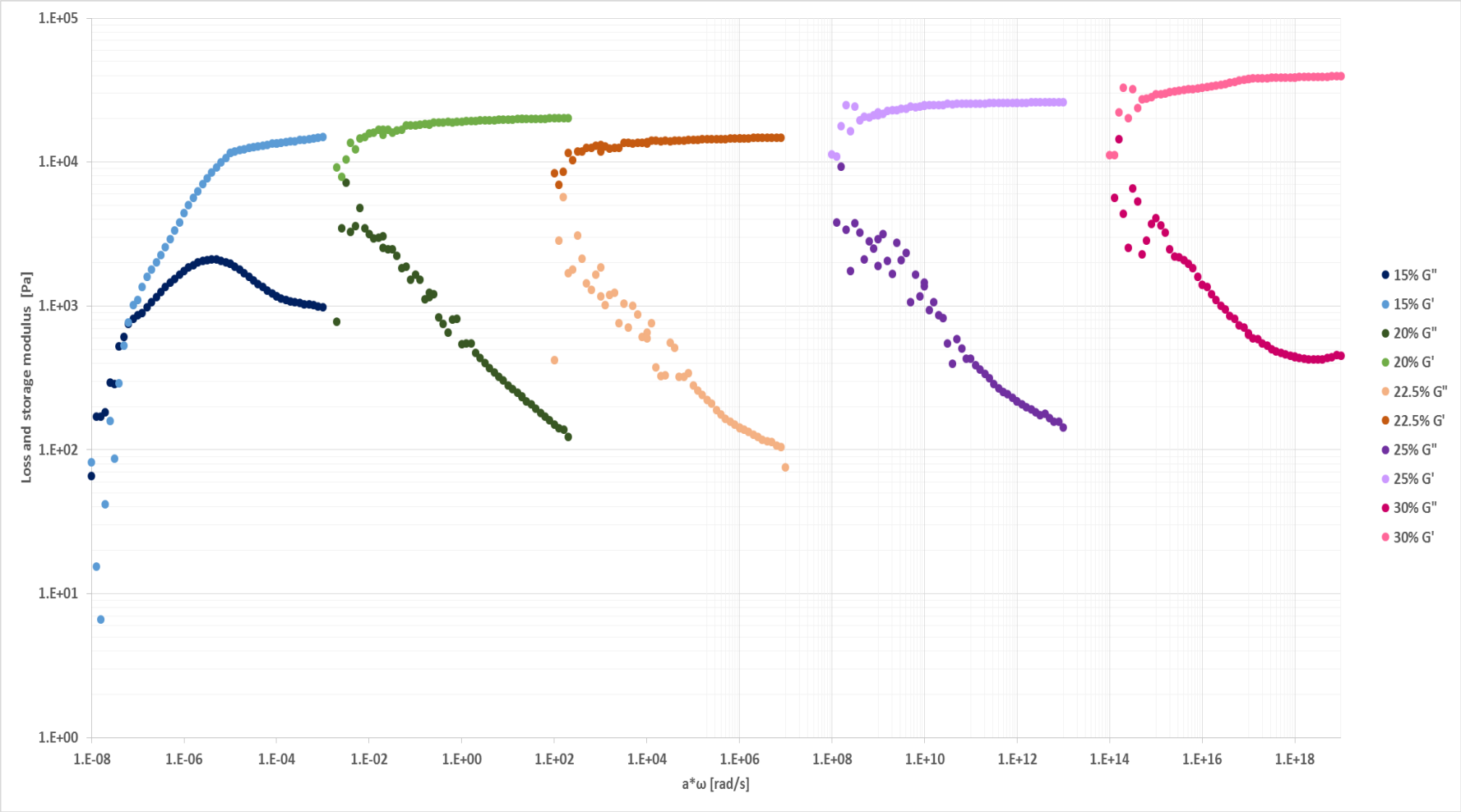

Figure 4-27 F127 dynamic moduli values during frequency sweeps, plots have been shifted for clarity.

4.2.2.4 Relaxation tests:

The relaxation modulus was acquired using a strain step value of 0.2% at 37°C. The results in Figure (4-28) showed an overall trend of exponential decay - although with increasing concentration the decay is flattened to plateaus with no indication of complete relaxation within the experimental conditions, proving relaxation to be a long and slow process within the linear viscoelastic range. The 15% sample shows a clear decay that flattens as the test proceeds. A similar system demonstrated analogous behaviour for results in the LVE region (Hamley, 2005).

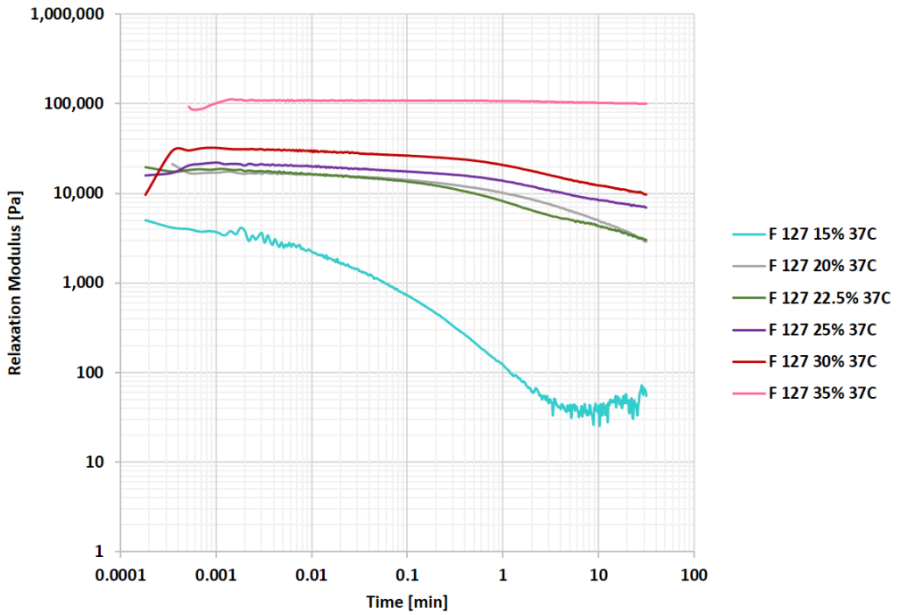

Figure 4-28 F127 relaxation modulus values after step-strain test at 37°C.

For viscoelastic liquids Relaxation time λ Maxwell model is reached if the initial stress τ ($\tau = \tau_{max}$ at $\lambda = 0$ [s]) has decreased to 36.8% after the step strain test. Based on the acquired results, all the formulations have reached this percentage except for 35%, where relaxation time increased a function of concentration as seen in Figure (4-29).

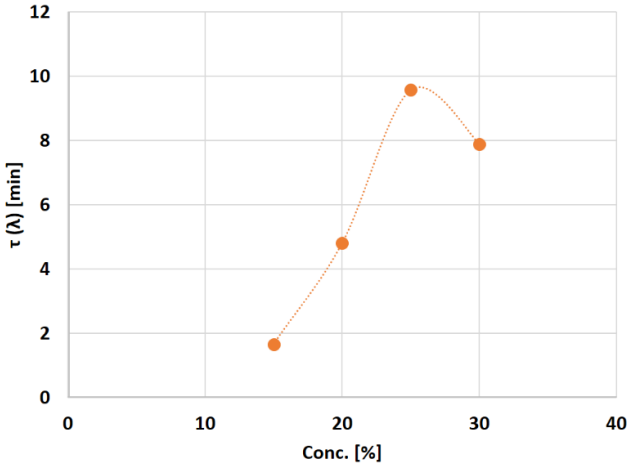

Figure 4-29 F127 relaxation time values acquired form step strain tests as a function of concentration at 37°C.

Attempts to obtain crossovers point have led to apply a reverse analysis on the relaxation data by calculating the dynamic moduli values from the relaxation modulus using two different methods. The first method utilised the Anton Paar's Rheoplus analysis method and the other using 'I-Rheo' based on Fourier transform (Tassieri et al., 2016) - shown in Figure (4-30).

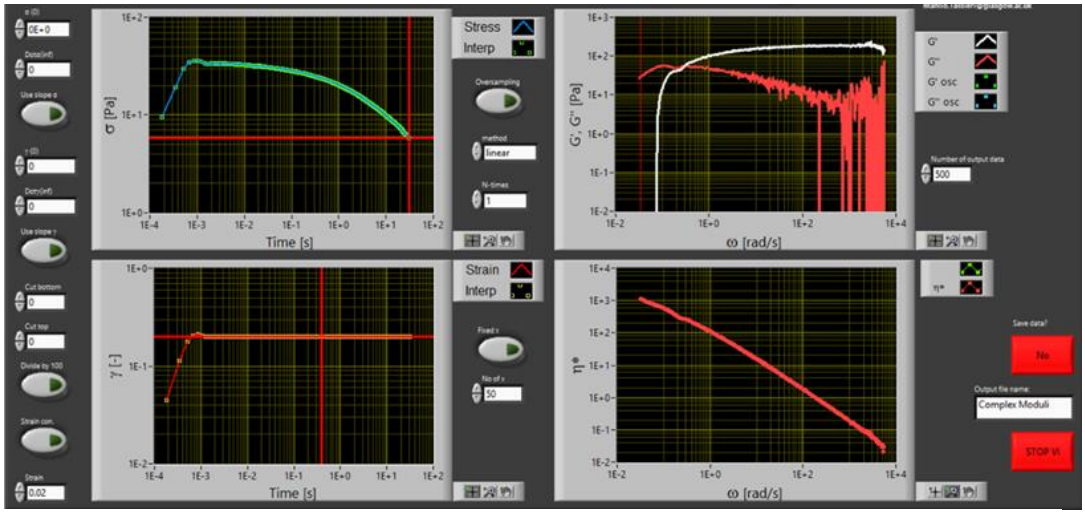

Figure 4-30 Screenshot of I-Rheo dynamic moduli output for F127 gel sample.

Plots in Figure (4-31) show the three frequency sweep results for 15% and 30% using the two methods; measured and the two sets generated from relaxation data using I-Rheo and Rheoplus. The moduli values generated from I-Rheo were noisy especially at low concentrations but when the analysis showed crossover points, they were within the experimental range tested by frequency sweeps which showed no crossovers. The dynamic moduli values calculated by Rheoplus where closer to the values measured from the frequency sweeps. For sample

15%, the terminal G' values for the different methods were close. The results from Rheoplus predicted two crossover points at mid- and low range, compared to just one value from I-Rheo. As For 30% only I-rheo indicated the existence of a crossover at about ω = 0.005 rad/sec. A new version of I-Rheo is under development to reduce the produced noise levels, however it was not released within the time frame to be tested in this project. Since none of softwares

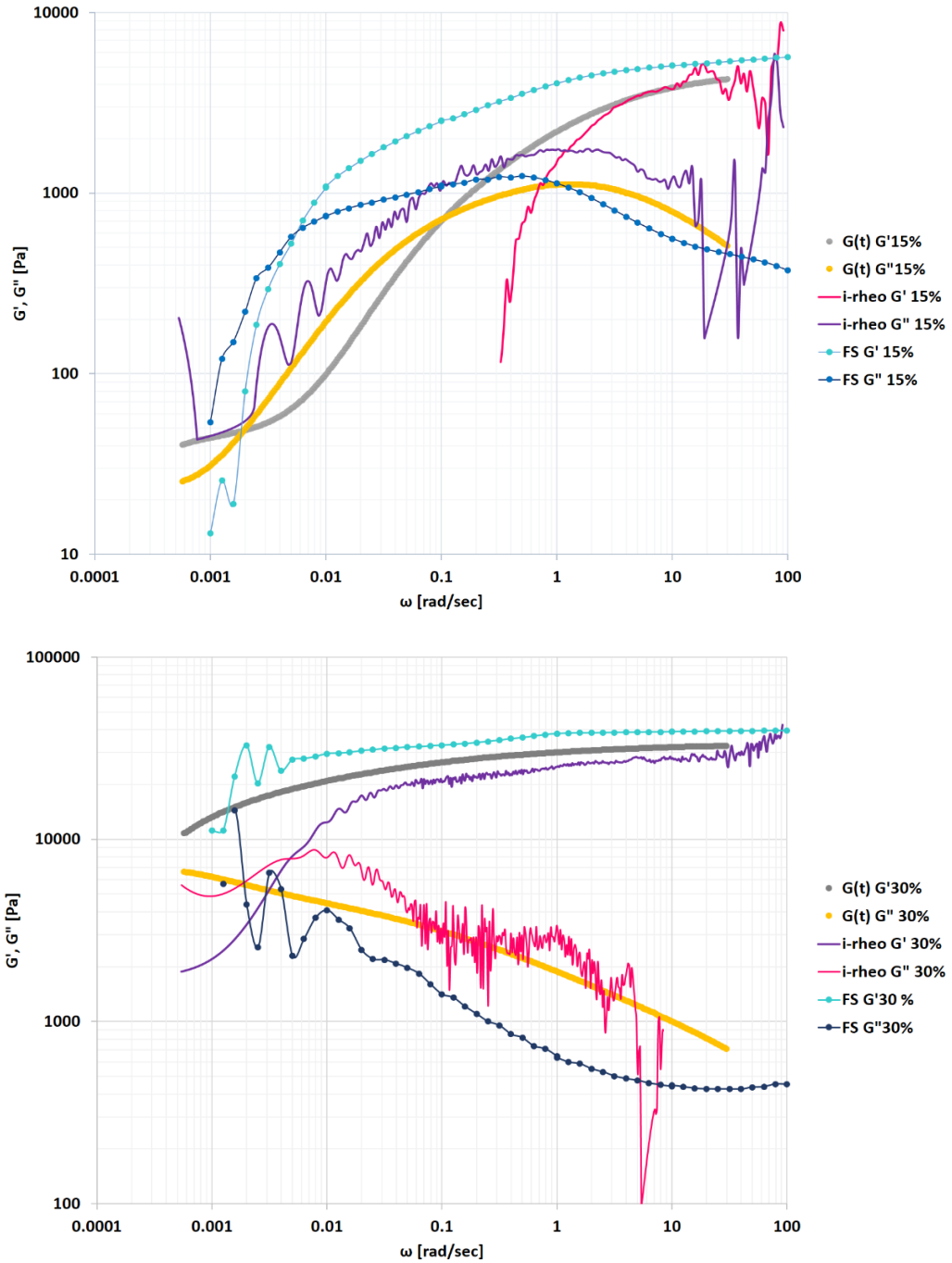

Figure 4-31 F127 dynamic shear moduli values acquired for 15 and 30% at 37°C using frequency sweeps and relaxation data processed by I-Rheo and Rheolpus.

generated data match with experimental values, their results should be disscused with caution and used for comparison purposes only.

4.2.2.5 Strain rate frequency sweep (SRFS):

Based on the previous attempts to acquire the relaxation frequency SRFS was used as a third method to determine cross-over point of the systems. A master curve was constructed from multiple shear rates in oscillation mode. The principle of these tests relates to the Temperature-Time Superposition (TTS) principle and temperature-concentration superposition tests commonly applied to study polymer melts, which cannot be applied due to the Pluronic system's temperature and concentration dependency. Soft glassy materials are known to experience relaxation time reduction with increasing shear rate – analogous to the injection process where the applied strain drives the relaxation to higher frequencies that would be otherwise accessible by standard methods (Wyss et al., 2007). SRFS is still a fairly a new and controversial method since it overestimates the terminal relaxation time (Li et al., 2017).

Technically, SRFS results are in the nonlinear regime but are still treated as linear rheological experiments. No special analysis packages or nonlinear instrument adjustments are required making it very attractive even as a comparative tool. Shear rates tested were 0.001, 0.005, 0.01, 0.05, 0.1, 0.2, 1 and 10 s^{-1} at 37°C. The extended master curve for 20% reveals a crossover point at 0.02 rad/sec and the slopes for G' and G" were calculated as 0.8 and 1.4, respectively. The moduli from the SRFS method were compared to the values recorded from frequency sweep measurements in Figure (4-32).

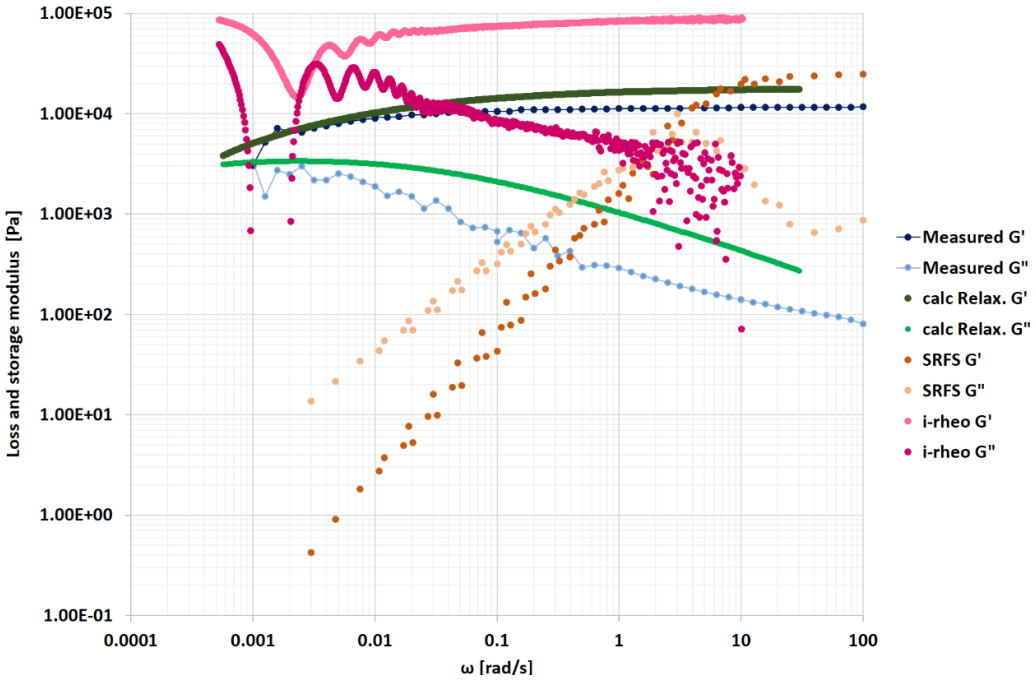

Figure 4-32 Dynamic shear moduli values acquired for F127 20% at 37°C using frequency sweeps, SRFS and relaxation data processed by I-Rheo and Rheolpus.

4.2.2.6 LAOS:

The nonlinear viscoelastic response of F127 samples was investigated in the strain amplitude range from 0.1 to 1500 % at fixed frequency of a 10 rad/sec and temperature of 37°C. The sweeps results are shown in Figure (4-34). The range covers both the small amplitude region (SAOS) and LAOS. Within the first region the moduli remain unchanged, similar to the results acquired in Figure (4-21) showing G' dominance. But as the strain exceeded the linear limit, the moduli exhibit a weak overshoot, where G' starts to decrease and G" increased until a crossover is reached before decreasing again. This drop in G" indicates that the lattice structure is broken, allowing a liquid like behaviour. The moduli decrease for the rest of the tests representing the alignment in the flow direction.

The corresponding Lissajous curves of the recorded stress-strain signal in Figure (4-33) show that different microstructures exist in the varying concentrations across the applied strain regions. For all samples, at the start-up strain, the pattern is almost a single value indicating a pure elastic behavior that progresses to an elliptic curve at γ = 1%. Increasing the strain further results in a lozenge like shape correlating to the macroscopic orientation of the sample during the moduli crossover between γ = 6-10% for the tested concentrations with a shift to the higher strains with higher concentrations (Hamley et al., 1998a). The pattern becomes rectangular with rounded corners which correlates to a saw-toothed stress-time signal. When strain is increased to 1000% the rectangular shape was maintained with symmetrical features appearing at higher concentrations.

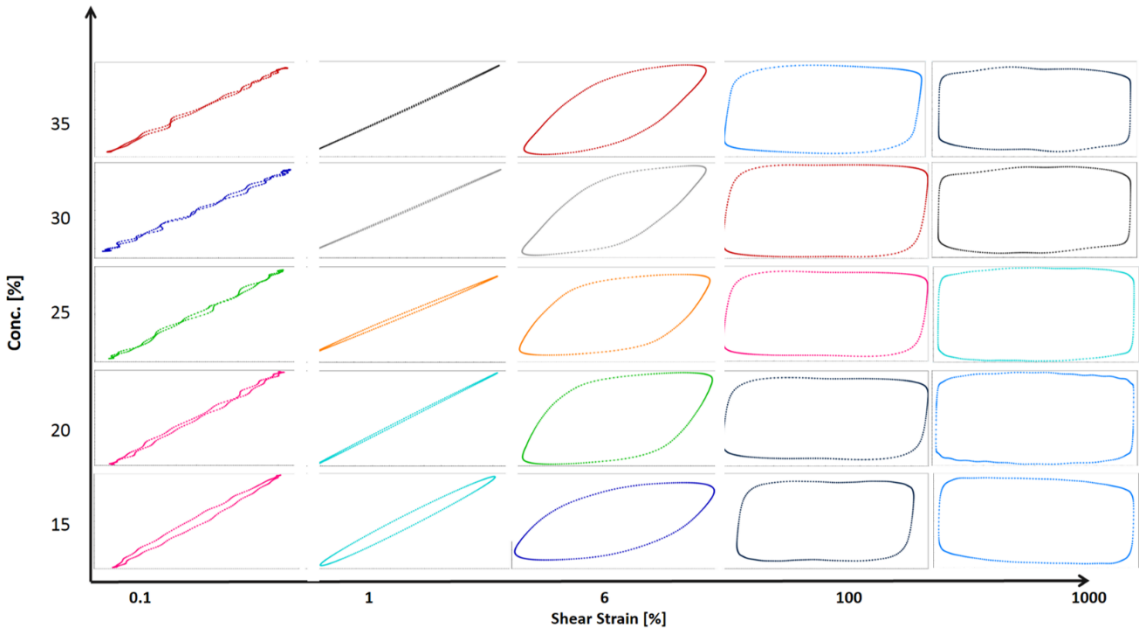

Figure 4-33 F127 LAOS Lissajous curves as function of concentration and strain. Where the y-axis of the individual plots represents the stress signal.

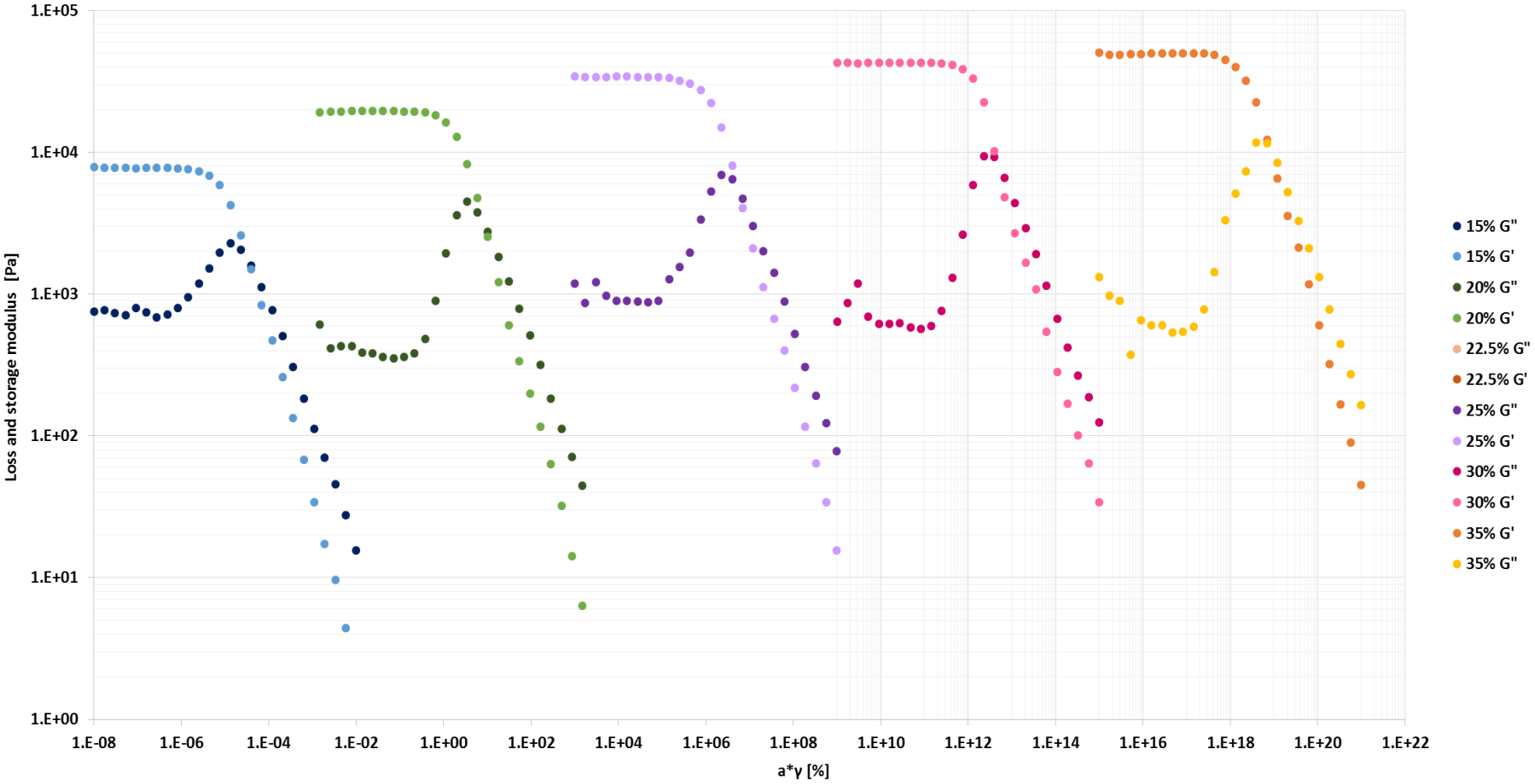

Figure 4-34 F127 dynamic moduli values during LAOS from γ= 0.001-1500 % at 37°C.

4.3. Structural results of Neat F127:

4.3.1 Static measurements:

4.3.1.1 SAXS:

Samples were tested using the Anton Paar SAXSpace at Bradford after loading into a 1 ml quartz capillary mounted on a temperature controlled stage. Temperature ramps were started from a low temperatures of -2°C to erase shear history and measurements were performed from 0 to 40°C. Figures (4-35) and (4-36) show the tested concentrations 1D and 2D scattering profiles, respectively.

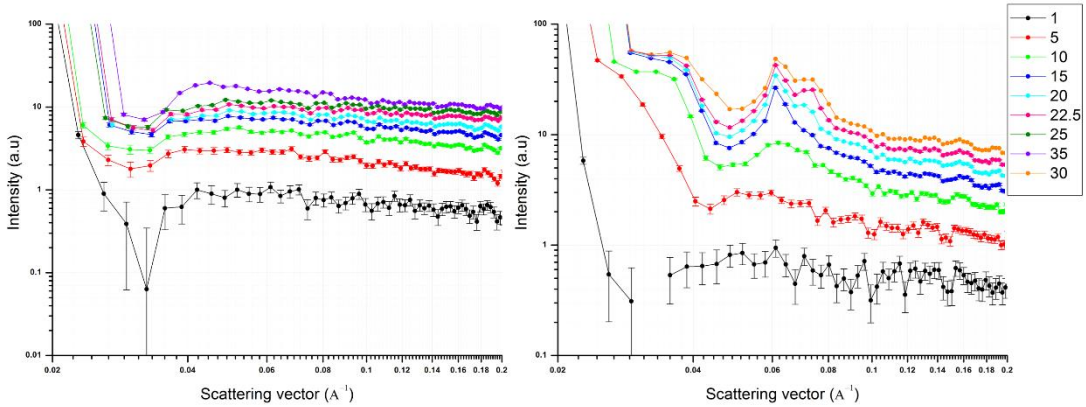

Figure 4-35 SAXSpace 1D scattering profile for samples 1-35% at two different temperatures: (left) 5°C and (right) 40°C, the profiles have been shifted vertically for clarity.

Within the tested temperature range, no scattering occurred from the lowest concentration of 0.1%. A similar lack of scattering was present in almost all of the samples at low temperatures. Structural changes started to appear above the corresponding CMT for each concentration, starting at 20°C for 10% and shifted to lower temperatures as the copolymer concentration increased in the solutions. The 2D structural changes were accompanied by a broad peak in the low q range observed in the 1D profiles. As the ramp proceeded to higher temperatures the scattering patterns started spreading and shifted to the higher q values, indicating an increasing order. Above CMT, attraction forces started to dominate and the amorphous micellar liquids were arranged onto periodic structures as temperatures gradually increased, as demonstrated by the double peak that developed to three distinctive peaks with either increasing concentration or temperature. The plotted 1D profiles for all formulations at 5 and 40°C in Figure (4-35) demonstrate the structural development as a function of concentration.

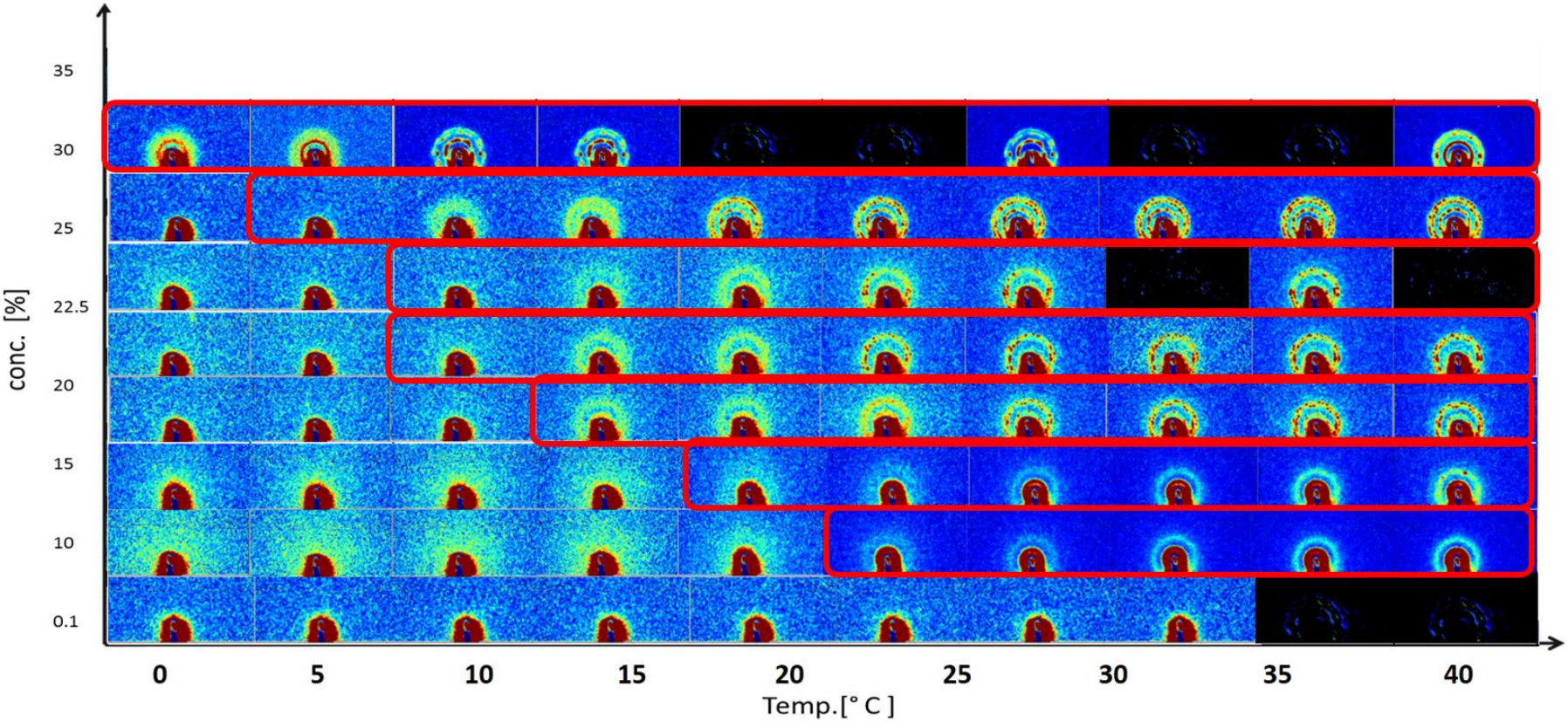

Figure 4-36 SAXSpace 2D scattering profiles for different concentrations of F127 as a function of temperature, where red frames represent the predicted transition temperatures from DSC measurements. The blackened out boxes were used in place of missing data.

The 2D scattering patterns are shown in Figure (4-36) for temperatures from 0 to 40°C and offer a more detailed picture of the structural ordering as a function temperatures and triblock fraction in the systems.

The lattice parameters can be approximated using from first peak position (q*) and assuming an FCC structure, the unit cell size (a) and the hard sphere radius (D_{HS}) can be estimated using, (Pozzo and Walker, 2007b):

$$a = \frac{2\pi}{q^*}\sqrt{h^2 + k^2 + l^2} = \frac{2\pi}{q^*}\sqrt{3}$$

Equation 4-1

$$D_{HS} = \frac{\pi\sqrt{6}}{q^*}$$

Equation 4-2

where h, k, ℓ, (hkℓ) are the three Miller indices planes orthogonal to the reciprocal lattice vector q. The calculated results show a trend in size reduction as the concentration increased, see Figure (4-37).

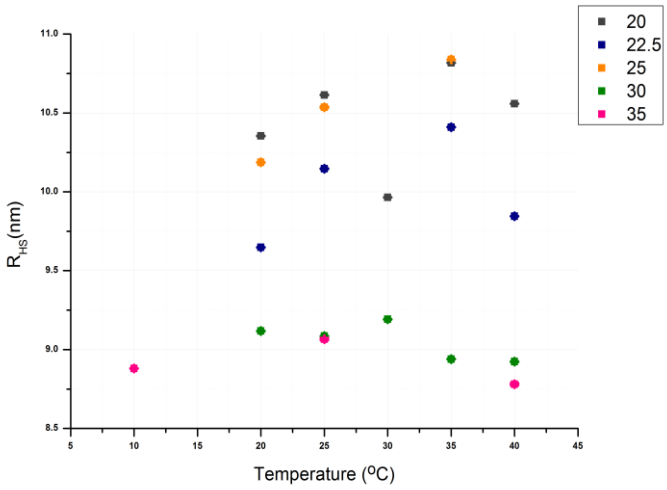

Figure 4-37 Calculated values of F127 hard sphere radii (with the respective errors) using equation 4-2 where the q values were fitted using Gaussian function.*

4.3.1.2 SANS:

For the SANS experiments, aqueous formulations were substituted with deuterated ones, and the loaded quartz cuvettes were mounted onto the LOQ instrument temperature controlled sample rack for testing. Sample concentrations of 10 to 30% F127 were tested at two temperatures; below gelation at sol state (5°C) and above gelation (37°C).

Figure (4-38) shows the plotted scattering results at 5°C. The scattering intensity can be seen to be proportional to the polymer concentration with all concentrations showing a broad micellar peak around q = 0.1 [$Å^{-1}$] which shifts to higher q values with increasing concentration. Peaks exhibited at higher concentrations were more defined albeit still broad. For 25% another peak appeared at q = 0.03 [$Å^{-1}$] indicating a structural transition was commencing. The sample containing 30% was exhibiting a prominent peak at q = 0.036 [$Å^{-1}$], in addition to the common broad peak in the lower concentrations. All samples can be described as monodisperse systems, except for 30% which already started to show some ordering.

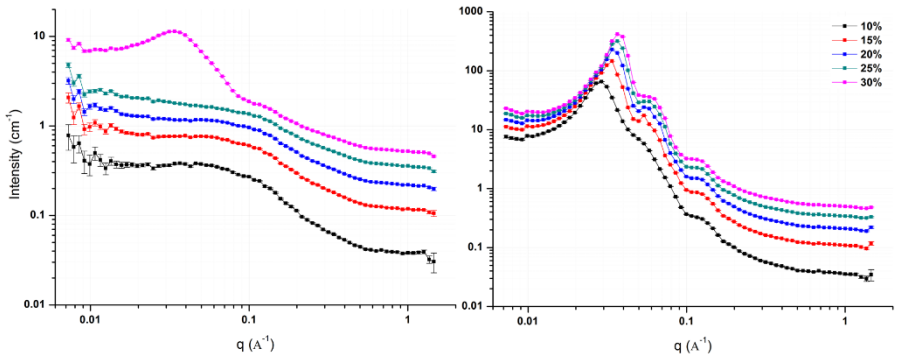

Figure 4-38 F127 static SANS profiles for samples 10-30% at two different temperatures: (left) 5°C and (right) 37° C. The profiles have been shifted vertically for clarity.

The results from the second experiment performed at 37°C were showing more defined scattering profiles and long range order evident by the defined peaks. The formulations here are better described as a gel with paracrystal structure. Peak sharpness and intensity were proportional to the concentration. The peaks of higher concentration samples were shifted to the lower q values compared to the lower concentrations, which correlates to a decrease in the lattice spacing and therefore increased packing density. In agreement with the literature, the

structure was FCC, identified based on the peak ratio to the first peak (q_n/q^*). For the different ratios and their respective lattices see table (4-1). The corresponding ratios for the highest concentration tested (30%) were 1, √4/3 and √8/3 for peak positions of 0.0462, 0.06532 and 0.0766 [$Å^{-1}$].

Two points need to be addressed regarding the presented dimensional values. D_{HS} is the hard sphere diameter representing the distance between two micelle centers thus $R_{HS} = D_{HS}/2$. And the total micellar radius calculated is a crude estimate based on the cubic unit cell value where the particles are spherical and the radius of the micelle $R_m = a\sqrt{3}/4$ (a is the unit cell size calculated from the first peak position). This approximation does not take into consideration the lattice distortion or the volume fraction and thus the values are most likely higher than values calculated by multivariable models. Similar approaches have been implemented to acquire the sphere dimensions in Hamley et al. (1998b) and Pozzo and Walker (2007a). The calculated parameters are tabulated in table (4-1) along with the fitted particle radius from FCC fitting.

Table 4-1 FCC fit parameters used in SASview:

Sample [%]	q_{max} [$Å^{-1}$]	a [nm]	R_{HS} [nm]	R_{FCC} fit [nm]
10	0.028	38.38 ∓ 7.63x10^{-03}	13.74	6.29 ∓ 1.17 x10^{-03}
15	0.034	32.46∓ 2.58x10^{-03}	11.32	5.14 ∓ 1.21 x10^{-03}
20	0.036	30.72∓ 2.05x10^{-03}	10.69	5.27 ∓ 0.82 x10^{-03}
25	0.038	29.34∓ 1.54x10^{-03}	10.13	4.92 ∓ 0.85 x10^{-03}
30	0.046	27.98∓ 1.54x10^{-03}	8.33	6.00 ∓ 1.17 x10^{-03}

The general trend can be observed is that the unit cell is reduced as function of concentration, suggesting that hard spheres are getting closer to each other and reduced radii values indicate that the spheres are getting smaller.

4.3.2 Dynamic Scattering

4.3.2.1 SAXS:

Two setups were utilised to investigate the shear induced structural changes using ; a) Linkam shear cell and b) a bespoke syringe pump - reservoir rig mounted on an xy-stage in front of beamline I22 at Diamond (see 3.2.3).

(a) Linkam shear cell:

These measurements were performed using different rotational continuous shear rates of 0, 10 and 20 s^{-1} at temperature ramps starting from 10 (below gelation transition) to 50°C at 2°C/min. Frames were acquired every 30 seconds with a total of 40 frames starting from 10°C at frame 0 (F0).

The static runs surprisingly did not show the distinctive scattering pattern recorded in previous scattering experiments. Two tested samples 20 and 25% had similar scattering behaviour, demonstrated by broad peaks at 0.043 and 0.048 [$Å^{-1}$], respectively. Ramping the temperatures led to an increased intensity and peak shift to 0.041 and 0.049 [$Å^{-1}$]. The recorded results can be attributed to the multiple experimental errors that might have occurred, including insufficient coverage of the gap due to a possible sample leaking when positioning the shear cell and in-homogeneous heat distribution across the sample gap, which according to another experiment, is improved by shear application (- see Chapter 3), or the disruption of the measurement due to the formation of air bubbles upon closing the shear cell leading to scattering flares that overshadow the gel scattering. Although the latest explanation is the weakest since the flare scattering is too strong to pass unnoticed and few tests had to be repeated when this occurred.

The investigated 10 s^{-1} shear effect on 25% during the ramp is presented in 1D and 2D formats in Figure (4-39). The formulation starts with weak twofold scattering increasing almost instantly in F1 (11 °C), showing first order Bragg peaks in 2D patterns before developing another ring at F10 (18°C) with notably higher intensity of the top and bottom spots in the first ring and two side spots of the second ring. The peaks experienced various intensity fluctuations with the

constant shear application throughout the test, correlating to peak positions of 0.04, 0.06 and 0.07 [$Å^{-1}$] in the 1D plots. The alternating intensity nature recorded between the top and bottom spots of the first order and the two side spots of the second can indicate the shear's role in moving the layers causing this phenomenon that can be equally seen in 2D with q1 having higher intensity than q*. Azimuthal representation of the peaks in F26 (35°C) to F28 (37°C) shows a symmetry of the spots in both rings, broken by a top/bottom asymmetry in the first order ring for the next two frames before resuming again to grow into near symmetry accompanied by the fading of the second order ring from F34 (40°C) onwards with having a slightly higher intensity. The 2D patterns show rings with higher intensity registered for the four side spots, which keep increasing to reach their maxima by the end of the test at 49°C, with one individual peak at 0.049 and a wide shoulder at 0.079 [$Å^{-1}$] in the corresponding 1D profile. The fading in the top/bottom Bragg peaks matches with the sliding layers zigzag mechanism of the sliding layers model Loose and Ackerson (1994).

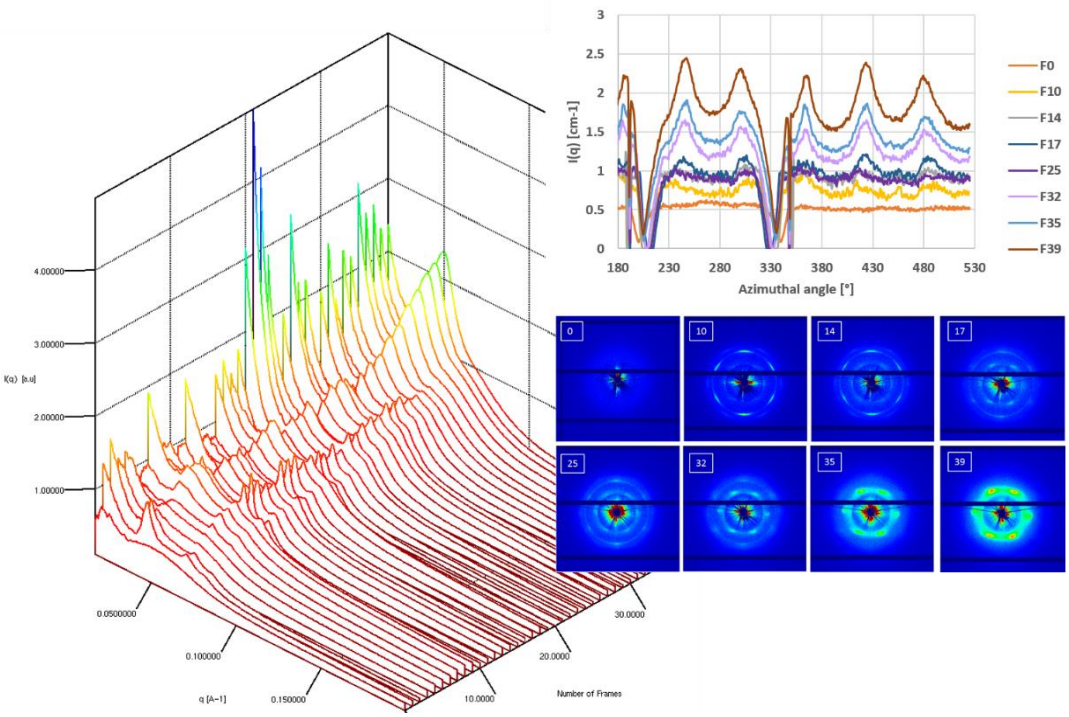

Figure 4-39 SAXS recorded for F127 25% at 10 s^{-1} with ramping temperature from 10 to 49°C.

Similar scattering development was recorded with the application of higher shear rate (20 s^{-1}) on the same sample. However the higher shear rate resulted in the appearance of sixfold spots in a hexagon from as early as 11°C with slightly

higher intensity in the top/bottom spots, which persisted with a weak second order ring until 21°C. The second ring disappeared afterwards and the sixfold peaks of the first order had equally increasing intensity through the test (data not shown).

Repeating the same experiment (under 20 s^{-1}) on 20% yielded more subtle transitions than 25% with the same distinguishable two ring structures at 22°C, and the lack of a final four sided spot structure recorded in 25% even under higher shear rates - see Figure (4-40).

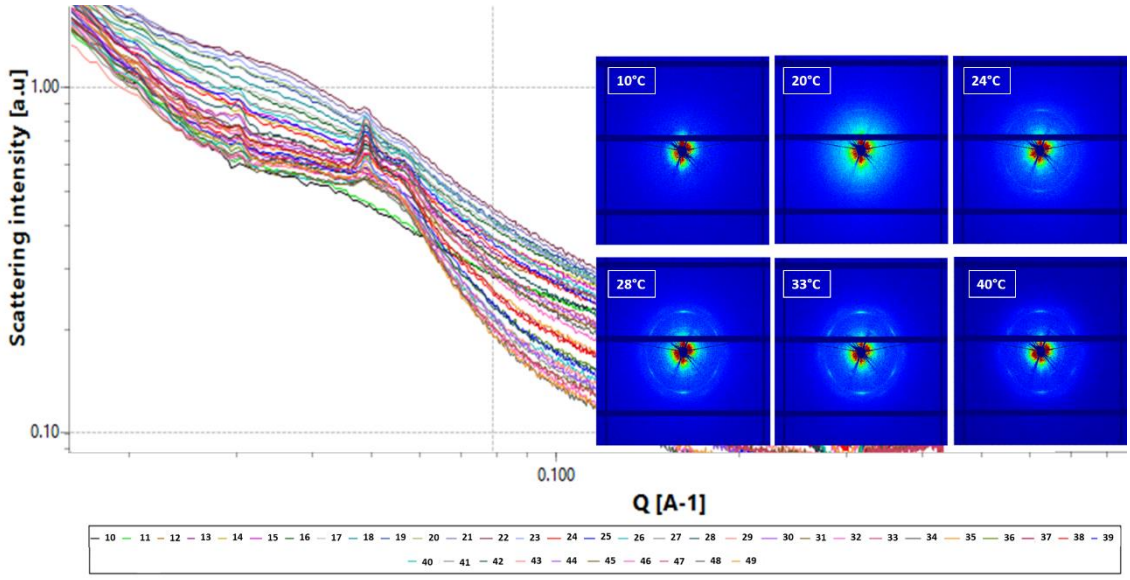

Figure 4-40 SAXS recorded for F127 20% sheared at 20 s^{-1} with ramping temperatures from 10 to 49°C.

This may suggest that higher temperatures or shear rates are needed to reach the similar symmetry levels witnessed in 25%. A comparison between the results acquired for the two samples is shown in Figure (4-41).

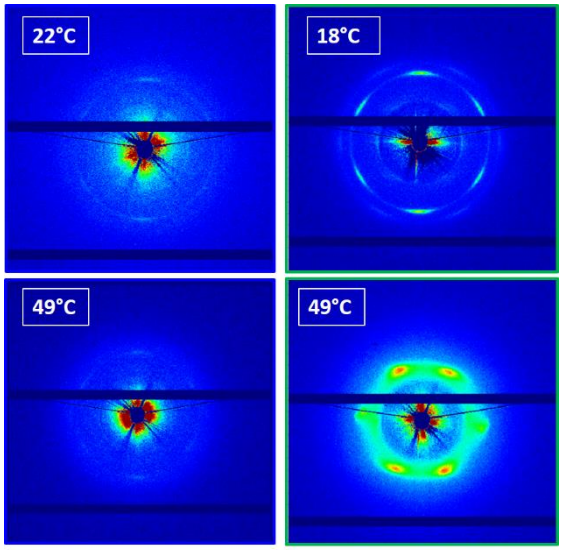

Figure 4-41 SAXS 2D scattering profiles of sheared samples, 20% at 20 s^{-1} and 25% at 10 s^{-1}; a) 20% at 22°C, b) 25% at 18°C, c) 20% at 49°C and d) 25% at 49°C.

(b) Syringe pump:

In this setup, the samples were loaded into a syringe at 5°C to be injected under different shear rates into an x-ray transparent channel at room temperature (23°C), the injection procedure to fill the channel took about 1 minute followed by x-ray measurements in the 1-2 plane. Frames were acquired every 60 seconds after cessation of shear. Tests were performed on two samples 25 and 30%. Sample 25% was tested at four shear rates 1, 10, 20 and 50 s^{-1}.

For 25% at 10 s^{-1} the sample 1D plot in Figure (4-42) shows three peaks at positions of 0.0536, 0.064 and 0.0726 [$Å^{-1}$] that merge forming a predominate peak at 0.063 with a nudging feature at 0.07 [$Å^{-1}$] by the end of the test. This slight shift indicates a loosening of the structure and reduced order. The corresponding 2D profiles show speckled patterns with matching three order rings to 1D at the beginning that morphed into one ring at the end. Two strong spikes appeared in the parallel position where Bragg peaks might be expected, which were accompanied by more growth in the positions of the four side peaks prior to

spreading in all directions in the first order ring resulting in noisy plots and preventing any meaningful azimuthal analysis.

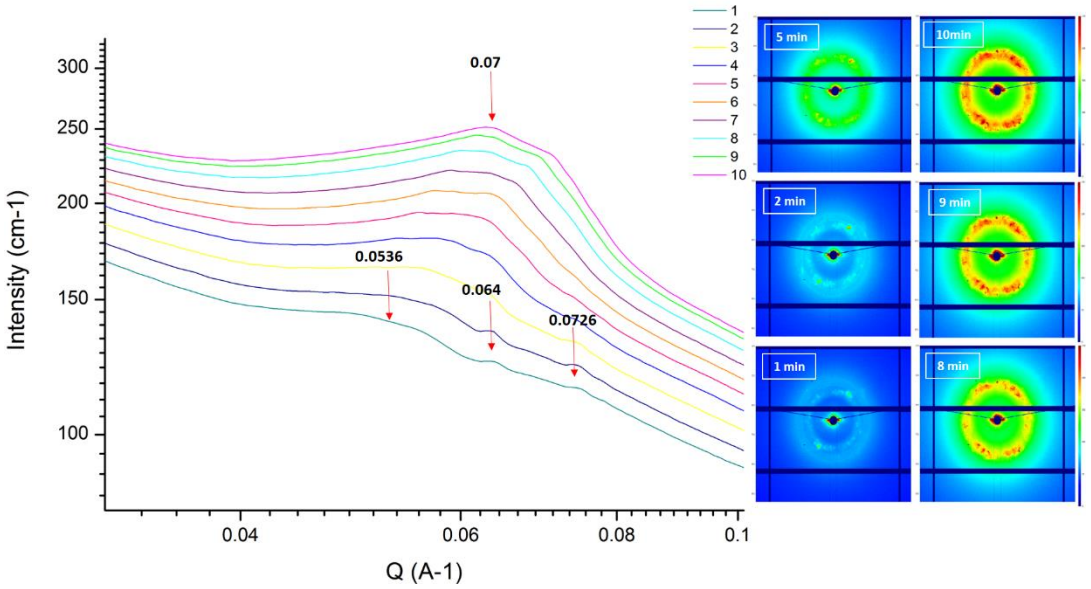

Figure 4-42 SAXS profiles for F127 25% tested using syringe pump injected at 10 s^{-1} where the legend represents the time.

At shear rate 20 s^{-1} (data not shown), the sample 2D profile exhibited an anisotropy with spikes of higher intensity at the four side peaks in the first ring, which grew in intensity with time. One peak appears across all 1D profile frames at 0.065 [$Å^{-1}$] and this sharpens and shifts slightly right to 0.066 [$Å^{-1}$] by the end of the measurement. The measurements taken after the application of 50 s^{-1} and 1 s^{-1} were very similar to 20 s^{-1} in both 1 and 2D profiles. The single peak shifted from 0.066 at the beginning to 0.063 [$Å^{-1}$] after the application of 50 s^{-1} and from 0.065 to 0.066 [$Å^{-1}$] after shearing at 1 s^{-1}.

The exact same experiment was replicated using 30% and injection shear rates of 1, 10, 50 and 90 s^{-1}.

After the injection at 1 s^{-1}, the scattering was completely isotropic until the 6th frame, in which twofold anisotropy appeared in the first order ring which reached its maximum in the last frame; this trend being observed in all three orders as seen in Figure (4-43). The 1D profiles reflect a structural ordering with highly defined peaks in the first half of the measurement with main peaks located at 0.04, 0.066 and 0.077 [$Å^{-1}$] indicating an FCC structure. In the next half of the measurement the peaks got weaker but maintained a more or less defined structure at 0.046, 0.065 and 0.074 [$Å^{-1}$].

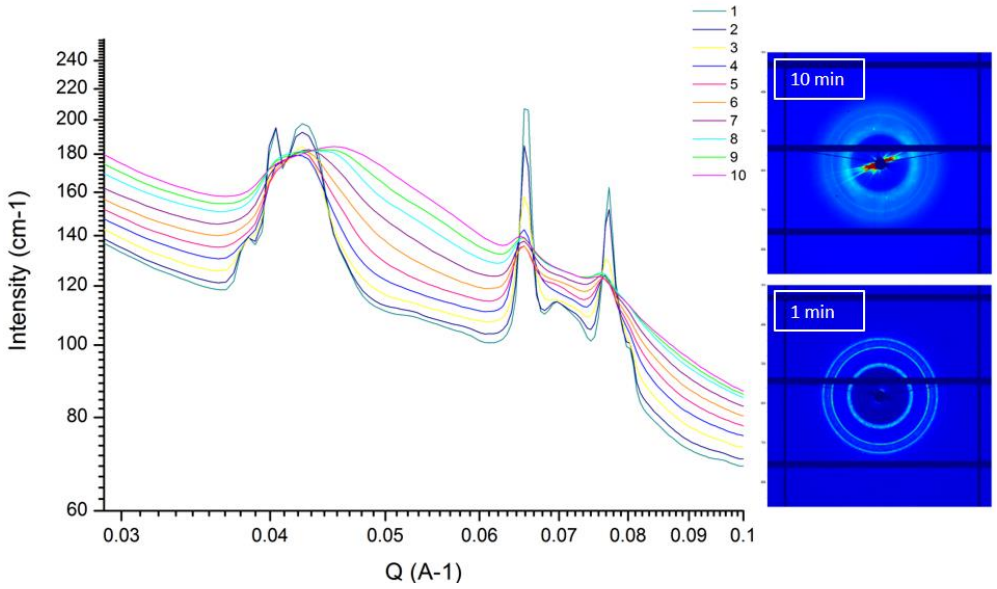

Figure 4-43 SAXS scattering profiles for F127 30% tested using syringe pump injected at 1 s^{-1} where the legend represents the time in minutes.

The 1 s^{-1} run was repeated. At the measurement start-up after injection, the 1D profile showed a complex peak concealing three weak peaks, as can be seen in Figure (4-44) with q values of 0.0416, 0.0587 and 0.071 [$Å^{-1}$]. The individual peak's intensity was overshadowed by the broad peak, which kept shifting to the right. In the last frame, traces of the previously mentioned peaks can be seen in shoulders at 0.035 and 0.075 with the total peak q value at 0.062 [$Å^{-1}$]. The frames second run had notably higher intensity than recorded in the first run, which increased gradually. Spikes appeared from the first frame giving the scattering a grainy appearance as they grew in numbers covering the first order ring. Another notable feature in this dataset is the overall 2D scattering shape, where the sample has lost the annular scattering shape replaced by an elliptical shape which had not been recorded in the previous samples. Plotting the frames

azimuthal profile revealed that this shape is actually due to sixfold symmetry with higher intensity in the meridional peaks.

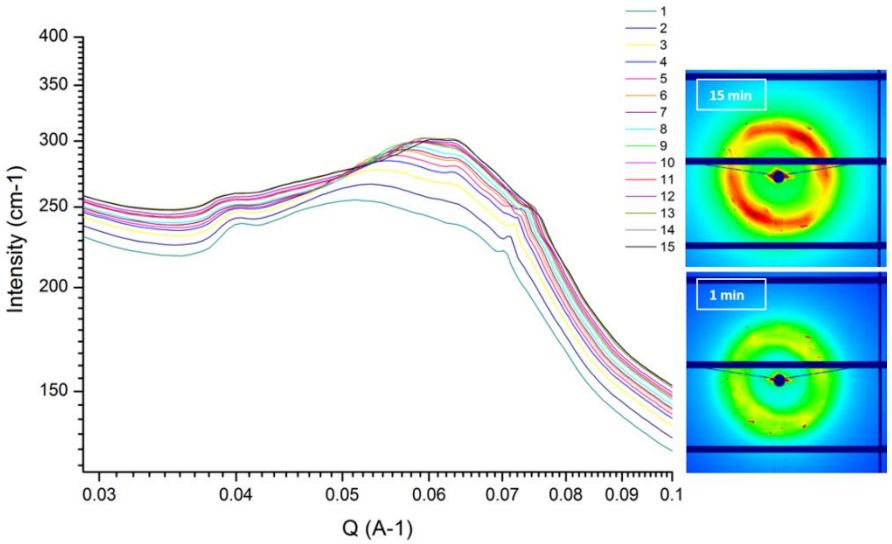

Figure 4-44 SAXS scattering profiles for the second run of F127 30% injected at $1s^{-1}$ where the legend represents the time in minutes.

The same experimental procedure was followed for the two runs – with the same measuring time for each frame, 60 seconds. Although the second run was performed after running multiple higher shear rates using the same concentration, this should not have any effect on the runs since the channel was cleaned after each measurement.

Similar FCC structuring to the first 1 s^{-1} order was registered in 1D profiles after shearing at 10 s^{-1} - see Figure (4-45). The peak merger was of larger extent than that observed for 1 s^{-1}, resulting in one single peak at 0.059 [$Å^{-1}$]. The 2D profiles were covered with high intensity spikes making it difficult to extract any definite information regarding orientation. Nonetheless, the scattering displayed a lozenge like Figure similar to the one recorded in the 1 s^{-1} rerun.

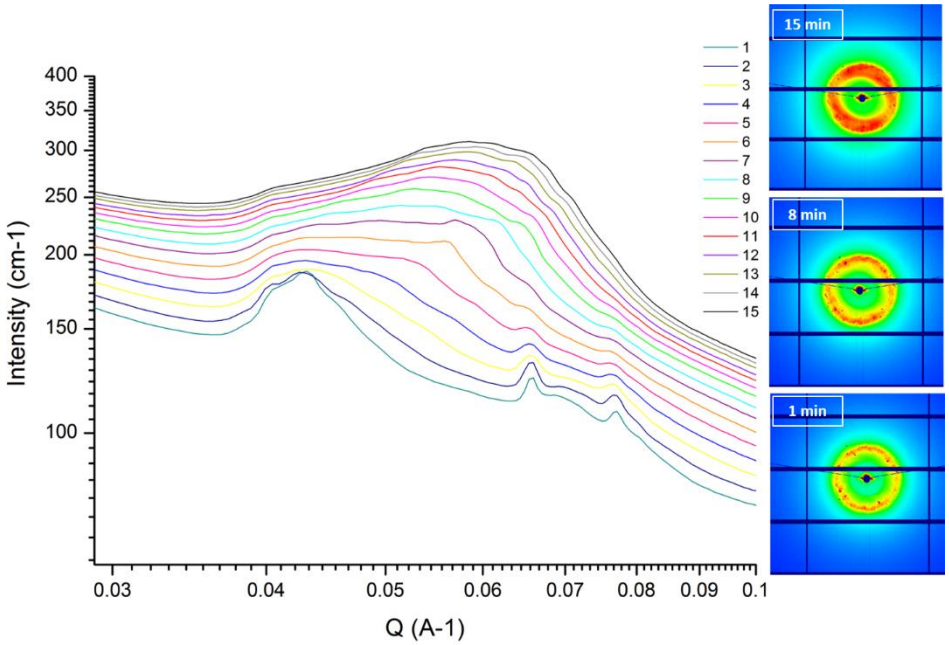

Figure 4-45 SAXS scattering profiles for F127 30% tested using syringe pump injected at 10 s^{-1}.

Similar results were observed upon repeating 10 s^{-1}, with a little shift in peak numbers from 0.0655 to 0.069 [$Å^{-1}$] with a common feature at 0.041 [$Å^{-1}$] that persisted until the end of the measurement. One distinctive peak was observed in the early frames after the application of 50 s^{-1}, located at 0.061 and a shoulder around 0.04 [$Å^{-1}$], the main peak shifted to 0.068 [$Å^{-1}$] by the time the last frame was taken. The 2D frames displayed a speckled ring with equal intensity sixfold peaks that grew larger as the measurement proceeded (data not shown).

90 s^{-1} was the highest shear rate applied on the samples. The 1D plots are showing highly ordered structure at the measurements beginning with defined peaks at 0.041, 0.046, 0.071 and 0.08 [$Å^{-1}$]. The peaks fused into one main peak with a q value of 0.06 [$Å^{-1}$] with an intensity almost twice higher than the q* as shown in Figure (4-46).

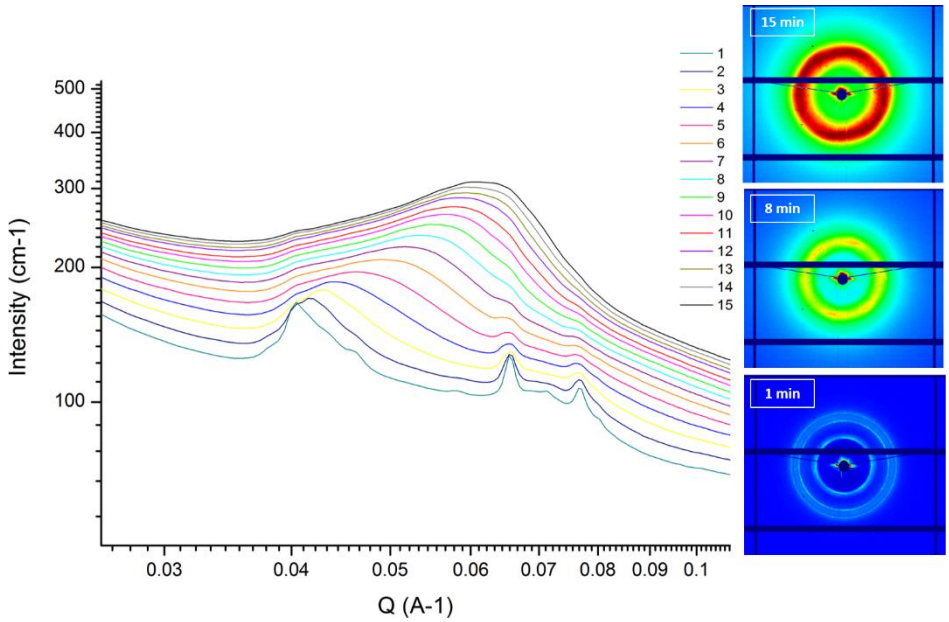

Figure 4-46 SAXS scattering profiles for F127 30% tested using syringe pump injected at 90 s^{-1}.

4.3.2.2 Rheo-SANS:

Rheo-SANS experiments were acquired by performing simultaneous rheological measurement using a rheometer mounted in front of SANS2D at ISIS-RAL. The samples were subjected to constant shear rates (10 and 100 s^{-1}) at three different temperatures representing the sol, gelation transition and gelation fixed at 37°C.

Under the two tested shear rates samples at low temperatures below gelation lacked organisational structure, demonstrated by D_2O scattering in 20% and the characteristic disordered micellar fluid broad peak seen in 1D profiles of 25 and 30%. However this does not apply for sample 35%, which even at 2°C showed an isotropic scattering pattern. The recorded intensity of the peaks was proportional to the temperature and concentration of the copolymer as demonstrated by the 1D plots in Figure (4-47). Similar disorder state was seen in the 2D profiles displayed in Figure (4-48).

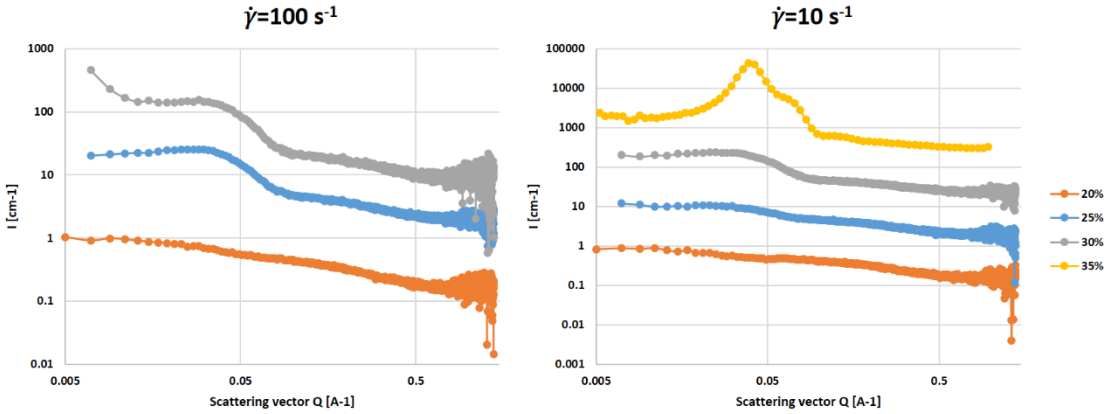

Figure 4-47 Rheo-SANS 1D scattering profiles pre-gelation of F127 formulations, profiles have been shifted vertically for clarity.

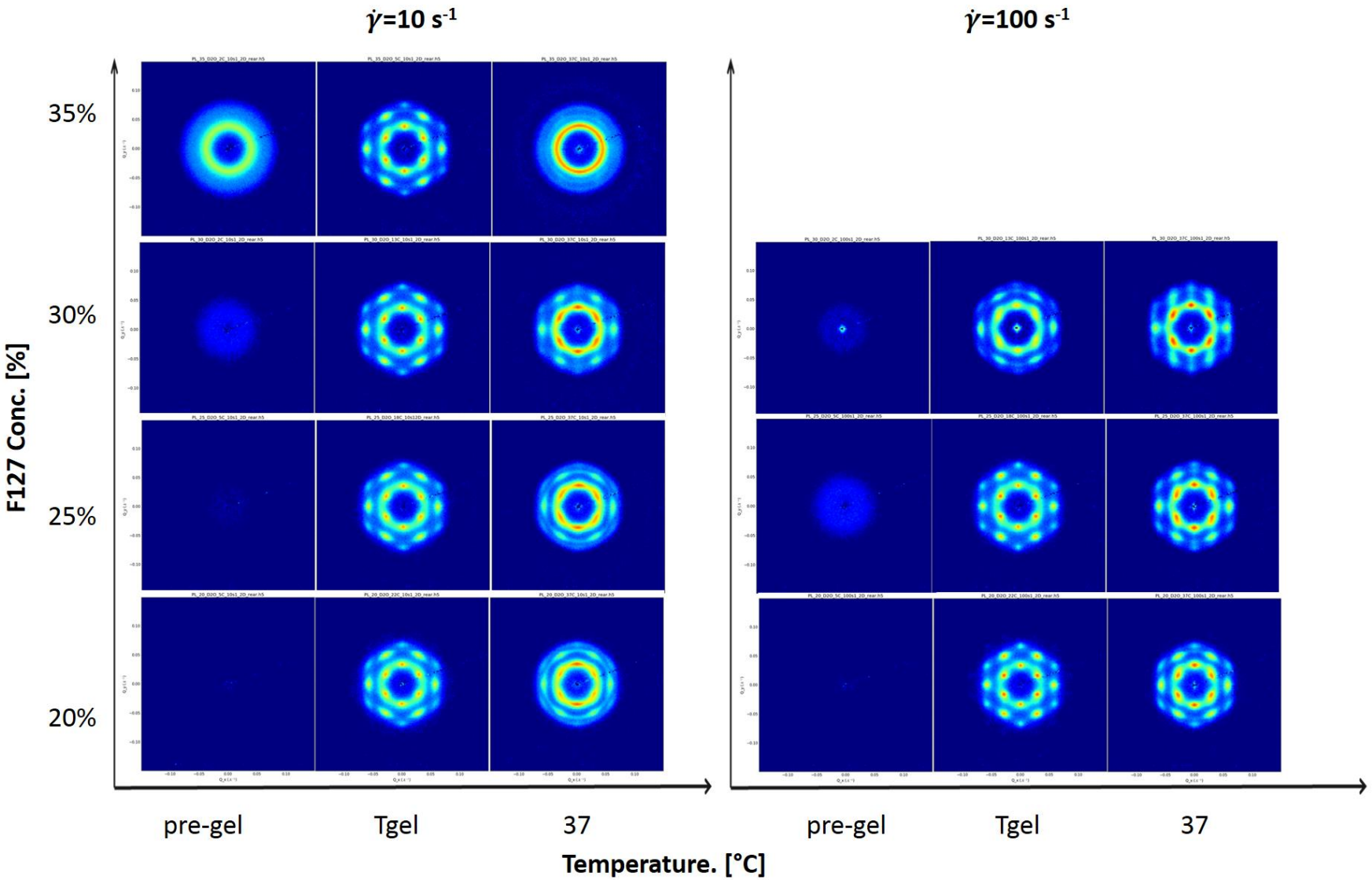

Figure 4-48 Rheo-SANS 2D scattering profiles for two shear rates at different temperatures; pre, during and post gelation as function of the F127 concentration.

(a) Low shear rates 10 s^{-1}:

As the temperatures increased to the sample's respective gelation transition temperatures, strong Bragg peaks appeared with sixfold symmetry that persisted over three orders, indicating the formation of close packed structures. Fitting quality is dependent on the reduction binning. Efforts were made to ensure the application of the finest binning settings to acquire the most accurate results. Based on the region of interest, linear binning at a step of 0.002 was applied, however this doesn't guarantee elimination of total error in indexing which can arise from peak shifts leading to slightly different structures. 2D profiles are displayed in Figure (4-48) and1D scattering results are plotted in Figure (4-49).

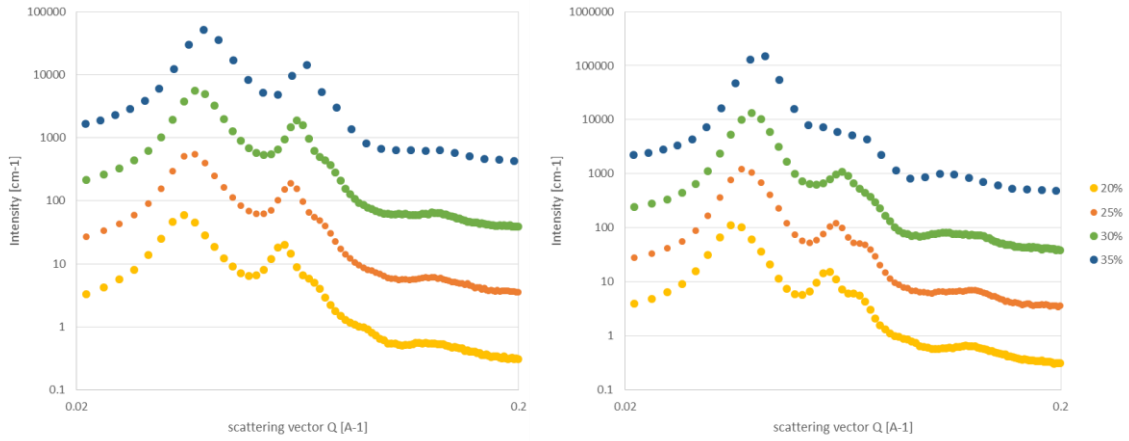

Figure 4-49 Rheo-SANS 1D scattering profiles for F127 samples sheared at 10 s^{-1}; (left) transition gelation and (right) at 37°C – profiles have been shifted vertically for clarity.

From the 1D profiles, sample's 20% and 25% first peak positions remained constant with the temperature change from transition to gelation. In 20% the recorded q values at both temperatures were 0.0350, 0.059, 0.069, 0.09 and 0.127 [$Å^{-1}$], which correspond to positions in both FCC and HCP structures √3 (FCC), √4 (FCC/HCP), √20/3 (FCC), √12 (FCC). 25% was found to fit FCC and HCP with peaks 0.0370, 0.061, 0.073 (FCC/HCP) and 0.129 [$Å^{-1}$] (HCP) matching positions at √8/3, √4 and √12.

However, the situation becomes more complicated with increasing concentration, making the structure determination inconclusive. Based on q values of 30%, the positions match √8/3, √12/3 and √27/3 in FCC, and √3, √4 and √12 in HCP at the transition temperature 13°C. As for 35%, at lower the temperature, two peaks were observed at 0.0388 and 0.066 [$Å^{-1}$]. The last peak shifted with temperature

where it was at 0.1139 for 2°C and 0.1328 [$Å^{-1}$] at 5°C, corresponding to √3, √7 at 2°C and √9 for 5°C which can indicate either BCC or HCP structures.

After gelation, the first peak q* shifted to the right to 0.0418 and the rest were positioned at 0.066 and 0.1054 [$Å^{-1}$] leading to FCC indexing of √8/3, √19/3.

The 2D azimuthal angle averaging at the transition temperatures showed sixfold symmetry for all concentrations from 20 to 30% with meridional peaks in top and bottom positions having slightly higher intensity. The difference between top and bottom peaks and the other peaks grow as a function of temperature, as represented by Figure (4-50).

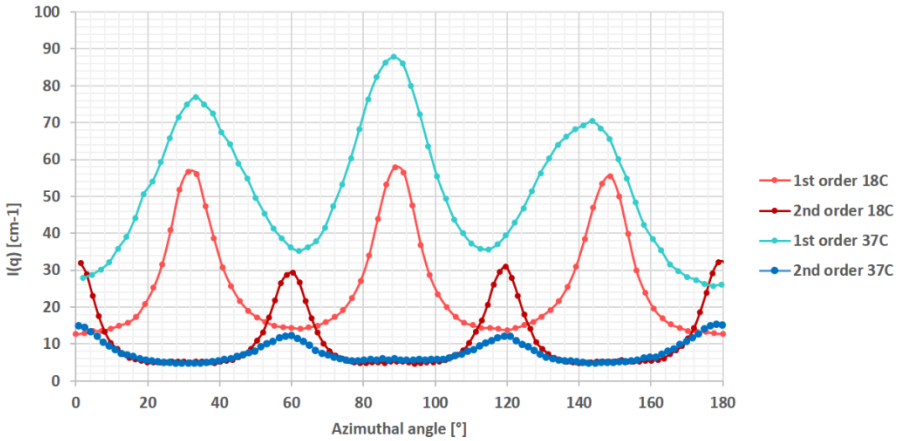

Figure 4-50 Rheo-SANS azimuthal profile for sample 25% at $10s^{-1}$.

The sample containing 35% exhibited a higher intensity at 37°C and the azimuthal plots in Figure (4-51) looked very similar to the 2D profile showing almost isotropic scattering in the first hexagon. Various degrees of weak diffused intensity peaks were seen in all samples, a typical feature of block copolymers.

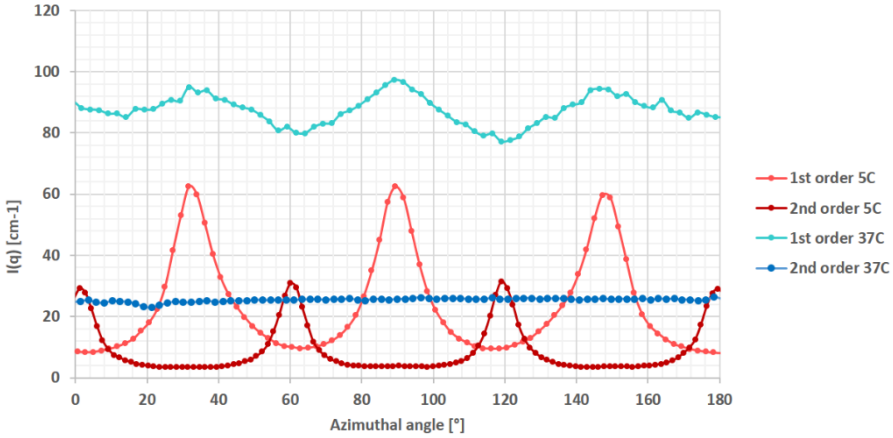

Figure 4-51 Rheo-SANS Azimuthal profile for sample 35% at $10s^{-1}$.

(b) High shear rates 100 s^{-1}:

The F127 systems under high shear rates show behavioural similarity to low shear with strong Bragg peaks appearing across all concentrations1D and 2D scattering profiles– see Figures (4-48, 52).

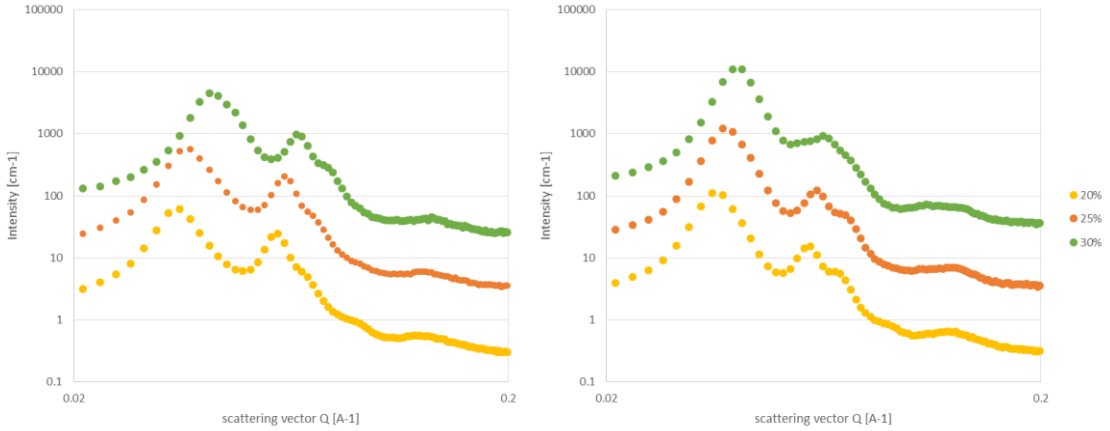

Figure 4-52 Rheo-SANS 1D scattering profiles for F127 samples sheared at 100 s^{-1}; (left) transition gelation and (right) at 37°C -– profiles have been shifted vertically for clarity .

The azimuthal profiles in Figure (4-53) revealed distinctive anisotropic patterns for 20 and 25% at the transition temperatures, clearly seen in of their first and second order hexagons, where highest scattering intensities were recorded at the four-sided peaks. Above reaching gelation, the same sample's four parallel side peaks were stronger than the meridional peaks of the 1st hexagon and the equatorial ones in the 2nd hexagon. This fits with Loose and Ackerson's model predictions of hexagonal layers stacking by zig-zag motion, although this movement was predicted to occur under low shear (Loose and Ackerson, 1994).

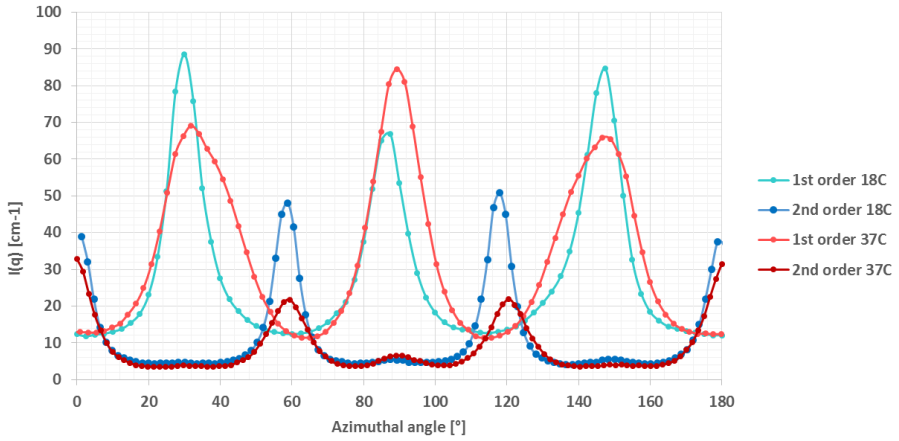

Figure 4-53 Rheo-SANS Azimuthal profile for sample 25% at 100 s^{-1}, similar results were recorded for 20%.

However, this motion did not appear in 30% which for both temperatures, the two meridional peaks were stronger in both orders with a new column like feature connecting the two orders with the faint 3rd order – see Figure (4-54).

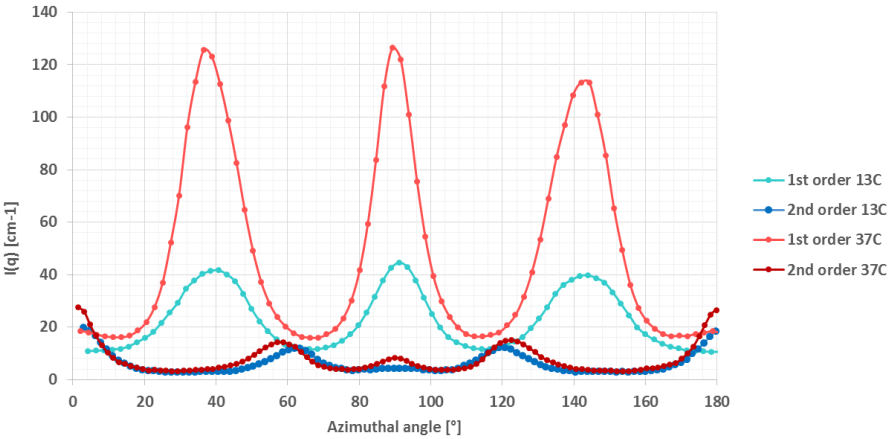

Figure 4-54 Rheo-SANS Azimuthal profile for sample 30% at 100 s^{-1}

4.3.3 Size correlation:

For the static samples assigning a fit was not complicated, however with complexity arising from the imposed shear the task was challenging when the lattice is described in mixed crystal terms with no suitable descriptive model. The system originally exhibits a spherical packing, which according to Jiang et al. (2007) was maintained to 600 s^{-1}.

Above gelation temperature (37°C) the 1st and 2nd order scattering patterns were symmetrical with meridional and equatorial peaks having the higher intensities than their neighbouring peaks for each order respectively. The peak positions recorded were identical under both 10 and 100 s^{-1}.

Like the static measurements, there are clear q* shifts to higher q-values with increasing the triblock concentration, this correlates to an increase in the number of micelles available to associate and reduction in the domain sizes, leading to the growth of the attraction forces that drives hard sphere crystallisation.

Based on SANS results from both sets, globally across the samples, the particle size (micelles) increased upon forming the crystals (hard spheres) with increasing temperatures for the same concentration, and between different formulations higher copolymer content led to the formation of compact particles with smaller radii. At the low temperatures the micelles are susceptible to shear, as observed from the R_g values acquired from the gel-fit model which decreased at higher shear rates. However this trend was not evident for higher temperatures and the crystallite's R_{HS} values were almost identical, which can be attributed either to the sphere's resistance to deformation causing unchanging size or the reduction method applied, since the shifts registered can be a result of the binning quality during data reduction. Ergo, hard sphere R_{HS} estimates during and after the gelation transition are approximately the same for both imposed shear experiments as seen in table (4-2) and the only notable changes were as a function of concentration.

Table 4-2 Rheo-SANS main parameters resulted from Sasview gel-fit (solution) or FCC (gel) model fits:

Shear rate [s^{-1}]	Conc. [%]	T [°C]	q* [$Å^{-1}$]	a [Å]	R_g or R_{HS} [nm]
10	20	5	-	-	6.86
	25	5	-	-	5.46
	30	5	-	-	3.52
	35	5	-	-	4.47
10	20	22	0.0350	308.10∓0.05	6.70∓ 0.002
	25	18	0.0370	295.36∓0.05	6.66∓ 0.002
	30	13	0.0370	286.27∓0.02	8.94∓ 0.002
	35	5	0.0388	283.94∓0.05	4.53∓ 0.001
10	20	37	0.0350	295.62∓0.04	9.07∓ 0.002
	25	37	0.0370	293.86∓0.02	8.68∓ 0.003
	30	37	0.0390	283.97∓0.02	5.14∓ 0.001
	35	37	0.0419	276.84∓0.01	5.06∓ 0.001
100	20	5	-	-	5.42
	25	5	-	-	3.87
	30	5	-	-	3.45
100	20	22	0.0350	312.84∓0.05	6.78∓ 0.002
	25	18	0.0370	295.42∓0.05	6.81∓ 0.002
	30	13	0.0390	270.80∓0.04	6.65∓ 0.002
100	20	37	0.0350	295.62∓0.04	9.07∓ 0.002
	25	37	0.0370	288.78∓0.02	8.53∓ 0.003
	30	37	0.0390	276.08∓0.01	7.93∓ 0.002

The R_{HS} values at 37°C are compared to the static SANS measurements in Figure (4-55):

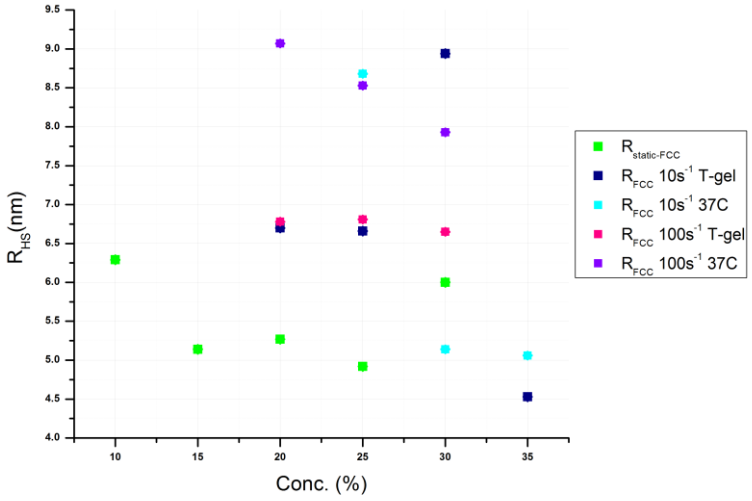

Figure 4-55 F127 radii values acquired from different SANS experiments static and under imposed shear –error values are too small to appear within the chosen scale .

4.4. Thermal properties of F108 and F68:

Similar to the recorded thermal transition recorded in F127 the prepared formulations show analogous endothermic peaks correlating to thermal transitions attributed to micellisation and gelation. The dependence of the thermal properties on the F108 and F68 concentration is shown in monotonic correlations across the different recorded variables in Figures (4-56,57), where the onset, endset and peak temperatures shifted to lower values with increasing the copolymer percentage in the formulations.

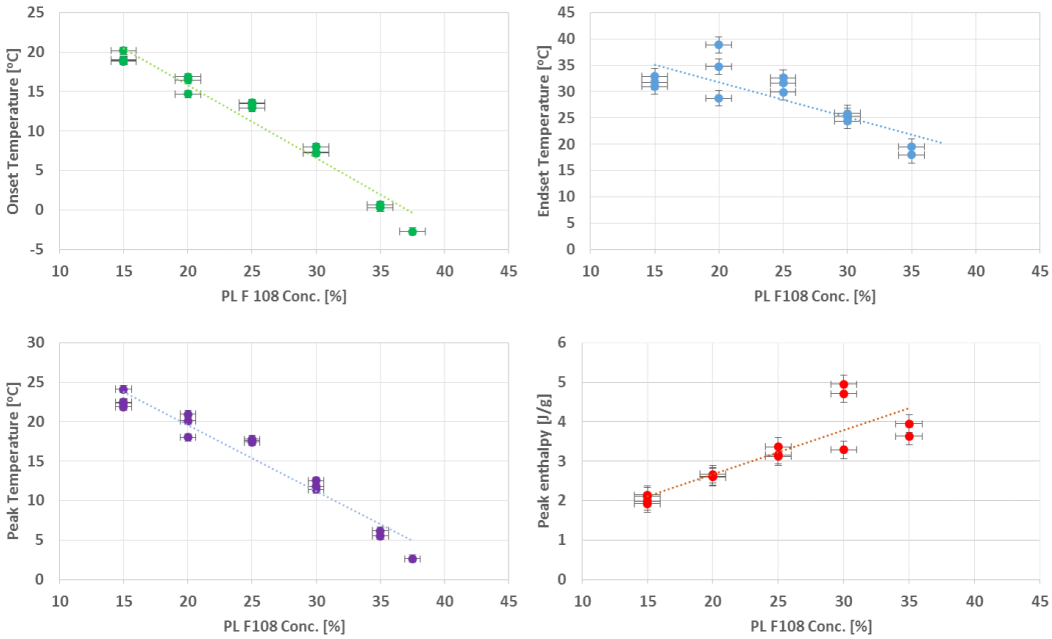

Figure 4-56 variables obtained from the different F108 concentrations thermograms, indicating onset, peak and endset temperatures. In addition to the endothermic peak enthalpies for each respective concentration.

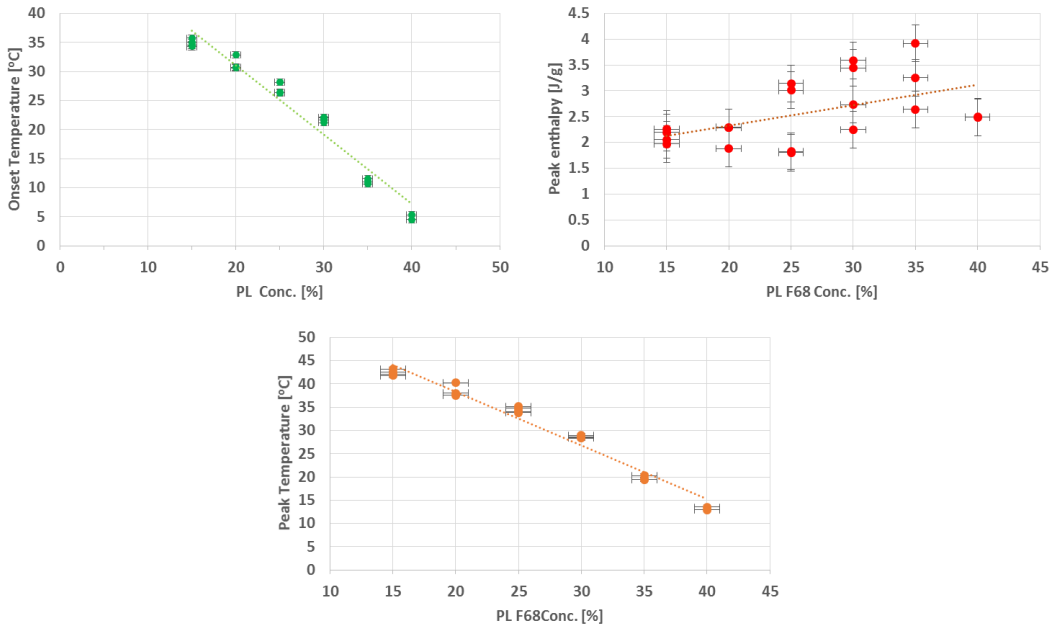

Figure 4-57 variables obtained from the different F108 concentrations thermograms, indicating onset and peak temperatures. In addition to the endothermic peak enthalpies for each respective concentration.

4.5. Rheological properties of F108 and F68:

4.5.1 Steady Shear

4.5.1.1 Temperature ramps at constant shear:

The same tests in section (4.2.1) were performed on the two other Pluronics; F68 and F108 to study the shear and thermal dependency. The samples were subjected to four tests with constant shear rate values of 10 , 20, 50 and 100 s^{-1} while ramping the temperature at 2°C/min within the same range as F127 from 5 to 40°C, the results are plotted in Figures (4-58) and (4-58) as functions of shear rate and concentrations.

a) F108

Figure (4-58) shows different concentrations of F108 ranging from 15 to 39%. The same trend is observed across the different sample concentrations. All samples exhibit Newtonian behaviour at low temperatures. The viscosity of the lowest concentration prepared 15% was experiencing a minimum at 22.6°C followed by a continuous increase. The sample flow curves can be divided into

three distinctive regions of different rheological behaviours; the low viscosity region described as Newtonian, a transition region followed by abrupt increase in viscosity marking the beginning of new region at 35.5°C, marked by the bifurcation of the curves corresponding to the of the different shear rates applied, where the lowest viscosity recorded was for highest shear rate 100 s^{-1} and a decade difference separating it from the viscosity under the lowest shear rate, confirming the shear thinning properties.

Identical behavioural properties were observed for the higher concentrations, where the increasing F108 concentration drove the thermal transition and shear dependency critical points to the lower temperature as demonstrated in Figure (4-59).

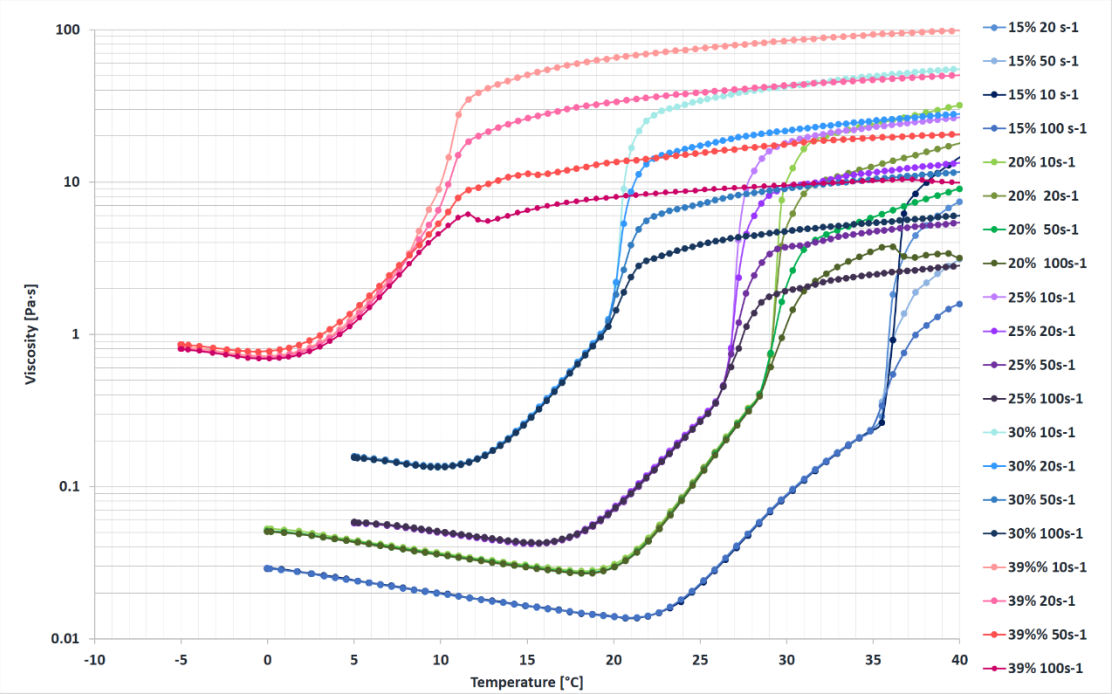

Figure 4-58 F108 Temperature ramps at constant shear rates on sample concentration from 15 to 39%.

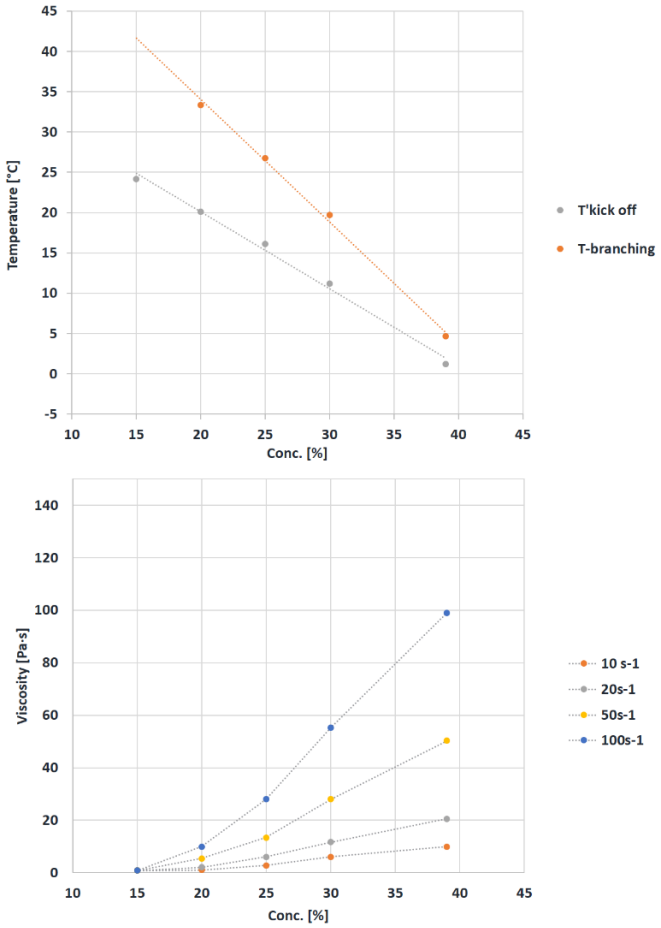

Figure 4-59 F108 critical points marking the transitions for temperature ramp results under constant shear plotted as a function of temperature (top) and viscosity (bottom.)

b) F68

The same experiments were conducted on a series of F68 containing 15 to 40% of the copolymer. The rheological responses are shown in Figure (4-60). Concentrations 15 and 20% have relatively similar responses to water with about a decade higher viscosity, reducing with temperature. As the temperature increases, the formulation containing 25% exhibited the same trend as lower concentrations. However, upon reaching 34°C the viscosity was observed to increase finishing the test with an upward slope although the initial viscosity value hasn't been recovered. The temperature response becomes stronger with increasing copolymer concentration to reach the initial viscosity value in 30% and exceed it in 40% which ended the test with a viscosity almost decade higher than its initial viscosity value. Based on the viscosity values measured, the

formulations are in the solution state across the tested temperature range. They exhibit two different (though rather weak) trends as a function of the increased temperature. The lower concentrations displayed viscosity decreases only (15 and 20%) while the higher concentrations showed a minima followed by an increase (25 to 40%). The viscosity values recorded were shear independent and correlated to the copolymer percentage present in the formulation. Among the concentrations prepared and across the ramp's experimental temperature range no gelation was detected in F68.

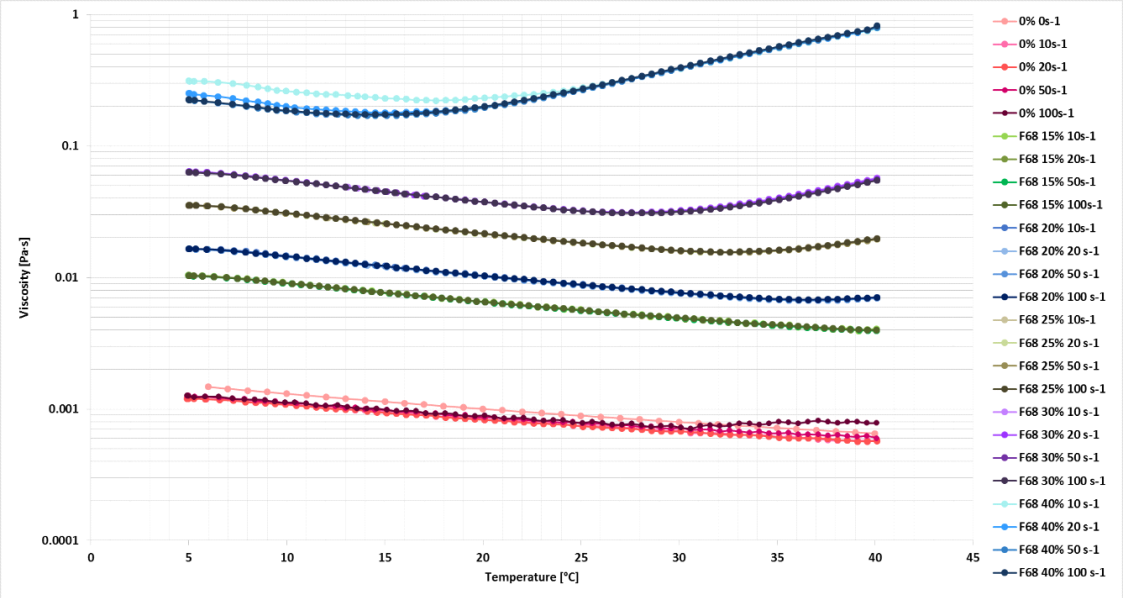

Figure 4-60 F68 Temperature ramps at constant shear rates on sample concentration from 0 to 40%.

4.5.1.2 Shear rate ramps at constant temperature:

In Figures (4-61, 62) the different concentrations of F108 and F68 were sheared at rates from 0.001 to 1500 s^{-1} at two temperatures 5 and 37°C.

a) F108

As seen in Figure (4-61) all concentrations tested at 5°C appear unstable in both plots of shear stress and viscosity at shear rates below 1 s^{-1}, except for the highly concentrated formulation 39% which shows a high yield stress at the shear start up. The viscosity of 39% drops after reaching 0.1 s^{-1} allowing it to show the same trend as the rest of the concentrations once they overcome wall-slip effect and

act like a viscous fluid. A different trend was observed in the shear ramps at 37°C, which is above the critical gelation temperature for all the concentrations in this series as previously demonstrated from the temperature ramps at constant shear in Figure (4-58). All samples displayed similar tendencies; a shear thinning behavior through the whole ramp, yield stress and non-monotonic stress response, demonstrated by the formation of stress plateau between two critical stress values that ends with an upward slope, indicating a transient behavior or the formation of shear bands in the vicinity of shear gap.

The sample containing 20% exhibited slightly higher viscosity values than 25% - a discrepancy that might have arisen from phase separation due to long storage time and insufficient homogenisation before the test or preparation inaccuracy.

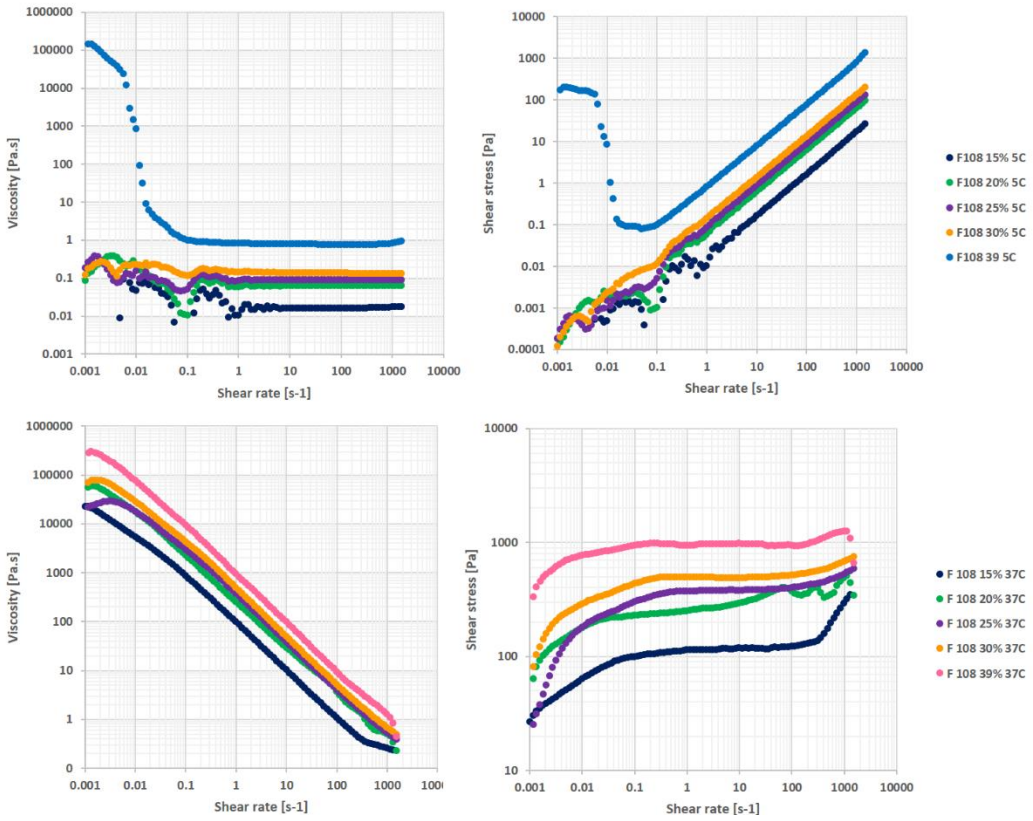

Figure 4-61 F108 shear ramps at 5 ad 37°C on sample concentrations 15 -39%.

b) F68:

Figure (4-62) shows the shear ramp results for F68 15 to 40% at 5 and 37°C. At these two temperatures the formulation would be still in the solution state. The viscosity values recorded at the two temperatures look fairly similar with slightly higher values at 37°C. Wall-slip is predominant at shear rates below 1 s^{-1} evident

by the data recording breakage. Samples containing 15 and 20% experienced unexpected increases in viscosity at values of 731 s^{-1} that persisted until the end of the test at 1500 s^{-1}.

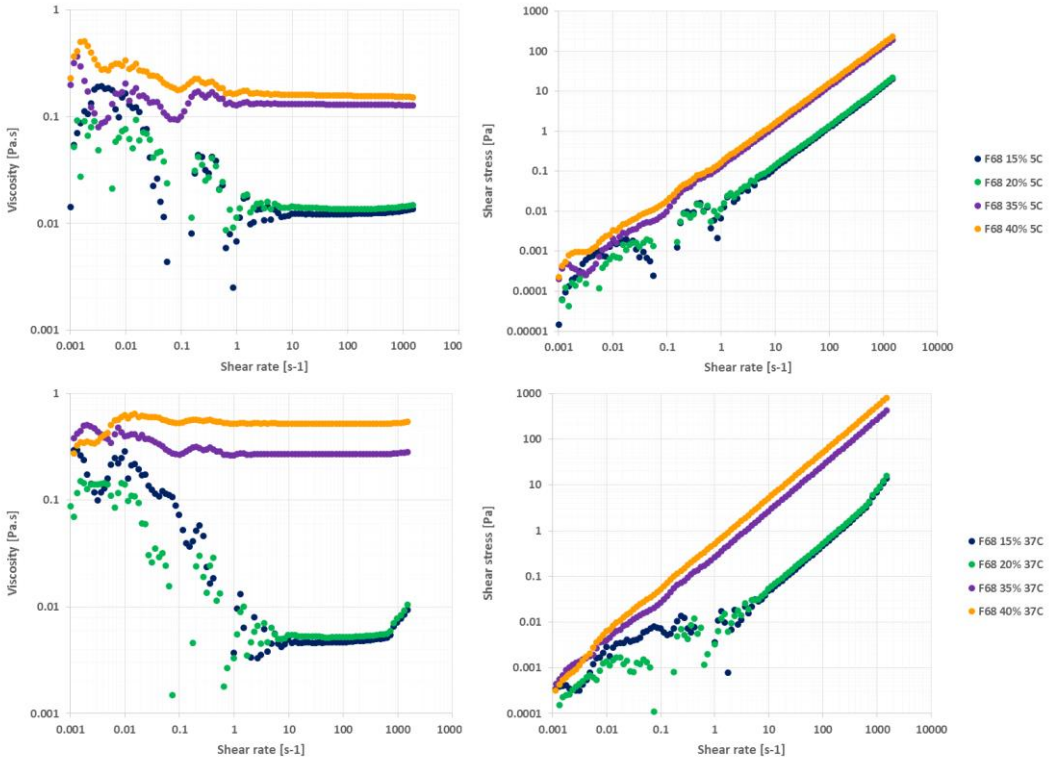

Figure 4-62 F68 shear ramps at 5 ad 37°C on sample concentrations 25-40%.

4.5.2 Oscillation:

a) F108

Oscillatory shear of 10 rad/sec was applied on the series of F108 concentrations while ramping the temperature by 2 °C/min, the dynamic shear moduli values are plotted in Figure (4-63). At low temperatures, G" > G' indicating the viscous dominance in this region until a critical temperature is reached where the moduli undergo an abrupt increase as G" = G', followed by G" < G' signifying the gel formation. The CGT was determined by the elastic modulus increase by at least three decades. It was observed that as concentration increases CGT is shifted to lower temperatures and higher dynamic moduli values are recorded. After gelation has been reached, the dynamic moduli values plateau until a critical temperature where the structure starts softening and the dynamic moduli gradually decrease. However, none of the tested systems experienced a complete fall back to the initial values as was observed for some F127

concentrations. The same rheological behavior is apparent in the complex viscosity curves, similar to what was previously reported in F127.

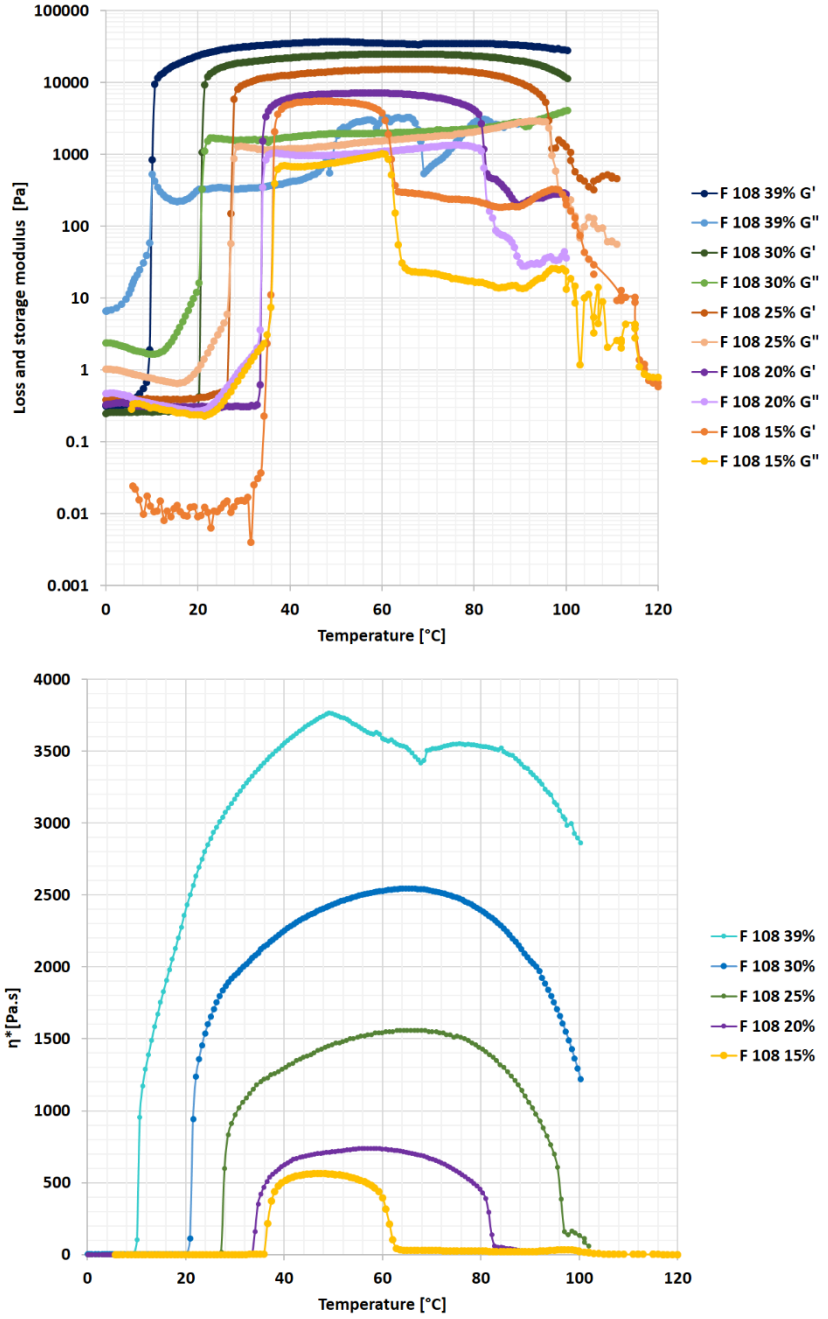

Figure 4-63 F108 temperature ramp under oscillatory shear from 0 to 100°C. Top: the dynamic moduli and bottom the complex viscosity values as a function of the applied temperature

b) F68

The same experiment was repeated on a series of F68 concentrations ranging from 20 to 40%. The results displayed in Figure (4-64) show dynamic moduli increase in all concentrations above a critical temperature indicating a structural change with the G' dominant over the G", as previously seen in F108 and F127.

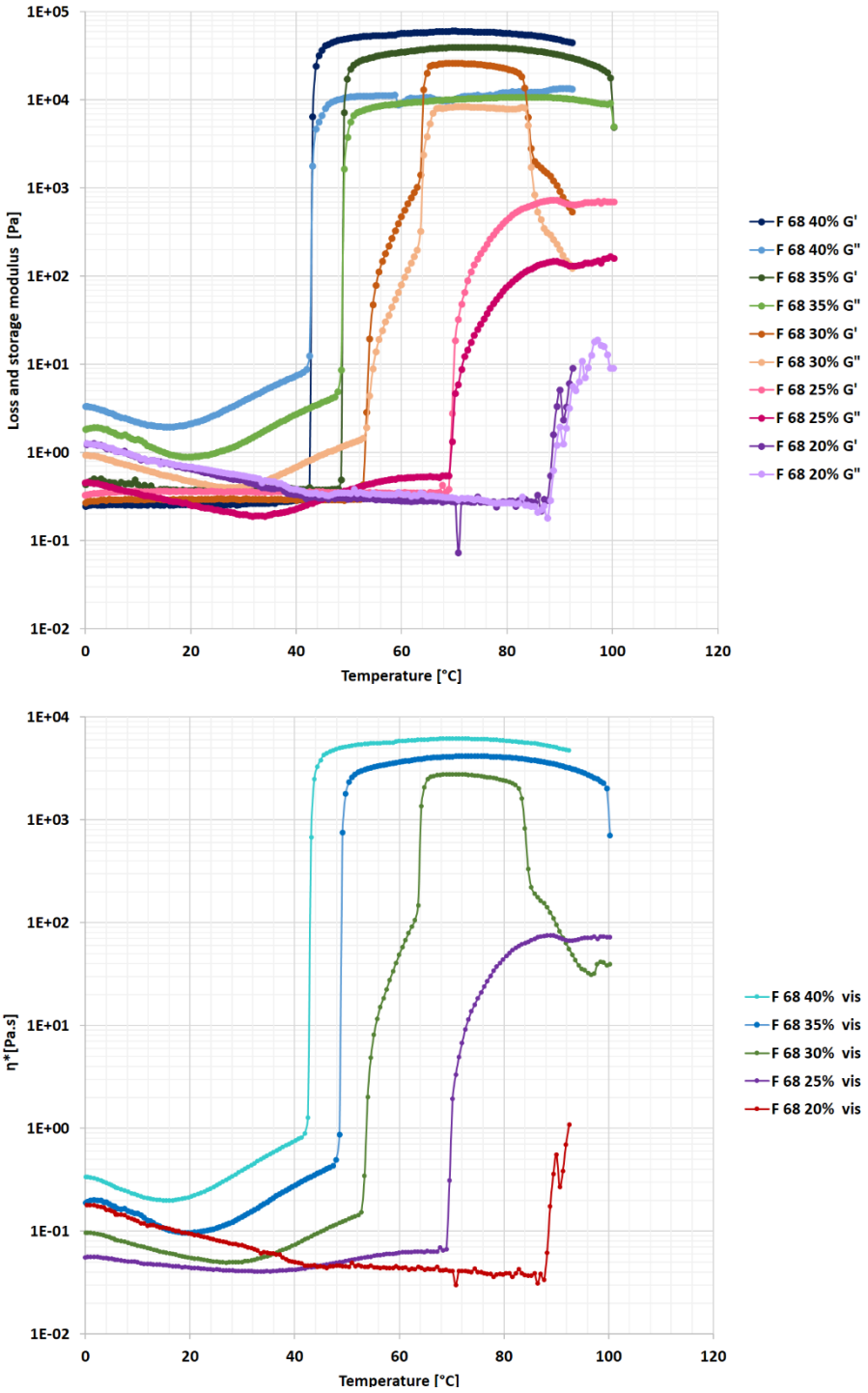

Figure 4-64 F68 temperature ramp under oscillatory shear from 0 to 100°C. Top: the dynamic moduli and bottom the complex viscosity values as a function of the applied temperature

However the corresponding complex viscosity graph demonstrates that the transition only caused gelation in concentrations above 25% with the lower content samples had almost constant complex viscosity values across the tested ramp range until approximately 75°C where the complex viscosity exhibited some increase.

4.6. Structural analysis -SAXS:

As for previous static SAXS experiments, the samples were loaded into quartz capillaries and tested across a range of temperatures to monitor their structural development.

a) F108*:*

Figures (4-65) and (4-66) show the 2D SAXS profiles from the different F108 concentration from zero to 40°C and the 1D profile at 40°C, respectively. The 2D patterns demonstrated the gradual ordering as a function of temperature and concentration, which was of low scattering intensity for concentrations below 30% with a broad peak at 0.034 [$Å^{-1}$] for 15%, 0.037 [$Å^{-1}$] for both 20 and 25% at 40°C. The formulations became more ordered with increasing the copolymer percentage giving a defined structure at 40% that is indexed as FCC, matching the reported structure in the literature with peak positions at √8/3, √11/3 and √12/3.

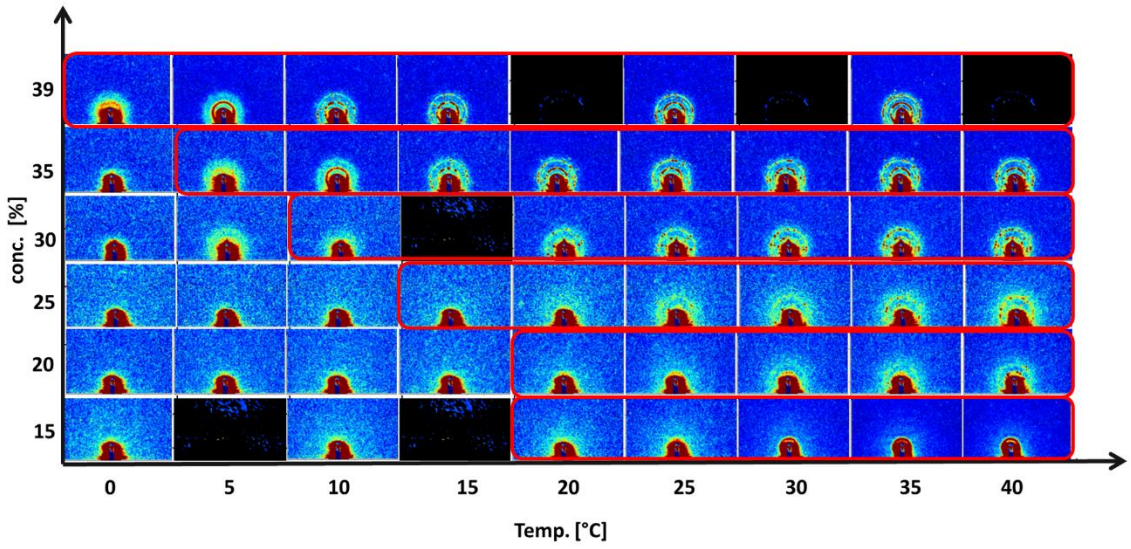

Figure 4-65 SAXSpace 2D scattering profiles for F108 samples as a function of temperature, where red frames represent the predicted transition temperatures from DSC measurements. The blackened out boxes were used in place of missing data.

Applying same analysis from the F127 section (equation 4-2) on the structurally defined formulations at 40°C would give hard sphere radii of 8.5, 8.6, 8.1 nm for 30, 35 and 40%.

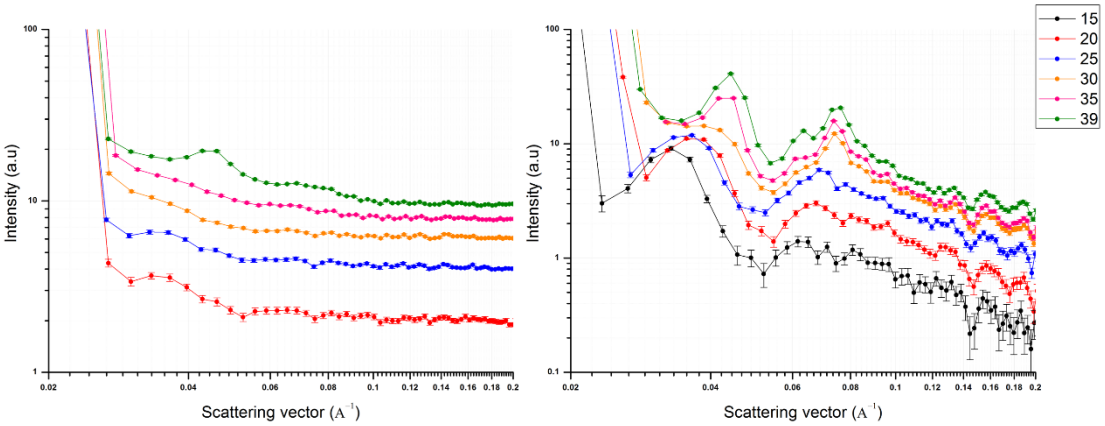

Figure 4-66 SAXSpace 1D scattering profile for F108 samples 15-39% at 40°C, profiles have been shifted vertically for clarity.

b) F68:

Figure (4-67) shows the scattering 2D profile of F68 concentrations from 20 to 40%. The majority of the profiles are dominated by water scattering across most of the temperature range tested. At the highest temperature tested (40°C) 30% was showing a faint halo indicating the start of micellar ordering. A similar halo can be identified in 35 and 40% at lower temperatures starting from 25°C which grow to develop ordered ring(s) by the end of the test. The corresponding 1D plots in Figure (4-68) at 40°C reflect the same result, where no defined peaks were recorded for concentrations below 35%. The most clear peak positions for 40% and 35% were at 0.067 and 0.064 [$Å^{-1}$] respectively, with a common second peak at 0.106 [$Å^{-1}$] for both concentrations though the data resolution made it difficult allocate extra peaks confidently. The copolymer is known to form BCC crystals which means that for 40% the position recorded at 0.096 [$Å^{-1}$] is a real peak rather than a noise signal. Using the first peak to calculate the approximate hard sphere radius gives; 6 and 5.7 nm for 35 and 40% at 40°C.

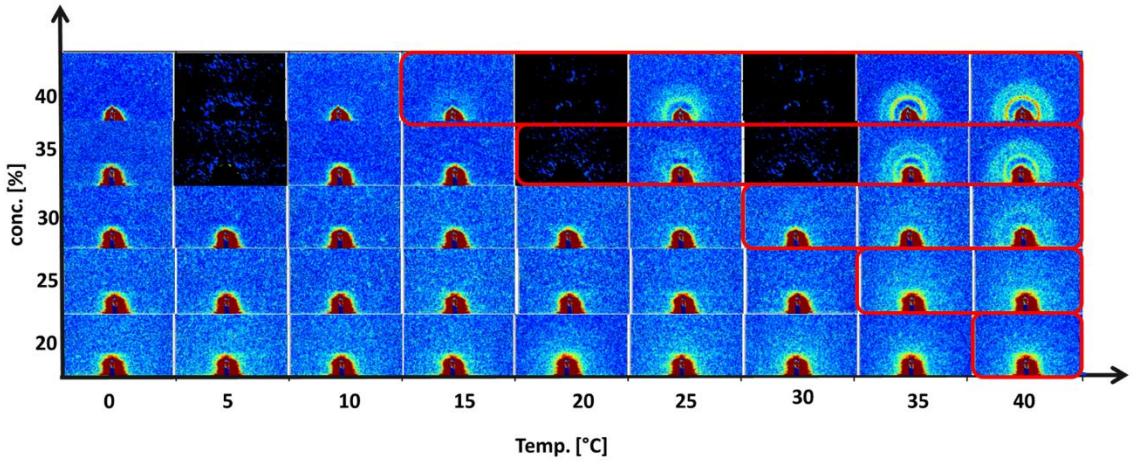

Figure 4-67 SAXSpace 2D scattering profile for F68 samples as a function of temperature, where red frames represent the predicted transition temperatures from DSC measurements. The blackened out boxes were used in place of missing data.

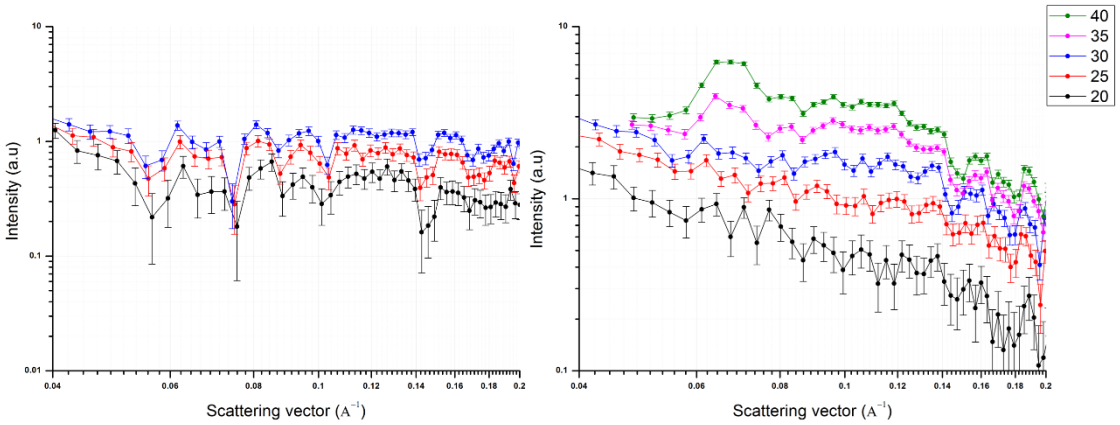

Figure 4-68 SAXSpace 1D scattering profile for F108 samples 20-40% at 40°C, profiles have been shifted vertically for clarity.

4.7. Results discussion

4.7.1 Neat PL F127 systems:

The properties of the F127 neat gels have been probed by different methods to elucidate the structural and behavioural characteristics under controlled static and dynamic conditions.

4.7.1.1 Equilibrium measurements:

Thermogravimetric inspections revealed a correlation between stability / water retention and the polymer concentration in the formulated systems, where the gels containing higher percentages were able to conserve the water for longer periods. Calorimetry emphasised the thermal events the system undergoes to reach the gel structure, starting with CMT that progresses to reach gelation. The spontaneous phase change attributes were demonstrated in Figure (4-7), showing omnipresent linear responses to thermal stimuli as a function of concentration, inversely proportional in the case of transitional temperatures (onset, peak and endset), where thermograms shifted to lower temperatures with increasing copolymer percentage while directly proportional for enthalpy. A linear correlation was found between the transition period represented by ΔT (the difference between the onset and onset temperatures) in Figure (4-69) and the formulation concentrations, which lasted between one and half to two minutes for all transitions to complete.

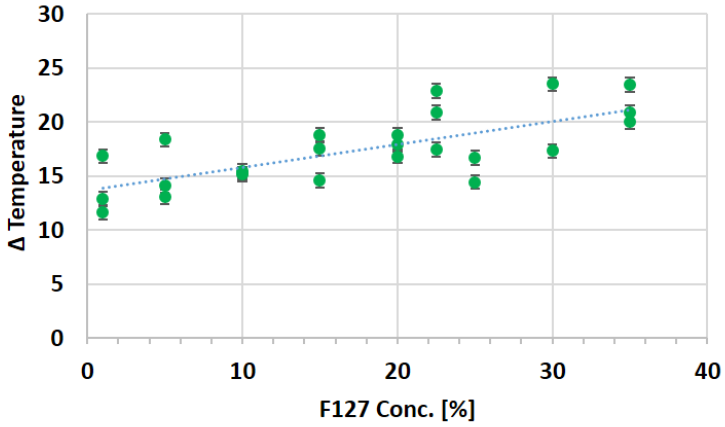

Figure 4-69 The difference between onset and endset temperatures based on the samples thermal data.

Several groups have recorded the appearance of a secondary peak within the main endothermic peak at higher concentrations that reportedly indicates gelation

Pham Trong et al. (2008), Meznarich (2012), Liu and Li (2015), however this peak was not detected in the current study, which expands over a wider range than most of these papers who reported it. DSC is informative to determine the phase change limits as reported in the results, yet for the systems in the study it cannot distinguish the different structures growing or breaking within the thermal cycles applied.

Scattering techniques (SAXS and SANS) were utilised to monitor the structural development as a function of temperature and concentration, allowing the interlinking of the thermal and structural results.

At low temperatures, the sample's x-ray scattering was faint showing wide featureless peaks, as expected for samples in the solution state below CMT. When CMT is reached, a scattering halo develops, representing gradual micellar growth in intensity seen across all samples above 10%. As the temperature increases further, the scattering intensifies to indicate the micellar association into ordered domains. The onset of structural changes were observed in almost identical temperatures to the ones registered by the DSC onset temperatures. These periodic structures, as demonstrated by peaks in the 1D and 2D spots build up to isotropic high intensity scattering peaks (1D) or rings (2D) in each respective profile with either increasing the concentration or elevating the temperature, correlating to what has been reported in the literature. Above room temperature, formulations higher than 15% experienced high levels of packing that can be traced to a cubic paracrystalline structure.

SANS scattering profiles performed on concentrations 10-30% confirmed the previous SAXS findings, although it revealed that 10% at 5°C was in the micellar stage rather than the unimeric solution state with a broad peak similar to that of higher concentration. The application of gel-fit model demonstrated that micellar size decrease was proportional to the concentration of the triblock copolymer. At 37°C, the concentration dependency is signified by the appearance of three distinctive peaks in 1D plots for all samples, that shift in chronological order from the lower to higher q values with increasing concentration, where q* values for 10 and 30% are 0.028 and 0.046 [$Å^{-1}$], respectively. Based on the nearest-neighbour distance and hard sphere radius calculation, the hard spheres became

closer and smaller in size with increasing concentration, indicating higher packing order. This is expected since increasing the copolymer concentration introduces higher numbers of polymeric chains capable of forming more micelles and therefore higher number of self-associated micelles into hard spheres constructing the cubic lattice. Based on the reciprocal positions of the peaks the structure was confirmed as FCC, in agreement with reports in literature of systems formed from unpurified F127 (Jiang et al., 2007, Jiang et al., 2008, Meznarich, 2012).

4.7.1.2 Nonequilibrium measurements:

a) T-ramps const. shear

Rheological measurements offered the ability to perform in-depth macroscopic behaviour investigations that directly correlate to the microstructures formed in the system during processing and application. Constant shear cycles with temperature ramps demonstrated a shear and temperature dependency as summarised in Figure (4-70).

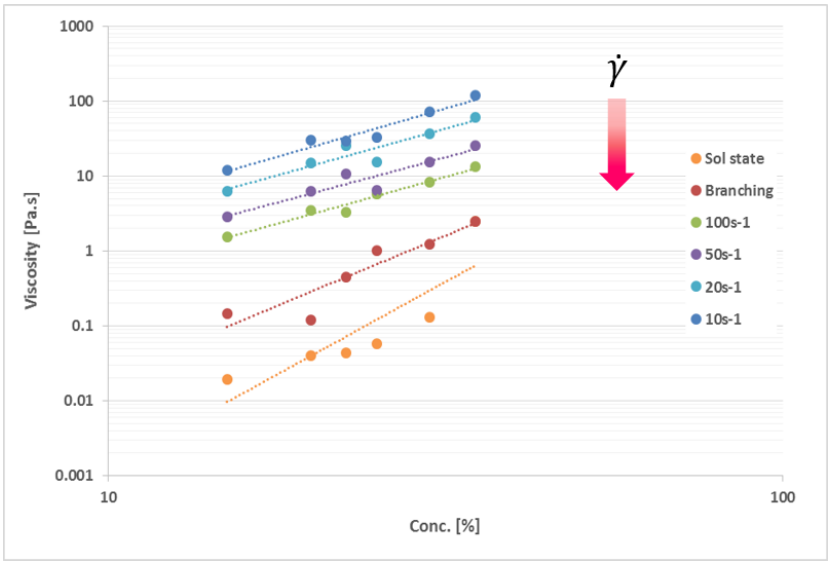

Figure 4-70 F127 viscosity values plotted as function of concentration according to the applied Shear.

The accuracy has been validated in Figure (4-9) by showing that the overlapping temporal shear viscosity decreases with the DSC thermal transition signal before the viscosity increases declaring the loss of Newtonian behaviour. Once gelation has initiated, the system starts responding to the shear stimulus, confirming clear

shear dependency across different shear rates both of which have been proven to be directly proportional to concentration.

The concentration dependency - discussed previously in the thermodynamic aspects of CMT and CMC can be quantified here in viscosity terms. For polymeric solutions the value of η_o can only be obtained above a critical concertation C_{crit}, required for the formation of entanglements (Mezger, 2011). As demonstrated in Figures (4-13, 15) there was no rheological response for concentrations of 10% and below where these systems shared ideally viscous flow behaviour. The respective η_o values for all concentrations under low shear rate (10 s^{-1}) are plotted in Figure (4-71). The results point to different plateaus after two critical concentrations 10 and 25% within three different regions. The first region is occupied by low concentrations, where the viscosity is a function of temperature. A plateau is reached above the critical concentration to exhibit a rheological response, this is demonstrated by the abrupt η_o increase presented at two temperatures of 5 and 40°C. The plot shows a significant three decade difference between η_o values caused by the temperature. The second plateau represents a different regime of highly concentrated systems with different shear response than the first, this behavioural distinction being highlighted in different tests. This plot can be utilised to predict the yield stress of the different regions based on initial viscosity values.

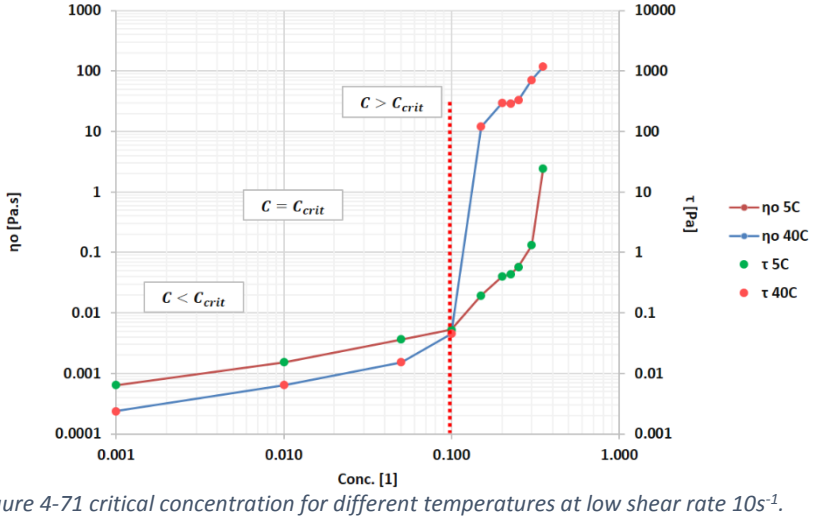

Figure 4-71 critical concentration for different temperatures at low shear rate 10s^{-1}.

The behavioural complexity was indicated by the formation of non-equilibrium microstructure in the presence of hydrodynamic shear fields - see Figures (4-17, 18). In correlation with the temperature/ physical state, one behaviour was

observed at each temperature. At the low temperature of 5°C, when the solution overcame wall-slip at low shear rates, it was predominantly a Newtonian fluid. In contrast, the gel at 40°C can described as a shear thinning Herschel-Bulkley fluid, with a transient behaviour across the shear ramp demonstrated by plateaus indicating the formation of the shear bands.

b) Shear flow scattering:

Figure (4-72) shows the shear response recorded by rheological measurements at 10 s^{-1} using Couette cylinder geometry and the matching SAXS 2D patterns recorded during the application of rotational shear using the Linkam shear cell 'parallel plate geometry' on the I22 beamline, both heated at 2 °C/min.

Since the recorded shear response in the shear cell is approximately comparable to the Couette (see 3.4.3). The scattering profiles acquired were overlaid to their corresponding temperatures to relate the thermo-rheological events to the structural changes recorded.

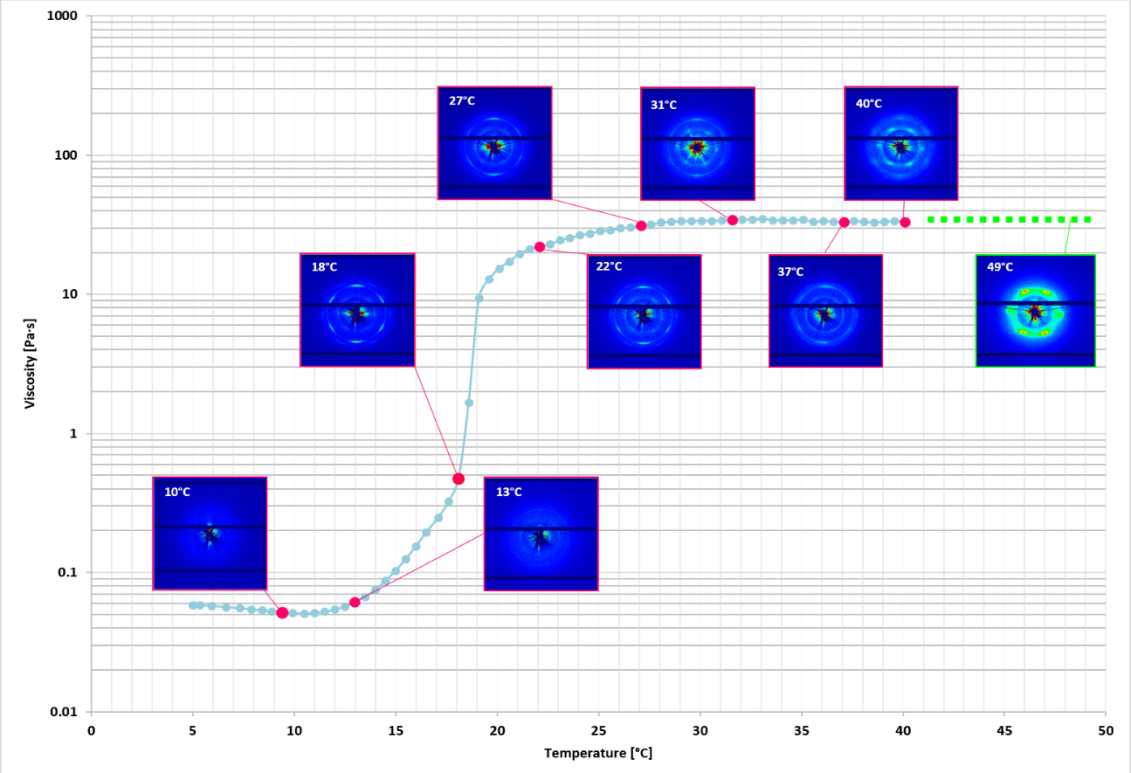

Figure 4-72 SAXS collected using shear cell during temperature ramps for F127 25% under constant shear of 10 s^{-1}.

The system shows a reduced viscosity with a weak halo at 10°C indicating the micellar state which, according to the DSC thermograms, starts at around 8°C.

Upon reaching transition at 13°C, two faint rings appeared that grew stronger when the critical gelation point is approached at 18°C - where the curve's branching usually starts. This coincides with strong structures depicted by three Bragg rings, with high intensity in the meridional and equatorial peaks, in the first and second rings, respectively. Depending on the frames recorded, the scattering profiles fluctuate in intensity as expected under shear application and the short measuring acquisition time.

After that point, the second ring's intensity was stronger than the first until reaching 30°C, where the intensity of the first order increased forming a more defined hexagon with higher intensity points at the previously mentioned positions. In this rheological range, the viscosity is constant with increasing temperature, indicating macrostructural stability. The gels have been described by multiple groups as 'hard' compared to the soft gels formed early after the transition (Hyun et al., 2006, Hamley, 2005, Hvidt et al., 1994). The structure keeps getting more ordered as implied by the continuing intensity increase in both rings. However this ceases at 40°C, and the scattering recorded was predominantly from the first order peaks showing almost symmetrical intensities across the hexagonal spots. Further increase in temperature resulted in the first order four sided peaks becoming stronger, consistent with Loose and Ackerson (1994) zig-zag motion predictions at low shear rate which has been recorded in FCC crystals under orientation forming 2D-HCP structure. This structure combines two types of crystals and has been referred to as RCP (McConnell et al., 1995, Pozzo and Walker, 2007a).

c) Mixed shear-SAXS (syringe pump):

In the injected gel experiments extensional flow was introduced to the system while collecting SAXS measurements on I22. The two tested samples 25 and 30% were injected in the solution state from a chilled syringe into a room temperature reservoir (ΔT=18°C), and considering the DSC peak temperatures were 12 and 8°C for each concentration respectively. This subjects the systems to instant yet incomplete gelation during the injection time allowed - as can be seen from ΔT in Figure (4-69) based on the results of 10°C/min heating rate. This will definitely put them in the gel transition, making them at this stage more

susceptible to shear effects at 18 and 13°C, according to the previous rheological measurements. The shear and combined extensional flow effects observed in the results section have led to the following conclusions:

a) The resultant structure is very ordered after injection, demonstrated by the sharpness of 1D peaks and strongly defined patterns in 2D, where the scattering intensity is a function of concentration.

b) The injection has resulted in the formation of spikes - that were not present in the steady shear experiments. These spikes correspond to locally more ordered domains which seed heterogeneous nucleation. Their growth density appears to be spatially linked to the disordered manner of initiation giving the scattering pattern a hazy speckled look. Meznarich (2012) has reported the appearance of individual spikes on the correlation ring and according to the published data they were stable with heating from 30 to 60°C with no surrounding localised growth although overall scattering intensity increased. These results were acquired under static conditions and only in one concentration 30%. Similarly, Prud'homme et al. (1996) reported the appearance of spikes in static SANS raw 2D data of 15%, which was attributed to the formation of large domains which disappeared with heating to 54°C.

The origin of the initial spike formation is likely to be connected to the unhomogenised flow arising in the channel accompanied by the continuous temperature change throughout the injection process, however the propagation of the spikes would be expected to be a product of temperature after shear cessation. Figure (4-73) shows the time-resolved peaks and their respective intensity progression recorded after different shear rates (1, 10 and 90 s^{-1}) for the sample containing 30% from Figures (4-44,45 and 46).

From the peak positions in Figure (4-73a), it can be seen that q* shifts to the higher q-values as the small peaks merge together indicating a reduction in domain sizes, matched by a steady increase in scattering intensity in in Figure (4-73b), signifying the continuous formation of ordered structures. The fitted peak values were similar for 10 and 90 s^{-1} while the recorded scattering intensities were inversely proportional to shear rate applied. However, the difference between the

values reduced as the tests progressed to almost identical values by the end of the test.

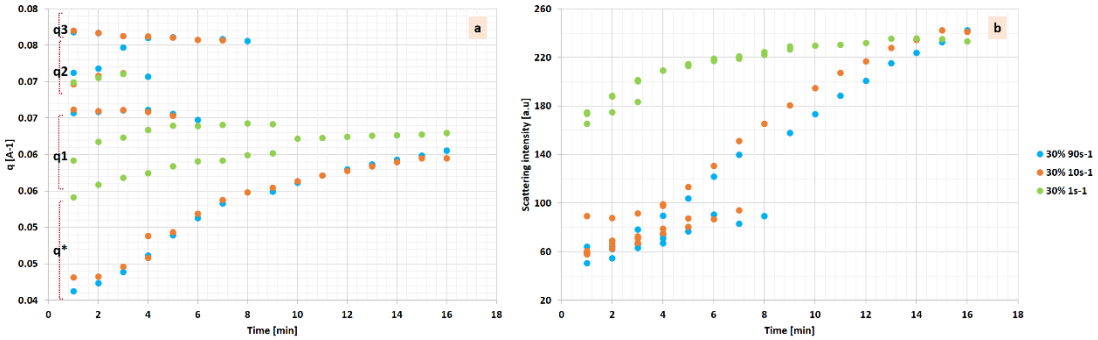

Figure 4-73 Progression of scattering vector and intensity values acquired for the injected F127 30% at three different shear rates.

c) The final structural orientation after injection is concentration dependent and directly linked to gelation boundaries, where samples containing 25% stabilised with first order rings having higher intensities in their four side peaks, while 30% stabilised to parallel arch like patterns with higher polar intensity. The annular intensity analysis was not accurate enough to determine the peaks distribution due to the high levels of noise recorded, with broad peaks that change between four and twofold depending on the shear rate applied. A solution of wormlike micelles under capillary flow have displayed analogous patterns. Under isotropic conditions diluted solutions of Pluronic P84, PI-PEO and PEB-PEO have formed cylindrical micelles in a hexagonal stretched lattice with ellipsoidal anisotropy in the flow direction. The anisotropy was lost after shear application to resulting in an isotropic structure as a result of micellar alignment (Castelletto et al., 2007, Trebbin et al., 2013).

In all previous shear alignment investigations performed on F127 (up to the time this text was written) experiments were restricted to steady shear or oscillation with no involvement of the extensional component. Under these conditions, the results indicated shear melting as a final structural transition with high values of imposed shear, as reported by Lopez-Barron et al. (2015) on F127 24% in ionic solvent. Jiang et al.(2007) reported that even after the application of shear rates up to 1000 s^{-1} deuterated gels of F127 20% maintained the layered structure with no distortions of the spherical structure's integrity although no further information was provided regarding the system physical status (softening or melting).

Based on the results indicating ordered close packed structure and the final lozenge structures that have been formed after shear cessation, it is suggested that the micelles might have lost their initial isotropy as a result of shear superposition, leading to induced orientation the flow direction. As shear is ceased two events are expected a) the layered structures will relax in the nearest register site to initial orientation, b) and since the temperature is lower than required for the stable gel formation, the gel will revert back to a weaker gel state ending in a mixed state of coexisting order-disorder, in this case hexagonal and cubic structures within the same matrix with extra spikes indicating a defected lattice.

A summary of all the SAXS experiments performed are presented in Figure (4-74).

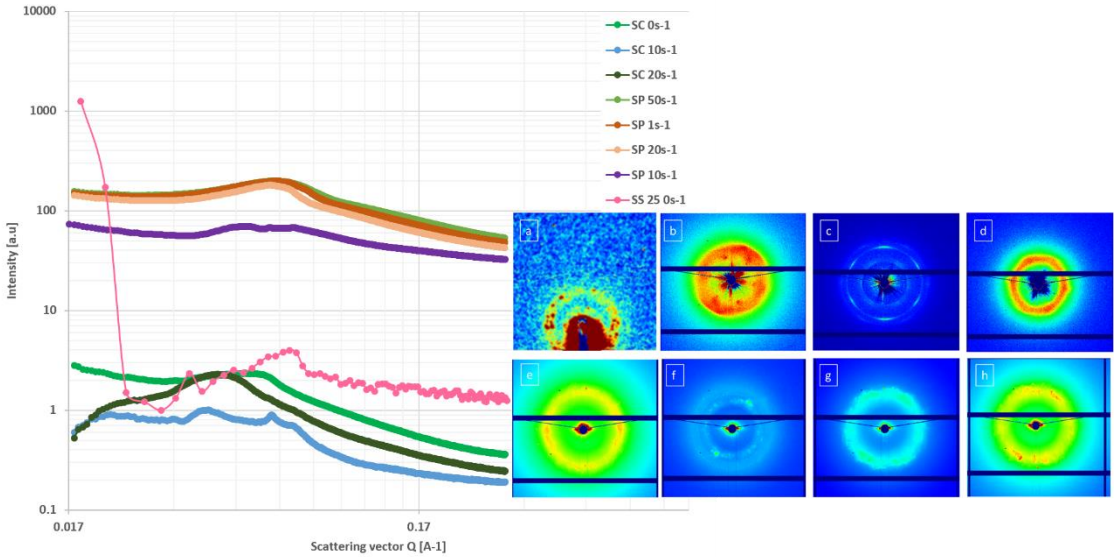

Figure 4-74 F127 25% measurements performed using multiple instruments; where SC= shear cell-SAXS (I22), SP= syringe pump-SAXS (I22) and SS=Static SAXS SAXSpace).

d) Rheo-SANS:

To elaborate on the constant shear-SAXS findings and reduce the inconsistencies rising from ramping the temperature, another set of rheological scattering experiments were performed. The simultaneous Rheo-SANS experiments were conducted using a Couette geometry with constant shear rates of 10 and 100 s^{-1} mounted in front of the SANS2D beamline at ISIS-RAL. The tests were repeated at constant temperatures according to each formulation's

respective viscosity curve; below gelation, transition and final gel formation at 37°C.

The datasets for two concentrations are displayed in Figure (4-75). Shearing the formulations at these two constant shear rates should ensure the steady state during the test period of 15 minutes to homogenise the sample and improve the data quality even though both shear rates lay in the middle tested shear banding transient regime - see Figure (4-18).

At low temperature, there was no apparent structure for all concentrations except sample containing 35%, where the scattering was isotropic with no orientational order.

Low shear 10 s^{-1}:

Under low shear rates at transition temperatures the samples showed a universal symmetry demonstrated by 3 orders of equal intensity Bragg peaks in an RCP lattice. Above gelation 35% displayed stronger isotropic scattering pattern compared to 25% (and the rest of the tested gels - see results section). This profile exhibited a sixfold symmetry with higher intensity in the meridional spots,

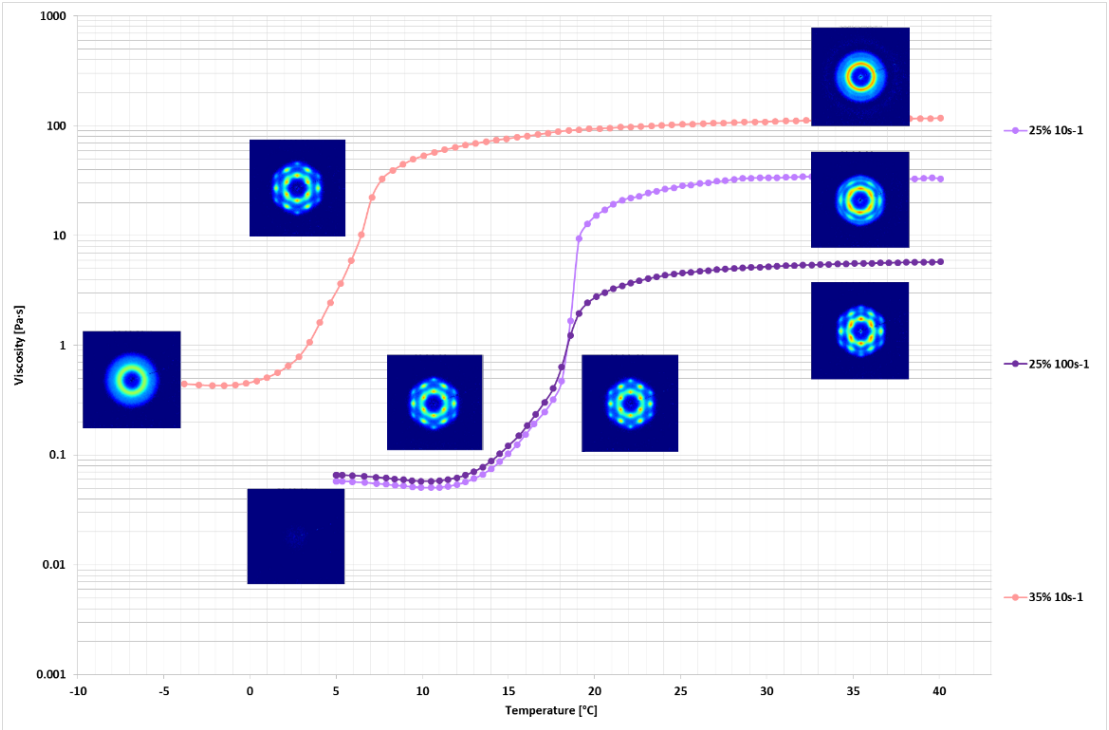

Figure 4-75 Rheo-SANS results for two different samples with the corresponding rheological steady shear profiles.

similar that recorded in the shear cell SAXS experiments under temperature ramps.

The isotropy recorded in 35% has three possible explanations. Either; 1) an experimental discrepancy during the measurement, where an unusual increase in viscosity was detected halfway through the test (result not shown). Or 2) a shear melting transition which has not been reported in concentrated F127 gel at these low shear rates. In high shear fields the structures of polymeric blocks and colloidal systems undergo an order-disorder transition, characterised by the disappearance of the sixfold scattering peaks in 2D profiles. 3) The third and most likely possible reason is a shear mediated tumbling, which creates a network of dislocated crystallites that have isotropic random orientation resembling the patterns acquired in the ‘powder’ state.

FCC crystals of deuterated polystyrene/polyisoprene diblock (d-PS/PI) suspended in a mixture of deuterated and hydrogenated decane have been reported to exhibit similar isotropy at low shear rates (below $1s^{-1}$). Although the published patterns display four spot asymmetry, the authors reported that at low shear rates the sheared crystallites support a rolling movement to create a random powder scattering patterns and as the shear increased they described the patterns as a combination of sliding layers and tumbling until 6 s^{-1} was reached and the 2D scattering displayed twinned FCC structures by zigzag movement McConnel et al. (1995).

Lopez-Barron et al. (2015) sheared a solution of F127 24% in deuterated ionic solvent ethylammonium nitrate (dEAN) at 40°C and attained high four intensity spots from shear rates starting from 1 up to 500 s^{-1} before reaching full isotropy due to shear melting .

High shear 100 s^{-1}:

The four sided higher intensity hexagons previously shown have been reported previously at temperatures higher than 40°C in shear-SAXS measurements and can be seen here at transition temperatures under the application of 100 s^{-1}. This has been recorded at this stage in Rheo-SANS samples across concentrations of 20 and 25%. This confirms that this state of ‘order’ can be either reached by

applying high shear rates resembling what can be accomplished at higher temperatures with lower shear rates as seen in Figure (4-75).

To compare the resulting degree of orientation under the two shear fields, the average full width at half maximum (FWHM) values of each azimuthal 1D Rheo-SANS experiment at the meridional positions (examples are shown in Figures 4-50-54) were used to quantify the orientation at the two temperatures of interest – see Figure (4-76).

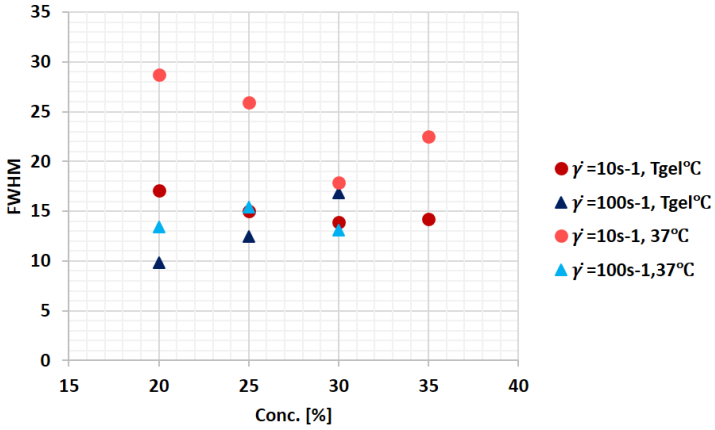

Figure 4-76 Changes in FWHM versus F127 concentrations.

The plotted results highlight two points, for T_{gel}, the orientation increases as function of concentration (FWHM values decrease) under 10 s^{-1} - as seen before the gels at this stage show a sixfold symmetry with higher intensity at the meridional positions. While at 100 s^{-1}, an opposite trend was observed where lower concentrations experienced higher degrees of orientation. Since only the meridional position averaged FWHM values were used here the results don't provide a fully accurate representation of the orientation since the gel containing 20 and 25% demonstrated different symmetry to 30% as seen in 4.3.2.2 b.

Above gelation, although azimuthal profiles indicated the same top/bottom anisotropy for all gels this did not reflect in a unified trend across the FWHM values. At 10 s^{-1} the orientation degree increased with concentration up to 30% followed by a drop for 35%. Revisiting the recorded viscosity values for 35% when temperature was held constant at 37°C showed an instrumental failure to reach the appointed shear rate due to reaching maximum torque values by the measuring system and the true shear rate values averaged at 0.1 s^{-1} making the fitting value for 35% unsuitable to be used in this comparison.

No clear trend was observed at 100 s^{-1}, where the intermediate concentration of 25% showed higher value than 20 and 30%. It is worth mentioning that the Lorentzian fit applied on 20% profile had the lowest confidence value of R^2= 0.95 compared to 0.98 and 0.99 for 25 and 30% respectively.

At isothermal conditions shear thinning arises from the ordering of layers by sliding in the shear direction and at high enough shear rates this results in shear melting. To quantify the effects of each variant on the structure at each shear rate comparisons should be made to the isotropic 'quiescent' samples. The shear induced melting proportion can be determined by the degree of order ratio (DOO) in the 1st order peaks at any shearing stage, where the paracrystalline phase represents the disordered phase and the sliding layers are the ordered equivalent. Different methods based on the same principle have been utilised. The ratio will remain constant until reaching the critical melting shear rate before dropping to null values depending on the material and shear limits. Based on the results presented the DOO is the most appropriate analysis to be performed (López-Barrón et al., 2015). However, the isotropic 2D profiles of the samples are not available for the comparison at the time being.

It was observed that at the transition temperatures, even though the rheological response for different shear rates looks identical, the underlying microscopic structure does not, where the near-to-symmetry was acquired at 10 s^{-1}, a clear fourfold symmetry was dominant at 100 s^{-1}. After gelation less prominent differences in the shear thinning region were displayed with ubiquitous six fold-higher meridional peak symmetry, suggesting that this morphological structure is the final and most stable over the applied temperature range, even after the application of high shear rates, which has not been predicted in sheared colloidal crystals. However these predictions have been on materials having the same flow mechanism. In reality this is hardly the case especially in systems like the one studied which might undergo several transitions during shearing making it even harder to determine the structure from the averaged collected data in one orthogonal direction or the underlying flow mechanisms without rigorous experimental work in multiple directions inside the shear gap.

The results correlate to those obtained by Pozzo and Walker (2007a) for F127 25% under the application of 10 and 100 s^{-1} at 25°C (above gelation temperature but before the gel plateau). Their sheared gels demonstrated similar anisotropic scattering showing higher intensities of top and bottom spots in the first order and second order displaying the four spots at 100 s^{-1}. The appearance of the fourfold symmetry in the second ring led the authors to suggest the system might be close to the sliding layers prediction and theorised that the peaks were a result of the coexistence of multiple crystal orientations within the shear gap: pure FCC and RCP, while the sliding layers was based on a single orientation of the entire sample. Jiang et al. (2007) studied F127 20% gel at different shear rates from 0.01 to 600 s^{-1}, and reported the formation of 2D-HCP stacks in the shear plane with 2D profiles similar to the recorded Rheo-SANS data but no azimuthal analysis was published.

Experiments performed on another shear banding gelling system of a lower molecular weight, F68 46% that forms BCC structures have demonstrated the existence of three coexisting orientations as a result of a layer slip mechanism imposed by an intermediate shear rate of 50 s^{-1} (Eiser et al., 2000a).

Based on the results presented in this study, similar assumptions are made supported by the wider sample pool tested in this study, where most of the samples displayed different 1st and 2nd order structures, indicating the possibility of formation of multiple structural orientations within the shear gap by different mechanisms.

Dimensionless shear rate - Peclet number

The F127 gel properties can be described in colloidal suspension terms. Displaying both Newtonian and non-Newtonian behaviour depending on environmental conditions, a medley of thermodynamic and hydrodynamic interactions. The coupled scattering and rheological measurements under different shear rates, temperatures and using multiple concentrations allow further analysis.

The thermal, structural and rheological terms can be combined to calculate the Peclet number (Larson, 1999):

$$Pe \equiv 6\pi\eta_0\dot{\gamma}a^3/k_BT$$

Equation 4-3

Here, the rheological conditions are represented by η_0 the zero shear viscosity (initial) and $\dot{\gamma}$ is the shear rate applied. a is the particle radius from scattering (using the micelle's R_g below CGT and R_{HS} for the crystal hard spheres above

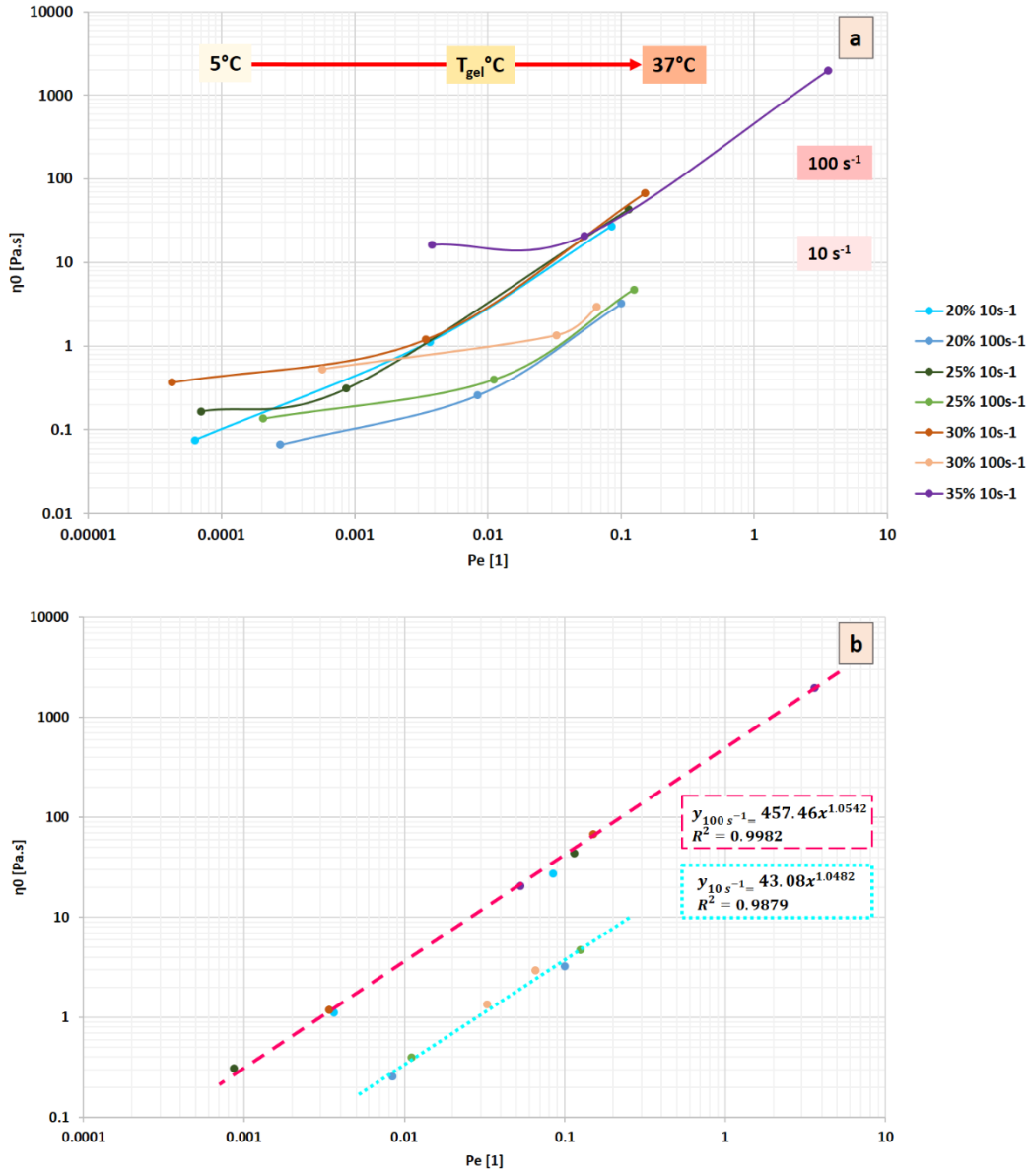

Figure 4-77 The calculated Pe numbers for F127 formulations from the Rheo-SANS data with their respective viscosities, where; (a)The Pe numbers calculated for two shear rates and the three temperatures 5, T_{gel} and 37°C. (b) The Pe numbers for T_{gel} and 37°C from (a) were found to follow the same trends under the same shear rate.

CGT). The thermal conditions are represented by k_BT the Boltzmann constant and the applied temperature. The calculated results are presented in Figure (4-77).

At low temperatures the systems are in the sol state and demonstrated a complete relaxation to shear by their constant viscosity values, although on a microscopic level the R_g is clearly prone to shear fluctuations. With elevation of the temperature, the graph highlights gelled system sensitivity to shear rate. Higher concentrations naturally display higher viscosities and have more compact spheres but, rheologically, they correspond to the shear in an identical fashion to the lower concentrations depicted by the trend line. The scaled power law observed in earlier measurements is illustrated here combining all the system properties inspected, where both shear rates 10 and 100 s^{-1} share a value of n~1 and the k is approximately ten times higher for 10 s^{-1} due to the shear thinning effect. This indicates the logarithmic scalability of the thermo-rheological response of the gels. Prior knowingly of shear conditions would be sufficient to determine the approximate hard sphere particle size making up the crystal lattice and allow prediction of the initial peak position if the sphericity is maintained.

The system was tested at two stable regimens governed by two vying forces, repulsion during micellisation and attraction during gelation and one intermediate representing the transition in between. The two system interactions respond to temperature and shear differently. As demonstrated in the results, micellar size fitting indicates an R_g decrease with increasing shear rate with no significant macroscopic effect on the system. It is highly unlikely that the shear effect is non-existent but within the time frame and the techniques used it is difficult to measure due to the rapid relaxation process connected to the fast kinetics of Brownian motion. However this was hardly the case for the associated micelles 'hard spheres' making up the gel bulk. R_{HS} values were almost identical for both shear rates (except for 30%) but the whole interconnecting layers moved with the flow creating the structures observed in rheological and scattering measurements.

Pe number values can be used to calculate the characteristic time for diffusion t_D - the time for a sphere to diffuse a distance equal to its size (Jones, 2002):

$$t_D = Pe/\dot{\gamma}$$

Equation 4-4

e) LAOS

Amplitude strain sweeps were applied to the gels in a range covering low to large amplitude oscillatory shear. The recorded behaviour correlates with LAOS measurements on F127 20% reported by Hyun et al. (2006), the gelled formulations can be described as a complex fluid type III, characterised by weak strain overshoot. Figure (4-78) demonstrates the different transitions the 20% gel structure undergoes upon strain application.

At low strains (region 1), G' and G" are constant (linear VE region) the elastic proportion resists deformation up to a certain value under the imposed strain and the structure is predominantly stable FCC. Above this critical strain the structure is broken into layers and the polymer chains are aligned in the flow field forming distorted crystals, which can be seen with characteristic G" overshoot that represents the increase of energy dissipation in the system due to structural breakage (region 2), this correlates to increased area of the ellipse seen in Lissajous diagram from Figure (4-33). At large strains both moduli are decreasing due to the sliding layers displayed by the viscous property dominance indicating shear melting (region 3). In the shown example the moduli values have dropped from 19249 and 613 [Pa] at the beginning of the test to 6 and 44 [Pa], for G' and G", respectively. The behaviour is equivalent to the non-linear response observed at high shear rates that has been widely referred to as slip-stick flow (Hamley, 1998).

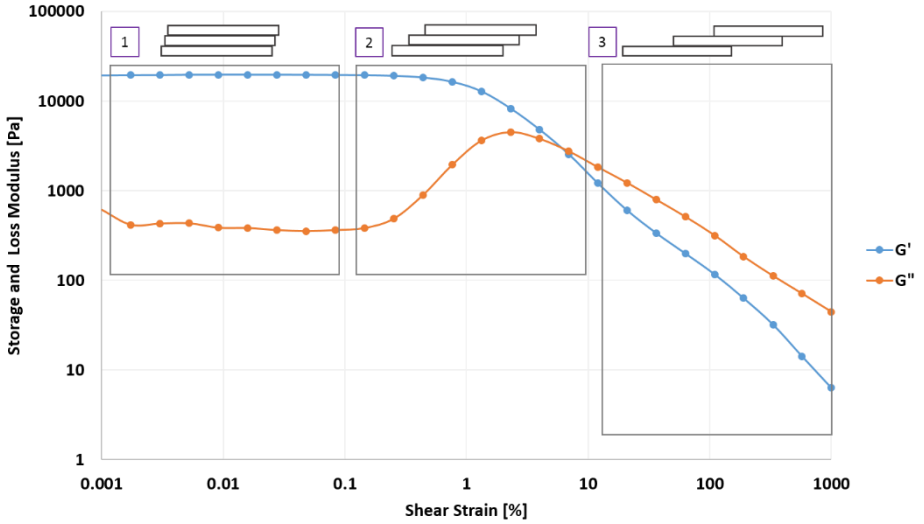

Figure 4-78 LAOS performed on F127 20% at ω=10 rad/sec and 37°C.

4.7.2 Pluronics discussion:

The properties of F127 which contains 70% PEO have been compared to two different molecular weight Pluronics; F108 and F68 with molecular weights of 14600 g/ml and 8600 g/mol which both on average contain about 80% PEO. The copolymers comparison/details were provided earlier in materials and methods (-see Chapter 3).

4.7.2.1 Thermal properties:

The peak temperatures and enthalpies for the different systems are plotted in Figure (4-79). It can be clearly seen that that formulations of F127 have lower peak temperatures for the same copolymer fraction, signifying that the thermal transition would occur in F127 earlier than F108 and F68 - which comes last with the highest peak temperatures.

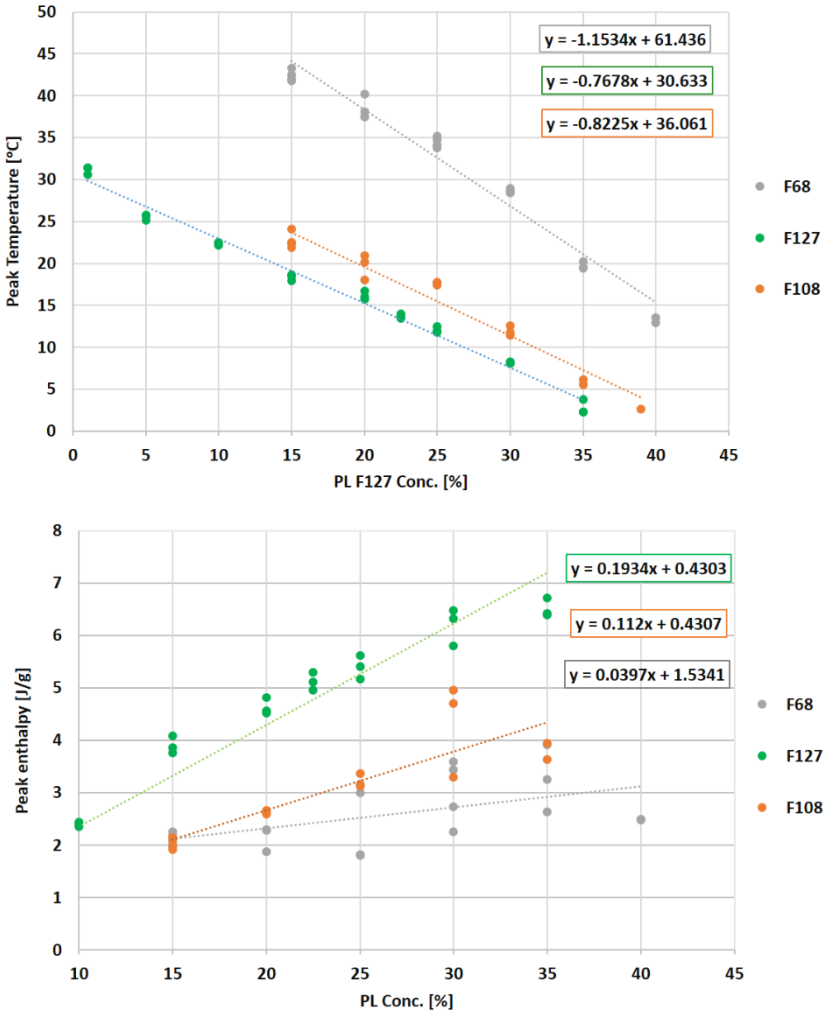

Figure 4-79 DSC peak temperatures and enthalpies of F127, F108 and F68, each run was repeated three times.

This can be used as an indicator of gelation and a factor to take into consideration to predict the thermal properties of mixed system of Pluronics. The thermal transition depends on the balance between PEO and PPO units with CMC (or CMT and therefore CGT) and decreases with increasing the number of hydrophobic PPO units.

For the same copolymer content of F68 and F108, formulations of F108 had earlier transition onset signifying, even though F108 has slightly less PPO content, its higher overall molecular weight (chain length) aids the thermal response leading to the observed trend as in agreement with Alexandridis and Alan Hatton (1995).

4.7.2.2 System morphology:

The structure of the formed lattices were investigated by SAXS. The peak positions for each Pluronic agrees with the literature, where F68 forms a BCC and both F127 and F108 micelles associate onto an FCC matrix. The ordering onset and structural development were functions of temperature and copolymer content as seen in Figures (4-35, 66, 68). The micelles grow smaller in size with increasing concentration. Figure (4-80) shows a comparison between formulations containing 30% of each Pluronic at 40°C. At this concentration both F108 and F127 are at the gel state exhibiting hard sphere crystallisation with hard sphere radii of 8.5 and 9.53 nm.

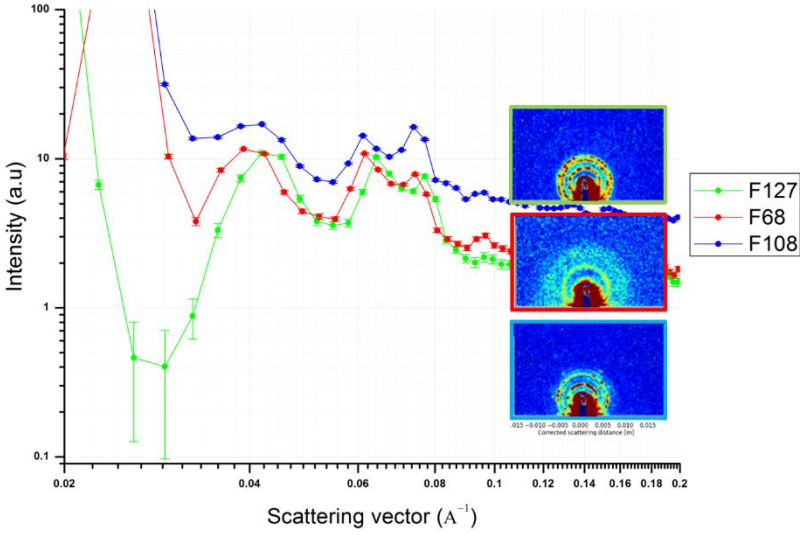

Figure 4-80 SAXS 1D profiles for the same concentration of F68, F127 and F018 at 40°C.

The critical issue of determining the particle size in Pluronics is still a matter of ongoing uncertainty in the literature, especially in gel forming concentrations. At low concentrations just above CMC, the measurement is straight forward using light scattering techniques; dynamic or static which often record values of hydrodynamic radius (R_h) of 10-11 nm for F127 1% (Wu et al.,1997, Meznarich, 2012). However these methods do not accommodate higher concentrations. SAXS and SANS offer accurate dimensional information, and more detail when selective deuteration is applied in SANS, providing the micellar core and shell dimensions. But most of the micellar/hard sphere radius values published are model dependent with a scarcity in referring to the scattering vector or cell parameters which does not allow a robust comparison from different research group measurements. The values reported here were compared to the published data when possible using cell size. The values reported for the same diluted region acquired by SANS were quite low compared to light scattering. Dreiss et al. (2007) reported R_g values of 5.3 and 4.3 nm for F127 1 and 3% at room temperature, both above CMC and CMT. In the same range, Valero et al. (2018) reported almost double the size with 10.9 nm for 4% at 37°C. Table (4-3) shows a round up for some reported values and measurements techniques. This applies to a lesser extent on F108 and F68 since these are not widely used as F127.

Table 4-3 A collection of reported radii values highlighting the technique and concentration used.

Method	Conc.[%]	reported values [nm]	T [°C]	Ref.
DLS	0.1,0.5	R_h=10.5	37	(Singla et al., 2016)
GPC	1	R_h=10	50	(Malmsten and Lindman, 1992)
DLS	1	11	25	(Wu et al., 1997)
SANS	1	R_{HS}=16	50	(Lin and Alexandridis, 2002)
DLS	1	R_h=12.18	37	(Pragatheeswaran and Chen, 2013)
DLS	2	R_h=10.2	35 -45	(Attwood et al., 1985)
SANS	1 , 3	R_g=5.3, 4.3	25	(Joseph et al., 2007)

DLS	4	R_h=10.9	37	(Valero et al., 2016)
DLS	5.26	R_h=18.7,10,9.9	25,40,60	(Basak and Bandyopadhyay, 2013)
DLS	1	R_h=10nm	70	(Meznarich, 2012)
SANS	20,25,30	a=31.9, 30.6, 29.3	40	
SANS	15	a=32, R_{Hs} =11.3 (based on q value)	50	(Li et al., 2006)
SANS	18	a=29, R_{BCC}=4.3	gel	(Dreiss et al., 2009)
SANS	20	a= 28,R_{HS} =12 (based on q value)	17	(Mortensen and Talmon, 1995)
SANS	5	R_g=2.2	5	
Cryo-TEM	11.7	interlayer=14	-170	
Sans	9.97-19.4	a(BCC)=25.6-20.8	29.6	(Prud'homme et al., 1996)

The cell parameters reported in this study align with values reported in multiple studies where enough data is provided for comparison. However, no data was found for sheared system as discussed previously in the results section.

4.7.2.3 Rheological properties:

It is expected that the gelation mediated by the hydrophobic transition in F108 and F68 will require higher quantities to establish the same distinctive gelation observed in the F127 systems since both Pluronics have lower PPO content. For the sake of simplicity, the rheological behaviour formulations with the exact content of each copolymer at 20% under different shear rates and ramping temperatures are compared in Figure (4-81). For the concentration tested, F68 acted like an ideal Newtonian fluid with ten times viscosity than pure water. Temperature and shear dependencies were obvious in F127 and F108, with the characteristic three regions of; temperature dependent viscous fluid at low temperatures, thermal transition and shear dependent gel. The rheological results correlate to the previously discussed thermal transitions detected by DSC,

where F127 experienced earlier transition onset than F108 and F68. The gel strength denoted by the recorded viscosity values for F127 and F108 are very similar for each applied shear rate.

Reports in the literature addressed the banding phenomena observed in multiple polymeric blocks including Pluronics; P84 (cylinders) by Manneville et al. (2007) and Waton et al. (2004), F68 (cubic-BCC) by Eiser et al. (2000a and 2000b) but no reports documenting its existence in F127 and F108 forming FCC crystals are available.

Eiser et al. (2000) performed rheological experiments on 35% F108 at 25°C, which is well above gelation as can be seen from the temperature ramps in Figure (4-58). Their results demonstrated unexpected shear thickening and no banding in F108 compared to its lower molecular weight counterpart F68.

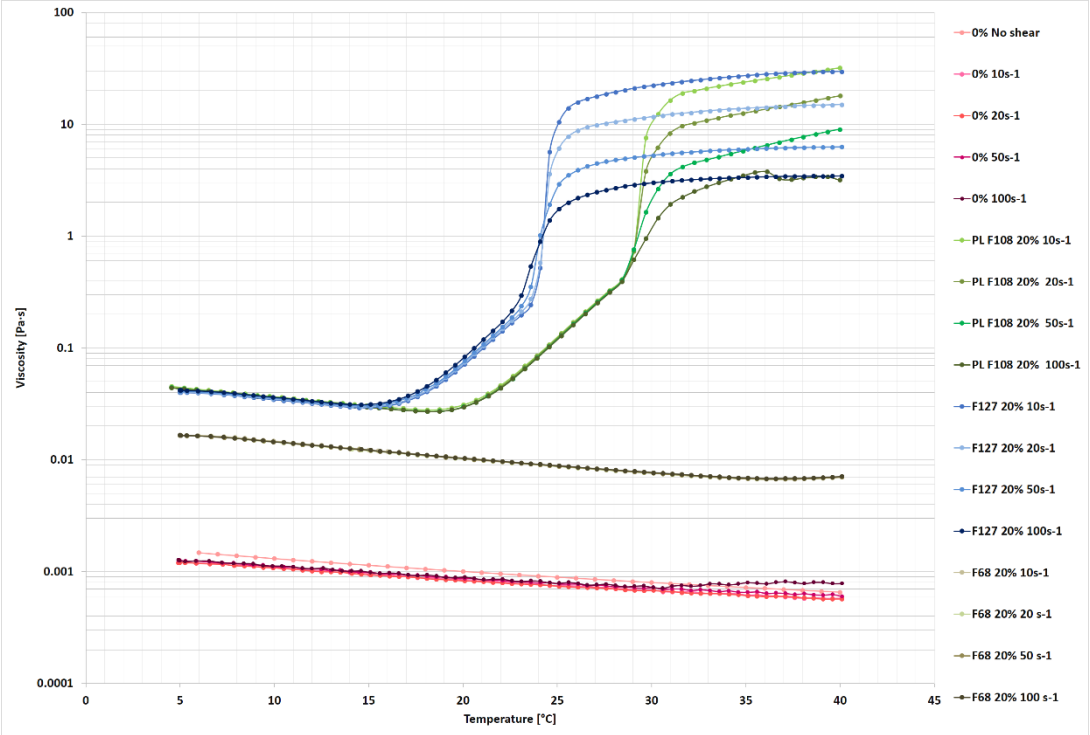

Figure 4-81 Temperature ramps at constant shear rates on 20% of each Pluronic compared to pure water.

The three triblocks behaviour under ramping shear using the same concentration from the T-ramp is compared in Figure (4-82). The constant temperature 37°C was above gelation for higher molecular weight blocks which exhibited the characteristic banding plateau. Shearing in the copolymers is attributed to the

sliding layers, that resulted in spatial coexistence of different orientation states under steady shear demonstrated by scattering patterns and the reported results on F68 (Eiser et al., 2000a).

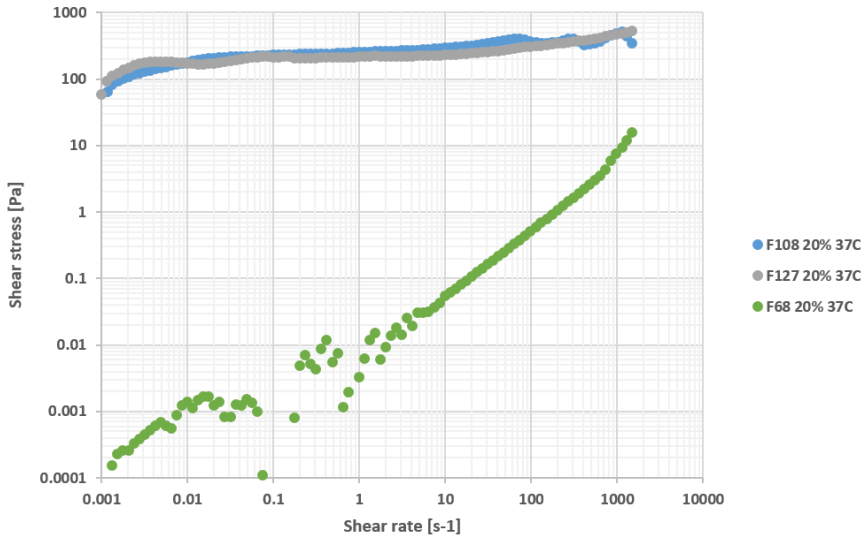

Figure 4-82 Shear ramp results for the same concentrations of F68, 127 and 108 at 37°C

The application of high strains resulted in annealing the defects from steady shear and resulted in one twin but with different confirmations across the Couette shear gap in F108 (Diat et al., 1996). Mohan and Bandyopadhyay (2008) performed a systematic study on F108 in the linear regimen that overall correlates with the results reported here taking into consideration a different heating rate but they did not report the behaviour under shear ramps. This makes this study the first to document such transient behaviour in F108. Though banding has been suspected in F127 (López-Barrón et al., 2015, Jalaal et al., 2017), no actual reports documenting the shear banding phenomena and its correlation to concentration can be found in the literature.

Chapter 5 PEG-blends

A group of varied molecular weight homopolymer (PEG) was utilised to probe the effects of introducing a common pharmaceutical ingredient with a range of different hydrophilicities to the aqueous systems of F127 to control their properties. The blends thermal, rheological and structural properties were elevated and compared to the neat systems as a function of PEG's concentration and Mw. The physical blends were prepared with the introduction of the PEG homopolymer; weighing from 1000 to 2000000 g/mol into gel formulation of F127 20%. The blends preparation method was previously discussed in section (3.1.2).

5.1. Thermal Analysis:

5.1.1 TGA

PEG-blends containing 1% of each homopolymer were tested to determine weight stability and their ability to retain water as compared to the neat formulation. Figure (5-1) shows an overlay of PEG-blend results acquired during temperature ramps from 27 to 400°C.

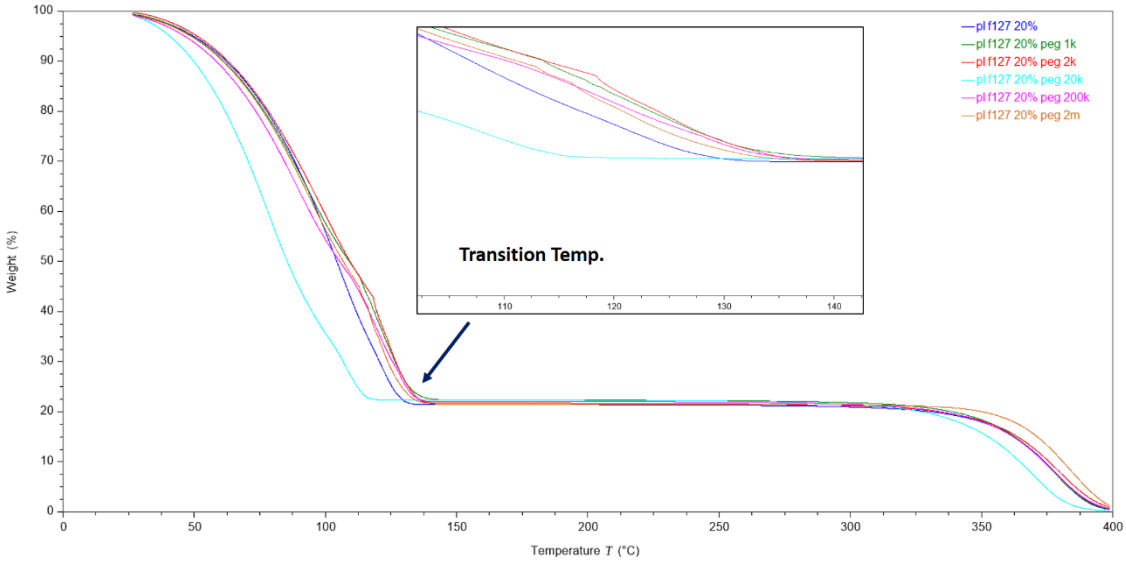

Figure 5-1 TGA heating ramp from room temperature to 400°C.

The curves showed a step transition, where the first weight loss correlates to water content loss and the second for the polymer's degradation. Most of the blends transition temperatures were close to that of the neat 20% F127 gel, which recorded a slightly lower transition temperature than the blends at 140.9°C. The

blend containing 20K recorded the lowest transition temperature at 124.4°C, which persisted when the test was repeated using different batches. Figure (5-2) show the formulation's corresponding transition temperatures.

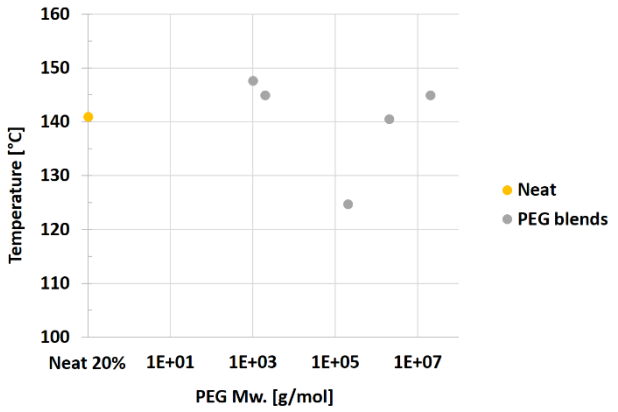

Figure 5-2 TGA transition temperatures for PEG-blends as function of PEG Mw.

5.1.2 DSC

a) Static measurements:

The blends exhibited the same thermal transitions as the neat gels during the heat-cool-heat cycles. Blend's thermograms showed a single, broad endothermic peak in the heating ramps indicating micellisation/gelation, which was reciprocated by an exothermic peak in the opposite direction during the cooling cycle representing the gel melting at around the same temperature as the endothermic peak. Figure (5-3) shows the overlaid PEG-blend thermograms in

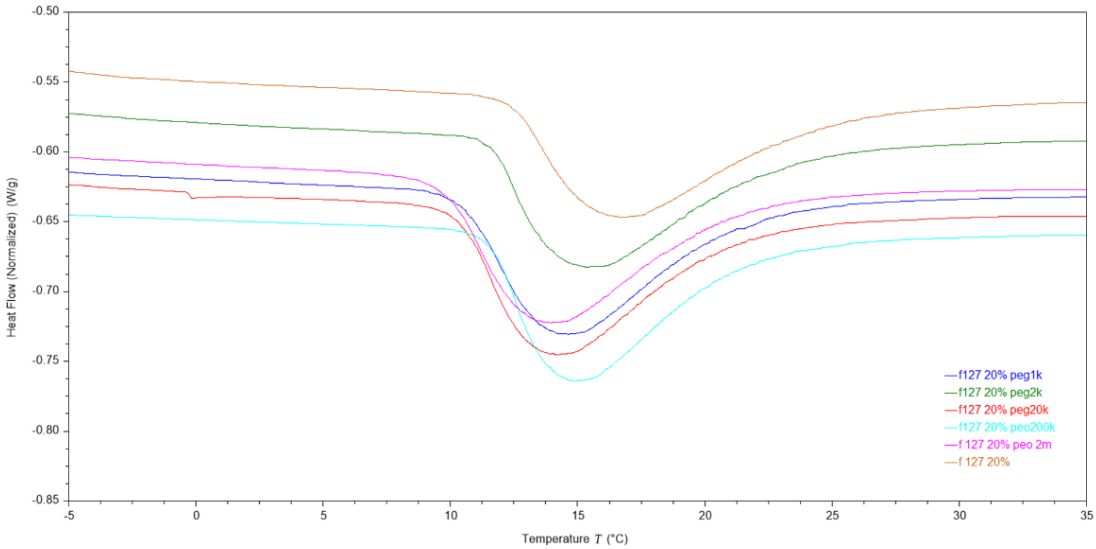

Figure 5-3 DSC thermograms curves for PEG-blends.-blends.

the range of -5 to 45°C. The thermal variables recorded during the heating step for PEG-blend formulations are plotted in Figure (5-4).

The results demonstrated a weak correlation with increasing PEG molecular weight, where the largest slope values were seen for the end-set temperatures. The blend values of T_{onset}, T_{endset} and T_{peak} were very close to what have been previously obtained for the pure F127 20% formulation. A similar trend was observed for the peak enthalpies, where the measured values had a slope of -0.02.The blend temperatures averaged at 10.9 and 14.8°C, for T_{onset} and T_{peak} with an averaged enthalpy of 4.5 J/g. These values were slightly lower than these recorded for the pure system values of 12.3, 16.1°C and 4.6 J/g.

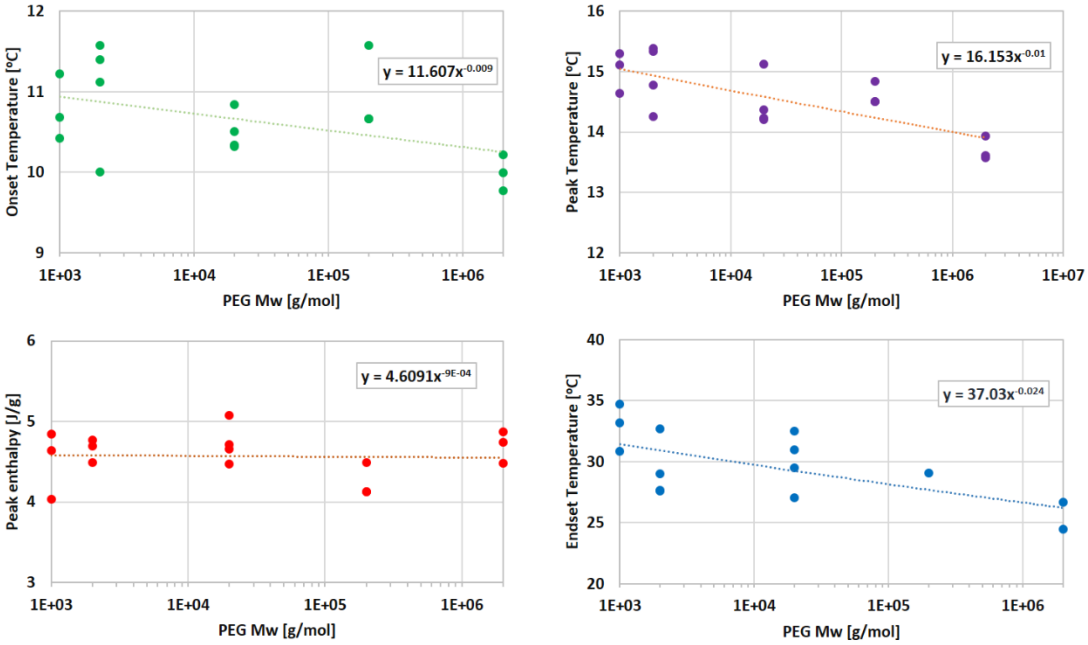

Figure 5-4 variables obtained from the different blend thermograms, indicating onset, peak and endset temperatures. In addition to the endothermic peak enthalpies for each respective blend.

MDSC:

The modulated DSC runs showed identical thermal responses to the neat gel. The thermograms exhibit the same peak from the standard DSC tests and did not reveal any additional peaks - see Figure (5-5) .The results demonstrate that the transition peak signals are the sum of the reversing and non-reversing signals, due to the change in heat capacity and the micellar ordering, similar to that observed in the neat gel experiments.

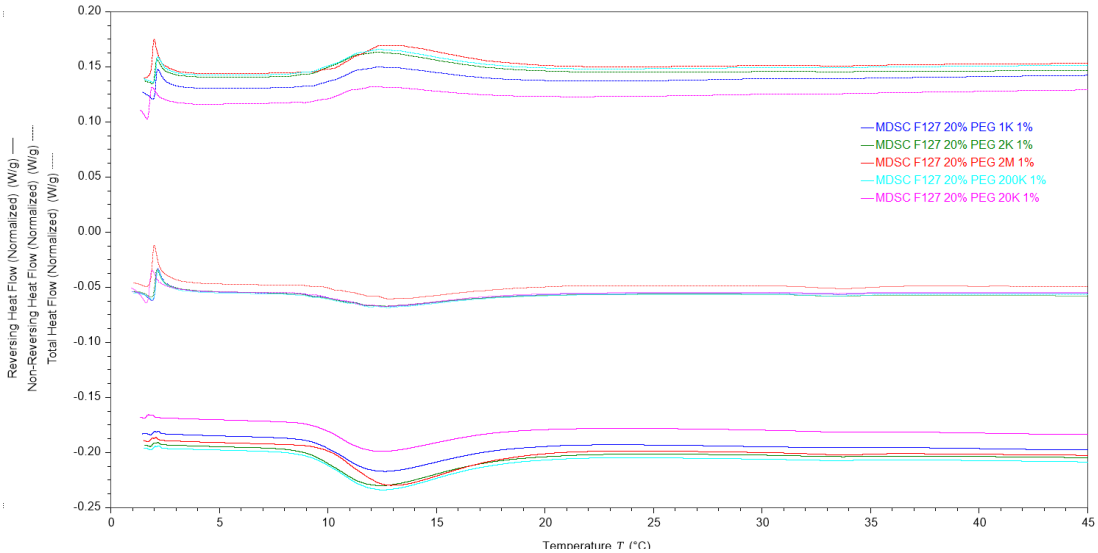

Figure 5-5 MDSC thermograms for PEG-blends.

b) Thermomechanical measurements:

The thermal properties of the sheared gel samples were investigated. Samples which had been previously sheared under constant shear rates, from 10 to 100 s^{-1} were tested after cessation of shear. The runs started in the gel state with cooling cycles from 40 to -20°C ensuring the gel structure had 'melted', then temperatures were increased in the heating step, which allowed the study of the dynamic effect of shear and temperature on gel transition compared to temperature only from the static DSC measurements.

Figure (5-6) shows four thermograms for PEG2M-blend which has been tested with and without shear.

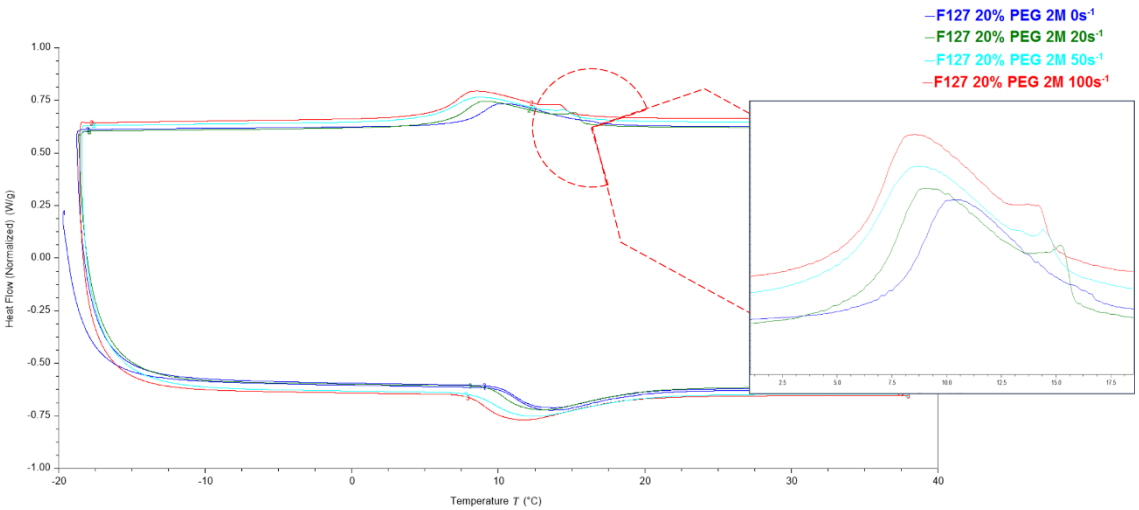

Figure 5-6 DSC thermograms for four different samples of 2M-blend; static and after the application of three shear rates of 20, 50 and 100 s^{-1}. The insert showing the peaks displayed in the cooling step.

As seen earlier for neat gels, the sheared PEG-blends displayed an extra feature within the usual broad exothermic peak in the first cooling cycle – which was directly performed after shear, indicating a structural order associated with shear. However, after cooling and reheating the sample again the additional peak disappeared. Except for this aforementioned small additional peak in the first step, the sheared sample thermogram looked identical to the one obtained under static conditions.

Thermograms of sheared 20K - blends did not display the extra peak the other formulations exhibited and they looked identical to the non-sheared gels, even when high shear rates were applied. Figure (5-7) shows the shear peak enthalpy values of the different blends. The gels were weak and the same challenges reported in Chapter 4 were encountered for these experiments including sampling position within the Couette, structural weakening during the loading which caused time variation, all of which might have affected the test results.
Neat gels containing 20% F127, as demonstrated in Chapter 4, formed weak structures compared to gels containing higher concentrations of the copolymer. Therefore the detected peaks here confirms that PEG addition has aided the structural order under shear and made it more visible for most of the samples.

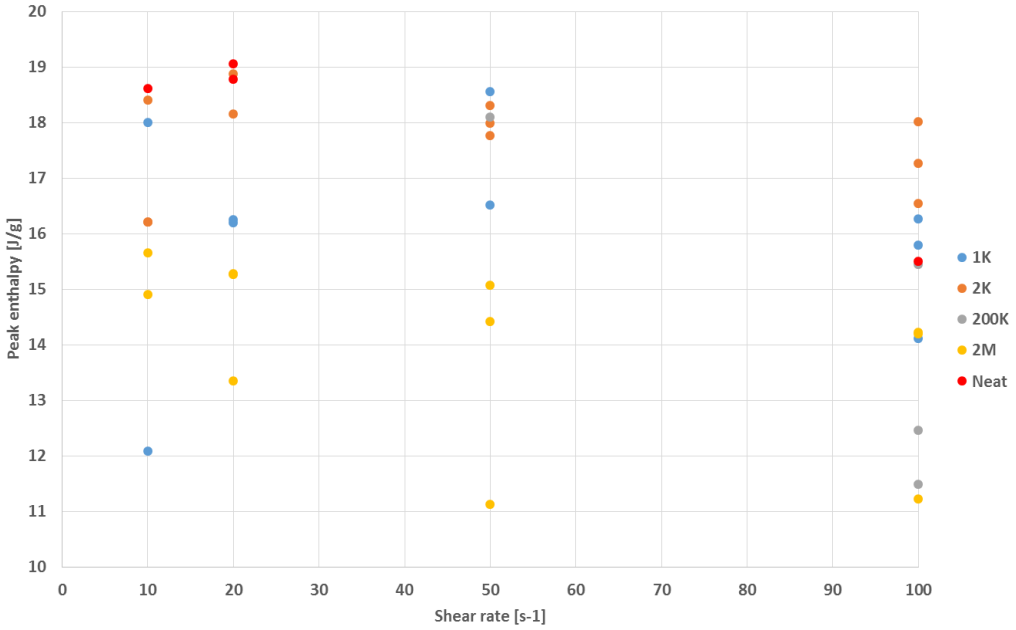

Figure 5-7 Enthalpy values of the shear exothermic peak recorded after applying different shear rates (10-100 s^{-1}), multiple points indicate the test repetitions.

5.2. Rheology results:

5.2.1. Temperature ramps at constant shear:

These experiments were performed as previously discussed in Chapter 3 where samples were subjected to a variety of constant shear rates with ramping temperatures up to 40°C. The results will highlight the effects of the PEGs addition, the concentration of the added homopolymer and its molecular weight.

a) The concentration effect

To investigate the concentration effect on the rheological properties, two different concentrations of low molecular weight PEG 1K and PEG 2K were tested at two copolymer fractions of 1 and 5%, the results being shown in Figure (5-8). In an identical trend to the neat F127 systems, the blends show the same three regions based on viscosity values; low, transitional and high. At low temperatures the formulations are Newtonian liquids exhibiting decreased viscosity with increasing temperature. Viscosity values increased by a decade in the second region as the ramp continues.

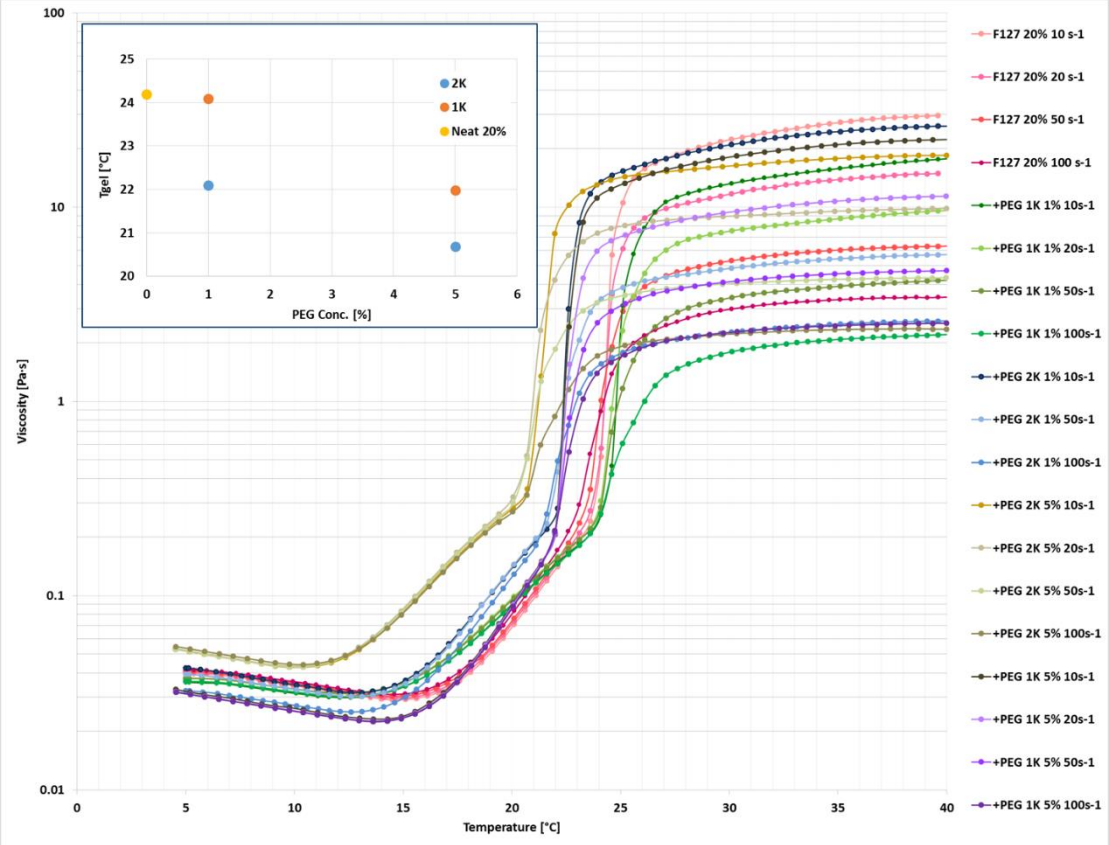

Figure 5-8 PEG-blends temperature ramps at constant shear rates on concentration of 1 and 5% of PEG 1 and 2K.

At a critical temperature, the formulations experienced an abrupt increase in viscosity to result in a gel structure. For the neat F127 20% formulations this occurred at 24.2°C, however for blends with the added 1% of each homopolymer the transition temperature dropped slightly to occur at 24.09 and 22.1°C in PEG blends of 1K and 2K, respectively.

Increasing the homopolymer concentration in the blend to 5% led to a further reduction in the transition's onset compared to the 1% PEG formulations. This

effect can be observed strongly in the blend containing 5% PEG 1k, where the transition initiated at 12.97°C compared to 17.6°C for the neat formulation and 16.6°C for 1% blend of the same homopolymer. The 5% blend exhibited an earlier gelation transition than aforementioned samples to reach the gel state at 20.68°C. The concentration effect on gelation is more prominent in the PEG 1K sample, where the difference between the gelation temperatures of 1 and 5% is 2.11°C compared to 1.42°C in the case of PEG 2K. The homopolymer content led to a slight weakening of the final gel structure. All blends had lower viscosities than the neat gel, and this reduction can be observed at its highest in PEG 1K 5% sample – as seen in the insert in Figure (5-8).

b) The molecular weight effect

The PEG molecular weight effect of the rheological response was explored using the same concentration of 1% for different PEGs with varied Mw. Figure (5-9) show the formulations rheological behaviour with temperature.

From the plotted flow curves at different shear rates, it can be seen that all of the blends had a lower gelation transitions than the neat gel system. PEG 2M had the earliest transition onset, where even at low temperatures the blend exhibited shear dependency displaying an unusual well-defined drop starting from 14.1°C to reach a minimum at 15.6°C before the characteristic gelation overshoot where the multiple shear curves shared the same viscosity values up to 19.6°C before branching according to their respective applied shear rates.

The rest of the PEG-blends demonstrated subtle differences. The 2nd highest molecular weight 200K had the second highest viscosity in the low temperature region, and it exhibited a similar behaviour to its lower molecular weight counterparts with relatively earlier gelation transition at 23.6°C compared to the neat 20% at 24.2°C respectively. Formulations containing PEG 20K, 2K and 1K exhibited decreased gelation temperatures to 24.5°C, 22.1°C and 24.09°C respectively. Comparing final viscosity values of the neat system to PEG-blends show that closest viscosities were recorded for PEG 20K and 200K.

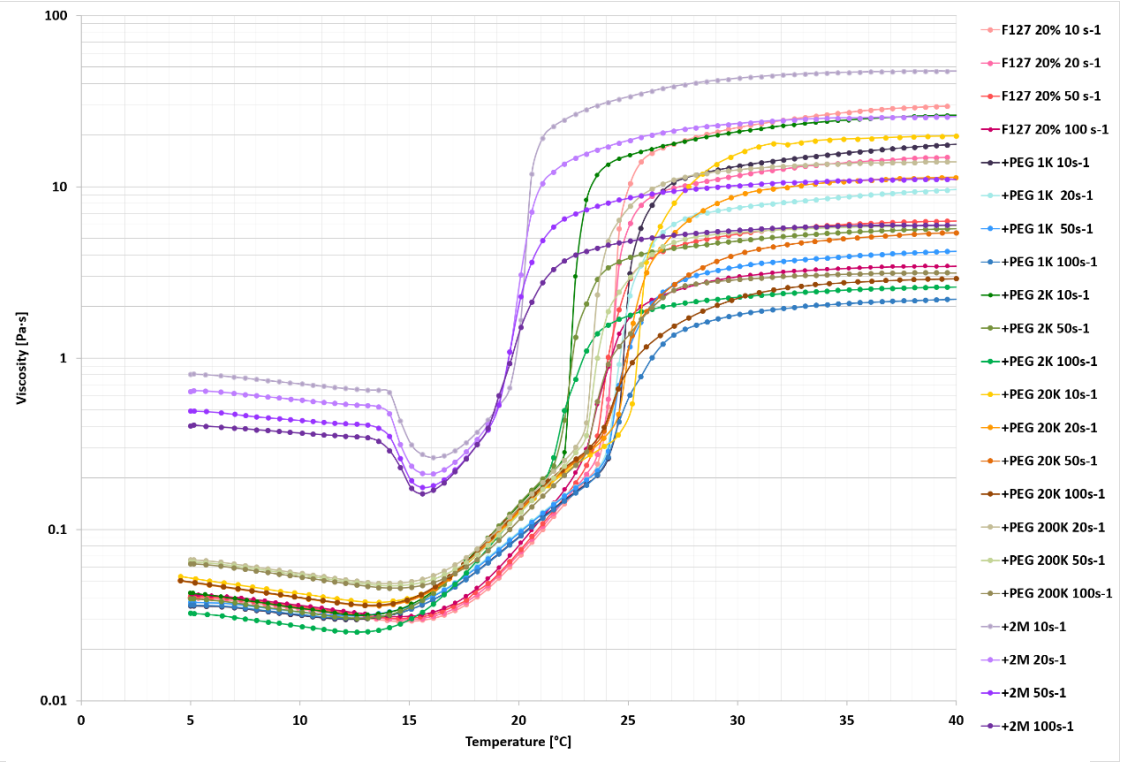

Figure 5-9 Temperature ramps on different molecular weight PEG-blends at constant shear rates.

c) Constant temperature – Shear ramps

The shear ramps were performed at 37°C for all samples, the corresponding flow curves of PEG-blends along with the neat 20% are displayed in Figure (5-10). The stress responses show yield stress values for all the blends followed by a plateau and upward slope indicating a continuous transient behaviour, similar to the results observed in neat gel systems. No apparent relationship between the yield stress values and the PEG chain length at early stages of the ramp was observed. However at shear rates higher than 100 s^{-1} the curves were aligned according to the molecular weight of the PEG in each formulation where $\tau_{neat} < \tau_{PEG\ 1K} \approx \tau_{PEG\ 2K} < \tau_{PEG\ 20K} < \tau_{PEG\ 200K} < \tau_{PEG\ 2M}$.

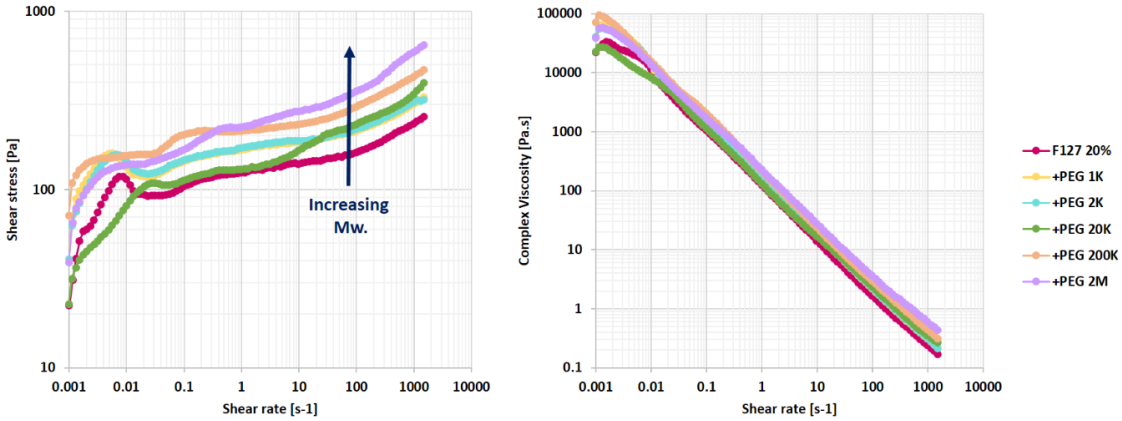

Figure 5-10 PEG-blends shear ramps at 37°C.

The viscosity curves demonstrated shear thinning behaviour, with the values of the K constant for the fitted power law of the viscosity curves correlating to the added homopolymer chain length except in the case of PEG 20K where lower value of K was apparent. The test has been repeated on 20K gels multiple times using different batches but the same result was prevalent. The K values for all the blends are plotted in Figure (5-11).

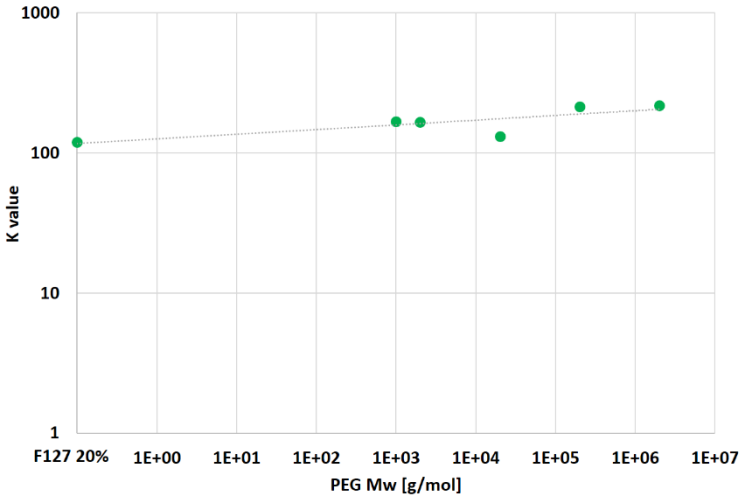

Figure 5-11 PEG blends viscosity power law K values- from shear rate results.

5.2.2. Oscillatory shear:

Due to the recorded structural similarities, the LVE limits obtained from amplitude sweeps on the neat systems were used for oscillatory shear measurements on PEG-blends. As strain value of 0.2% and an angular frequency of 10 rad/sec were applied for all oscillatory shear experiments.

a) Temperature sweep:

This set of experiments aimed to determine the gelation boundary for each formulation. Runs were performed from 5°C to 120°C. The plotted results in Figure (5-12) show that the tested blends exhibited G" > G' pre-gelation followed by an abrupt increase in the moduli and a crossover of the two curves indicating gelation at G"= G'. After gelation the formulations were stable with G' dominating by almost a decade over G". A further temperature increase led to a decrease in the moduli values indicating the destruction of the gel structure. Unlike the rest of the formulations, at low temperatures, the 1K-blend showed G' > G" values, which were the highest recorded for the samples.

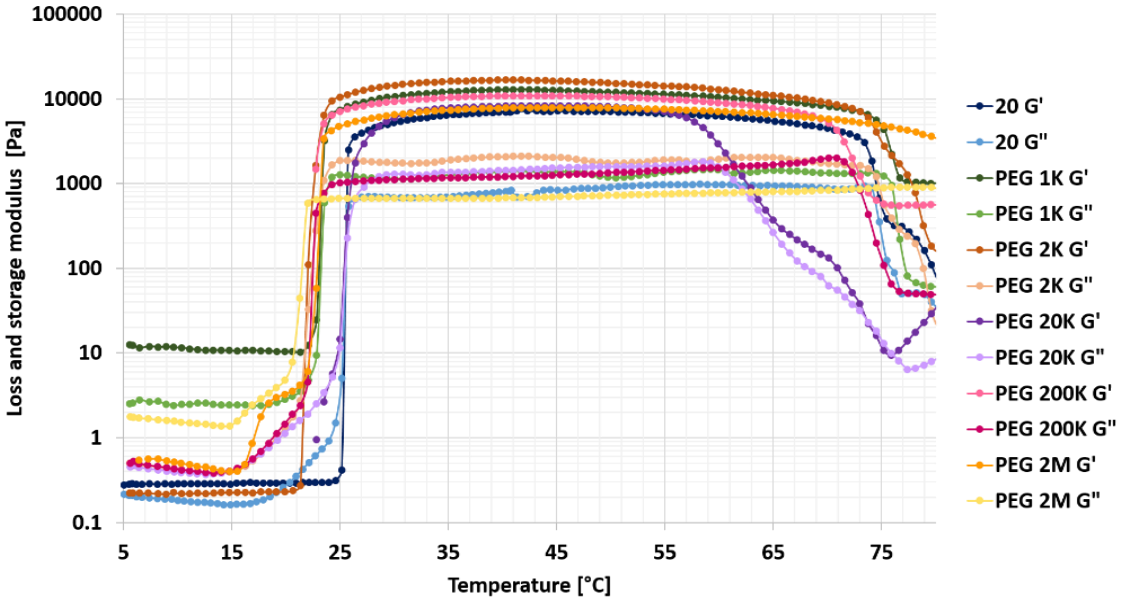

Figure 5-12 PEG-blends Temperature sweeps under oscillatory shear.

The gel boundaries were determined from the two crossover points of the shear moduli, where the lower gelation boundary (LT_{gel}) was assigned to the first crossover point indicating the gel structure formation and upper gelation boundary (UT_{gel}) to the second crossover for its destruction. All samples exhibited a reduction in LT_{gel} compared to the neat gel, expect for the sample containing 20K. However, less uniformity was observed in UT_{gel} shifts. Samples containing lower molecular weights (1K and 2K) and the highest molecular weight had increased UT_{gel} in comparison to the values for 20K and 200K. The experimental results are summarised in Figure (5-13) along with data from Li and Hyun (2018)

25% blends for comparison. As a results of the two boundary shifts, sample containing 20K has the smallest gelation window among the blends.

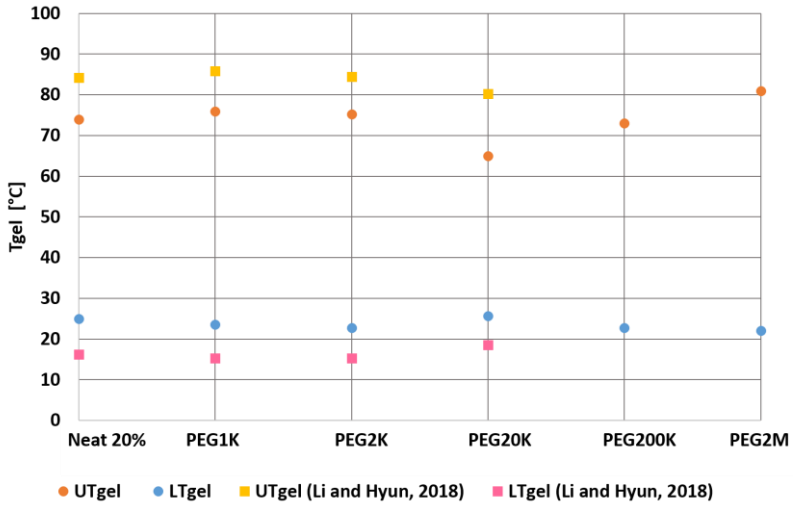

Figure 5-13 PEG-blends gelation boundary results compared with published data (Li and Hyun, 2018)

The complex viscosity profiles affirmed the same trends from the shear moduli plot, where low viscosity values were recorded at lower temperatures followed by an abrupt increase corresponding to the moduli crossover at gelation to reach a plateau corresponding to the G' dominance at the higher end temperature range. According to Figure (5-14) the blend containing PEG 2K had the highest complex viscosity among the tested blends whilst the neat formulation had the lowest values.

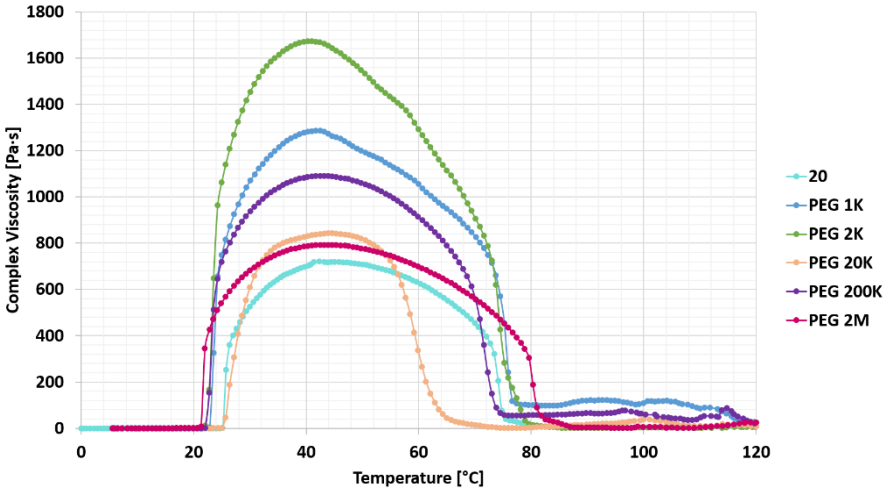

Figure 5-14 PEG-blends complex viscosity values under oscillatory shear- temperature ramps.

b) Frequency sweeps:

Figures (5-15) and (5-16) show the recorded results of the dynamic shear moduli and complex viscosity at 37°C. The dynamic moduli values for the tested samples share the same dependency on the applied frequency as the neat gels.

This was demonstrated by the storage modulus almost constant slope values across the frequency range although the loss modulus was showing a stronger correlation to the applied frequency values, where it exhibited almost a decade difference between the initial starting and final recorded values. There was no evident correlation between the measured moduli and the PEG molecular weight. All blends - except the sample 1K exhibited crossovers, the observed values lay in the high noise - low frequency region for the blends between 0.00158 and 0.002 rad/sec.

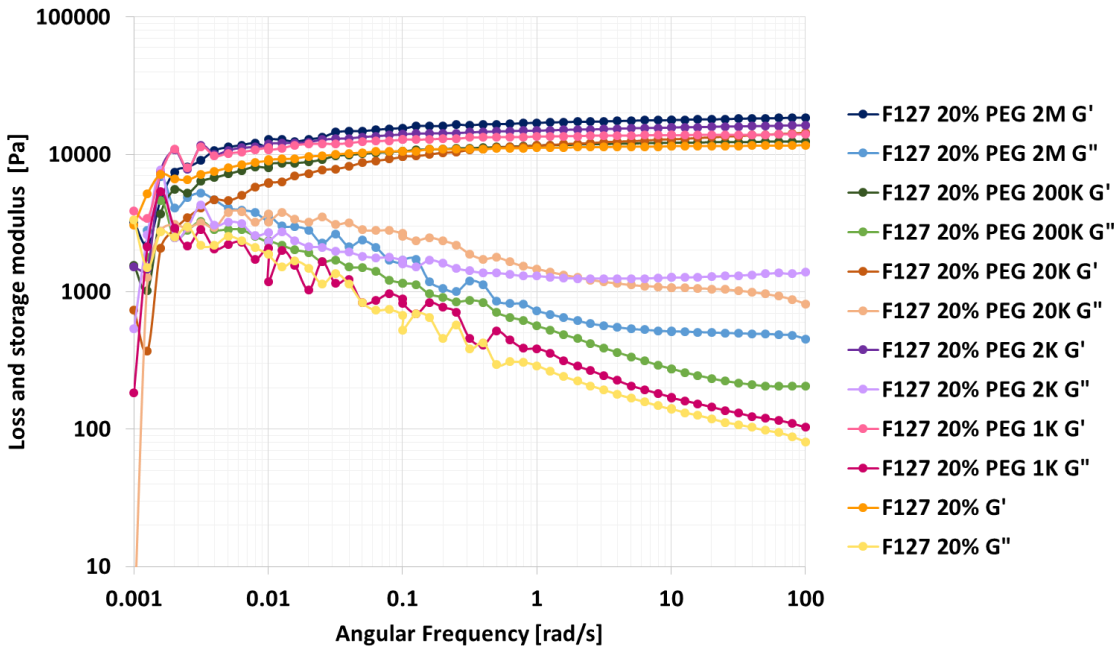

Figure 5-15 PEG-blends dynamic moduli values during frequency sweep at 37°C.

The complex viscosity values exhibit shear thinning behaviour for blends with a negative power law index of 0.9 and varying K constant. The power law K values for the different formulations are plotted in Figure (5-17). The neat gel exhibited the highest value and the PEG addition reduced this as a function of molecular weight. The K plot displays a quadratic curve that divides the PEGs according to their induced shear thinning behaviour into two regions of a) high shear thinning

(highest and lowest Mw; 1K, 2K and 2M), and b) low shear thinning (20 and 200K).

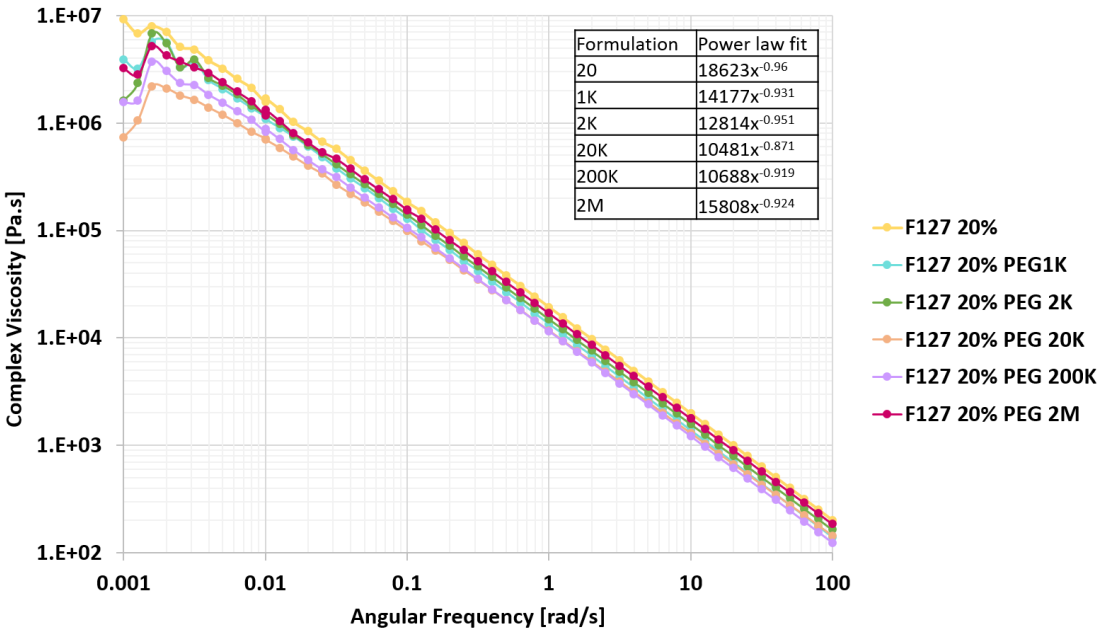

Figure 5-16 PEG-blends complex viscosity values during frequency sweep at 37°C with their respective power law equations.

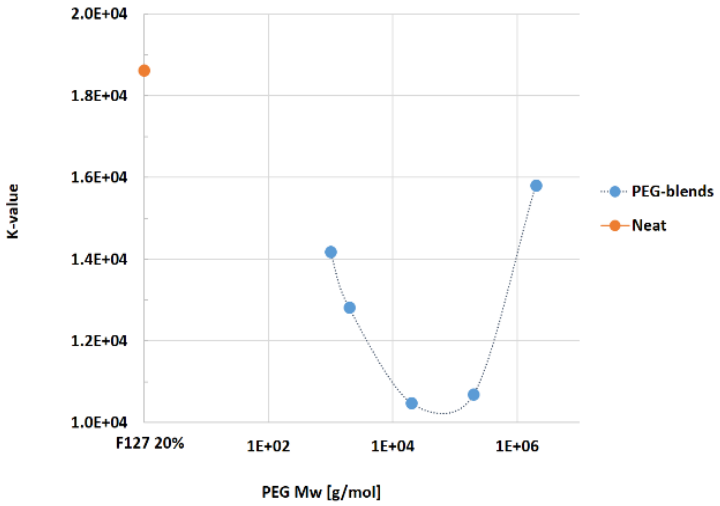

Figure 5-17 PEG-blends K-values from the complex viscosity power law fits from figure (5-16).

c) Relaxation:

The relaxation tests were performed in a step strain of 0.2% at 37°C. The corresponding relaxation modulus results are displayed in Figure (5-18). The blends τ(λ) values (according to Maxwell's model where τ (λ) = 0.368 τ_{max}) were plotted as a function of PEG's Mw in Figure (5-19). All gel blends exhibited a reduction in τ(λ) values compared to the neat gel, proportional to PEG's chain length. Where blends containing 20K, 200K- and 2M were almost completely relaxed by the end of the test.

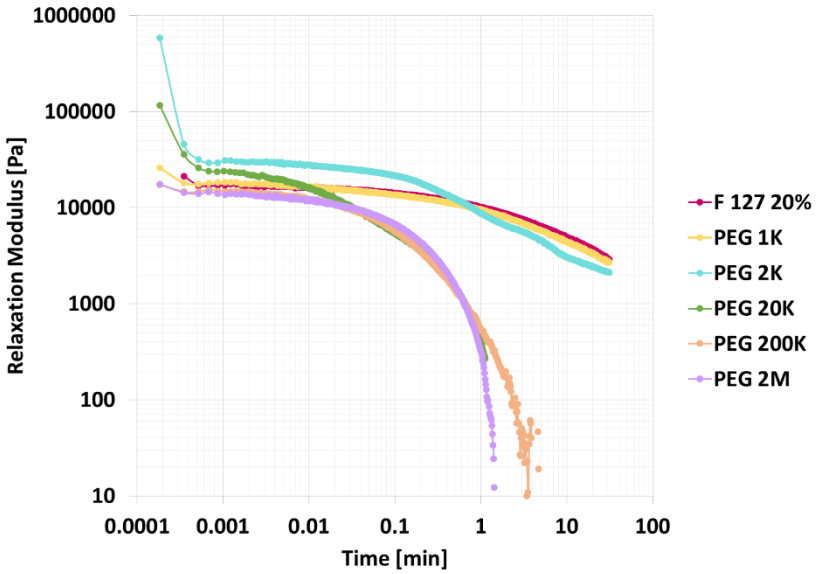

Figure 5-18 PEG-blends relaxation results at 37°C.

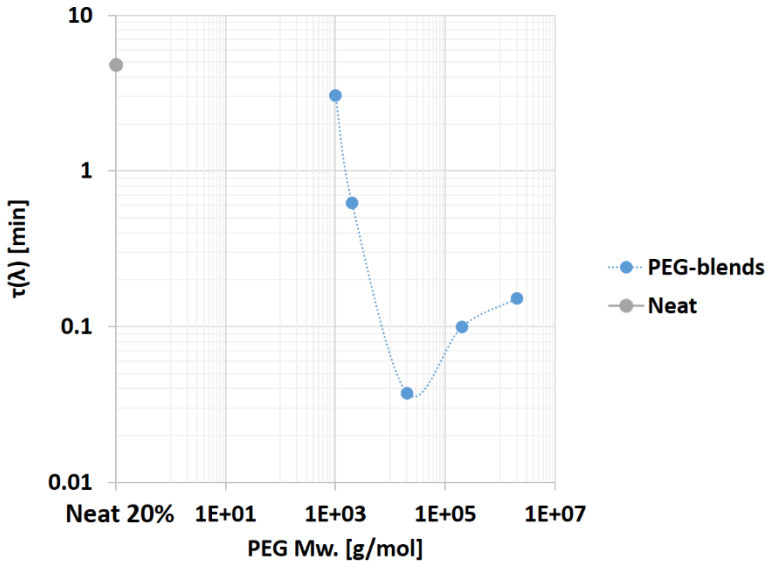

Figure 5-19 Relaxation time values acquired form step strain tests as function of PEG's Mw at 37°C.

d) SRFS:

Tests was performed at six shear rate values covering the range from 0.01 to 10 s^{-1} on two samples containing 1K and 200K to generate a master curve to be compared to the measured frequency sweep and the calculated moduli values from relaxation modulus data using I-Rheo. The combined graph is shown in Figure (5-20).

The results demonstrate a good correlation between the measured moduli values and the I-Rheo calculated ones – which has expanded the low frequencies range to give a possible crossover point that is not effected by the instrumental noise at low frequencies. On the other hand the SRFS master curve vertical shift (for this curve auto shift of b=1 has been applied) still need some adjustment since it is clearly over-estimating the curve's crossover.

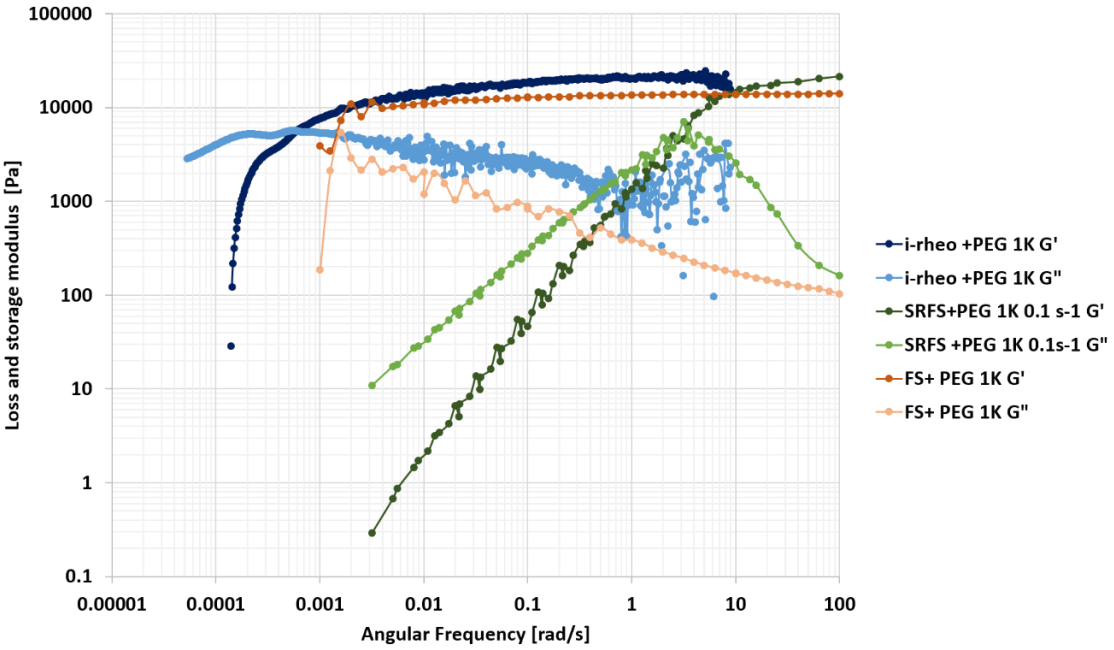

Figure 5-20 comparison between measured dynamic shear moduli values from frequency sweep and generated values from SRFS measurement master curve and I-Rheo.

5.3. Structural results

5.3.1 Static measurements:

a) SAXS- SAXSpace

The PEG-F127 blends were tested across the temperature range from 0 to 40°C, the 1D scattering profiles for 5 and 40°C are plotted in Figure (5-21) and the 2D results for the whole tested range are provided in Figure (5-22).

The PEG-F127 blends lacked any structural order below the gel transition at 5°C. The structural development was triggered with temperature increase, reaching its highest order at 40°C. The PEG- gel systems displayed at least three distinctive peaks around the same positions as the neat F127 20% - see table (5-1), although there were notable shifts in the peak positions. These shifts are indicative of the PEG's effect on the system crystal structure. However the data collected were inconclusive to assign a specific type of close packed paracrystal for blends containing 1K and 20K. The only two blends that exhibited clear indexable peak positions were 2K and 200K, with fittings matching FCC and BCC structures, respectively. The sample containing PEG 2M did not show the characteristic q* peak around 0.036 [$Å^{-1}$] at 40°C probably due to signal smearing. The same sample exhibited a weak peak at the same position at 60°C supporting the previous assumption.

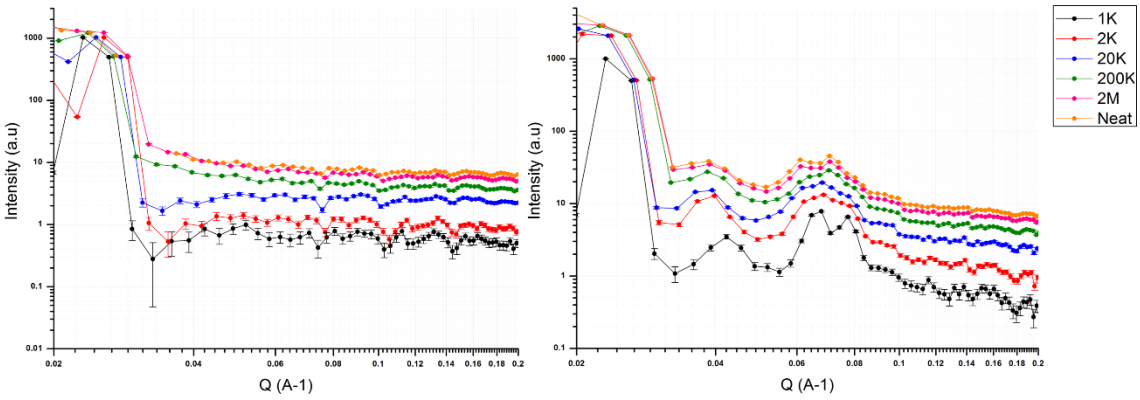

Figure 5-21 SAXSpace 1d profiles for PEG-blends tested constant temperatures at 5°C, profiles have been shifted vertically for clarity.

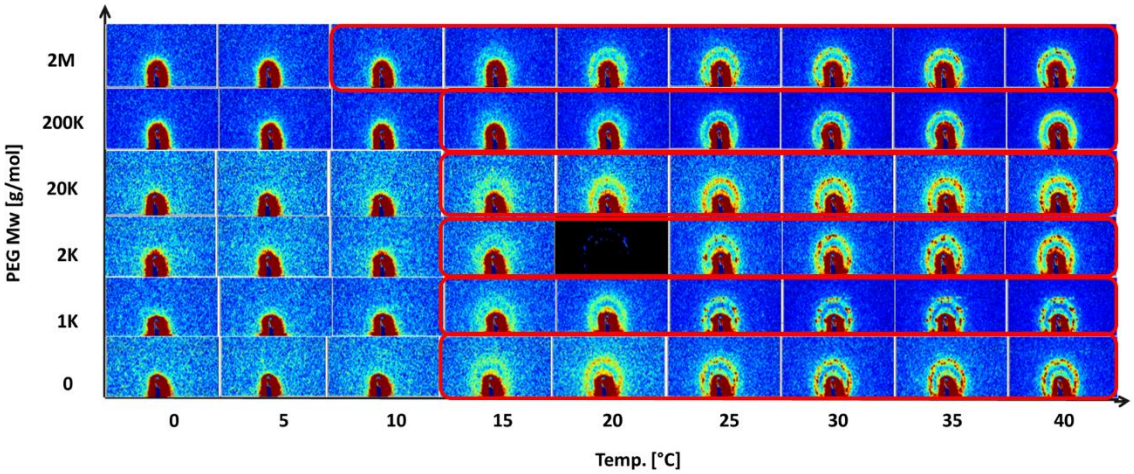

Figure 5-22 SAXSpace 2D scattering profiles for different PEG-blends as a function of temperature, where red frames represent the predicted transition temperatures from DSC measurements. The blackened out boxes were used in place of missing data.

Table 5-1 q-values recorded for different blends at 40°C.

formulation	q*	q_1[Å^{-1}]	q_2[Å^{-1}]	q_3[Å^{-1}]	q_4[Å^{-1}]
Neat	0.0355	0.061	0.070	0.080	-
1k	0.0423	0.064	0.077	-	0.096
2K	0.0398	0.062	0.071	-	0.090
20K	0.0362	0.061	0.068	0.080	0.096
200K	0.0362	0.060	0.070	-	0.092
2M	0.0356	0.061	0.070	0.089	-

b) SAXS- I22:

As explained in experimental set-up (Chap. 3), the samples were loaded to quartz capillaries and mounted on a stage in front of beamline I22 at Diamond. Tests were performed; after refrigeration at 5°C and again at room temperature with no active temperature control. The results are shown in Figures (5-23). After refrigeration the first sample to be tested was the neat 20%, which did not exhibit any structural features.

As for the blends, intermediate structuring had already started by the time measurements are taken. The two distinctive peak positions were at 0.035 and 0.067 [Å^{-1}]. These values are almost identical to those observed when the samples were left to stabilise at room temperature for the second set of

measurements, although the second set demonstrated higher intensities. This confirms that the formulations had already started their thermal transition, probably due to the lack of active thermal control or insulation that allowed rapid heat transfer through the capillaries thin walls.

Based on the recorded results, the blends appear to be locked in an intermediate stage below the structurally defined gelation and above the completely disordered micellar state. The two peaks affirms that they might be closer to the former than the latter. The sample containing 2M exhibited the same two peaks with additional high intensity overshoots at 0.0377, 0.0616, 0.0723,0.0755,

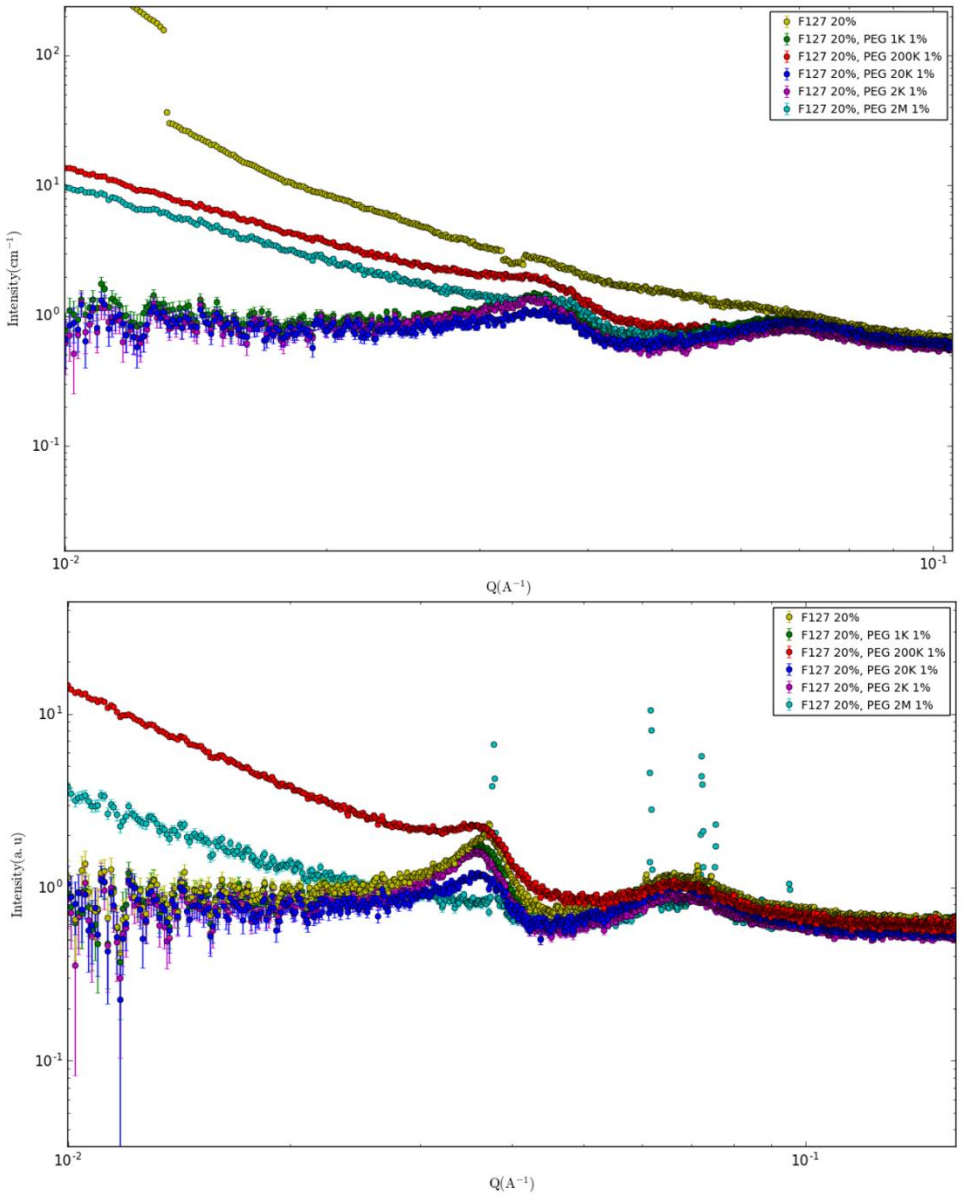

Figure 5-23 I22 measurements of PEG-blends at (top) after refrigeration and (bottom) room temperature.

0.0872, and 0.095 [Å^{-1}] corresponding to 1, √8/3,√11/3,√12/3, √16/3, and √19/3 ratio values in an FCC lattice.

c) SANS:

These measurement were performed on deuterated systems at two controlled temperatures of 5 and 37°C on beamline LOQ at ISIS-RAL. Figure (5-24) shows the two 1D profiles for tested PEG-blends: PEG 1K and 2M along with the neat gel containing F127 20%. Similar to the neat formulation results and the PEG-blend measurements performed on SAXSpace, the two blends exhibited a broad micellar peak undistinguishable from the neat F127 20% at 5°C.
The same identical scattering trend was acquired at 37°C, although when fitted using FCC paracrystal model small differences arose from the different scaling leading to a nearest neighbouring distance of 32 , 30 and radii values of 5.1 and 4.9 [nm] for PEG 1K and 2M, respectively, compared to values 30.7 and 5.27 recorded in the neat 20%.

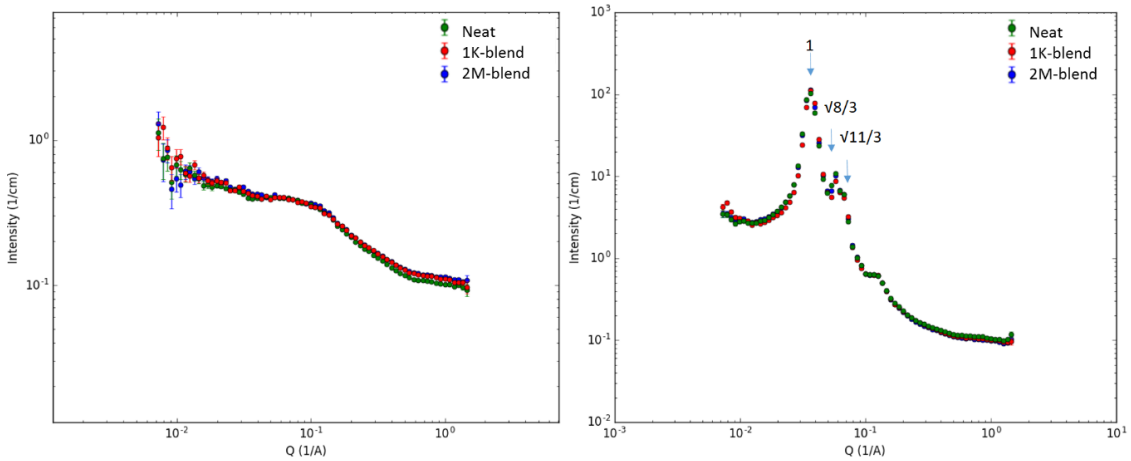

Figure 5-24 SANS results at 5°C(left) and 37°C (right) for 1K- and 2M-blends.

5.3.2 Dynamic measurements:

5.3.2.1 SAXS:

The same experimental procedure from (3.2.3) was followed using the Linkam shear cell with modified Kapton windows. Two PEG-blends; 1K and 2M were sheared at different rates with a heating ramp from 10 to 50°C at 2°C/min.
The scattering profiles of the sample containing 1K revealed no difference between static and sheared formulations at the two shear rates 10 and 20 s^{-1}

applied. For all experiments the scattering patterns were dominated by a decay/ wide peak at 0.02 [$Å^{-1}$] that persisted across all frames. As the tests progressed, the intensity of the peak increased as a function of temperature. Figures (5-25, 26 and 27) display the 1D and 2D scattering profiles of the 1K blend under the three different shear setups.

Similar results were acquired after the 2M-blend was sheared at 10 and 20 s^{-1} (data not shown). This notable behaviour demonstrates the absence of order in the scattering profiles. The same weak scattering was observed for some neat gels tested using the same set-up, as discussed previously in Chapter 4. The reoccurrence of the same issue with different samples/systems confirms the possibility that this may be due to issues with the experimental set-up.

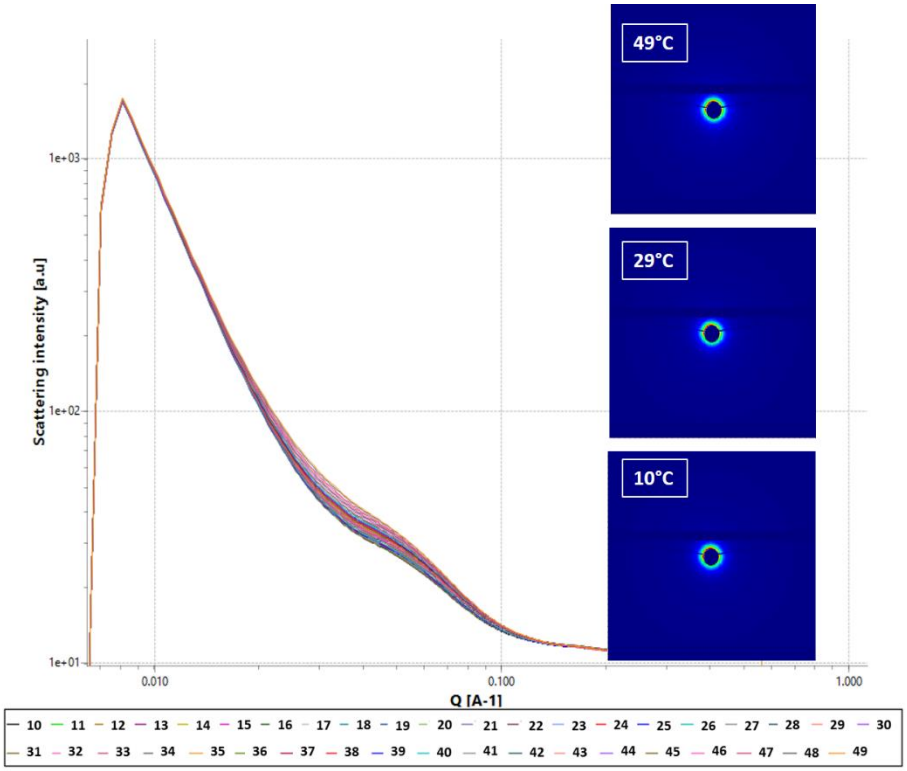

Figure 5-25 Static SAXS for 1K-blend recorded using Linkam at temperature ramp of 10-49°C.

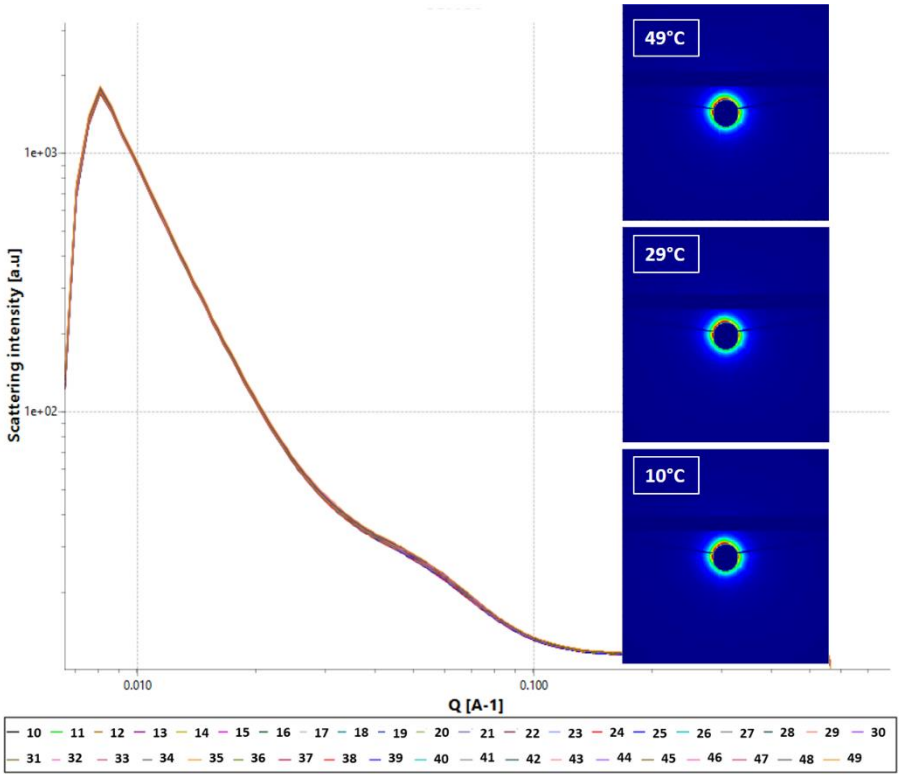

Figure 5-27 SAXS for sheared 1K-blend sheared at 20 s^{-1} and temperature ramp of 10-49°C.

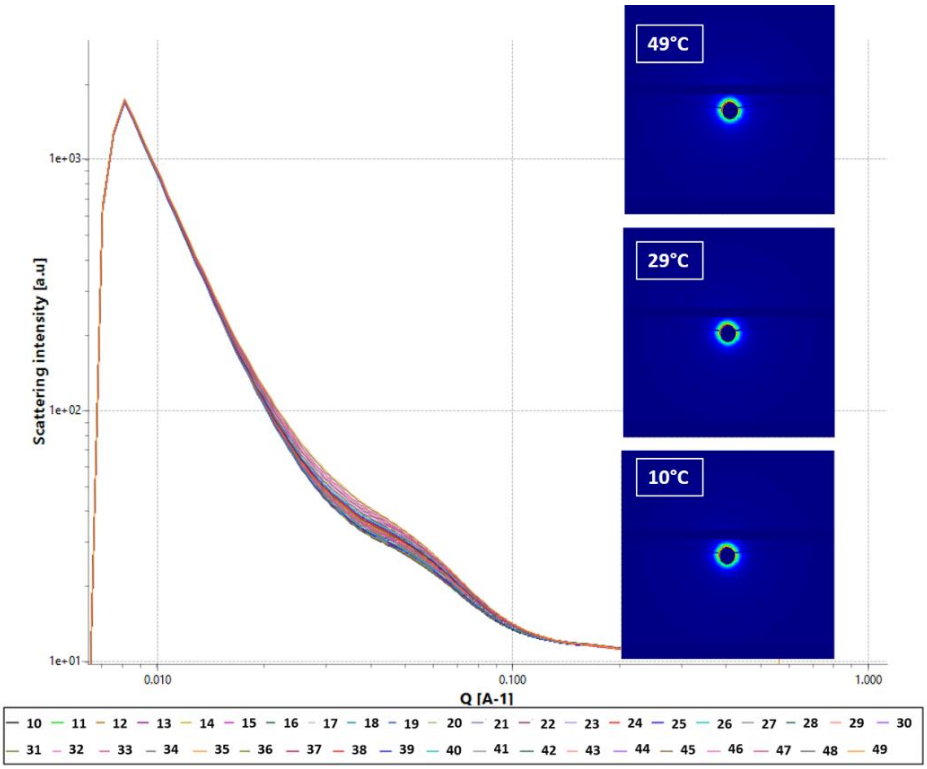

Figure 5-26 SAXS for sheared 1K-blend at 10 s^{-1} and temperature ramp of 10-49°C.

5.3.2.2 Rheo-SANS:

Rheo-SANS experiments were performed according to the procedure discussed in (Chap. 3) using an MCR 501 rheometer mounted in front of beamline SANS2D at ISIS-RAL, with temperatures adjusted to match the gelation transition in each respective formulation. The samples tested in this section contain F127 20% and 1% of each PEG homopolymer in the molecular weights specified in the previous tests. A summary of the results discussed in this section is provided in table (5-2).

Low temperature 5°C:

Similarly to the neat 20% sample, the PEG blends did not exhibit any organisational ordering at 5°C regardless of the imposed shear rate applied as demonstrated in both 1D and 2D scattering profiles seen in Figures (5-28) and (5-30, 32), receptively.

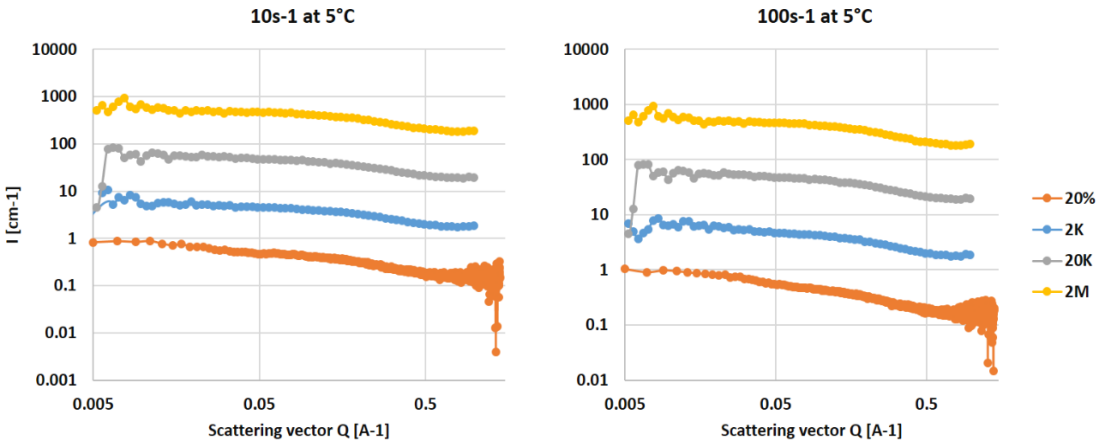

Figure 5-28 PEG-blends Rheo-SANS results performed under different shear rates (10 and 100 s^{-1}) at 5°C, profiles have been shifted for clarity.

a) Low shear rate 10 s^{-1}:

The structural development is evident through the intensity increase with temperature across all the PEG-blends at the same shear rates as seen in the 1 and 2D scattering profiles displayed in Figures (5-29) and (5-30).

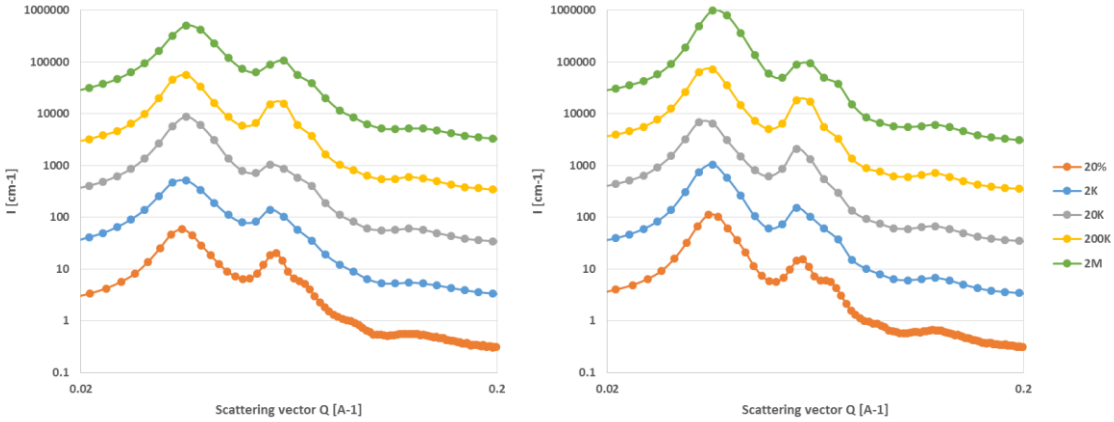

Figure 5-29 PEG-blends Rheo-SANS 1D results (left) T_{gel} and (right) 37°C at 10 s^{-1}, profiles have been shifted vertically for clarity

It was observed that the q* position shifted to slightly higher values with increasing the PEG chain length at the transition temperatures where 2K had the lowest q* value at 0.033 [$Å^{-1}$] while 2M had the highest value of 0.036 [$Å^{-1}$]. However, at 37°C the majority of the samples showed almost the same q* value at 0.036 [$Å^{-1}$]. The best fitting statistics were obtained after using an FCC model.

The model fit indicates that the PEG-blends follow the same trend as the neat gels, where particle size was smaller at the transition stage before increasing at 37°C. The size growth was dependent on the added PEG molecular weight although under both temperature conditions (transitional and 37°C) the recorded sizes were smaller than the value for neat 20%. The FCC fitting results are displayed in table (5-2). Among the datasets, only 20K exhibited a little deviation from the molecular weight order but still followed the same pattern as the rest of the blends in its q* shift and size increase.

The corresponding 2D-scattering patterns at the transition temperatures show common features indicating that orientation processes taking place demonstrated the sixfold symmetry over two orders. The profiles were understandably diverse, depending on PEG molecular weight in the blend and its interaction with the hydrodynamic shear field. At the transition temperatures the azimuthal profiles for 2K and 2M were relativity similar, exhibiting higher intensities in the first order's top and bottom peaks. While 20 and 200K displayed a different response signified by the brighter four sided peaks.

The results for the more structured gels at 37°C unveils similarities in the microscopic structures of 2K, 200K and 2M, where the blends showed sixfold symmetry that extends over two orders with higher intensity values recorded for the meridional peaks in the first order and the equatorial counterparts in the second order. The noted deviation from the one dimensional data of 20K resurfaces here as presented by the high four sided intensity in both rings.

In 20% the recorded q values at both temperatures were 0.0350, 0.059, 0.069, 0.09 and 0.127 [$Å^{-1}$], which correspond to positions in both FCC and HCP structures √3 (FCC), √4 (FCC/HCP), √20/3(FCC), √12 (FCC).

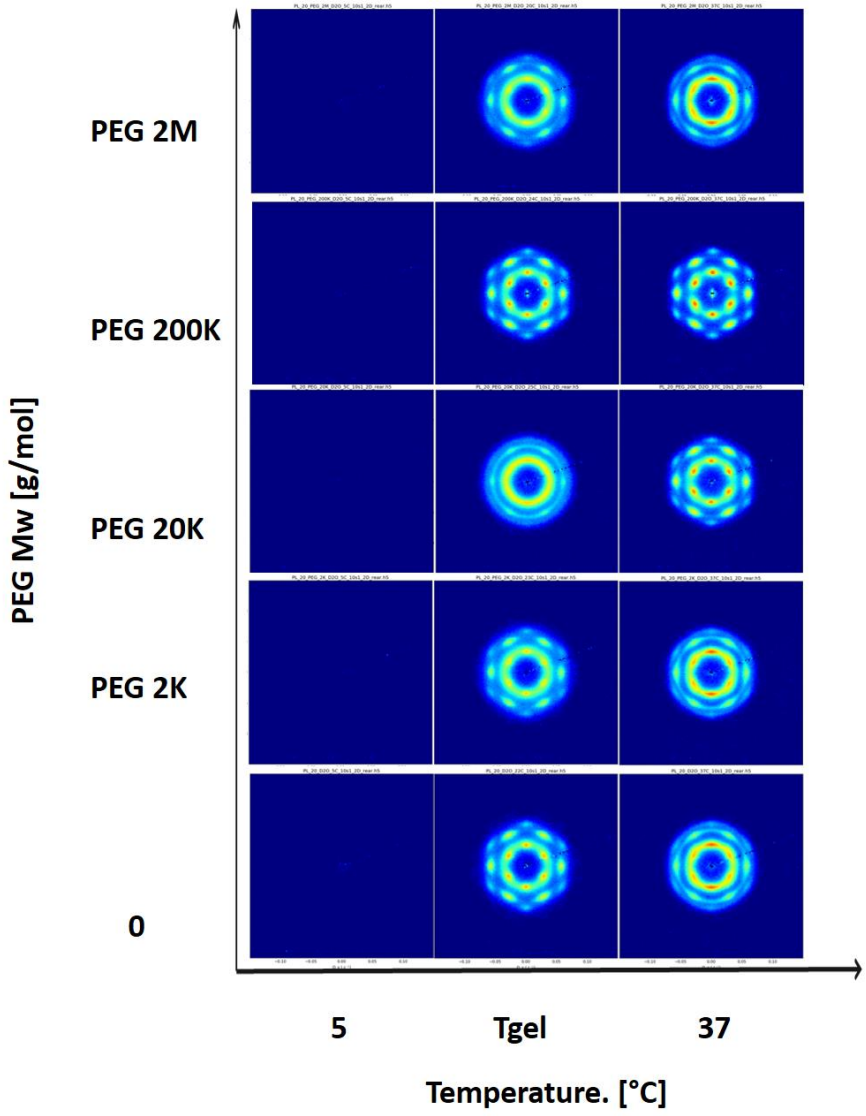

Figure 5-30 PEG-blends Rheo-SANS 2D results under 10 s^{-1}.

b) High shear rate 100 s^{-1}:

Unlike the previous experiment at low shear rate, there was a clear trend in q* shifts between transition and gelation temperatures. Both 2K and 2M blend's peak q* shifted to lower values, indicative of particle size increase. Whereas 20K first peak moved to the lower end and 200K remained approximately constant at 0.036 [$Å^{-1}$] - see Figure (5-31) and table (5-2).

The annular averages reflected less division than the 1D profiles at transition boundaries and stable gel temperatures. The plotted azimuthal data at the transition temperatures for the three blends containing; 2K, 200K and 2M displayed sixfold peaks with higher intensities at the four sided spots of the 2D profiles. This arrangement was only maintained in 200K after increasing the temperature to 37°C. Stronger patterns were recorded for the meridional/ equatorial positions in the first and the second orders of the 2K gel blend. Slightly irregular patterns were observed for the two orders of 2M blend, where the higher intensities of the first order were registered at the top/ bottom positions and for the four sided peaks in the second order - see Figure (5-32).

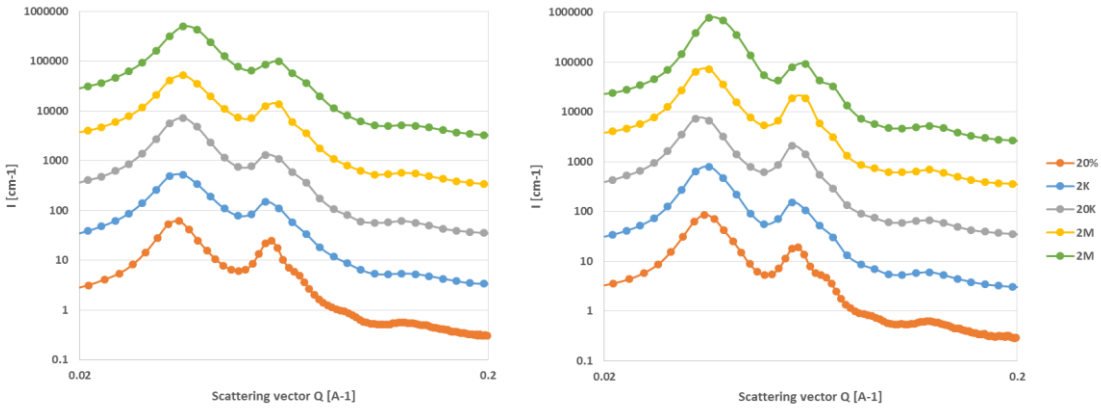

Figure 5-31 Rheo-SANS resutls recorded during; (left) T_{gel} (right) 37°C at 100 s^{-1}, profiles have been shifted vertically for clarity

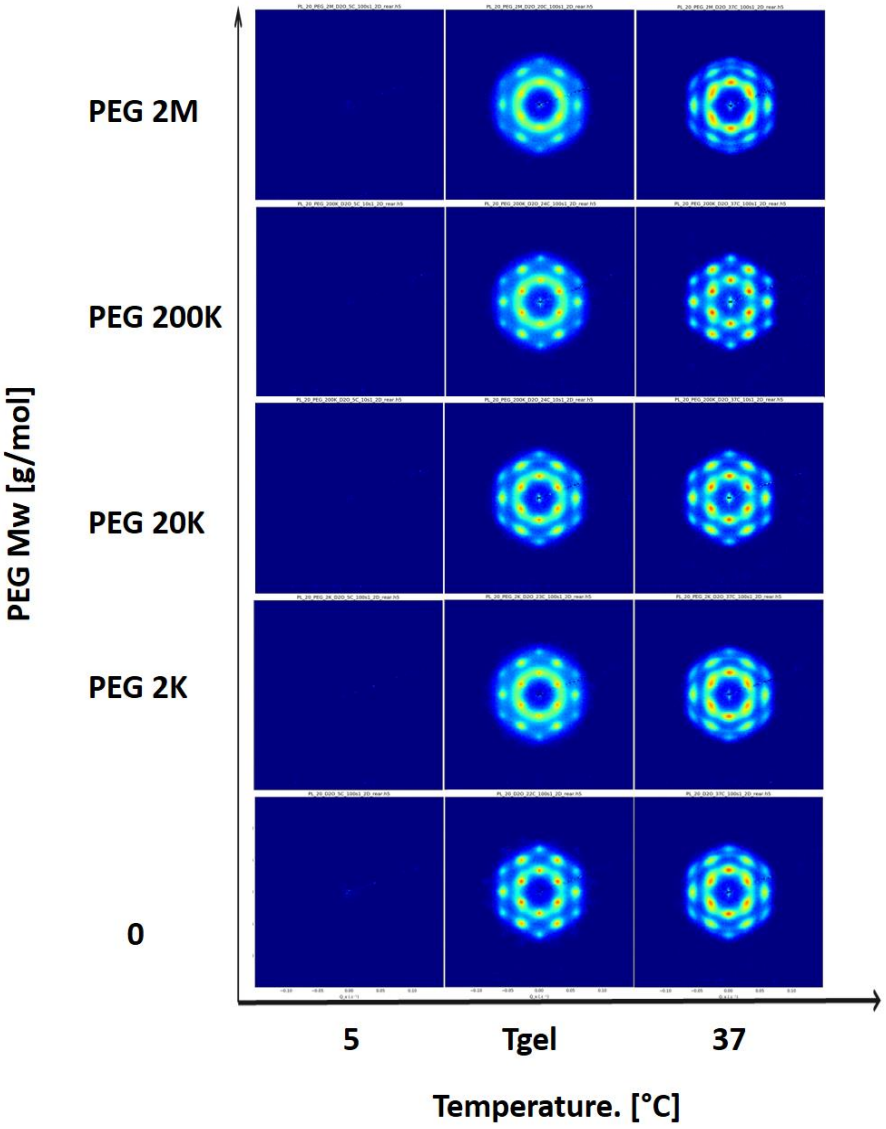

Figure 5-32 Rheo-SANS 2D results sheared under 100 s^{-1}.

Table 5-2 Summary of results acquired using FCC model on Rheo-SANS data

shear rate [s^{-1}]	sample	T [°C]	q*[$Å^{-1}$]	Unit cell [Å]	R_{FCC}[nm]
10	Neat	22	0.035	308.1 ∓ 0.002	6.70∓ 0.2 x10^{-03}
	2K	23	0.0331	316 ∓ 0.016	4.40∓1.65x10^{-03}
	20K	25	0.0358	307.86∓ 0.016	4.83∓1.64x10^{-03}
	200K	24	0.0355	315.87∓ 0.017	4.38∓1.72x10^{-03}
	2M	20	0.0356	304.07∓ 0.017	4.37∓1.73x10^{-03}
100	Neat	22	0.035	312.84∓ 0.002	6.78∓ 0.2x10^{-03}
	2K	23	0.0332	316.86∓ 0.016	4.42∓1.63x10^{-03}
	20K	25	0.0356	313.73∓ 0.016	4.67∓1.64x10^{-03}
	200K	24	0.0358	312.89∓ 0.017	4.39∓1.66x10^{-03}
	2M	20	0.0362	302.75∓ 0.018	4.42∓1.75x10^{-03}
10	Neat	37	0.035	295.62∓ 0.040	9.07∓ 0.2 x10^{-03}
	2K	37	0.0360	314.65∓ 0.028	5.01∓1.74x10^{-03}
	20K	37	0.0331	323.17∓ 0.036	4.55∓1.67x10^{-03}
	200K	37	0.0360	319.79∓ 0.024	4.56∓1.71x10^{-03}
	2M	37	0.0361	303.11∓ 0.032	4.85∓1.76x10^{-03}
100	Neat	37	0.035	295.62∓ 0.040	9.07∓ 0.8x10^{-03}
	2K	37	0.0359	315.83∓ 0.030	4.87∓1.78x10^{-03}
	20K	37	0.0333	324.83∓ 0.037	4.55∓1.66x10^{-03}
	200K	37	0.0359	319.67∓ 0.024	4.57∓1.67x10^{-03}
	2M	37	0.0358	297.58∓ 0.005	8.66∓ 3.4x10^{-03}

5.4. Results discussion:

Israelachvili (1997) highlighted PEG's interaction with other polymeric materials in solutions that results in either repulsion or attraction, depending on the homopolymer molecular weight, concentration or temperature. While low molecular weight PEGs will induce the cell's or vesicle's attraction the higher weights cause repulsion, with the critical change occurring over weights between 10K and 20K.

The dissolved PEG interactions in solution state were investigated by Singh and Pandey (2007). Aqueous solutions of PEGs were tested using solvatochromic probes at room temperatures and the molecular weights investigated ranged from 200 to 6000 g/mol at concentrations between 0 to 100% with 10% intervals. The group concluded that the effect of the homopolymer is due to its abilities to; a) reduce the hydrogen bond donation of water (HBD), b) increase its hydrogen accepting ability (HBA) when compared to pure water. These effects appeared more dependent on the concentrations than the molecular masses. As a result, the existence of PEG in the systems will decrease the water's hydrogen bonding capability with F127 leading to increased hydrophobicity, which results in earlier CMT than expected in neat aqueous F127 systems.

Lindman and Malmsten (1993) tried to interpret their experimental results of adding two PEGs with different molecular weights (6K and 20K) and concentrations to F127 systems. They approached the topic through the effects on micellisation and gelation. Longer PEG chains had more visible effects on the gel systems than shorter ones. Intermediate molecular weight PEGs reduce the solvent polarity, the solubility of PPO blocks is increased which results in delayed micellisation and therefore gelation. At higher PEG molecular weights and concentrations this effect is magnified to preclude the thermal transition demonstrated by the total inhibition of gelation. The authors suggested multiple possible explanations for the PEGs mechanism of action, one that relates directly to the homopolymers size. If PEG is around the same order of the micellar size two behaviours are expected based on the system's entropy; either the gel boundaries are lowered and micellar contraction occurs or alternatively the system phase separates at higher temperatures rather than melting. The authors were ambiguous with the term 'melting', but for this occasion it refers to any

values lower or higher than the gel boundaries. Lower molecular weights usually follow the former whilst the latter is preferred in the case of high molecular weights since phase separation is less unfavourable than the first option due to the produced system incompatibility. The authors reported phase separation for 200K but no results were published.

In reality, Pluronic gels prepared from un-purified copolymers are not strictly binary due to existence of diblocks impurities as polymerisation by-products. There haven't been any interpretations based on the interactions between the diblock with the added PEG. In a more recent paper, investigations of the nature of diblock interactions with the triblock in the gel systems have been attempted but no conclusive answers were found. The authors couldn't determine whether the diblocks were included in the micelles or excluded where the non-purified systems formed FCC even at high temperatures whereas the purified samples experienced additional order-order transition at the same conditions (Mortensen et al., 2008).

5.4.1 Equilibrium measurements:

5.4.1.1 Thermal measurements:

DSC measurements were performed to quantify the different homopolymer's effect on the thermal transition of micellisation attributed to the PPO chain dehydration in the main component F127 triblocks. The low quantities of added PEGs altered the thermal behaviour of the neat system leading to a reduction in the main variables recorded (T_{onset}, T_{peak} and T_{endset}). Thermally triggered micellisation transition shifted marginally to lower temperatures as the molecular weight or chain length increased, the largest difference being recorded for the PEG 2M formulation with a Δ of 2.5°C ($\Delta T = T_{endset} - T_{onset}$). These changes reflected equally on the other parameters, showing a weakly negative linear correlation between the transition period and the molecular weight of PEG in the formulation as demonstrated in Figure (5-33).

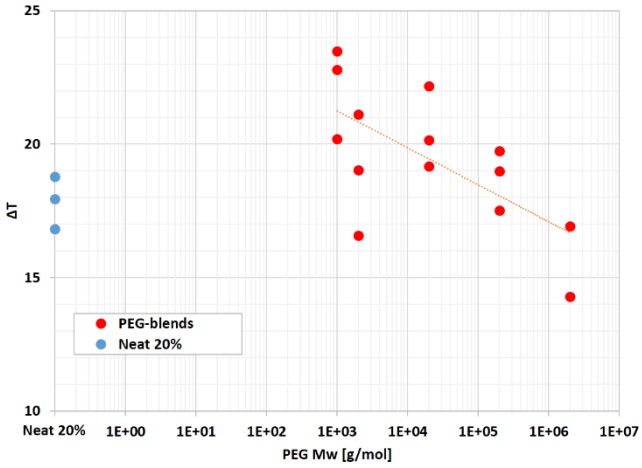

Figure 5-33 PEG-blends ΔT based on the samples DSC results.

Pragatheeswaran and Chen reported much lower decreases in their DSC measurements on a similar set PEG-blends with molecular weight range of 200 to 35K g/mol at 6% which naturally resulted in more pronounced reduction in the recorded onset temperature values (which they referred to as the formulation CMT) as can be seen in Figure (5-34).

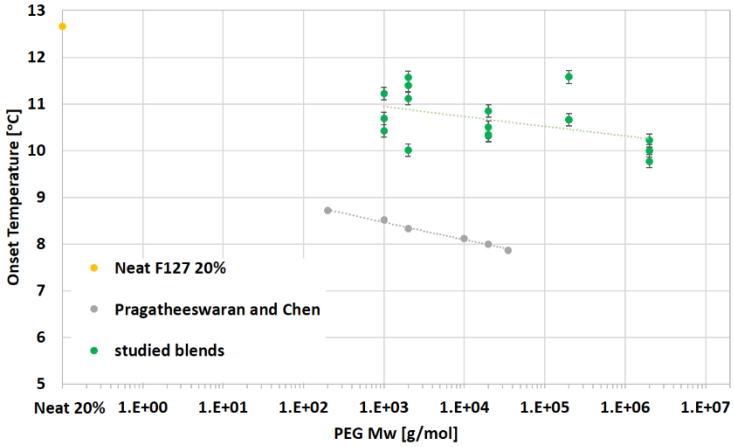

Figure 5-34 A comparison between; 1% blends prepared in this study and values reported by Pragatheeswaran and Chen (2008) for 6% blends. Neat system T_{onset} was equal in both studies.

5.4.1.2 Static Scattering

All the static SAXSpace measurements showed a structural development as function of the temperature. For the temperature at 40°C, the 1K-blend exhibited the largest q* value at 0.0422 [$Å^{-1}$] corresponding to smallest the unit cell size and thus hard sphere radius (R_{HS} = 9.10 nm). The sample of 2M suffered from smearing where q* was expected to appear. Although 20K had a less defined q* = 0.0329 [$Å^{-1}$] peak than the rest of the formulations its position still points the

lowest q* value, indicating that the blend's hard spheres are the largest with a R_{HS} value of 11.69 nm. The values recorded by the two SAXS instrument are plotted in Figure (5-35).

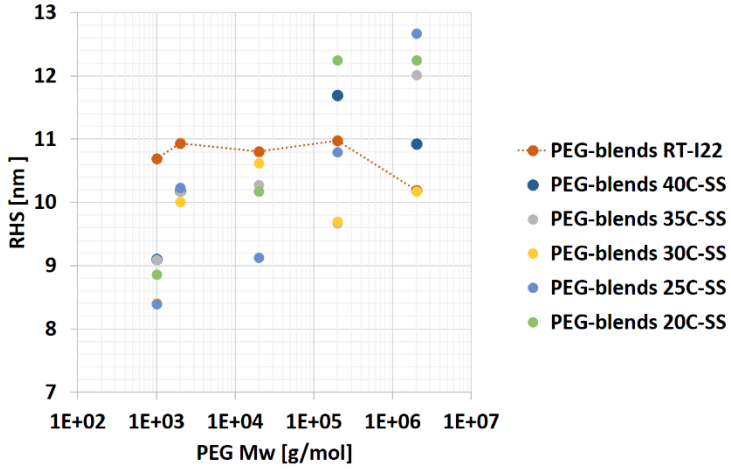

Figure 5-35 PEG-blends hard sphere radii values acquired using two instruments; I22 and SAXSpace (SS).

5.4.2 Non-Equilibrium measurements

5.4.2.1 Rotational shear

Similar to the trends seen in the neat formulations, the PEG-blends undergo the same step-like transitions before, during and after gelation. The rheological data show the transitional behaviour across the tested molecular weights where most of the formulations experienced a lower transitional onset and gelation transition temperatures compared to the neat system - closely correlated to the homopolymer chain length. The experiments allowed us to address two critical issues regarding the homopolymer blends, their chain length and concentration in the formulation.

a) Concentration effect:

The PEG fractional effect was investigated using two molecular weights added at two different concentrations. As observed from the results plotted in Figure (5-8) the blends containing higher (5%) concentration of PEG 2K exhibited early gelation (20.68°C) than the neat gel (24.2°C) and the 1% counterpart (22.1°C), in addition to lower viscosities across the shear rates tested.

The data acquired correlates well with the results obtained when the same homopolymers were used in different concentrations, the extra fraction of added PEG decreased the hydrogen bonding of water with F127 and therefore promoted earlier micellisation that led to reduced CGT. The introduction of 1K 5% resulted in approximately the same response of 2K when added at 1%, although the former had slightly higher viscosity values. Previous groups have reported similar results using; different concentrations of PEGs (Ricardo et al., 2012) or of F127 (Li and Hyun, 2018).

b) Molecular weight effect:

Molecular weight dependency was investigated using the same concentration for all the homopolymers. The data collected showed that the blends, as for the neat formulations lacked any shear dependency before gelation, except for PEG 2M. The 2M-blend showed a minimum in viscosity, resulting in a well-defined trough shape not documented for any other of the formulations in the study (or anywhere else) rather the usual gradient seen in the pre-gelation stage. This might have resulted from the hydrophobic PEG 2M long chains disturbing the system's hydrophilic-hydrophobic balance. The same blend exhibited shear thinning that persisted for all the tests except for the gelation 'bifurcation point', where all the curves were identical at 19.1°C. This minor shear thinning behaviour during pre-gelation might indicate the sample's tendency to phase separate or is a direct result of PEG chains drag reduction capacity. The 2M-blend had the highest viscosity in both sol and gel states. The gel blends viscosity during the ramps varied depending on the PEG used and the shear rate applied. The overall ranking of the gels based on their final viscosity values acquired at 100 s^{-1} is as follows; $\eta_{2M} < \eta_{Neat} < \eta_{200K} < \eta_{20K} < \eta_{2K} < \eta_{1K.}$

The results demonstrate that the blend containing 20K deviated from the lower molecular weight PEGs, where the CGT started increasing again after reductions connected to the addition of the lower molecular weight PEGs. This trend was emphasised by adding longer chains of 200K and 2M.

Low to intermediate Mw were tested by the tube inversion method on weights from 2K to 10K, confirmed the trend of the effectiveness of reducing gelation temperature as a function of Mw (Pandit and McGowan, 1998). Pragatheeswaran

and Chen (2013) performed heating ramps of 1°C/min on F127 20% PEG-blends containing 200 to 35K. They reported increased critical gelation temperatures with increasing the PEG molecular weight from complex modulus values for blends of 2, 10, 20 and 35K. The recorded CGT were 23.5, 25.6, 28.5 and 33°C compared with 23°C for neat 20%. Taking into consideration the two different heating rates applied in the mentioned paper and this study, the results follow the same trend and the differences in values recorded for 2K (which has more subtle effect on CGT) and 20K are within acceptable limits. Their PEG-blend containing 35K had a similar trend observed for lower molecular weights, filling the gap in this study between 20 and 200K, proving that up to at least 35K, PEG behaves in a similar manner.

5.4.2.2 Oscillatory shear

The effect on CGT was further explored by expanding the temperature range under the application of oscillatory shear. Rather than the usual abrupt transition recorded for all the samples, 2M-blend showed a gradual transition with a clear step in the elastic modulus at 18.4°C before the crossover and G' dominating throughout the gelation boundary. The PEGs had clear effects on the gelation boundaries coinciding with the temperature ramp at different shear rate results, where all the LT_{gel} have been reduced. Except for 20K, which correlates to the acquired data for this blend from the previous runs showing a slight increase. More diverse responses were recorded for the UT_{gel}, where the lower molecular weights, along with 2M, experienced an increase compared to decrease for both 20 and 200K-blends. Similar trends were recorded for PEG-blends prepared with 25% F127 and PEGs with molecular weights ranging from 1 to 20K (Li and Hyun, 2018).

Up to this point, three different trends for the same concentration of different molecular weights have been observed. For shorter chain lengths the gelation occurs earlier than the neat gel temperature e.g. 2K. Medium molecular weights shifted the gelation to higher temperatures than the neat systems as in 20K. The higher molecular weights shifted the gelation back to lower CGT. The argument based on increased polarity and enhanced PPO solubility holds for all PEG

molecular weights, however is also dependent on the homopolymer's own solubility.

High molecular weights of PEG exhibit a microphase separation as a result of solubility change due to concentration or temperature, and act as a non-ionic surfactant possessing both LSCT and USCT. Similar to Pluronic, they can aggregate in aqueous media driven by hydrophobic interactions. Experimentally, to determine the PEG globule 'cluster' size measurements should be performed in a system of the same solvent around the same temperature range (at low temperatures water is considered a good PEG solvent, upon temperature increase water reaches the theta solvent state). In this study, only R_g of 2M 1% after refrigeration was measured, which gave a value 22.5 nm. The value R_g of 1% PEG 41K was measured by Hammouda and Ho (2007) to be 5.6 nm and similarly the value was determined to be 2.1 nm for PEG 3400 at 25°C by Gurnev et al. (2017).

Even without any measurements both PEG 200K and 2M have longer chains than F127, therefore their respective R_gs are expected to be large. According to the previously discussed paper's values, the addition should have either inhibited micellisation or resulted in complete phase separation, but neither occurred. On the contrary, micellisation was facilitated (from the 2M DSC result), which resulted in lower CGT and the produced hard spheres from static SANS results showed the size was reduced compared to the neat gel.

One possible explanation would be based on the two non-ionic surfactant's interaction, which creates a synergistic effect by the increased hydrophobic interactions in the system resulting in early thermal transitions. This aligns with the explanation suggested by Malmsten and Lindman (1993). Assuming that the Pluronic micelles act as semipermeable membranes that are difficult to penetrate by the long homopolymer chains, the chain heterogeneous distribution in the system creates an osmotic pressure gradient, with higher molecular weight homopolymers producing larger gradients, resulting in increased CMC of the system and micellar size reduction.

The dynamic moduli values during frequency sweeps highlighted the system's linear viscoelastic properties above gelation temperature. All the formulations showed similar behaviour to the neat gel with close G' > G" throughout the test.

The difference between the two moduli values was reduced as the low frequencies were approached. Generally the elastic modulus values varied from 11700 for the neat gel to 18500 [Pa] for 2M-blend with no evidence of damaging structural weakening due to the PEG addition as witnessed by Malmsten and Lindman (1993).

5.4.2.3 Dynamic scattering:

Two samples containing 1K and 2M where tested using SAXS under constant shear rates and ramping temperatures. The results displayed weak scattering profiles that did not show a notable structural development, similar to that exhibited in clustering of PEG solutions (Hammouda and Ho, 2007). Both samples exhibited similar profiles to those recorded for sheared samples of F127 20 and 25%, where the frames show almost identical profiles with temperature. This raises the same question as before whereby a technical error may have occurred during experiments that prevented recording meaningful measurements.

Real time Rheo-SANS experiments were performed on the samples using a Couette geometry, at two imposed shear rate values (10 and 100 s^{-1}) and three temperatures; at 5°C, during the gelation transition and after gelation at 37°C. The transition temperatures were determined from the blends CGT points in Figure (5-9).

Similar to the neat 20% formulation, none of the blend's 1D scattering profiles showed any structural order pre-gelation at either shear rate. At the transition and after gelation there were only subtle peak shifts that enough to cause drastic size changes as seen in table (5-2). For all formulations the hard sphere radii were larger after gelation - except for the blend containing 20K which showed the opposite trend. This being exhibited under low and high shear rates.

a) Low shear rates 10 s^{-1}:

The 2D scattering profiles revealed the orientational ordering taking place in the blends. At the lower shear rate three behaviours were observed. 1) The first was exhibited by 2K and 2M formulations, where the azimuthal profiles showed sixfold peaks with higher intensity at the meridional positions in both first and second

order, that persisted during transitional and after gelation temperatures – as seen in Figures (5-36) for 2K at 23 and 37°C.

2) The second was exhibited only by 20K, where the sample demonstrated higher peak intensities at the four sided peaks. This trend appears stronger in the second order ring than the first at the transitional temperature and then after gelation – see Figure (5-37). This behaviour aligns with the predicted zig-zag flow mechanism predicated by Loose and Ackerson (1994) sliding layers model under low shear rates.

3) The third behaviour experienced by 200K, which had behaved like (2) during the transition and (1) after the gelation as shown in Figure (5-38). The first and last behaviours have already been reported for neat gels in this study, where the former was exhibited at 10 s^{-1} and the latter at higher shear rate 100 s^{-1}. The second however has not, where it has been assumed that this behaviour was a transitional step before reaching the uniform state of (1).

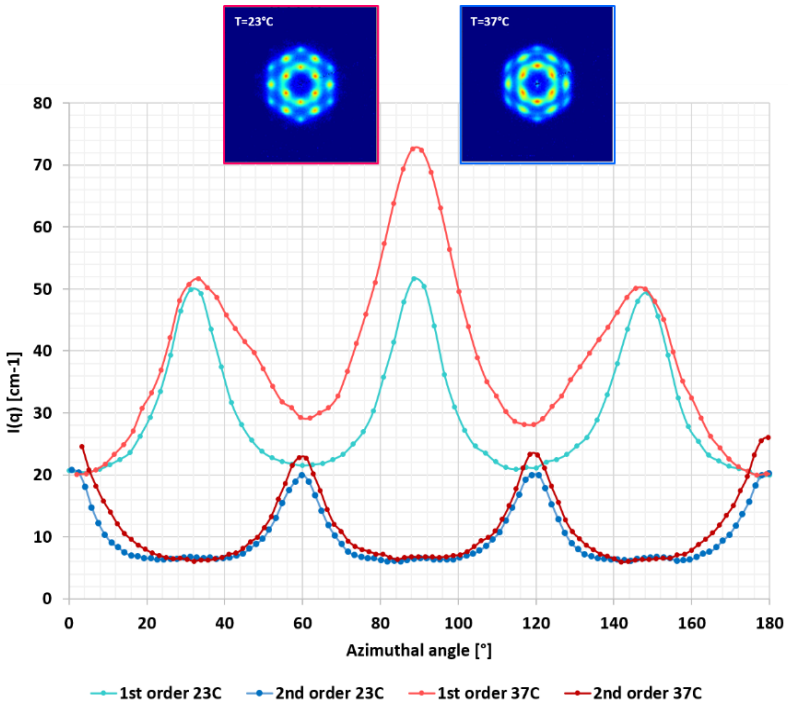

Figure 5-36 Rheo-SANS azimuthal intensity profiles of 2K-blend sheared at 10 s^{-1}.

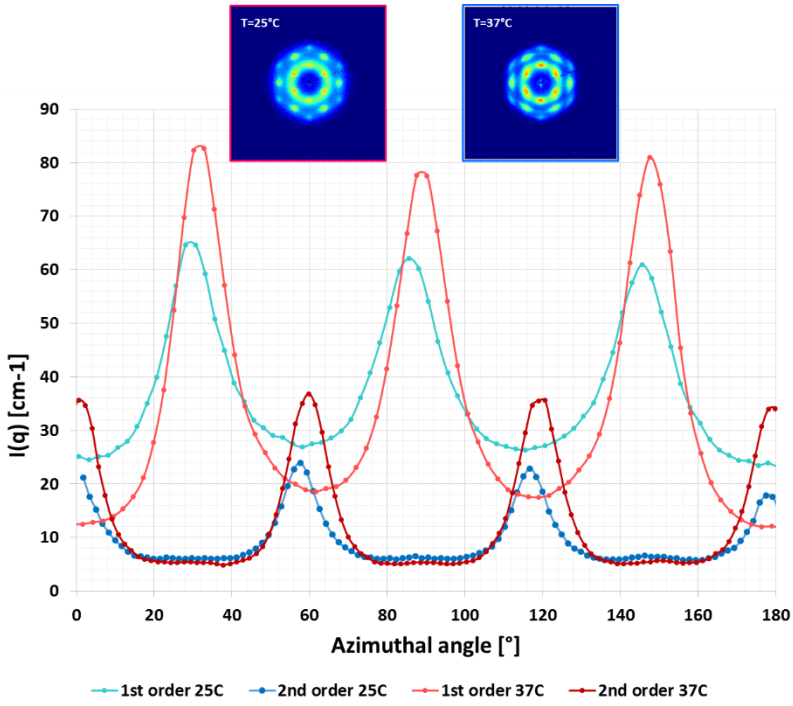

Figure 5-38 Rheo-SANS azimuthal intensity profiles of 20K-blend sheared at 10 s^{-1}.

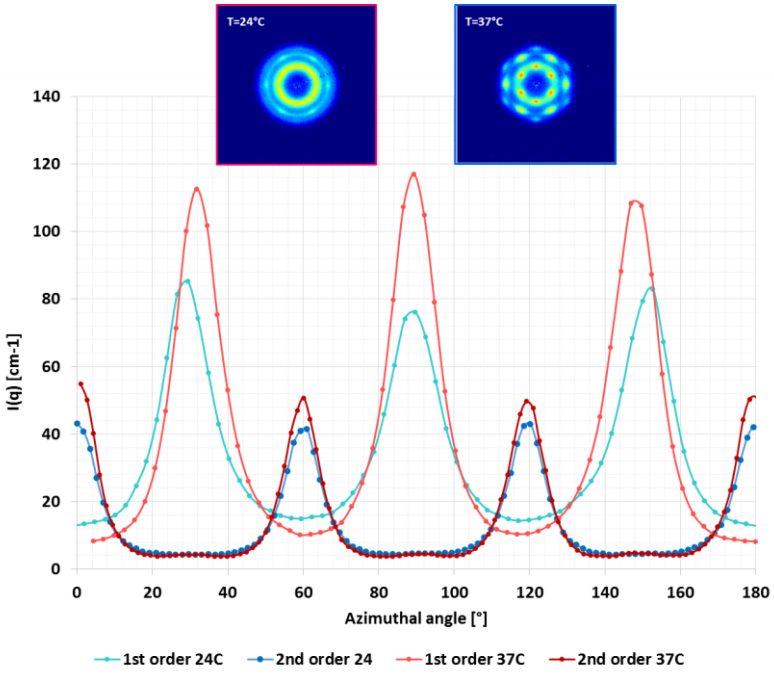

Figure 5-37 Rheo-SANS azimuthal intensity profiles of 200K sheared at 10 s^{-1}.

b) High shear rates 100 s^{-1}:

The 2D patterns showed less uniformity across their annular profiles after the application of 100 s^{-1} than 10 s^{-1}. At their respective transition temperatures, the blends displayed two orders of structure, sixfold peaks with higher intensities in the four sided positions. Above gelation temperature sample containing 2K was the most uniform sample, showing higher intensities in the top/bottom position across the two order rings as seen in Figure (5-39). In contrast 20 and 200K samples maintained their transitional temperature order of the four sided peaks in both orders – see Figure (5-40). The 2M sample exhibited a mixed state, where the highest intensities were recorded for meridional peaks in the first order and four sided peaks in the second order Figure (5-41). According to our knowledge there have not been any form of rheological scattering experiments performed on PEG-F127 blends. Scattering experiments in the literature have been solely used to determine the size and lattice type when possible, therefore it is not possible to compare the orientational ordering of the blends with literature values. As mentioned in the results section, and as supported by the static measurements results FCC model continued to provide a good fit for the 1D data. However similar to the sheared neat gels, the patterns acquired do not correlate to a pure FCC paracrystal and can be better described as an RCP.

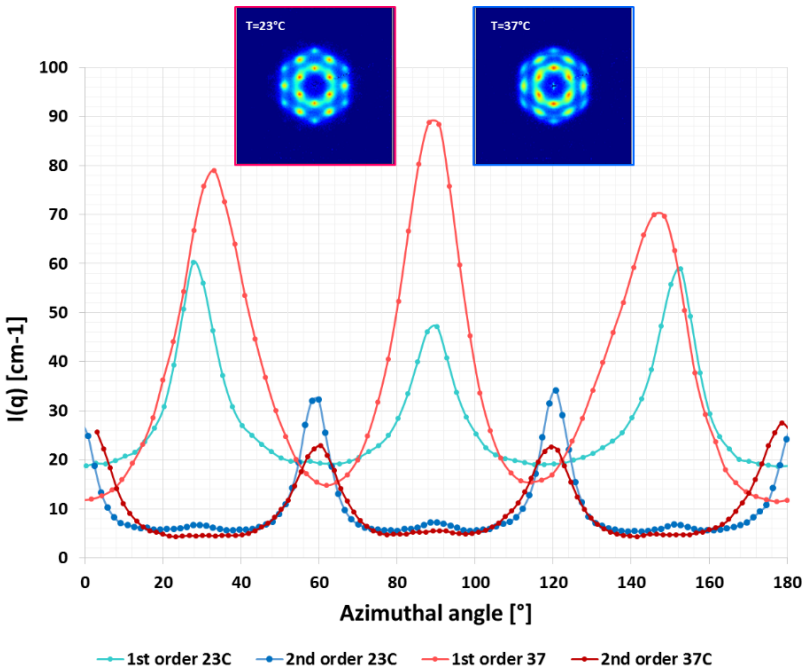

Figure 5-39 Rheo-SANS azimuthal intensity profiles of 2K sheared at 100 s^{-1}.

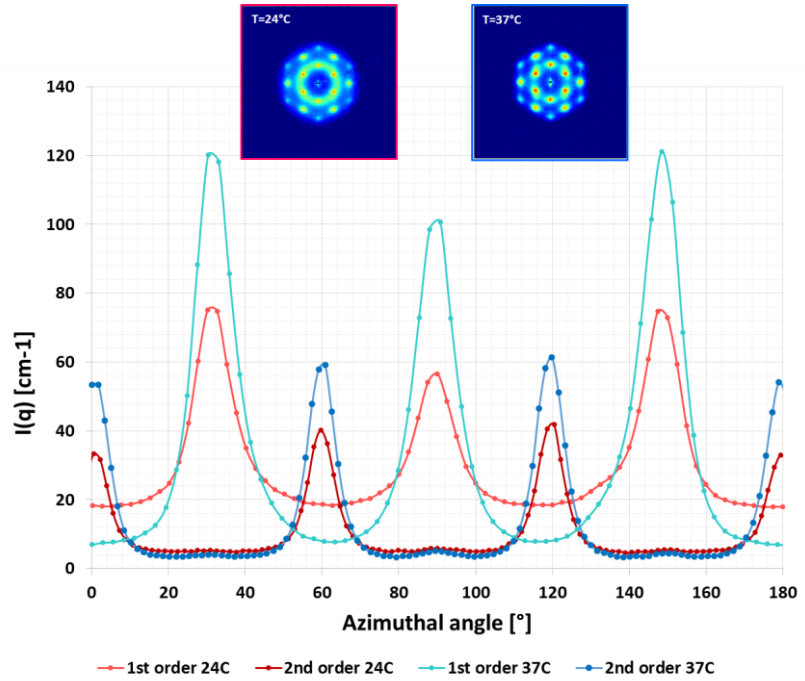

Figure 5-40 Rheo-SANS azimuthal intensity profiles of 200K-blend sheared at 100 s^{-1}.

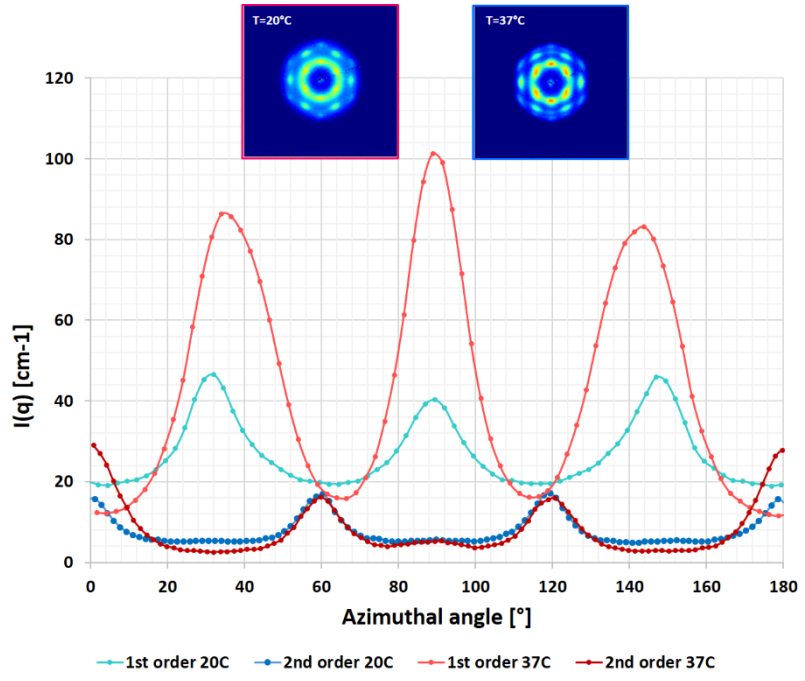

Figure 5-41 Rheo-SANS azimuthal intensity profiles of 2M sheared at 100 s^{-1}.

Chapter 6 IBU-blends:

To develop a model DDS an API Ibuprofen (IBU) was introduced to neat systems of F127 and PEG-blends with different Mw. The IBU-blends were studied and compared to the neat and PEG-blends to explore the resultant aspects of the addition on the formulation's structure. The DDS features were evaluated in comparison to results from Chapter 5.

6.1. Thermal properties:

6.1.1 TGA:

PEG-IBU blends of 20% F127 containing 1% of each additive were tested to determine their stability and ability to retain water within the gel matrix as compared to the neat formulation. Figure (6-1) shows an overlay of the different blend results obtained during temperature ramps from 27 to 400°C at 5°C/min Similar to the results acquired in chapter 5, the curves showed a step transition indicating two weight loss events. The first correlates to water loss from the gel matrix and the second for the polymer's degradation. All of the tested blends showed a reduction in the transition temperature, and the formulation containing only IBU exhibited the closest transition temperature to the neat's gel transition.

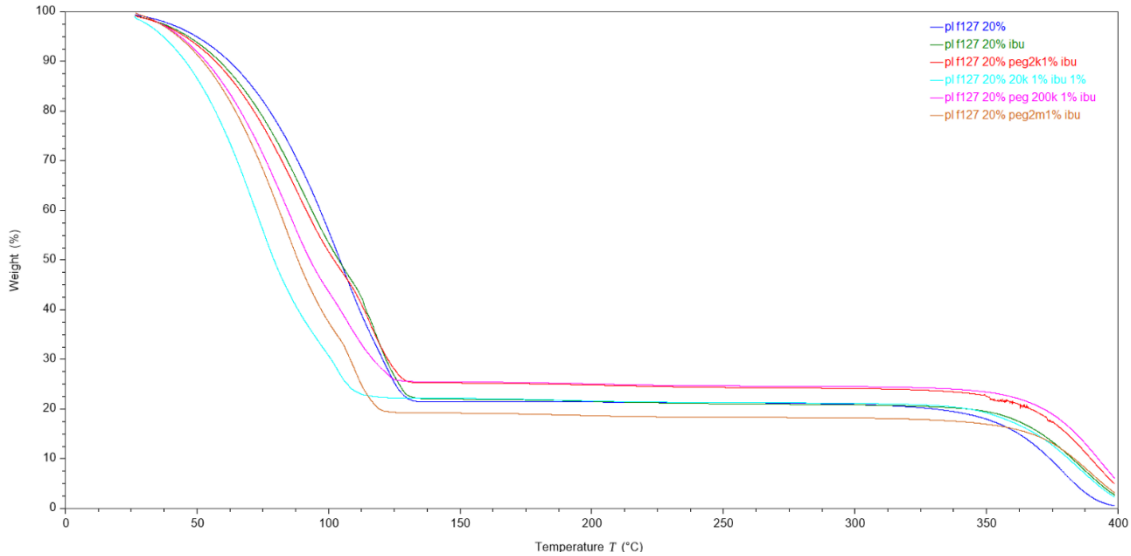

Figure 6-1 TGA curves from room temperature to 400°C.

The corresponding transition temperatures for each formulation are plotted in Figure (6-2) show a clear reduction in the transition temperatures of the PEG-IBU blends compared to non-IBU PEG-blends the lowest and highest molecular weights exhibited the largest differences, where 18.98°C and 12.5°C were recorded for 2M-IBU and 2K-IBU blends, respectively.

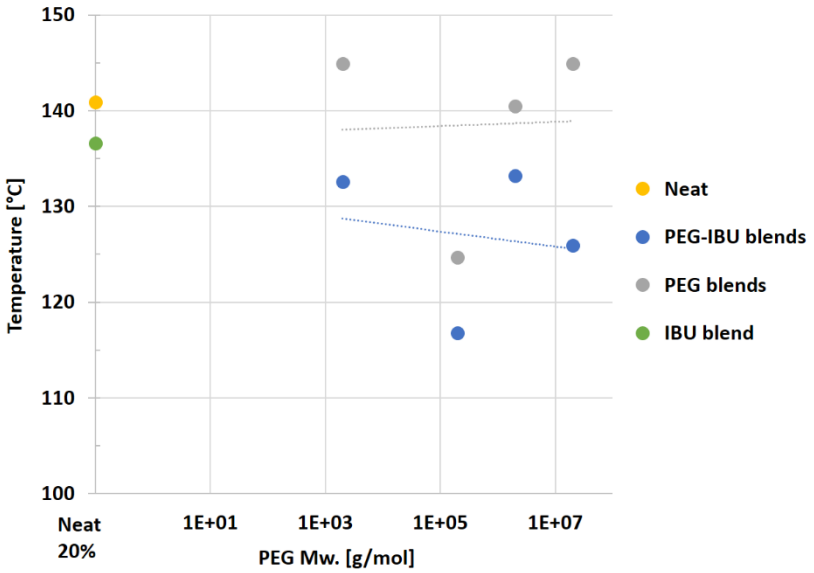

Figure 6-2 TGA transition temperatures for the different blends.

6.2. Rheology Results:

Two sets of rheological measurements were performed on the IBU blends to investigate the system's physical properties and their temperature response under shear; (a) temperature ramps at constant shear rate in the rotational mode and (b) temperature sweeps under oscillation mode. The experimental parameters are identical to those been used in Chapters: 4 and 5, the rotational tests having a ramp from 0 to 40°C under imposed shear rate values of 10, 20, 50 and 100 s^{-1}. A strain value of 0.2% and an angular frequency of 10 rad/sec were applied for the oscillatory shear experiments.

6.2.1. Temperature ramps at constant shear rate:

As can be seen in Figure (6-3), similar to the neat formulation, the IBU-blend was a Newtonian fluid at low temperatures. Thereafter viscosity values followed

the same pattern reported in this study for the majority of the formulations; a reduction as a function of temperature followed by an abrupt increase indicating the formation of a gel structure. The addition of IBU to neat F127 20% had a great impact of the formulation transitions, reducing the initial critical response by 7.2°C and the CGT by 8.5°C compared to the neat formulation.

The effects of IBU's addition to PEG-blends was found to be dependent on the PEG's Mw. For the 20 and 200K blends the CGT was decreased further in comparison to both the F127 IBU-blend and F127 PEG-blends. However, this effect was not observed in the 2M-IBU blend, where the formation exhibited the exact same CGT as the IBU-blend, although its viscosity was slightly reduced compared to IBU-blend. Additionally, introducing IBU to the 2M-blend results in unifying the shear response at lower temperatures, where all shear rates tested exhibited the same viscosity values and removed the characteristic peak observed for the blend just before gelation onset as previously recorded for the non-IBU 2M-blend– see Figure (5-9).

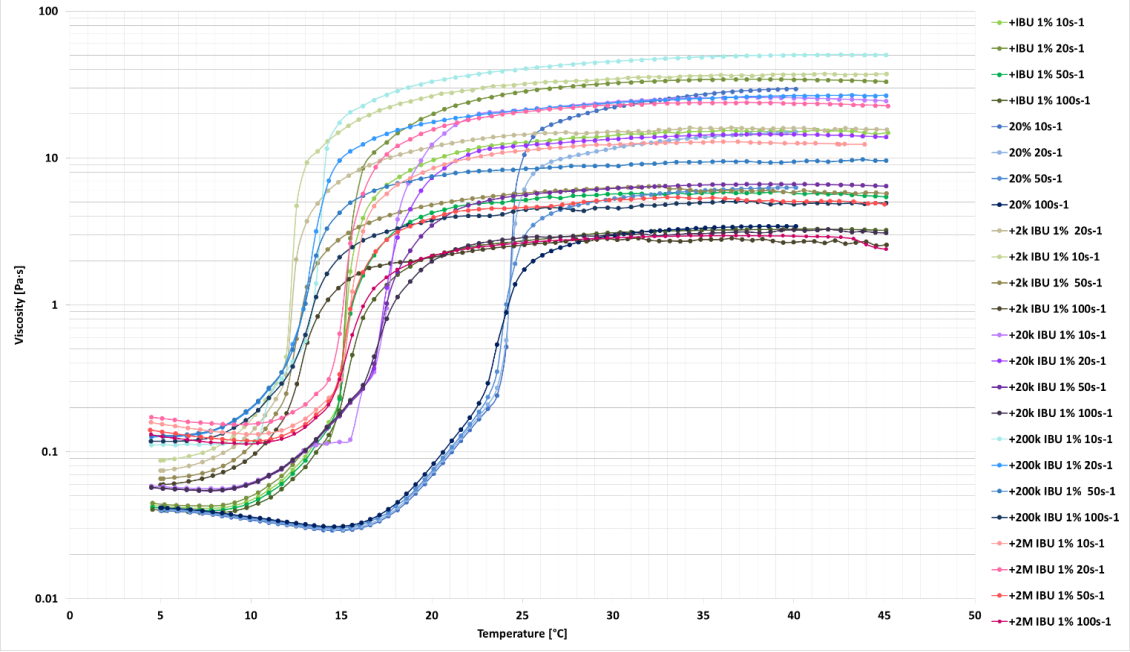

Figure 6-3 PEG-IBU blends temperature ramps at constant shear rates.

6.2.2. Oscillatory shear temperature sweeps:

This set of experiments was performed to explore the gelation limits while recording the dynamic moduli of the formulations. Figure (6-4) show the plotted results for the different blends. At low temperatures, the blends moduli were higher than the neat formulation but still significantly low at values around 1 [Pa] with the ramp progression the moduli crossover indicating gelation at G'= G". The formulations unanimously exhibited a moduli plateau where G' dominated by a decade over G" which remained stable for approximately 50°C. Upon increasing the temperature the moduli values decreased indicating softening and gel structure destruction.

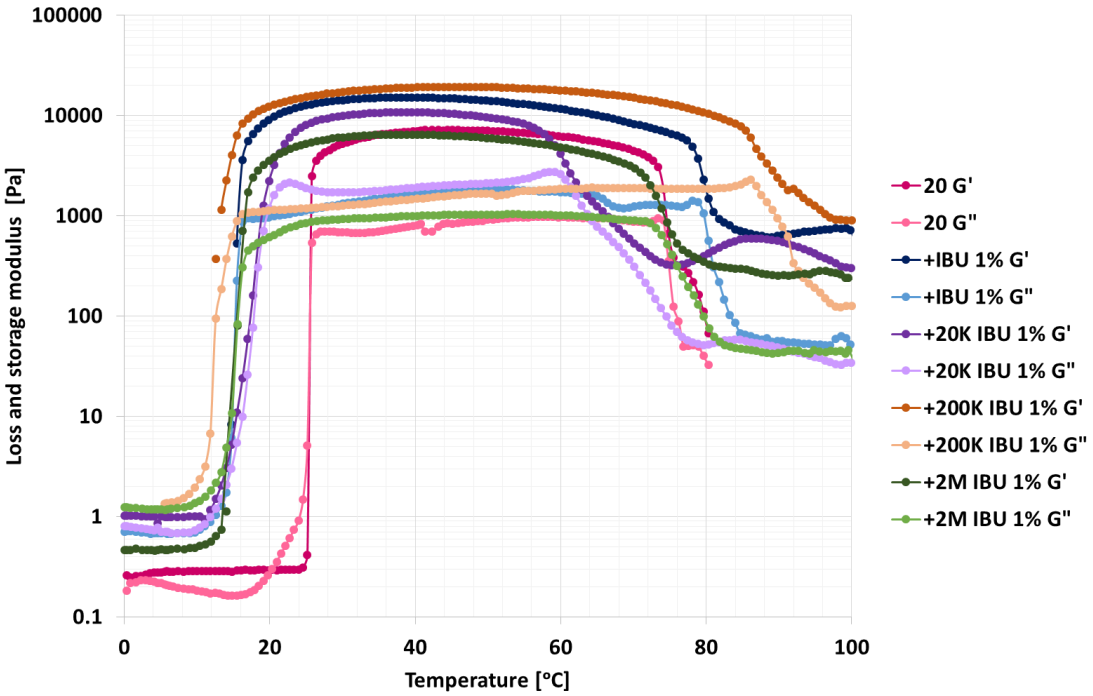

Figure 6-4 PEG-IBU blends temperature sweeps under oscillatory shear.

The complex viscosity profiles in Figure (6-5) exhibited the same response as a function of temperature affirming the results acquired for the shear moduli. Whereby low values were recorded in the pre-gelation stage followed by an abrupt increase resulting in a peak in the complex viscosity where the onset (LT_{gel}) and endset (UT_{gel}) indicate the structural transitions of gelation and softening, respectively.

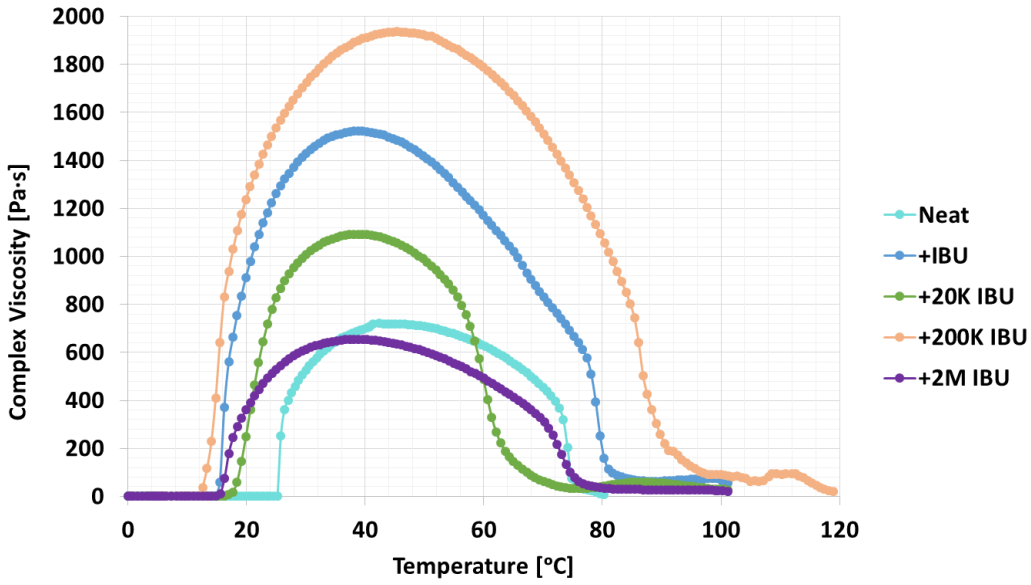

Figure 6-5 PEG-IBU blends complex viscosity values during the oscillatory shear temperature ramp.

6.3. Structural results:

Two x-ray scattering experiments were performed on the formulations containing IBU, using beamline I22 at Diamond – RAL and SAXSpace.

6.3.1. Static SAXS:

6.3.1.1 I22 beamline:

Measurements were taken using the same set up utilised for static PEG-blends experiments in Chapter 4, where loaded quartz capillaries were mounted in front of the beam. The measurements were performed on each sample twice, at room temperature and after refrigeration with no active temperature control.

a) Neat vs. IBU 1%:

Figure (6-6) shows the 1D scattering profiles of two samples, neat F127 20% and the same concentration containing 1% of IBU before and after refrigeration. The chilled neat sample is observed to lack any structural order while the sample containing IBU, exhibits distinctive sharp peaks rising from the bodies of two broad peaks indicating an ordered structure. At room temperature both formulations were observed to exhibit two main peaks with almost overlapping

outlines. The sample containing IBU showed the same sharp peak from before with one additional peak. The peak positions at 0.035, 0.041, 0.058, 0.068 and 0.071 [$Å^{-1}$] were found to match with an FCC lattice, similar to a fully developed neat gel as reported in Chapter 4.

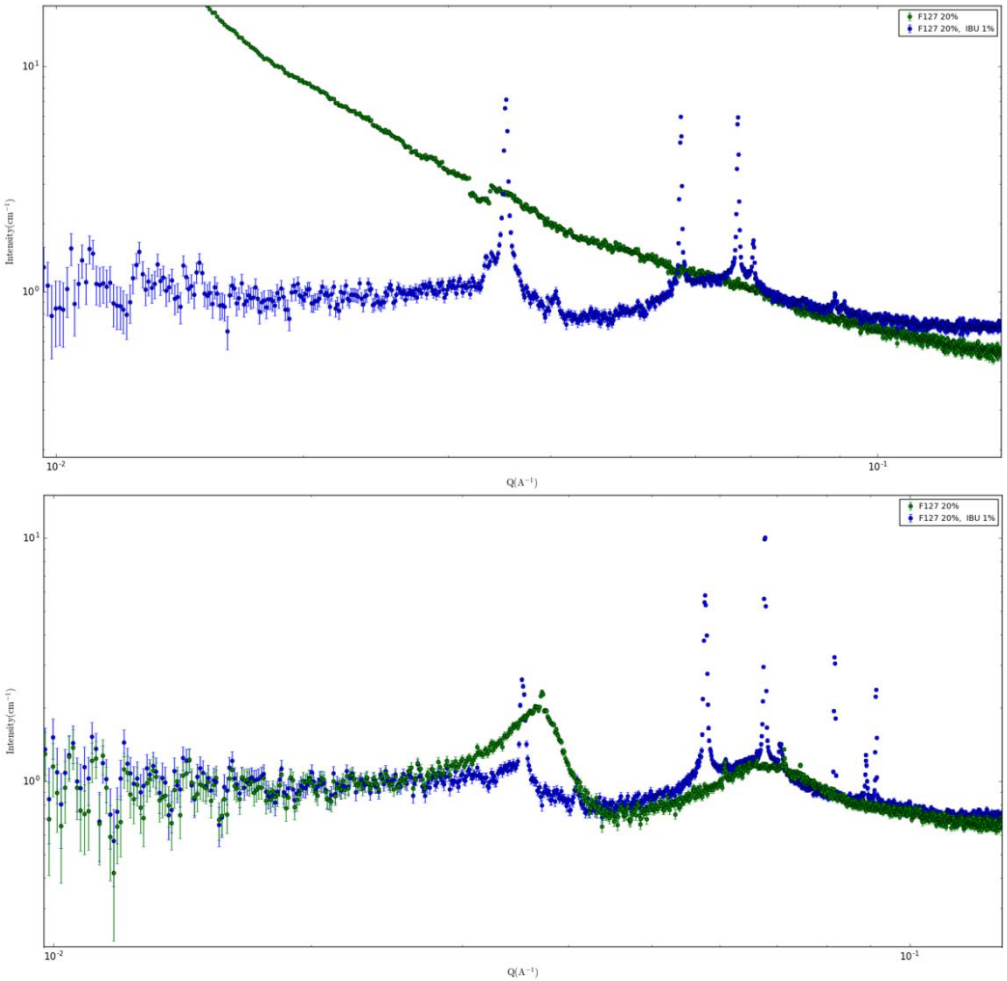

Figure 6-6 SAXS profiles for neat and a formulation containing 1% IBU, (top) after refrigeration and (left) at room temperature.

b) Neat vs. PEG-IBU blends:

Similar to before, the PEG-blends containing IBU showed the same distinctive peaks after refrigeration which were observed to become stronger when the samples were tested again at room temperature –see Figure (6-7).

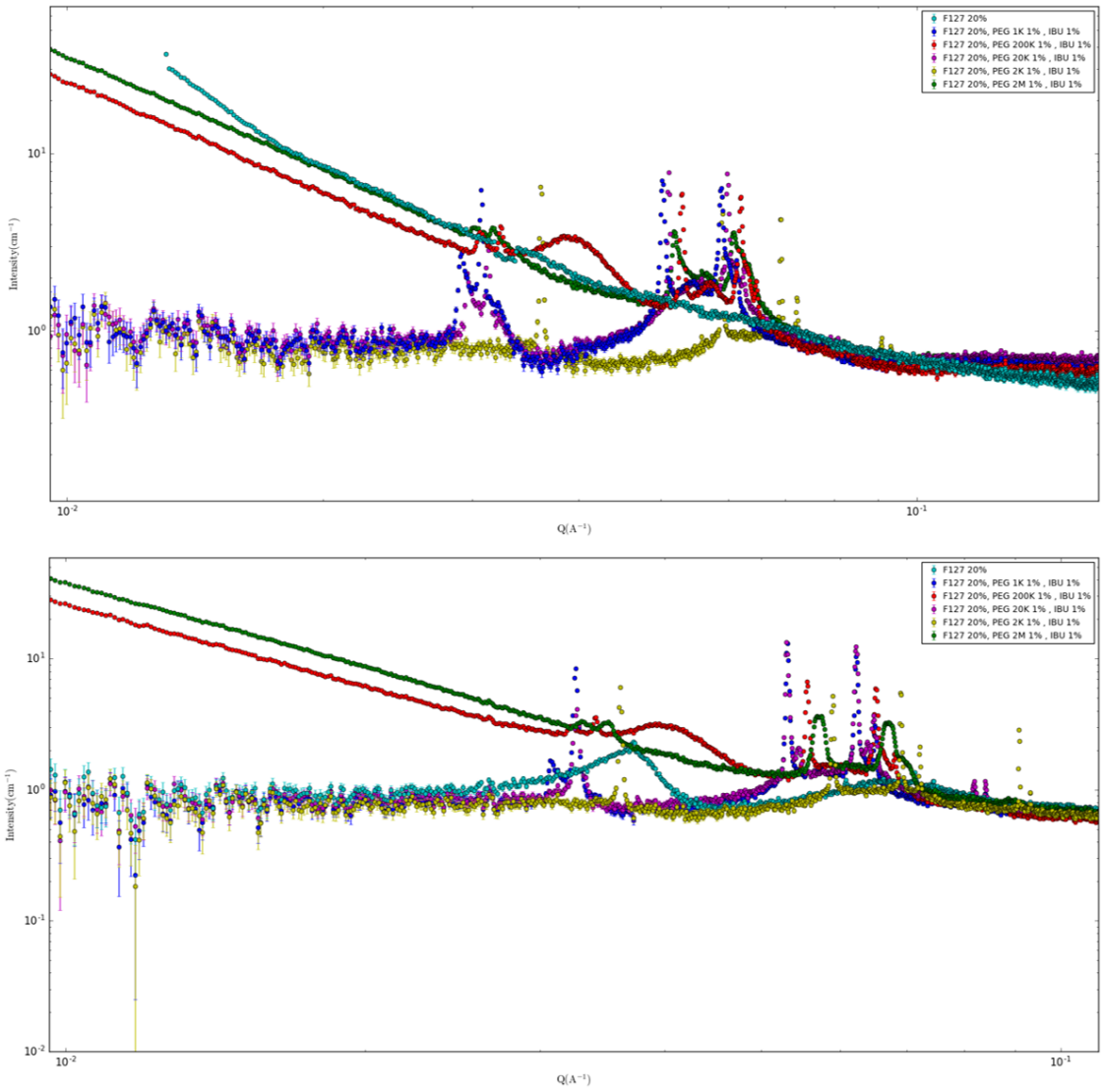

Figure 6-7 SAXS profiles for PEG-blends, (top) after refrigeration and (bottom) at room temperature.

6.3.1.2 SAXSpace:

The blends were tested following the same procedure from Chapters 4 and 5, where the samples were loaded into a quartz capillary mounted on a controlled temperature stage and then tested in the range from 0 to 40°C.

Two main events were observed for PEG-IBU blends in the temperature range of 25-40°C. From 25 to 30°C the blends containing 1 to 20K PEG exhibited a size reduction while within the same temperature range the higher Mw PEGs demonstrated a trend in the opposite direction, where R_{HS} increased. These size changes were functions of both Mw and temperature, though the former had the larger effect, though the calculated R_{HS} values of the blends did not exhibit a large variation across the temperature range. Only three blends were tested at 40°C: 1, 2 and 20K. The blends exhibited the same trend in size reduction with increasing temperature, similar to that previously recorded for lower temperatures. No size differences were recorded for the F127 gel containing IBU from the neat gel. A summary of these results is provided in table (6-1).

Table 6-1 calculated R_{HS} values from SAXS measurements .

Formulation	R_{HS} [nm]				
	20°C	25°C	30°C	35°C	40°C
Neat	10.61	10.61	10.57	10.84	10.61
F127-IBU	10.61	10.61	10.57	10.84	10.61
1K-IBU	10.92	10.66	11.06	11.05	13.46
2K-IBU	-	10.61	10.01	10.26	9.93
20K-IBU	10.54	7.4	7.4	-	9.8
200K-IBU	10.13	9.2	9.2	9.25	-
2M-IBU	7.386	11.66	-	-	-

6.3.2. Dynamic SAXS:

This set of experiments was performed using the same setup in Chapters 4 and 5 using the Linkam shear cell while ramping the temperature from 10 to 49°C at 2°C/min.

The following runs were performed on F127 20% IBU 1% with zero shear and shear rates of 10 and 20 s^{-1}. Figure (6-8) shows the 1D and 2D scattering profiles under heating ramp only. Both profiles show a gradual structural development with increasing temperature. Although weak, the first frame shows peaks at 0.034 and 0.055 [$Å^{-1}$], the first peak growing stronger in intensity and shifting to higher q as the test progressed to reach a q value of 0.062 [$Å^{-1}$] by the end of measurement at 49°C.

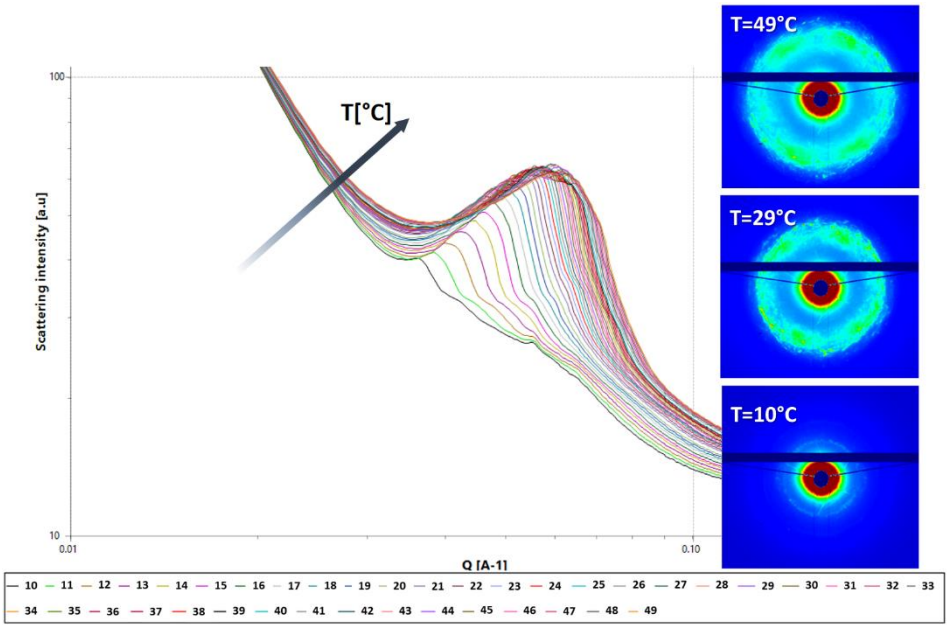

Figure 6-8 Static SAXS IBU-blend at temperature ramp from 10-49°C.

The 2D profiles from the 3rd frame onwards exhibit a higher intensity in the four sided peaks which increased as a function of temperature. Figure (6-9) shows the azimuthal profile of the final frame at 49°C.

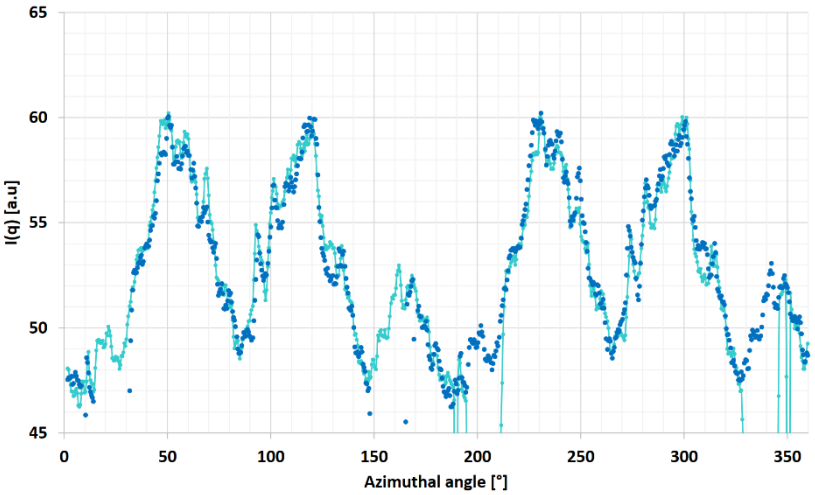

Figure 6-9 SAXS azimuthal profile for gel sample containing IBU 1% at 49°C. The light blue indicate the annular profile and the dark blue its symmetry profile to compensate for missing points due to the beamstop positioning.

When a shear rate of 10 s^{-1} was imposed on the sample the scattering patterns show similar peaks to those recorded in the static measurement, growing weaker as the test proceeded to reach the lowest intensity at the end of the run, as can be seen in Figure (6-10). The centre of the broad peak shifted slightly to the left from 0.060 in the first frame to 0.052 [$Å^{-1}$] in the last one.

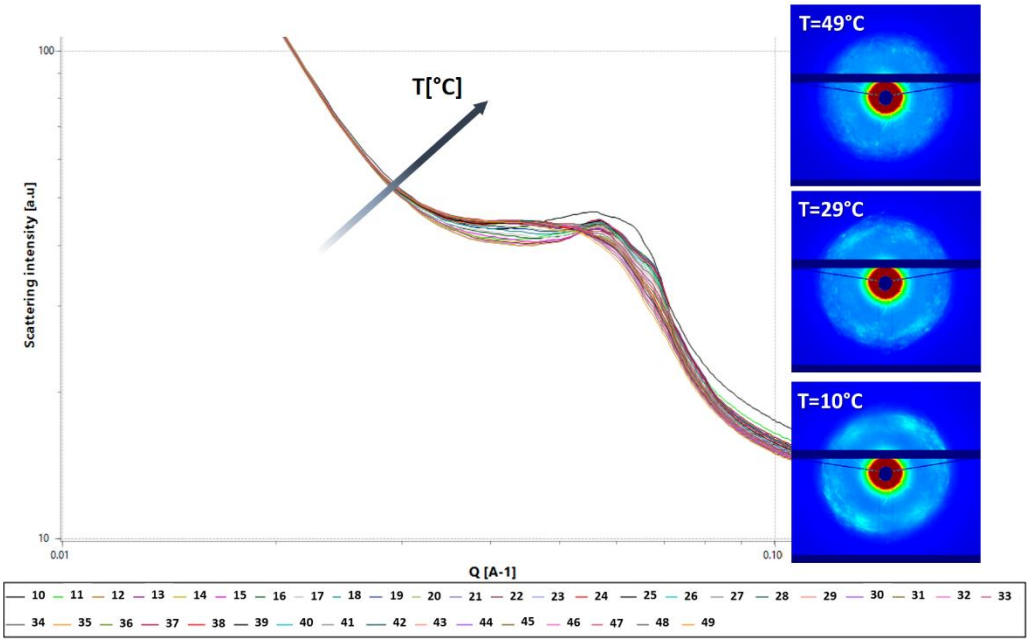

Figure 6-10 SAXS for sheared IBU-blend at 10 s^{-1} and temperature ramp of 10-49°C.

Upon the application of higher shear rate, 20 s^{-1}, two notable events were observed with increasing temperature. The increased intensity and the peak shift from the higher q value of 0.053 at the beginning to a lower one of 0.024 [$Å^{-1}$] at the test conclusion. The scattering profiles are displayed in Figure (6-11).

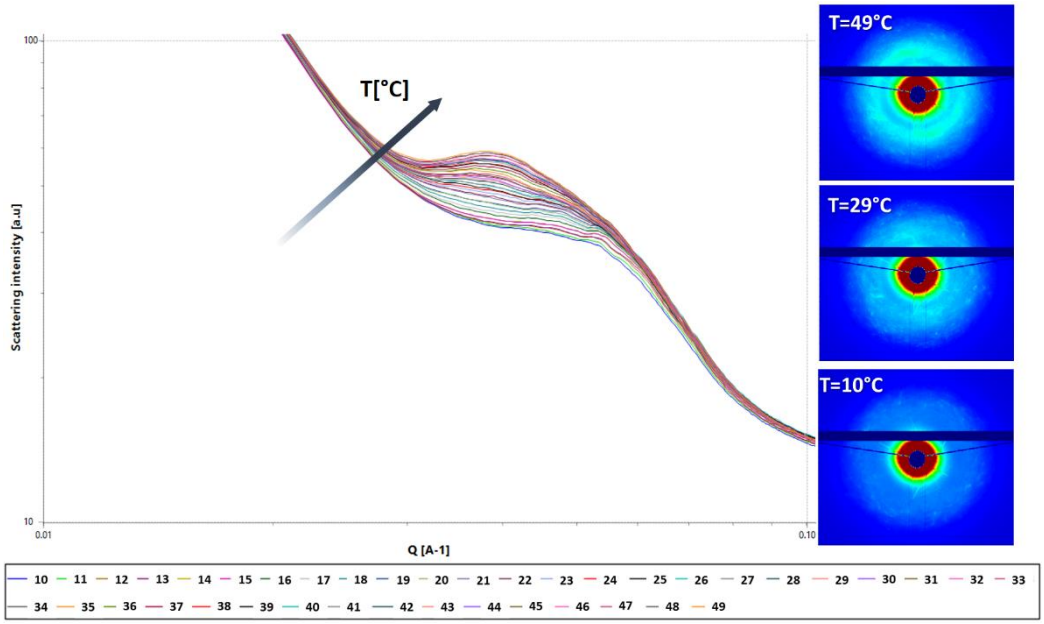

Figure 6-11 SAXS for IBU-blend at sheared 20 s^{-1} and temperature ramp of 10-49°C.

6.4. Results discussion:

The properties of different blends containing the main copolymer F127, high Mw PEGs and Ibuprofen was probed by different techniques under both static and dynamic conditions. The investigation of these properties is essential to predict the loaded DDSs behaviour during processing, administration and drug release. It has been reported that the solubility of Ibuprofen is improved when integrated into Pluronic formulations. The hydrophobic API introduction resulted in decreasing CMC, increasing the micellar aggregate number and increasing the micellar size (Foster et al., 2009, Basak and Bandyopadhyay, 2013)

The scattering experiments performed on the blends demonstrated that IBU's effect was prevalent in all the experiments even at low temperatures, with 'sharp peaks' appearing at cold and room temperature testing conditions using the I22 SAXS instrument. However, these peaks were stronger compared to

similar scattering studies performed on IBU loaded systems: Pluronic F127 by Foster et al. (2009) and Basak and Bandyopadhyay (2013) using P103, 104 and 105, where in both papers the formulations were prepared by adding IBU into the polymeric solutions. The indexed peaks correlate to FCC lattice – similar to the neat gels and patterns have been observed for 2M-blend (discussed in Chapter 5) that contained no IBU and tested using the same instrument. Therefore these peaks are most likely the same peaks detected previously in neat systems, however, due to the instrument's high resolution and low sample thickness they resemble spikes rather than the usual peaks observed by the other lower resolution and intensity instrument used, SAXSpace.

The results indicate that the majority of the formulations maintained the neat F127 FCC structure after the addition of IBU, except the 1K-IBU blend which showed a clear BCC structure. Inconclusive results were acquired for 200K- and 2M- IBU blends. Figure (6-12) shows the calculated R_{HS} values for measurements taken with the two instruments at approximately the same temperatures. The radii values acquired from I22 data sets displayed a more consistent trend where the size generally increased with addition of IBU to the neat formulation that persisted in PEG-IBU blends. Two radii were identical in both setups, the blends containing 2K- and 2M-IBU.

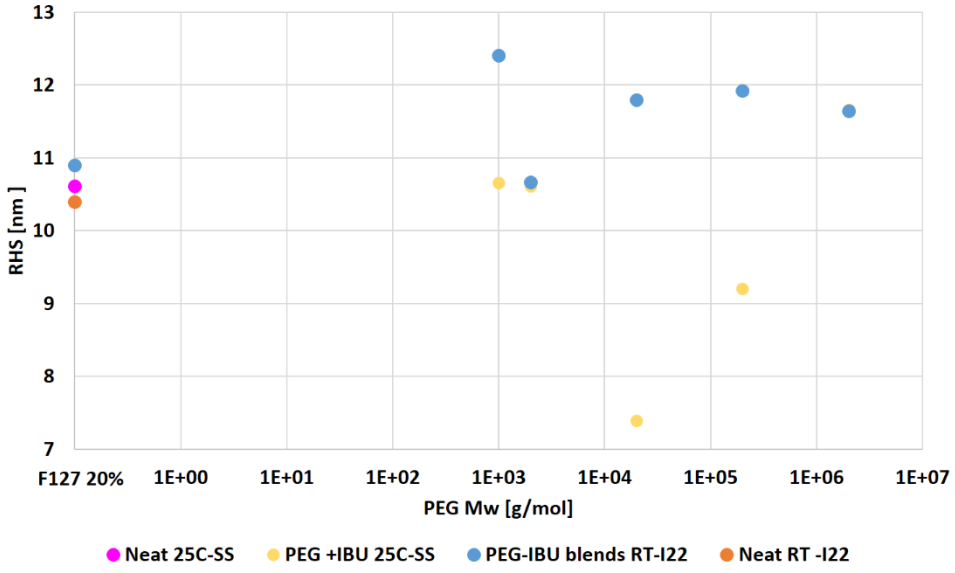

Figure 6-12 PEG-IBU bleds hard sphere radii calculated using data collected form I22 and SAXSpace (SS) at differernt tempeartures.

It is worth mentioning that the two measurements were taken 14 days apart, where the samples were tested first using I22 and followed by SAXSpace. This might have resulted in crystallisation of IBU portion, reducing the quality of the measurements and possibly the discrepancy seen in the results.

The thermorheological properties of the formulations were found to be strongly affected by the addition of the API. Figure (6-13) shows the CGT of PEG-IBU blends compared to the neat, IBU- and PEG-blends previously tested in this study. The results clearly show that although PEGs managed to reduce the gelation temperature of the neat F127- as demonstrated in the results from Chapter 5, IBU was more efficient in decreasing CGT than PEG, and blends containing both additives exhibited lower CGTs than the blends containing PEG only. For the three different Mw PEGs formulated with IBU, the relationship between the chain length of the CGT appear to be negatively proportional in both formulations with and without IBU, although in both cases sample containing 200K was off trend compared the other PEGs.

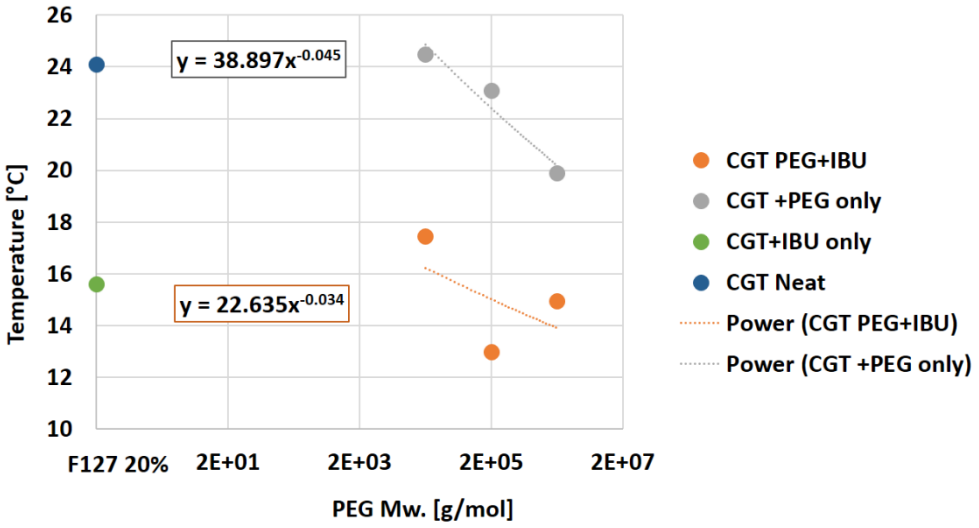

Figure 6-13 PEG and PEG-IBU blends CGT values from costant shear – temperature ramp tests.

Oscillatory shear temperature ramps were utilised to measure the dynamic moduli while expanding the temperature ramp range up to 120°C, which allowed the determination of the gelation boundaries of the blends. Figure (6-14) shows the gelation boundaries as a function the blend PEG's content with and without IBU. IBU's addition to the blends increased the limits ΔT_{gel} (UT_{gel} - LT_{gel}) for each blend. The 200K-IBU blend exhibited the largest difference recorded of 19.65°C compared to 2.92 and 0.44°C for 20K and 2M blends.

The trend observed for the blend CGTs was matched with LT_{gel} recorded from these sweeps. Minor discrepancies between the gelation temperatures recorded using the two different modes are expected, and the decrease in the LT_{gel} trend with Mw should be still valid across the blends. The 200K showed the same off-trend behaviour seen previously in the rotational tests, where LT_{gel} was lower than trend line. Even though the behaviour is reciprocated in the UT_{gel} , the PEG-IBU blends share the same trend line equation as PEG-blends, which indicates that the IBU addition had a bigger effect on the lower gelation limits rather than the gel softening.

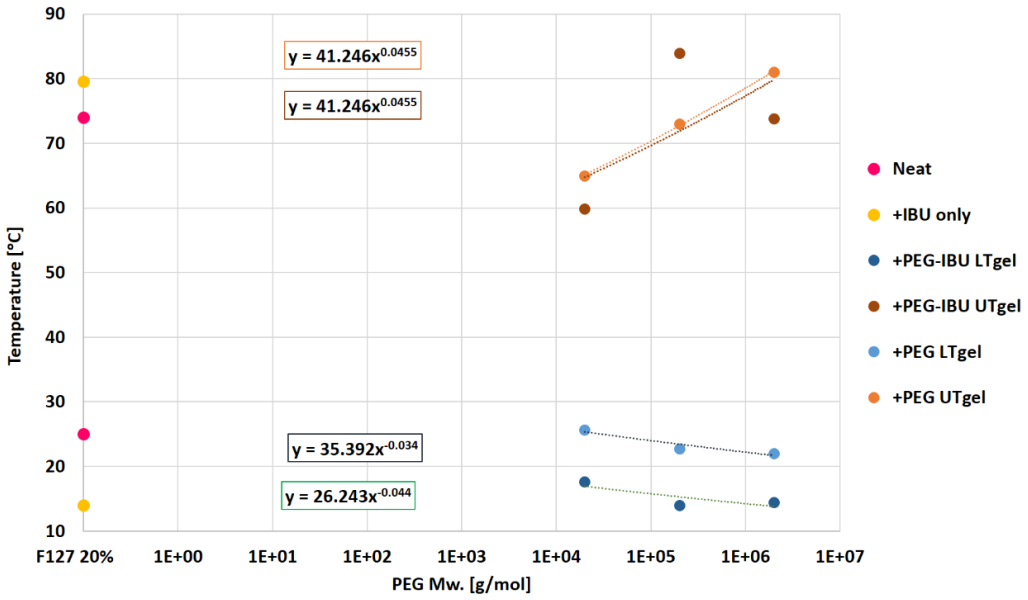

Figure 6-14 Gelation boundaries for PEG-IBU blends as fuction of PEG Mw.

Chapter 7 Conclusions and suggestions for future work:

7.1. Conclusions:

The aim of this thesis was to provide a comprehensive study of aqueous solutions of Pluronic F127 as injectable matrices for controlled drug delivery. The properties of these systems were investigated by thermal, rheological and scattering methods to elucidate the structural changes these systems undergo as a function of temperature and shear rate during production and administration.

Pluronic F127 was probed as the main ingredient for the systems in this study with two additional Pluronics F68 and F108 with different molecular weights, utilised to compare the matrix properties and suitability as injectable systems through a series of experiments as a function of concentration. Effects of additives were studied by preparing blends containing different Mw PEGs (possessing varied levels of hydrophobicity) and a model drug formulation with Ibuprofen (IBU).

Gelation occurs when the micellar volume fractions threshold is exceeded as a function of temperature causing the micelles to self-associate into hard spheres with defined colloidal crystal structures. As demonstrated by the thermal characterisation results, transition temperatures and gel stability were simply a function of the copolymer concentration used. Although no indication of gelation was detected by DSC, the technique is still useful to determine CMT, the overall transition enthalpy and therefore the transition free energy.

The system's structural evolution was observable rheologically in three stages:

1. The polymeric solutions state, where the three Pluronics behave as ideal Newtonian fluids at low temperatures with low viscosity values.
2. The transition stage, which has been bounded by a critical temperature. During this stage the solution viscosity values are reduced to a minimum proven to correspond to the endothermic transition detected by the DSC when the two experimental heating rates were matched.

3. The gelation stage, marked by a circa tenfold abrupt increase of viscosity followed by a stable plateau. In the first two stages, formulation's rheological behaviour is only temperature dependent while the third stage displays both shear and temperature dependency. Thermograms of sheared gels displayed an additional peak in their exothermic cooling step, indicating a detectable structural change due to imposed shear.

The gel hydrodynamic shear response was found to be dependent on the shear rate applied, where the resultant shear thinning behaviour was a macroscopic manifestation of the microscopic layer's motion. Even though the hard sphere radii remained constant under different shear rates, the final crystal morphology was altered from FCC to RCP. The environmental variance (shear and temperature) has a great role on the gel properties and the matrix type. This extends to the different flows applied to the micellar solutions to result in a different gel structure than obtained from the idealised experimental conditions – as demonstrated by the mixed flow SAXS results seen in 4.3.2.

Under the experimental conditions tested, both F108 and F127 displayed the three stages within the concentrations and temperature ramps tested. Unlike the triblock with approximately the same PEO ratio F108, F68 solution did not undergo gelation – although measurements indicate that, under high enough concentrations/temperature, F68 will exhibit similar transitions to the higher molecular weight triblocks F108 and F127. This proves that the PEO/PPO ratio is more important than each block's percentage in prompting gelation.

The system properties can be easily tuned by introducing different moieties to the formulation, which can be accomplished even by common pharmaceutical excipients and release modifiers. For this purpose, two additives were investigated for their effect on the gel properties and three blend types were formulated to include:

1. A homopolymer; PEG the largest constituent of the triblock's structure. Blends were prepared with PEGs with different molecular weights ranging from 1K to 2M [g/mol] - allowing a diverse range of hydrophobicities within the prepared blends.

2. A model hydrophobic API, Ibuprofen.
3. Blends containing both species, IBU and high molecular weight PEGs. The effects of additives on the gel's transition and structure were evaluated as functions of the blend's thermorheological behaviour.

For the first type, experiments have shown that the PEG addition is dependent on homopolymer concentration and chain length. Thermal characterisation indicated that PEG addition had a small effect on the transition's endothermic peak, this effect becoming stronger with increasing Mw. Similarly, rheological measurements demonstrated that for most blends, the gelation temperatures were decreased compared to the neat formulation. Although all blends exhibited shear thinning behaviour, its extent depended on the PEG's Mw – where the highest values were recorded for the blends with the shortest and longest chains. Scattering results showed that gel hard spheres were more resistant to size changes under imposed shear at the higher temperature (37°C) compared to transitional temperatures. Spheres grew larger upon increasing the shear rate at the same temperature during the transition but remained constant at 37°C, except for an Mw of 20K, which exhibited a size reduction when the shear was increased from 10 to 100 s^{-1}.

The F127-IBU blend exhibited a pronounced reduction in CGT compared to the neat gel without altering the FCC structure and maintaining almost the same viscosity values. The blends containing both PEG and IBU displayed a stronger reduction than blends containing either additive alone, proving the synergistic effect of the two additives. Both species increase the system's hydrophobicity, thus decrease CMC and result in an earlier gelation than that recorded for F127-IBU and PEG-blends. Similarly, to the PEG-blends, the final product's properties and gelation boundaries were functions of the PEG chain length. In all three types, the gel hard spheres were mostly larger than the neat gel under both static and dynamic conditions.

The additives substantially affected thermal, rheological and structural properties of the gel systems, which proves the importance of in-depth individual formulation studies when an API is added to the matrix.

7.2. Future work:

The results presented in this study demonstrated the promising properties of these systems which can be further investigated from chemical, biological and physical perspectives. A further detailed investigation of the systems would include:

- Utilising the rheological and scattering measurements data acquired in this study to develop a universal model for Pluronics and similar systems under realistic application conditions. This will require focus on mixed shear environments and their effects on the system's kinetics, final structure and ultimately drug release. We have already demonstrated the injection effect on the structure, however the experiments should be performed under more controlled conditions (active temperature control) to study the stability of the gel with time. Rigs have been manufactured for both SAXS and SANS measurements equipped with cooling channels. However it was not feasible to perform the experiments due to time constraints.
- Since RCP structures contain 2D-HCP, unlike the pure cubic lattice, this should exhibit some birefringent properties which can be probed under shear, either by using a Linkam shear cell or by similar injection rigs to those produced for SAXS and SANS studies.
- As mentioned briefly in 3.3.2b, SANS-LAOS experiments were performed but the analysis is not fully complete to be included in this thesis. This analysis will allow determination of the ordered crystalline to disordered melt changes in the system at any strain (time) with the range covered. And the determination of the optimal strain values required to reach the desired crystallinity levels required for the application. Similarly, time resolved SANS data were collected through all measurements to monitor structural evolution of disorder-order-disorder transitions, these datasets require further processing that has not been completed yet.
- Comprehensive injectability tests to determine the optimal administration force required correlating to the system yield stress. Preliminary studies have been performed and results look promising.

- Implementation of the thermo-rheological results into developing a CFD model that takes into consideration yield stress and shear inhomogeneities including; wall-slip and shear banding to predict the formulation's behaviour during processing and administration. This will allow efficient modification of the manufacturing conditions or the formulation recipe to refine the final product properties.

Taking the formulation a step closer to the clinical application would require more control over the used API and its properties. Which would require:

- To investigate the types of the intermolecular interaction formed between Pluronics (in both purified and non-purified forms) and the additives. Nuclear Magnetic Resonance (NMR) has been suggested to be promising by some groups for these studies.
- To introduce two (or more) moieties with varied hydrophobicity levels into the same matrix to investigate the effects of their interactions with the gel matrix, each other and on the overall formulation properties.
- Using multiple loaded drug formats, as in micro- and nano-suspensions. A DDS of F127 loaded with Disulfiram nano-suspension has been successfully utilised in animal studies to deliver the drug into lab rat brain stems. However, no characterisation has been performed on the system yet.
- To introduce another stimulus responsive gelling agent, whether by grafting the copolymer, adding charged moieties or proteins. This would offer more control over the system's properties (longevity inside the body, allow more targeted release rather than physical diffusion and enhance biocompatibility).
- To perform the essential regulatory tests such as: the matrix loading efficiency (micellar capacity), cellular bio-stability, and swelling and degradation in both in vitro and in vivo. This will allow the determination of the exact release rate from the gel matrix and full evaluation the system interactions with living cells.

References:

AGUADO, B. A., MULYASASMITA, W., SU, J., LAMPE, K. J. & HEILSHORN, S. C. 2012. Improving Viability of Stem Cells During Syringe Needle Flow Through the Design of Hydrogel Cell Carriers. *Tissue Engineering. Part A,* 18**,** 806-815.

AHUJA, A. & SINGH, A. 2009. Slip velocity of concentrated suspensions in Couette flow. *Journal of Rheology,* 53**,** 1461-1485.

ALEXANDER, A., AJAZUDDIN, KHAN, J., SARAF, S. & SARAF, S. 2014. Polyethylene glycol (PEG)-Poly(N-isopropylacrylamide) (PNIPAAm) based thermosensitive injectable hydrogels for biomedical applications. *Eur J Pharm Biopharm,* 88**,** 575-85.

ALEXANDRIDIS, P. & ALAN HATTON, T. 1995. Poly(ethylene oxide)-poly(propylene oxide)-poly(ethylene oxide) block copolymer surfactants in aqueous solutions and at interfaces: thermodynamics, structure, dynamics, and modeling. *Colloids and Surfaces A: Physicochemical and Engineering Aspects,* 96**,** 1-46.

ALEXANDRIDIS, P. & HATTON, A. 1994. Poly(ethylene oxide)-poly(propylene oxide)-poly (ethylene oxide)

block copolymer surfactants in aqueous solutions and at interfaces:

thermodynamics, structure, dynamics, and modeling. *Colloids Surfaces A: Physicochem. Eng. Aspects,* 96**,** I -46.

ALI, M., AKIN, A., BAHAMONDES, L., BRACHE, V., HABIB, N., LANDOULSI, S., HUBACHER, D. & FOR THE, W. H. O. S. G. O. S. C. I. F. W. 2016. Extended use up to 5 years of the etonogestrel-releasing subdermal contraceptive implant: comparison to levonorgestrel-releasing subdermal implant. *Human Reproduction,* 31**,** 2491-2498.

ALLEN, L. & ANSEL, H. C. 2013. *Ansel's Pharmaceutical Dosage Forms and Drug Delivery Systems*, Wolters Kluwer Health.

ALLMENDINGER, A., FISCHER, S., HUWYLER, J., MAHLER, H.-C., SCHWARB, E., ZARRAGA, I. E. & MUELLER, R. 2014. Rheological characterization and injection forces of concentrated protein formulations: An alternative predictive model for non-Newtonian solutions. *European Journal of Pharmaceutics and Biopharmaceutics,* 87**,** 318-328.

ALMEIDA, H., AMARAL, M. H., LOBAO, P. & LOBO, J. M. 2014. In situ gelling systems: a strategy to improve the bioavailability of ophthalmic pharmaceutical formulations. *Drug Discov Today,* 19**,** 400-12.

ALVAREZ-LORENZO, C. & CONCHEIRO, A. 2014. Smart drug delivery systems: from fundamentals to the clinic. *Chemical Communications,* 50**,** 7743-7765.

AMER, M. H., ROSE, F. R. A. J., SHAKESHEFF, K. M., MODO, M. & WHITE, L. J. 2017. Translational considerations in injectable cell-based therapeutics for neurological applications: concepts, progress and challenges. *npj Regenerative Medicine,* 2**,** 23.

ANTON-PAAR 2018. Viscosity of Water. Anton-Paar.

APPEL, E. A., TIBBITT, M. W., WEBBER, M. J., MATTIX, B. A., VEISEH, O. & LANGER, R. 2015. Self-assembled hydrogels utilizing polymer–nanoparticle interactions. *Nat Commun,* 6.

ARAKI, T., SHIBAYAMA, M. & TRAN-CONG, Q. 1998. *Structure and Properties of Multiphase Polymeric Materials*, Taylor & Francis.

ASIUS, J., FESSI, H., GOUCHET, F., LAGLENNE, B. & LAUGIER-LAGLENNE, E. 2004. Implant for subcutaneous or intradermal injection. Google Patents.

ATTWOOD, D., COLLETT, J. H. & TAIT, C. J. 1985. The micellar properties of the poly(oxyethylene) - poly(oxypropylene) copolymer Pluronic F127 in water and electrolyte solution. *International Journal of Pharmaceutics,* 26**,** 25-33.

ATTWOOD, D. & FLORENCE, A. T. 1983. *Surfactant systems: their chemistry, pharmacy and biology*, Chapman and Hall.

AYANO, E., KARAKI, M., ISHIHARA, T., KANAZAWA, H. & OKANO, T. 2012. Poly (N-isopropylacrylamide)–PLA and PLA blend nanoparticles for temperature-controllable drug release and intracellular uptake. *Colloids and Surfaces B: Biointerfaces,* 99**,** 67-73.

BAE, K. H., WANG, L.-S. & KURISAWA, M. 2013. Injectable biodegradable hydrogels: progress and challenges. *Journal of Materials Chemistry B,* 1**,** 5371-5388.

BAIN, M. K., BHOWMICK, B., MAITY, D., MONDAL, D., MOLLICK, M. M. R., PAUL, B. K., BHOWMIK, M., RANA, D. & CHATTOPADHYAY, D. 2012. Effect of PVA on the gel temperature of MC and release kinetics of KT from MC based ophthalmic formulations. *International Journal of Biological Macromolecules,* 50**,** 565-572.

BARICHELLO, J. M., MORISHITA, M., TAKAYAMA, K. & NAGAI, T. 1999. Absorption of insulin from Pluronic F-127 gels following subcutaneous administration in rats. *International Journal of Pharmaceutics,* 184**,** 189-198.

BARNES, H. A. 1995. A review of the slip (wall depletion) of polymer solutions, emulsions and particle suspensions in viscometers: its cause, character, and cure. *Journal of Non-Newtonian Fluid Mechanics,* 56**,** 221-251.

BARNETT, D., CHALMERS, CHALMERS 1997. Industrial Analysis with Vibrational Spectroscopy. P001-380.

BASAK, R. & BANDYOPADHYAY, R. 2013. Encapsulation of Hydrophobic Drugs in Pluronic F127 Micelles: Effects of Drug Hydrophobicity, Solution Temperature, and pH. *Langmuir,* 29**,** 4350-4356.

BASF 2004. Technical Bulletin Pluronic® Block Copolymer. *In:* CORPORATION, B. (ed.). BASF Corporation.

BEARAT, H. H., LEE, B. H. & VERNON, B. L. 2012. Comparison of properties between NIPAAm-based simultaneously physically and chemically gelling polymer systems for use in vivo. *Acta Biomaterialia,* 8**,** 3629-3642.

BERRADA, M., SERREQI, A., DABBARH, F., OWUSU, A., GUPTA, A. & LEHNERT, S. 2005. A novel non-toxic camptothecin formulation for cancer chemotherapy. *Biomaterials,* 26**,** 2115-2120.

BHATTARAI, N., GUNN, J. & ZHANG, M. 2010. Chitosan-based hydrogels for controlled, localized drug delivery. *Advanced Drug Delivery Reviews,* 62**,** 83-99.

BRUN-GRAEPPI, A. K. A. S., RICHARD, C., BESSODES, M., SCHERMAN, D., NARITA, T., DUCOURET, G. & MERTEN, O.-W. 2010. Study on the sol–gel transition of xyloglucan hydrogels. *Carbohydrate Polymers,* 80**,** 555-562.

CASTELLETTO, V., PARRAS, P., HAMLEY, I. W., BÄVERBÄCK, P., PEDERSEN, J. S. & PANINE, P. 2007. Wormlike Micelle Formation and Flow Alignment of a Pluronic Block Copolymer in Aqueous Solution. *Langmuir,* 23**,** 6896-6902.

CATES, M. E. & FIELDING, S. M. 2006. Rheology of giant micelles. *Advances in Physics,* 55**,** 799-879.

CHEN, S.-C., WU, Y.-C., MI, F.-L., LIN, Y.-H., YU, L.-C. & SUNG, H.-W. 2004. A novel pH-sensitive hydrogel composed of N,O-carboxymethyl chitosan and alginate cross-linked by genipin for protein drug delivery. *Journal of Controlled Release,* 96**,** 285-300.

CHEN, S., ZHONG, H., GU, B., WANG, Y., LI, X., CHENG, Z., ZHANG, L. & YAO, C. 2012. Thermosensitive phase behavior and drug release of in situ N-isopropylacrylamide copolymer. *Materials Science and Engineering: C,* 32**,** 2199-2204.

COLOMBO, P., BETTINI, R., SANTI, P. & PEPPAS, N. A. 2000. Swellable matrices for controlled drug delivery: gel-layer behaviour, mechanisms and optimal performance. *Pharmaceutical Science & Technology Today,* 3**,** 198-204.

CROMPTON, T. R. 2010. *Thermo-oxidative Degradation of Polymers,* Shrewsbury, Shropshire, GBR, Smithers Rapra.

DAO, M. M., DOMACH, M. M. & WALKER, L. M. 2017. Impact of dispersed particles on the structure and shear alignment of block copolymer soft solids. *Journal of Rheology,* 61**,** 237-252.

DAS, D., GHOSH, P., GHOSH, A., HALDAR, C., DHARA, S., PANDA, A. B. & PAL, S. 2015. Stimulus-Responsive, Biodegradable, Biocompatible, Covalently Cross-Linked Hydrogel Based on Dextrin and Poly(N-isopropylacrylamide) for in Vitro/in Vivo Controlled Drug Release. *ACS Applied Materials & Interfaces,* 7**,** 14338-14351.

DE LIMA, C. M., SIQUEIRA, S. M. C., DE AMORIM, A. F. V., COSTA, K. B. S., DE BRITO, D. H. A., RIBEIRO, M. E. N. P., RICARDO, N. M. P. S., CHAIBUNDITC, C., YEATES, S. G. & RICARDO, N. M. P. S. 2015. Effects of Polypropylene Glycol 400 (PPG400) on the Micellization and Gelation of Pluronic F127. *Macromolecules*.

DEWAN, S. S. 2014. Global Markets and Technologies for Advanced Drug Delivery Systems -- Focus on Routes of Administration.

DIAT, O., PORTE, G. & BERRET, J.-F. 1996. Orientation and twins separation in a micellar cubic crystal under oscillating shear. *Physical Review B,* 54**,** 14869-14872.

DINARVAND, R. & D'EMANUELE, A. 1995. The use of thermoresponsive hydrogels for on-off release of molecules. *Journal of Controlled Release,* 36**,** 221-227.

DIVOUX, T., FARDIN, M. A., MANNEVILLE, S. & LEROUGE, S. 2016. Shear Banding of Complex Fluids. *Annual Review of Fluid Mechanics,* 48**,** 81-103.

DOMB, A. J., KUMAR, NEERAJ 2011. *Biodegradable Polymers in Clinical Use and Clinical Development,* Hoboken, NJ, USA, John Wiley & Sons.

DRAGAN, E. S. 2014. Design and applications of interpenetrating polymer network hydrogels. A review. *Chemical Engineering Journal,* 243**,** 572-590.

DREISS, C. A., NWABUNWANNE, E., LIU, R. & BROOKS, N. J. 2009. Assembling and de-assembling micelles: competitive interactions of cyclodextrins and drugs with Pluronics. *Soft Matter,* 5**,** 1888-1896.

DURAND, A. & HOURDET, D. 1999. Synthesis and thermoassociative properties in aqueous solution of graft copolymers containing poly(N-isopropylacrylamide) side chains. *Polymer,* 40**,** 4941-4951.

EBARA, M., KOTSUCHIBASHI, Y., UTO, K., AOYAGI, T., KIM, Y.-J., NARAIN, R., IDOTA, N. & HOFFMAN, J. M. 2014. Smart Hydrogels. *Smart Biomaterials.* Tokyo: Springer Japan.

EISER, E., MOLINO, F., PORTE, G. & DIAT, O. 2000a. Nonhomogeneous textures and banded flow in a soft cubic phase under shear. *Physical Review E,* 61**,** 6759.

EISER, E., MOLINO, F., PORTE, G. & PITHON, X. 2000b. Flow in micellar cubic crystals. *Rheologica Acta,* 39**,** 201-208.

EUROPE, C. O. & COMMISSION, E. P. 2004. *European Pharmacopoeia*, Council of Europe.

FIELDING, S. M. 2016. Triggers and signatures of shear banding in steady and time-dependent flows. *Journal of Rheology,* 60**,** 821-834.

FIELDING, S. M. & OLMSTED, P. D. 2003. Flow phase diagrams for concentration-coupled shear banding. *The European Physical Journal E,* 11**,** 65-83.

FOSTER, B., COSGROVE, T. & HAMMOUDA, B. 2009. Pluronic Triblock Copolymer Systems and Their Interactions with Ibuprofen. *Langmuir,* 25**,** 6760-6766.

FUJIMOTO, K. L., MA, Z., NELSON, D. M., HASHIZUME, R., GUAN, J., TOBITA, K. & WAGNER, W. R. 2009. Synthesis, characterization and therapeutic efficacy of a biodegradable, thermoresponsive hydrogel designed for application in chronic infarcted myocardium. *Biomaterials,* 30**,** 4357-68.

FURIA, T. E. 1973. *CRC Handbook of Food Additives, Second Edition*, Taylor & Francis.

GILL, P., SAUERBRUNN, S. & READING, M. 1993. Modulated differential scanning calorimetry. *Journal of Thermal Analysis and Calorimetry,* 40**,** 931-939.

GONG, C., SHI, S., DONG, P., KAN, B., GOU, M., WANG, X., LI, X., LUO, F., ZHAO, X., WEI, Y. & QIAN, Z. 2009. Synthesis and characterization of PEG-PCL-PEG thermosensitive hydrogel. *International Journal of Pharmaceutics,* 365**,** 89-99.

GOU, M., LI, X., DAI, M., GONG, C., WANG, X., XIE, Y., DENG, H., CHEN, L., ZHAO, X., QIAN, Z. & WEI, Y. 2008. A novel injectable local hydrophobic drug delivery system: Biodegradable nanoparticles in thermo-sensitive hydrogel. *International Journal of Pharmaceutics,* 359**,** 228-233.

GURNEV, P. A., STANLEY, C. B., AKSOYOGLU, M. A., HONG, K., PARSEGIAN, V. A. & BEZRUKOV, S. M. 2017. Poly(ethylene glycol)s in Semidilute Regime: Radius of Gyration in the Bulk and Partitioning into a Nanopore. *Macromolecules,* 50**,** 2477-2483.

HABAS, EMMANUEL PAVIE, ALAIN LAPP & PEYRELASSE, J. 2004. Understanding the complex rheological behavior of PEO–PPO–PEO copolymers in aqueous solution. *Journal of Rheology,* 48**,** 1-21.

HAMLEY, I. W. 1998. *The Physics of Block Copolymers*, Oxford University Press.

HAMLEY, I. W. 2000. *Introduction to soft matter: polymers, colloids amphiphiles, and liquid crystals*, Wiley.

HAMLEY, I. W. 2005. *Block Copolymers in Solution: Fundamentals and Applications*, Wiley.

HAMLEY, I. W., POPLE, J. A., BOOTH, C., DERICI, L., IMPÉROR-CLERC, M. & DAVIDSON, P. 1998a. Shear-induced orientation of the body-centered-cubic phase in a diblock copolymer gel. *Physical Review E,* 58**,** 7620-7628.

HAMLEY, I. W., POPLE, J. A., BOOTH, C., YANG, Y. W. & KING, S. M. 1998b. A Small-Angle Neutron-Scattering Study of Shear-Induced Ordering in the Cubic Phase of a Block Copolymer Gel. *Langmuir,* 14**,** 3182-3186.

HAMMOUDA, B. & HO, D. L. 2007. Insight into chain dimensions in PEO/water solutions. *Journal of Polymer Science Part B: Polymer Physics,* 45**,** 2196-2200.
HATEFI, A. & AMSDEN, B. 2002. Biodegradable injectable in situ forming drug delivery systems. *Journal of Controlled Release,* 80**,** 9-28.
HAUPTMEIER, B. & BECKER, A. 2007. *Neramexane MR matrix tablet* US patent application.
HENNINK, W. E. & VAN NOSTRUM, C. F. 2002. Novel crosslinking methods to design hydrogels. *Advanced Drug Delivery Reviews,* 54**,** 13-36.
HENRY, N., CLOUET, J., FRAGALE, A., GRIVEAU, L., CHÉDEVILLE, C., VÉZIERS, J., WEISS, P., LE BIDEAU, J., GUICHEUX, J. & LE VISAGE, C. 2017. Pullulan microbeads/Si-HPMC hydrogel injectable system for the sustained delivery of GDF-5 and TGF-β1: new insight into intervertebral disc regenerative medicine. *Drug Delivery,* 24**,** 999-1010.
HERRERO-VANRELL, R., RINCON, A. C., ALONSO, M., REBOTO, V., MOLINA-MARTINEZ, I. T. & RODRIGUEZ-CABELLO, J. C. 2005. Self-assembled particles of an elastin-like polymer as vehicles for controlled drug release. *J Control Release,* 102**,** 113-22.
HEYMANN, E. 1935. Studies on sol-gel transformations. I. The inverse sol-gel transformation of methylcellulose in water. *Transactions of the Faraday Society,* 31**,** 846-864.
HIGGINS, J. S., BLAKE, S., TOMLINS, P. E., ROSS-MURPHY, S. B., STAPLES, E., PENFOLD, J. & DAWKINS, J. V. 1988. Comparison of the structural and rheological consequences of micelle formation in solutions of a model di-block copolymer. *Polymer,* 29**,** 1968-1978.
HOARE, T. R. & KOHANE, D. S. 2008. Hydrogels in drug delivery: Progress and challenges. *Polymer,* 49**,** 1993-2007.
HOFFMAN, A. S. 1995. "Intelligent" Polymers in Medicine and Biotechnology. *Artificial Organs,* 19**,** 458-467.
HÖHNE, G., HEMMINGER, W. & FLAMMERSHEIM, H.-J. 2003. *Differential scanning calorimetry*, Springer Science & Business Media.
HUH, K. M., OOYA, T., LEE, W. K., SASAKI, S., KWON, I. C., JEONG, S. Y. & YUI, N. 2001. Supramolecular-Structured Hydrogels Showing a Reversible Phase Transition by Inclusion Complexation between Poly(ethylene glycol) Grafted Dextran and α-Cyclodextrin. *Macromolecules,* 34**,** 8657-8662.
HVIDT, S., JOERGENSEN, E. B., BROWN, W. & SCHILLEN, K. 1994. Micellization and Gelation of Aqueous Solutions of a Triblock Copolymer Studied by Rheological Techniques and Scanning Calorimetry. *The Journal of Physical Chemistry,* 98**,** 12320-12328.
HWANG, M. J., SUH, J. M., BAE, Y. H., KIM, S. W. & JEONG, B. 2005. Caprolactonic Poloxamer Analog: PEG-PCL-PEG. *Biomacromolecules,* 6**,** 885-890.
HYUN, K., NAM, J. G., WILHELLM, M., AHN, K. H. & LEE, S. J. 2006. Large amplitude oscillatory shear behavior of PEO-PPO-PEO triblock copolymer solutions. *Rheologica Acta,* 45**,** 239-249.
HYUN, K., WILHELM, M., KLEIN, C. O., CHO, K. S., NAM, J. G., AHN, K. H., LEE, S. J., EWOLDT, R. H. & MCKINLEY, G. H. 2011. A review of nonlinear oscillatory shear tests: Analysis and application of large amplitude oscillatory shear (LAOS). *Progress in Polymer Science,* 36**,** 1697-1753.

ICHIKAWA, H. & FUKUMORI, Y. 2000. A novel positively thermosensitive controlled-release microcapsule with membrane of nano-sized poly(N-isopropylacrylamide) gel dispersed in ethylcellulose matrix. *Journal of Controlled Release,* 63**,** 107-119.

ISRAELACHVILI, J. 1997. The different faces of poly(ethylene glycol). *Proceedings of the National Academy of Sciences,* 94**,** 8378-8379.

JALAAL, M., COTTRELL, G., BALMFORTH, N. & STOEBER, B. 2017. On the rheology of Pluronic F127 aqueous solutions. *Journal of Rheology,* 61**,** 139-146.

JEONG, B., BAE, Y. H. & KIM, S. W. 1999a. Thermoreversible Gelation of PEG−PLGA−PEG Triblock Copolymer Aqueous Solutions. *Macromolecules,* 32**,** 7064-7069.

JEONG, B., CHOI, Y. K., BAE, Y. H., ZENTNER, G. & KIM, S. W. 1999b. New biodegradable polymers for injectable drug delivery systems. *J Control Release,* 62**,** 109-14.

JEONG, B., KIM, S. W. & BAE, Y. H. 2002. Thermosensitive sol–gel reversible hydrogels. *Advanced Drug Delivery Reviews,* 54**,** 37-51.

JEONG, B., KIM, S. W. & BAE, Y. H. 2012. Thermosensitive sol–gel reversible hydrogels. *Advanced Drug Delivery Reviews,* 64, Supplement**,** 154-162.

JIANG, J., BURGER, C., LI, C., LI, J., LIN, M. Y., COLBY, R. H., RAFAILOVICH, M. H. & SOKOLOV, J. C. 2007. Shear-Induced Layered Structure of Polymeric Micelles by SANS. *Macromolecules,* 40**,** 4016-4022.

JIANG, J., LI, C., LOMBARDI, J., COLBY, R. H., RIGAS, B., RAFAILOVICH, M. H. & SOKOLOV, J. C. 2008. The effect of physiologically relevant additives on the rheological properties of concentrated Pluronic copolymer gels. *Polymer,* 49**,** 3561-3567.

JIN, R., HIEMSTRA, C., ZHONG, Z. & FEIJEN, J. 2007. Enzyme-mediated fast in situ formation of hydrogels from dextran–tyramine conjugates. *Biomaterials,* 28**,** 2791-2800.

JONES, R. A. 2002. *Soft condensed matter*, Oxford University Press.

JØRGENSEN, E. B., HVIDT, S., BROWN, W. & SCHILLÉN, K. 1997. Effects of Salts on the Micellization and Gelation of a Triblock Copolymer Studied by Rheology and Light Scattering. *Macromolecules,* 30**,** 2355-2364.

JOSEPH, J., DREISS, C. A., COSGROVE, T. & PEDERSEN, J. S. 2007. Rupturing Polymeric Micelles with Cyclodextrins. *Langmuir,* 23**,** 460-466.

JOSHI, S. C. 2011. Sol-Gel Behavior of Hydroxypropyl Methylcellulose (HPMC) in Ionic Media Including Drug Release. *Materials,* 4**,** 1861-1905.

KABASCI, S., & STEVENS, C 2013. *Wiley Series in Renewable Resource : Bio-Based Plastics : Materials and Applications,* Somerset, NJ, USA, John Wiley & Sons.

KATONO, H., SANUI, K., OGATA, N., OKANO, T. & SAKURAI, Y. 1991. Drug Release OFF Behavior and Deswelling Kinetics of Thermo-Responsive IPNs Composed of Poly(acrylamide-co-butyl methacrylate) and Poly(acrylic acid). *Polym J,* 23**,** 1179-1189.

KLOUDA, L. & MIKOS, A. G. 2008. Thermoresponsive hydrogels in biomedical applications. *Eur J Pharm Biopharm,* 68**,** 34-45.

KOBAYASHI, K., HUANG, C.-I. & LODGE, T. P. 1999. Thermoreversible Gelation of Aqueous Methylcellulose Solutions. *Macromolecules,* 32**,** 7070-7077.

LAFOLLETTE, T. A. & WALKER, L. M. 2011. Structural and Mechanical Hysteresis at the Order-Order Transition of Block Copolymer Micellar Crystals. *Polymers,* 3**,** 281.

LARSON, R. G. 1999. *The structure and rheology of complex fluids,* New York, Oxford university press.
LÄUGER, J. 2014. Strain-Rate Controlled Oscillation.
LAVAN, D. A., MCGUIRE, T. & LANGER, R. 2003. Small-scale systems for in vivo drug delivery. *Nat Biotechnol,* 21**,** 1184-91.
LEE, K. Y. & MOONEY, D. J. 2012. Alginate: Properties and biomedical applications. *Progress in Polymer Science,* 37**,** 106-126.
LEE, Y. S. 2008. *Self-Assembly and Nanotechnology: A Force Balance Approach*, John Wiley & Sons, Inc.
LEWIS, R. A., CHRISTIE, W. C., DAY, D. G., CRAVEN, E. R., WALTERS, T., BEJANIAN, M., LEE, S. S., GOODKIN, M. L., ZHANG, J., WHITCUP, S. M. & ROBINSON, M. R. 2017. Bimatoprost Sustained-Release Implants for Glaucoma Therapy: 6-Month Results From a Phase I/II Clinical Trial. *American Journal of Ophthalmology,* 175**,** 137-147.
LI, J., NI, X. & LEONG, K. W. 2003. Injectable drug-delivery systems based on supramolecular hydrogels formed by poly(ethylene oxide)s and α-cyclodextrin. *Journal of Biomedical Materials Research Part A,* 65A**,** 196-202.
LI, L., THANGAMATHESVARAN, P. M., YUE, C. Y., TAM, K. C., HU, X. & LAM, Y. C. 2001. Gel Network Structure of Methylcellulose in Water. *Langmuir,* 17**,** 8062-8068.
LI, X. & HYUN, K. 2018. Rheological study of the effect of polyethylene oxide (PEO) homopolymer on the gelation of PEO-PPO-PEO triblock copolymer in aqueous solution. *Korea-Australia Rheology Journal,* 30**,** 109-125.
LI, X., PARK, E.-K., HYUN, K., OKTAVIA, L. & KWAK, M. 2017. Rheological analysis of core-stabilized Pluronic F127 by semi-interpenetrating network (sIPN) in aqueous solution. *Journal of Rheology,* 62**,** 107-120.
LI, Y., SHI, T., SUN, Z., AN, L. & HUANG, Q. 2006. Investigation of Sol−Gel Transition in Pluronic F127/D2O Solutions Using a Combination of Small-Angle Neutron Scattering and Monte Carlo Simulation. *The Journal of Physical Chemistry B,* 110**,** 26424-26429.
LIN, G., COSIMBESCU, L., KARIN, N. J. & TARASEVICH, B. J. 2012. Injectable and thermosensitive PLGA-g-PEG hydrogels containing hydroxyapatite: preparation, characterization and in vitro release behavior. *Biomed Mater,* 7**,** 024107.
LIN, Y. & ALEXANDRIDIS, P. 2002. Temperature-Dependent Adsorption of Pluronic F127 Block Copolymers onto Carbon Black Particles Dispersed in Aqueous Media. *The Journal of Physical Chemistry B,* 106**,** 10834-10844.
LINSE, P. & MALMSTEN, M. 1992. Temperature-dependent micellization in aqueous block copolymer solutions. *Macromolecules,* 25**,** 5434-5439.
LIU, L., TANG, X., WANG, Y. & GUO, S. 2011. Smart gelation of chitosan solution in the presence of NaHCO3 for injectable drug delivery system. *International Journal of Pharmaceutics,* 414**,** 6-15.
LIU, S. & LI, L. 2015. Multiple Phase Transition and Scaling Law for Poly(ethylene oxide)–Poly(propylene oxide)–Poly(ethylene oxide) Triblock Copolymer in Aqueous Solution. *ACS Applied Materials & Interfaces,* 7**,** 2688-2697.
LIU, W., ZHANG, B., LU, W. W., LI, X., ZHU, D., DE YAO, K., WANG, Q., ZHAO, C. & WANG, C. 2004. A rapid temperature-responsive sol–gel reversible poly(N-isopropylacrylamide)-g-methylcellulose copolymer hydrogel. *Biomaterials,* 25**,** 3005-3012.

LÓPEZ-BARRÓN, C. R., WAGNER, N. J. & PORCAR, L. 2015. Layering, melting, and recrystallization of a close-packed micellar crystal under steady and large-amplitude oscillatory shear flows. *Journal of Rheology,* 59**,** 793-820.
MACOSKO, C. W. 1994. *Rheology: principles, measurements, and applications*, VCH.
MADLENER, K., FREY, B. & CIEZKI, H. 2009. Generalized reynolds number for non-newtonian fluids. *Progress in Propulsion Physics,* 1**,** 237-250.
MALMSTEN, M. & LINDMAN, B. 1992. Self-assembly in aqueous block copolymer solutions. *Macromolecules,* 25**,** 5440-5445.
MALMSTEN, M. & LINDMAN, B. 1993. Effects of homopolymers on the gel formation in aqueous block copolymer solutions. *Macromolecules,* 26**,** 1282-1286.
MANNEVILLE, S. 2008. Recent experimental probes of shear banding. *Rheologica Acta,* 47**,** 301-318.
MANNEVILLE, S., COLIN, A., WATON, G. & SCHOSSELER, F. 2007. Wall slip, shear banding, and instability in the flow of a triblock copolymer micellar solution. *Physical Review E,* 75**,** 061502.
MARTÍNEZ-SANZ, E., OSSIPOV, D. A., HILBORN, J., LARSSON, S., JONSSON, K. B. & VARGHESE, O. P. 2011. Bone reservoir: Injectable hyaluronic acid hydrogel for minimal invasive bone augmentation. *Journal of Controlled Release,* 152**,** 232-240.
MASSODI, I., THOMAS, E. & RAUCHER, D. 2009. Application of thermally responsive elastin-like polypeptide fused to a lactoferrin-derived peptide for treatment of pancreatic cancer. *Molecules,* 14**,** 1999-2015.
MATANOVIĆ, M. R., KRISTL, J. & GRABNAR, P. A. 2014. Thermoresponsive polymers: Insights into decisive hydrogel characteristics, mechanisms of gelation, and promising biomedical applications. *International Journal of Pharmaceutics,* 472**,** 262-275.
MAYOL, L., DE STEFANO, D., DE FALCO, F., CARNUCCIO, R., MAIURI, M. C. & DE ROSA, G. 2014. Effect of hyaluronic acid on the thermogelation and biocompatibility of its blends with methyl cellulose. *Carbohydrate Polymers,* 112**,** 480-485.
MCCONNELL, G. A., LIN, M. Y. & GAST, A. P. 1995. Long Range Order in Polymeric Micelles under Steady Shear. *Macromolecules,* 28**,** 6754-6764.
MEZGER, T. G. 2011. *The rheology handbook : for users of rotational and oscillatory rheometers,* Hannover, Vincentz Network GmbH & Co KG.
MEZGER, T. G. 2015. *Applied Rheology: With Joe Flow on Rheology Road*, Paar.
MEZNARICH, N. A. K. 2012. *Effect of Ternary Solutes on the Evolution of Structure and Gel Formation in Amphiphilic Copolymer Solutions.* Ph.D. Thesis, The University of Michigan.
MORTENSEN, K., BATSBERG, W. & HVIDT, S. 2008. Effects of PEO−PPO Diblock Impurities on the Cubic Structure of Aqueous PEO−PPO−PEO Pluronics Micelles: fcc and bcc Ordered Structures in F127. *Macromolecules,* 41**,** 1720-1727.
MORTENSEN, K. & PEDERSEN, J. S. 1993. Structural study on the micelle formation of poly(ethylene oxide)-poly(propylene oxide)-poly(ethylene oxide) triblock copolymer in aqueous solution. *Macromolecules,* 26**,** 805-812.
MORTENSEN, K. & TALMON, Y. 1995. Cryo-TEM and SANS Microstructural Study of Pluronic Polymer Solutions. *Macromolecules,* 28**,** 8829-8834.

MUELLER, K. F. & HEIBER, S. J. 1985. *Crosslinked, porous polymers for controlled drug delivery* US patent application. 1985-10-22.

MUKAE, K., BAE, Y. H., OKANO, T. & KIM, S. W. 1990. A Thermo-Sensitive Hydrogel: Poly (ethylene oxide-dimethyl siloxane-ethylene oxide)/Poly (N-isopropyl acrylamide) Interpenetrating Polymer Networks II. On-Off Regulation of Solute Release from Thermo-Sensitive Hydrogel. *Polymer Journal,* 22**,** 250-265.

MURDAN, S., ANDRÝSEK, T. & SON, D. 2005. Novel gels and their dispersions—oral drug delivery systems for ciclosporin. *International Journal of Pharmaceutics,* 300**,** 113-124.

NISBET, D. R., CROMPTON, K. E., HAMILTON, S. D., SHIRAKAWA, S., PRANKERD, R. J., FINKELSTEIN, D. I., HORNE, M. K. & FORSYTHE, J. S. 2006. Morphology and gelation of thermosensitive xyloglucan hydrogels. *Biophysical Chemistry,* 121**,** 14-20.

PADOŁ, A. M. 2016. Influence of oligoguluronates on alginate gelation and on alginate gel properties.

PANDIT, N. K. & MCGOWAN, R. 1998. Gelation of Pluronic® F127-Polyethylene Glycol Mixtures: Relationship to PEG Molecular Weight. *Drug Development and Industrial Pharmacy,* 24**,** 183-186.

PARK, K. M. & PARK, K. D. 2017. Injectable Hydrogels: Properties and Applications. *Encyclopedia of Polymer Science and Technology.*

PATENAUDE, M., SMEETS, N. M. B. & HOARE, T. 2014. Designing Injectable, Covalently Cross-Linked Hydrogels for Biomedical Applications. *Macromolecular Rapid Communications,* 35**,** 598-617.

PENG, Q., SUN, X., GONG, T., WU, C. Y., ZHANG, T., TAN, J. & ZHANG, Z. R. 2013. Injectable and biodegradable thermosensitive hydrogels loaded with PHBHHx nanoparticles for the sustained and controlled release of insulin. *Acta Biomater,* 9**,** 5063-9.

PEPPAS, N. A., BURES, P., LEOBANDUNG, W. & ICHIKAWA, H. 2000. Hydrogels in pharmaceutical formulations. *European Journal of Pharmaceutics and Biopharmaceutics,* 50**,** 27-46.

PHAM TRONG, L. C., DJABOUROV, M. & PONTON, A. 2008. Mechanisms of micellization and rheology of PEO–PPO–PEO triblock copolymers with various architectures. *Journal of Colloid and Interface Science,* 328**,** 278-287.

POCHAN, D. J., SCHNEIDER, J. P., KRETSINGER, J., OZBAS, B., RAJAGOPAL, K. & HAINES, L. 2003. Thermally Reversible Hydrogels via Intramolecular Folding and Consequent Self-Assembly of a de Novo Designed Peptide. *Journal of the American Chemical Society,* 125**,** 11802-11803.

POZZO, D. C. & WALKER, L. M. 2007a. Shear Orientation of Nanoparticle Arrays Templated in a Thermoreversible Block Copolymer Micellar Crystal. *Macromolecules,* 40**,** 5801-5811.

POZZO, D. C. & WALKER, L. M. 2007b. Small-angle neutron scattering of silica nanoparticles templated in PEO–PPO–PEO cubic crystals. *Colloids and Surfaces A: Physicochemical and Engineering Aspects,* 294**,** 117-129.

PRAGATHEESWARAN, A. M. & CHEN, S. B. 2013. Effect of Chain Length of PEO on the Gelation and Micellization of the Pluronic F127 Copolymer Aqueous System. *Langmuir,* 29**,** 9694-9701.

PRICE, R., POURSAID, A. & GHANDEHARI, H. 2014. Controlled release from recombinant polymers. *Journal of Controlled Release,* 190**,** 304-313.

PRIYA JAMES, H., JOHN, R., ALEX, A. & ANOOP, K. R. 2014. Smart polymers for the controlled delivery of drugs – a concise overview. *Acta Pharmaceutica Sinica B,* 4**,** 120-127.

PRUD'HOMME, R. K., WU, G. & SCHNEIDER, D. K. 1996. Structure and Rheology Studies of Poly(oxyethylene−oxypropylene−oxyethylene) Aqueous Solution. *Langmuir,* 12**,** 4651-4659.

QIAO, M., CHEN, D., MA, X. & LIU, Y. 2005. Injectable biodegradable temperature-responsive PLGA–PEG–PLGA copolymers: Synthesis and effect of copolymer composition on the drug release from the copolymer-based hydrogels. *International Journal of Pharmaceutics,* 294**,** 103-112.

QIU, Y. & PARK, K. 2012. Environment-sensitive hydrogels for drug delivery. *Advanced Drug Delivery Reviews,* 64, Supplement**,** 49-60.

RANADE, V. V. & CANNON, J. B. 2011. *Drug Delivery Systems, Third Edition*, Taylor & Francis.

RICARDO, N. M. P. S., RICARDO, N. M. P. S., COSTA, F. D. M. L. L., BEZERRA, F. W. A., CHAIBUNDIT, C., HERMIDA-MERINO, D., GREENLAND, B. W., BURATTINI, S., HAMLEY, I. W., KEITH NIXON, S. & YEATES, S. G. 2012. Effect of water-soluble polymers, polyethylene glycol and poly(vinylpyrrolidone), on the gelation of aqueous micellar solutions of Pluronic copolymer F127. *Journal of Colloid and Interface Science,* 368**,** 336-341.

ROE, R. J. 2000. *Methods of X-ray and Neutron Scattering in Polymer Science*, Oxford University Press.

ROWLEY, J. A., MADLAMBAYAN, G. & MOONEY, D. J. 1999. Alginate hydrogels as synthetic extracellular matrix materials. *Biomaterials,* 20**,** 45-53.

RUEL-GARIÉPY, E., CHENITE, A., CHAPUT, C., GUIRGUIS, S. & LEROUX, J. C. 2000. Characterization of thermosensitive chitosan gels for the sustained delivery of drugs. *International Journal of Pharmaceutics,* 203**,** 89-98.

RUEL-GARIÉPY, E. & LEROUX, J.-C. 2004. In situ-forming hydrogels—review of temperature-sensitive systems. *European Journal of Pharmaceutics and Biopharmaceutics,* 58**,** 409-426.

RUEL-GARIÉPY, E., SHIVE, M., BICHARA, A., BERRADA, M., LE GARREC, D., CHENITE, A. & LEROUX, J.-C. 2004. A thermosensitive chitosan-based hydrogel for the local delivery of paclitaxel. *European Journal of Pharmaceutics and Biopharmaceutics,* 57**,** 53-63.

SADEGHI, G. M. M. & SAYAF, M. 2014. Chapter 7 - Nanostructure Formation in Block Copolymers. *In:* THOMAS, S., SHANKS, R. & CHANDRASEKHARAKURUP, S. (eds.) *Nanostructured Polymer Blends.* Oxford: William Andrew Publishing.

SANOJ REJINOLD, N., SREEREKHA, P. R., CHENNAZHI, K. P., NAIR, S. V. & JAYAKUMAR, R. 2011. Biocompatible, biodegradable and thermo-sensitive chitosan-g-poly (N-isopropylacrylamide) nanocarrier for curcumin drug delivery. *International Journal of Biological Macromolecules,* 49**,** 161-172.

SCHMOLKA, I. R. 1972. Artificial skin I. Preparation and properties of pluronic F-127 gels for treatment of burns. *Journal of Biomedical Materials Research,* 6**,** 571-582.

SELIKTAR, D. 2012. Designing Cell-Compatible Hydrogels for Biomedical Applications. *Science,* 336**,** 1124-1128.
SHARMA, S., NIJDAM, A. J., SINHA, P. M., WALCZAK, R. J., LIU, X., CHENG, M. M. C. & FERRARI, M. 2006. Controlled-release microchips. *Expert Opinion on Drug Delivery,* 3**,** 379-394.
SHIN, Y., CHANG, J. H., LIU, J., WILLIFORD, R., SHIN, Y.-K. & EXARHOS, G. J. 2001. Hybrid nanogels for sustainable positive thermosensitive drug release. *Journal of Controlled Release,* 73**,** 1-6.
SHIRAKAWA, M., YAMATOYA, K. & NISHINARI, K. 1998. Tailoring of xyloglucan properties using an enzyme. *Food Hydrocolloids,* 12**,** 25-28.
SIGMA-ALDRICH 2018. Sigma Aldrich.
SIM, H. G., AHN, K. H. & LEE, S. J. 2003. Large amplitude oscillatory shear behavior of complex fluids investigated by a network model: a guideline for classification. *Journal of Non-Newtonian Fluid Mechanics,* 112**,** 237-250.
SIMÕES, S. M. N., VEIGA, F., RIBEIRO, A. C. F., FIGUEIRAS, A. R., TABOADA, P., CONCHEIRO, A. & ALVAREZ-LORENZO, C. 2014. Supramolecular gels of poly-α-cyclodextrin and PEO-based copolymers for controlled drug release. *European Journal of Pharmaceutics and Biopharmaceutics,* 87**,** 579-588.
SIMÕES, S. M. N., VEIGA, F., TORRES-LABANDEIRA, J. J., RIBEIRO, A. C. F., SANDEZ-MACHO, M. I., CONCHEIRO, A. & ALVAREZ-LORENZO, C. 2012. Syringeable Pluronic–α-cyclodextrin supramolecular gels for sustained delivery of vancomycin. *European Journal of Pharmaceutics and Biopharmaceutics,* 80**,** 103-112.
SINGH, P. & PANDEY, S. 2007. Solute–solvent interactions within aqueous poly(ethylene glycol): solvatochromic probes for empirical determination and preferential solvation. *Green Chemistry,* 9**,** 254-261.
SINGLA, P., CHABBA, S. & MAHAJAN, R. K. 2016. A systematic physicochemical investigation on solubilization and in vitro release of poorly water soluble oxcarbazepine drug in pluronic micelles. *Colloids and Surfaces A: Physicochemical and Engineering Aspects,* 504**,** 479-488.
ŠKVARLA, J., ZEDNÍK, J., ŠLOUF, M., PISPAS, S. & ŠTĚPÁNEK, M. 2014. Poly(N-isopropyl acrylamide)-block-poly(n-butyl acrylate) thermoresponsive amphiphilic copolymers: Synthesis, characterization and self-assembly behavior in aqueous solutions. *European Polymer Journal,* 61**,** 124-132.
SLAWECKI, T. M., GLINKA, C. J. & HAMMOUDA, B. 1998. Shear-induced micellar crystal structures in an aqueous triblock copolymer solution. *Physical Review E,* 58**,** R4084-R4087.
SOLEDAD LENCINA, M. M., IATRIDI, Z., VILLAR, M. A. & TSITSILIANIS, C. 2014. Thermoresponsive hydrogels from alginate-based graft copolymers. *European Polymer Journal,* 61**,** 33-44.
SUN, G., ZHANG, X.-Z. & CHU, C.-C. 2008. Effect of the molecular weight of polyethylene glycol (PEG) on the properties of chitosan-PEG-poly(N-isopropylacrylamide) hydrogels. *Journal of Materials Science: Materials in Medicine,* 19**,** 2865-2872.
TAN, R., SHE, Z., WANG, M., FANG, Z., LIU, Y. & FENG, Q. 2012. Thermo-sensitive alginate-based injectable hydrogel for tissue engineering. *Carbohydrate Polymers,* 87**,** 1515-1521.

TASSIERI, M., LAURATI, M., CURTIS, D. J., AUHL, D. W., COPPOLA, S., SCALFATI, A., HAWKINS, K., WILLIAMS, P. R. & COOPER, J. M. 2016. i-Rheo: Measuring the materials' linear viscoelastic properties “in a step”! *Journal of Rheology,* 60**,** 649-660.

TATE, M. C., SHEAR, D. A., HOFFMAN, S. W., STEIN, D. G. & LAPLACA, M. C. 2001. Biocompatibility of methylcellulose-based constructs designed for intracerebral gelation following experimental traumatic brain injury. *Biomaterials,* 22**,** 1113-1123.

THOMAS, L. C. 2001. Use of multiple heating rate DSC and modulated temperature DSC to detect and analyze temperature-time-dependent transitions in materials. *American Laboratory,* 33**,** 26-31.

THOMAS, L. C. 2005. Modulated DSC paper 3: Modulated DSC basics; Optimization of MDSC experimental conditions. *Technical report, TA Instruments*.

THOMPSON, A. L. & LOVE, B. J. 2017. Thermodynamic properties of aqueous PEO–PPO–PEO micelles of varying hydrophilicity with added cisplatin determined by differential scanning calorimetry. *Journal of Thermal Analysis and Calorimetry,* 127**,** 1583-1592.

TREBBIN, M., STEINHAUSER, D., PERLICH, J., BUFFET, A., ROTH, S. V., ZIMMERMANN, W., THIELE, J. & FÖRSTER, S. 2013. Anisotropic particles align perpendicular to the flow direction in narrow microchannels. *Proceedings of the National Academy of Sciences,* 110**,** 6706-6711.

TROY, D. B., REMINGTON, J. P. & BERINGER, P. 2006. *Remington: The Science and Practice of Pharmacy*, Lippincott Williams & Wilkins.

URAKI, Y., IMURA, T., KISHIMOTO, T. & UBUKATA, M. 2004. Body temperature-responsive gels derived from hydroxypropylcellulose bearing lignin. *Carbohydrate Polymers,* 58**,** 123-130.

URAKI, Y., IMURA, T., KISHIMOTO, T. & UBUKATA, M. 2006. Body temperature-responsive gels derived from hydroxypropylcellulose bearing lignin II: adsorption and release behavior. *Cellulose,* 13**,** 225-234.

VALERO, M., CASTIGLIONE, F., MELE, A., DA SILVA, M. A., GRILLO, I., GONZÁLEZ-GAITANO, G. & DREISS, C. A. 2016. Competitive and Synergistic Interactions between Polymer Micelles, Drugs, and Cyclodextrins: The Importance of Drug Solubilization Locus. *Langmuir,* 32**,** 13174-13186.

VINTILOIU, A. & LEROUX, J.-C. 2008. Organogels and their use in drug delivery — A review. *Journal of Controlled Release,* 125**,** 179-192.

WACH, R. A., MITOMO, H., YOSHII, F. & KUME, T. 2002. Hydrogel of Radiation-Induced Cross-Linked Hydroxypropylcellulose. *Macromolecular Materials and Engineering,* 287**,** 285-295.

WANKA, G., HOFFMANN, H. & ULBRICHT, W. 1990. The aggregation behavior of poly-(oxyethylene)-poly-(oxypropylene)-poly-(oxyethylene)-block-copolymers in aqueous solution. *Colloid and Polymer Science,* 268**,** 101-117.

WANKA, G., HOFFMANN, H. & ULBRICHT, W. 1994. Phase Diagrams and Aggregation Behavior of Poly(oxyethylene)-Poly(oxypropylene)-Poly(oxyethylene) Triblock Copolymers in Aqueous Solutions. *Macromolecules,* 27**,** 4145-4159.

WARD, M. A. & GEORGIOU, T. K. 2011. Thermoresponsive Polymers for Biomedical Applications. *Polymers,* 3**,** 1215-1242.

WATON, G., MICHELS, B., STEYER, A. & SCHOSSELER, F. 2004. Shear-Induced Demixing and Shear-Banding Instabilities in Dilute Triblock Copolymer Solutions. *Macromolecules,* 37**,** 2313-2321.

WEI, H., ZHANG, X.-Z., CHEN, W.-Q., CHENG, S.-X. & ZHUO, R.-X. 2007. Self-assembled thermosensitive micelles based on poly(L-lactide-star block-N-isopropylacrylamide) for drug delivery. *Journal of Biomedical Materials Research Part A,* 83A**,** 980-989.

WERBOWYJ, R. S. & GRAY, D. G. 1980. Ordered Phase Formation in Concentrated Hydroxpropylcellulose Solutions. *Macromolecules,* 13**,** 69-73.

WU, C., LIU, T., CHU, B., SCHNEIDER, D. K. & GRAZIANO, V. 1997. Characterization of the PEO−PPO−PEO Triblock Copolymer and Its Application as a Separation Medium in Capillary Electrophoresis. *Macromolecules,* 30**,** 4574-4583.

WYSS, H. M., MIYAZAKI, K., MATTSSON, J., HU, Z., REICHMAN, D. R. & WEITZ, D. A. 2007. Strain-Rate Frequency Superposition: A Rheological Probe of Structural Relaxation in Soft Materials. *Physical Review Letters,* 98**,** 238303.

YAN, C., MACKAY, M. E., CZYMMEK, K., NAGARKAR, R. P., SCHNEIDER, J. P. & POCHAN, D. J. 2012. Injectable Solid Peptide Hydrogel as Cell Carrier: Effects of Shear Flow on Hydrogel and Cell Payload. *Langmuir : the ACS journal of surfaces and colloids,* 28**,** 6076-6087.

YOSHIDA, T., LAI, T. C., KWON, G. S. & SAKO, K. 2013. pH- and ion-sensitive polymers for drug delivery. *Expert opinion on drug delivery,* 10**,** 1497-1513.

YU, Y., DENG, C., MENG, F., SHI, Q., FEIJEN, J. & ZHONG, Z. 2011. Novel injectable biodegradable glycol chitosan-based hydrogels crosslinked by Michael-type addition reaction with oligo(acryloyl carbonate)-b-poly(ethylene glycol)-b-oligo(acryloyl carbonate) copolymers. *Journal of Biomedical Materials Research Part A,* 99A**,** 316-326.

ZENG, F., LEE, H., CHIDIAC, M. & ALLEN, C. 2005. Synthesis and Characterization of Six-Arm Star Poly(δ-valerolactone)-block-Methoxy Poly(ethylene glycol) Copolymers. *Biomacromolecules,* 6**,** 2140-2149.

ZHANG, M., DJABOUROV, M., BOURGAUX, C. & BOUCHEMAL, K. 2013. Nanostructured fluids from pluronic® mixtures. *International Journal of Pharmaceutics,* 454**,** 599-610.

ZHANG, X.-Z. & CHU, C.-C. 2005. Fabrication and characterization of microgel-impregnated, thermosensitive PNIPAAm hydrogels. *Polymer,* 46**,** 9664-9673.

ZHOU, Q., RUTLAND, M., TEERI, T. & BRUMER, H. 2007. Xyloglucan in cellulose modification. *Cellulose,* 14**,** 625-641.

ZHOU, Z. & CHU, B. 1988. Anomalous micellization behavior and composition heterogeneity of a triblock ABA copolymer of (A) ethylene oxide and (B) propylene oxide in aqueous solution. *Macromolecules,* 21**,** 2548-2554.